EPFL

Thèse n° 8627

Non-destructive Prediction of the Buckling Load of Cylindrical Shells

Présentée le 7 octobre 2022

Faculté des sciences et techniques de l'ingénieur
Complexité émergente dans les systèmes physiques
Programme doctoral en mécanique

pour l'obtention du grade de Docteur ès Sciences

par

Emilio José LOZANO VAZQUEZ

Acceptée sur proposition du jury

Prof. F. Gallaire, président du jury
Prof. T. Schneider, directeur de thèse
Prof. S. Pellegrino, rapporteur
Prof. S. Rubinstein, rapporteur
Prof. J.-F. Molinari, rapporteur

École polytechnique fédérale de Lausanne

2022

Ad Astra
Per Aspera

To my family

Acknowledgements

Thank you to everyone that supported and helped me through all the effort that lead to this thesis.

Lausanne, August 16, 2022 E. L.

Abstract

The current research focuses on the prediction of the maximum axial compression load a cylindrical shell is able to bear. This maximum axial compression load is the value at which a cylindrical shell loses stability and abruptly buckles. After the buckling event the shells are permanently damaged and become unfit for any structural function. Hence, buckling is a critical not admissible failure mode in the design of shell structures. Standard methodologies available in the literature such as linear stability analysis fail to deliver an accurate prediction and overestimate the value of the load at which collapse occurs. The reason for this deviation between real shells and theory is the presence of geometric imperfections that are unique for each shell. In fact, nominally identical shells exhibit large variations in their load bearing capability. This variability means that the only reliable approach able to obtain the real loading bearing capability previous to this research is a destructive compression test.

In this thesis, a new conceptual approach to describe the behaviour of cylindrical shells is introduced. The new description is based on the dynamical systems approach used to study turbulence in the field of fluid dynamics. Using the dynamical systems approach applied to a non-linear formulation of the shell equations, fixed points of the dynamical system are calculated and their stability under finite amplitude perturbations characterised. The boundary delimiting the transitions to a buckled state or returning to the unbuckled one is also characterised. The basin enclosed by this boundary, the basin of attraction, becomes smaller as the axial load is increased, vanishing at the compression load at which a cylindrical shell buckles. The shrinking of the basin of attraction can be characterised by evaluating its extension at different axial loads. This can be done by probing cylindrical shells. This probing at different axial compression loads defines a landscape that can be used to extrapolate the load at which the landscape, together with the basin of attractions vanishes. This axial compression load is the buckling load of the shell.

The framework described theoretically is implemented in a series of test campaigns to show the predictive capability of stability landscapes in real shells. Stability landscapes are the experimental technique employed to explore and characterise the basin of attraction associated with each fix point. The exploration of the basin of attraction is performed using a single poker that represents only one of the directions to perturb a fix point of the dynamical system towards the boundary of the basin of attraction. The success of extrapolating the buckling load with stability landscapes constructed with a single poker at a single location does not provide a perfect predictive capability in real shells. The reason for this is the complex interaction

between the imperfections present in real shells. The complex interaction between imperfections was also studied during this research, revealing that the buckling load of cylindrical shells is a function of all the imperfections present in the shell. The buckling load of a cylindrical shell is not dictated by the strongest imperfection alone, but by the combination of all defects.

The key output of the current research is a non-destructive test procedure based on constructing stability landscapes at different locations of the cylindrical shells. A test following this procedure has been able to provide a successful accurate prediction of the buckling load of a shell with realistic imperfections. This test procedure is believed to be a viable option to test in a non-destructive manner any cylindrical shell relevant for engineering applications.

Zusammenfassung

Die vorliegende Forschungsarbeit ist auf die Vorhersage der maximalen axialen Drucklast, der eine zylindrische Schale widerstehen kann, fokussiert. The maximale axiale Drucklast ist der Wert bei dem eine zylindrische Schale die Stabilität verliert und abrupt beult. Nach dem Beulvorgang sind die Schalen permanent beschädigt und können keine strukturelle Funktion mehr erfüllen. Daher ist das Beulen ein nicht zulässiger Fehlermodus in der Auslegung von Schalenstrukturen. Standardmethoden wie lineare Stabilitätsanalyse sind nicht in der Lage genaue Vorhersagen zu treffen und überschätzen die Last unter welcher das Beulen eintritt. Der Grund für diese Abweichung zwischen realen Schalen und der Theorie liegt in der Anwesenheit geometrischer Imperfektionen, welche einzigartig für jede einzelne Schale sind. In Realität zeigen augenscheinlich identische Schalen große Abweichungen in ihrer Lastkapazität. Diese Varianz bedeutet, dass die einzig verlässliche Methode die wahre Tragfähigkeit zu ermitteln darin liegt, zerstörende Tests durchzuführen.

In dieser Forschungsarbeit wird ein neuer konzeptioneller Ansatz zur Beschreibung des Verhaltens zylindrischer Schalen eingeführt. Die neue Beschreibung basiert auf dem dynamischen Systemansatz, der für die Untersuchung von Turbulenz im Bereich der Fluiddynamik verwendet wird. Unter Anwendung dieses Ansatzes auf die lineare Formulierung der Schalengleichungen werden Fixpunkte des dynamischen Systems berechnet und deren Stabilität unter finiten Amplitudenperturbationen charakterisiert. Die Grenzen, die die Transition von einem gebeulten Zustand in den ungebeulten Zustand und trennen, werden auch charakterisiert. Das Basin, welches von diesen Grenzen eingeschlossen wird, das Attraktionsbasin , wird mit der Erhöhung der axialen Last kleiner und verschwindet bei erreichen der Beullast. Das Schrumpfen des Attraktionsbasins kann charakterisiert werden, indem dessen Ausmaße unter den verschiedenen axialen Lasten durch testen zylindrischer Schalen ermittelt werden. Das Testen unter verschiedenen axialen Drucklasten definiert eine Charakteristik, welche für die Extrapolierung der Last unter welcher die Charakteristik zusammen mit dem Attraktionsbasin verschwindet. Diese axiale Drucklast ist die Beullast der Schale.

Das theoretisch beschriebene Rahmenwerk ist in einer Reihe von Testkampagnen implementiert, um die Vorhersagekraft der Stabilitätscharakteristiken in realen Schalen aufzuzeigen. Stabilitätscharakteristiken sind die experimentelle Methodik um das Attraktionsbasin an jedem Fixpunkt zu erforschen und zu beschreiben. Die Erforschung des Attraktionsbasins wird mit einem einzelnen Prüfstab durchgeführt, welcher eine einzelne Richtung für die Störung eins Fixpunktes des dynamischen Systems hinsichtlich der Grenze des Attraktionsbasins re-

präsentiert. Die Extrapolation der Beullast mit Stabilitätscharakteristiken, welche mit einem einzelnen Druckstab an einer einzelnen Stelle generiert wurden, liefert keine perfekte Vorhersagekapazität in realen Schalen. Der Grund dafür liegt in der komplexen Interaktion der Imperfektionen untereinander, welche in realen Schalen existiert. Die komplexe Interaktion der Imperfektionen untereinander wurde ebenfalls in dieser Forschungsarbeit untersucht und zeigt auf, dass die Beullast zylindrischer Schalen eine Funktion aller Imperfektionen in realen Schalen ist. Die Beullast einer zylindrischen Schale wird nicht ausschließlich durch die größte Imperfektion bestimmt.

Die Hauptergebnis der vorliegenden Forschung is eine zerstörungsfreie Testprozedur, welche auf Stabilitätscharakteristiken an verschiedenen Stellen der zylindrischen Schalen basiert. Ein Test nach dieser Testprozedur hat nachweislich die genaue Beullast einer Schale mit realen Imperfektionen.

Résumé

Cette recherche se concentre sur la prédiction de la charge de compression axiale maximale qu'une coque cylindrique est capable de supporter. Cette charge de compression axiale maximale est la valeur à laquelle une coque cylindrique perd sa stabilité et flambe brusquement. Après le flambage, les coques sont définitivement endommagées et deviennent impropres à toute fonction structurelle. Par conséquent, le flambement est un mode de défaillance critique non admissible dans la conception des structures en coque. Les méthodologies standard telles que l'analyse de stabilité linéaire ne parviennent pas à fournir une prédiction précise et surestiment la valeur de la charge à laquelle l'effondrement se produit. La raison de cet écart entre la théorie et la pratique est la présence d'imperfections géométriques propres à chaque coque. En effet, des coques supposées identiques présentent de grandes variations dans leur capacité de charge. Cet écart est la raison pour laquelle la seule approche fiable permettant d'obtenir la capacité portante réelle est un test de compression destructif.

Dans ce travail de recherche, une nouvelle approche conceptuelle pour décrire le comportement des coques cylindriques est introduite. Cette nouvelle approche est basée sur la théorie des systèmes dynamiques. Cette dernière est utilisée pour étudier la turbulence dans le domaine de la dynamique des fluides. En appliquant cette approche à une formulation non linéaire des équations de coque, les points fixes du système dynamique sont calculés et leur stabilité, sous des perturbations d'amplitude finie, caractérisée. La frontière, délimitant les transitions vers un état déformé ou retournant vers l'état non déformé, est également caractérisée. Le bassin entouré par cette limite, le bassin d'attraction, devient plus petit à mesure que la charge axiale augmente, disparaissant à la charge de compression à laquelle une coque cylindrique flambe. Le rétrécissement du bassin d'attraction peut être caractérisé en explorant, à différentes charges axiales, l'extension de celui-ci en sondant des coques cylindriques. Ce sondage à différentes charges de compression axiale définit un paysage qui peut être utilisé pour extrapoler la charge à laquelle le paysage ainsi que le bassin d'attractions disparaissent. Cette charge de compression axiale est la charge de flambement de la coque.

Ce cadre théorique est éprouvé dans une série de campagnes de tests pour montrer la capacité prédictive des paysages de stabilité dans des coques réelles. Les paysages de stabilité sont la technique expérimentale pour explorer et caractériser le bassin d'attraction associé à chaque point fixe. L'exploration du bassin d'attraction s'effectue à l'aide d'un tisonnier qui ne représente qu'une des directions pour perturber un point fixe du système dynamique vers la frontière du bassin d'attraction. L'extrapolation de la charge de flambement, avec

des paysages de stabilité construits avec un seul tisonnier à un seul endroit, ne fournit pas une capacité prédictive parfaite dans des coques réelles. La raison est l'interaction complexe entre les imperfections présentes dans les coques réelles. Cette interaction complexe entre les imperfections a également été étudiée au cours de cette recherche, révélant que la charge de flambement des coques cylindriques est fonction de toutes les imperfections présentes dans la coque. La charge de flambement d'une coque cylindrique n'est pas dictée par la seule imperfection la plus forte.

Un résultat clé de la recherche actuelle est une procédure de test non destructif basée sur la construction de paysages de stabilité à différents endroits des coques cylindriques. Un test, suivant cette procédure, a été en mesure de fournir une prédiction précise de la charge de flambement d'une coque avec des imperfections réalistes. Cette procédure de test est considérée comme une option viable pour tester de manière non destructive toute coque cylindrique utilisée dans des applications d'ingénierie.

Contents

Introduction

0.0.1 Buckling of Cylindrical Shells: The problem

Cylindrical shell structures are among the most efficient load bearing elements available to the structural engineering community. The main reason why cylindrical shell structures are so efficient structurally is the fact that they posses a high stiffness per unit of mass to react to in-plane loads and the associated membrane dominated stress states. The high stiffness per unit of mass that makes cylindrical shells structurally efficient also contributes to the main challenge to accurately predict their behaviour and stability.

One of the reasons for the difficulty in predicting the behaviour of real cylindrical shells lays in the fact that the bending stiffness of a cylindrical shell is much lower than its membrane stiffness. The membrane stiffness of a cylindrical shell is linearly proportional to the Young's modulus of the material E and the shell thickness h. While the bending stiffness, D, is proportional to h^3 and the Young's modulus of the material E in the following form $Eh^3/12(1-\nu)$ with ν being the Poisson's ratio of the material. Thus as h approaches small values, the bending stiffness decreases much faster than the membrane stiffness.

The difference between membrane and bending stiffness together with the zero Gauss curvature of perfect cylindrical shells makes any small deviation from an in-plane stress component induce significant radial displacements in the cylindrical shell. The consequence of those radial displacements is that as the load increases, radial deformation grows at a higher rate than in-plane deformations because radial deformations have a lower energy cost. Perfect shells can bend without stretching. Hence, the ease to develop radial deformations undermines the capability of a cylindrical shell to maintain a membrane dominated stress state.

Real shells have geometric imperfections that are not known. These unknown imperfections deteriorate membrane dominated states and promote radial deformations. The presence of the unknown geometric imperfections makes the application of standard stability theory an inaccurate tool to predict the stability behaviour of cylindrical shells. In the case where the imperfections are known, linear stability analysis is able to provide an accurate prediction but in most practical applications the imperfections are not know. The presence of the unknown geometrical imperfections decreases significantly the load bearing capabilities of cylindrical shells.

Despite the disadvantage of the difference between the membrane and the bending stiffness, and the influence of geometric imperfections, the advantages of using structural concepts based on cylindrical shells,namely their stiffness per unit of mass. This is the main reason for their ubiquity in high performance structures in use these days. Cylindrical shells can be found in a wide variety of applications ranging from offshore platforms to space launchers, wind turbines and aircraft. A small sample of these structures is shown in figure 1. These examples are small sample of the engineering achievements enabled by cylindrical shells structures.

(a) Offshore jig used in the extraction of oil. The main support structure are the cylindrical shells at the base.

(b) GE Heliade-X wind power generator. The tower lifting the generator unit is a shell structure that needs to accommodate the ever larger blades required to achieve the energy generation goals

(c) The A350-100 is one of the latest generation wide body aircraft where the main passenger volume is a cylindrical shell optimized to increase range and minimize fuel consumption

(d) Space Exploration technologies Starship is a next generation space launcher with all its main structural component based on cylindrical shells with the exceptions of the tank domes.

Figure 1 – Examples of engineering structures where structural concepts based on cylindrical shells are critical to perform the required mission.

The difference between membrane and bending stiffness of cylindrical shells is the root cause for the so-called imperfection sensitivity of these structures. The geometric imperfections are the factor making this difference of stiffness come into play affecting and influencing the behaviour and stability of thin cylindrical shells. The shell structures shown in figure 1 need to be manufactured and assembled. It is during these processes, with their characteristic tolerances and defects, that cylindrical shells become imperfect. The presence of these imperfections, mainly geometric, mean that the final shape presents deviations from the intended ideal cylindrical shape. An example of the imperfections of real cylindrical shells that have undergone a complex manufacturing and assembly process are shown in figure 2.

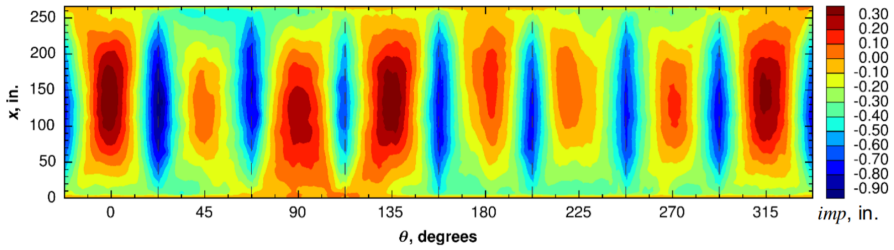

(a) Radial displacement deviation form the a perfect cylindrical shape obtained by NASA in a sub-scale legacy space shuttle cylindrical shell of 2.4 meters diameter. (Hilburger, 2012)

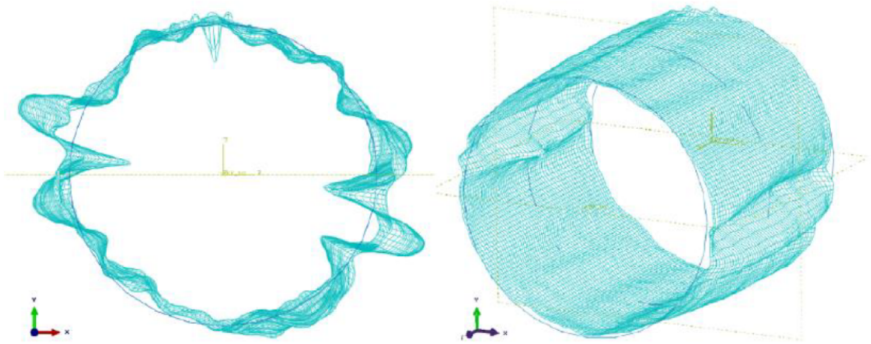

(b) Amplification of a 3 Dimensional representation of a measured imperfection of a cylindrical shell Degenhardt et al. (2012)

Figure 2 – Examples of characteristic imperfections present in aerospace grade cylindrical shells

It is nowadays an accepted fact that geometric imperfections distort cylindrical shells to the point where they can only bear less than half of the load that stability analysis predicts for the ideal geometry. There are other factors like loading or material imperfections, but geometrical imperfections are the main contributor (Babcock, 1983). An example of how the buckling load of cylindrical shells differs from the theoretical prediction of linear stability for the perfect cylindrical shell is shown in figure 3.

In this graphic, the solid line represents the normalized linear stability prediction. While the

dots correspond to experimental data from destructive compression tests of aerospace grade shells. The dashed line is an envelope of the empirical data known as the SP-8007. The SP-8007 guideline describes the knock-down factor to be applied to the linear stability buckling load prediction in order to have a conservative estimation of the actual load a cylindrical shell can bear. The knock-down factor is thus the ratio between the real buckling load of a cylindrical shell and that predicted by linear stability. The difference between the solid line and the dots representing experiments in figure 3 is the empirical evidence that motivates the current research.

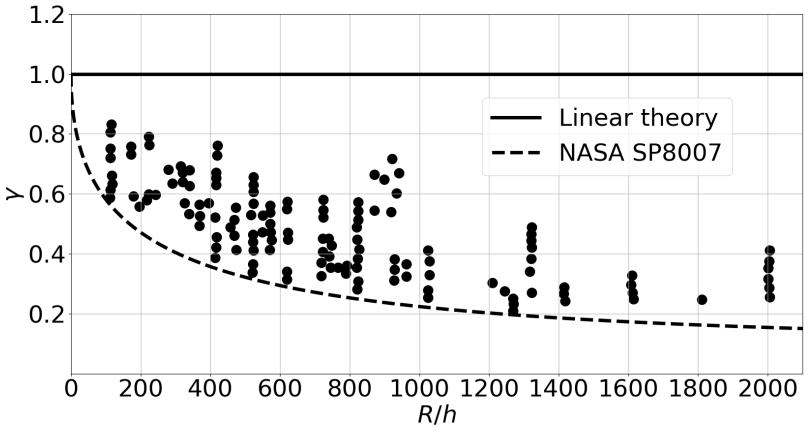

Figure 3 – Test data from the NASA SP-8007, this is a data set coming from a large test campaign of aerospace grade shells related to the development of the Apollo program (Seide, 1969)

The imperfections causing the deviation between the linear stability predictions of the buckling load and the real one are of stochastic nature. This means that beforehand, i.e. before the cylindrical shell is constructed, it is impossible to determine the exact imperfections present in it. In fact, if the buckling load of a cylindrical shell needs to be known with absolute certainty, a destructive compression test is the most reliable tool for this end. Indeed, to best of the knowledge of the author, there is no non-destructive test technique that has been used successfully in a full scale cylindrical shell to predict its buckling load.

In the case of cylindrical shells, the compression test is necessarily destructive because once the maximum force that the structure can bear is reached, the cylinder becomes unstable and loses a large portion of its load bearing capability. The implications of the lost of load bearing capability is that a large portion of the strain energy that was mostly stored in the form of membrane strain energy becomes bending strain energy (Almroth et al., 1973). Due to the difference between membrane and bending stiffness, storing similar amount of energy in the form of bending strain energy requires large radial displacements. These large displacements result in permanent damage for most material systems. This destructive nature of the buckling event of cylindrical shells is an additional motivation to be able to predict the buckling load of cylindrical shells in engineering applications. Because in engineering catastrophic failures

like the one characteristic of cylindrical shells are to be avoided.

Hence the main challenges to predict the buckling load of cylindrical shells can be summarised in the following points:

- The buckling load of a real shell cannot be predicted from the linear stability analysis of the perfect cylinder.
- The stochastic nature of the imperfections makes impossible to determine accurately the buckling load of a cylinder until it is manufactured.
- The destructive nature of the buckling event in cylindrical shells implies that currently there is no non-destructive approach to determine the buckling load of a cylindrical shell.

0.0.2 Shell buckling: Historical overview

The first formal studies about buckling of slender structures can be attributed to the Swiss mathematician Leonhard Euler in the $XVIII$ century (Euler, 1759). Afterwards, one century had to pass for the first experimental studies about buckling of cylindrical shells to occur. They were performed in the XIX century by Fairbairn and Hodgkinson to verify the tubular structures of a newly designed bridge (Fairbairn, 1859). The initial investigation about buckling of shells was done experimentally and there was no comparison established with any theoretical prediction.

The first theoretical prediction of the buckling load of a cylindrical shell would arrive at the beginning of the XX century. Based upon linear stability theory, Timoshenko (1914), Lorenz (1911) and Southwell (1914) derived independently the critical stress value at which a cylindrical shell buckles:

$$\sigma_{cr} = \frac{Eh}{\sqrt{3(1-\nu^2)}} \tag{1}$$

As the XX century progressed, the rapid evolution of the aeronautical industry dramatically increased the utilization of slender components like struts and shells. The utilization of these components led to intensive testing campaigns to verify the different designs. It was during these first testing campaigns that Lundquist (1934), Donnell (1933) and Flügge (1932) realised independently the large scatter of values of the buckling load for nominally identical shells and the deviation of these values with respect to the theoretical buckling load predicted by linear stability analysis of the perfect shell.

The deviation between experimental data and analytical predictions triggered a significant interest in the research community to tackle this apparent discrepancy. The seminal work of von Karman and Tsien suggested that the deviation between the linear stability threshold and

the experimental data was caused by the presence of geometric imperfections (Von Karman et al., 1940; Von Karman and Tsien, 1941). The hypothesis of von Karman and Tsien was proven mathematically by Koiter (1945). Koiter provided an analytical solution of the buckling load of a cylindrical shell including geometrical imperfections, obtaining a much lower buckling load than the one of the original perfect shell. Koiter used as a geometrical imperfection a superposition of trigonometric series that degraded the geometry in the radial direction of the cylindrical shell.

The next major leap in the research of buckling of cylindrical shells occurred at the beginning of the second half of the XX century. The space race encouraged the creation of ever larger and more efficient launchers that made extensive use of cylindrical shells. The issue of the deviation between theoretical predictions and experimental values became worse as the cylindrical shells got more slender (larger radius R over thickness h ratios). This worsening of the discrepancy between theoretical predictions and experimental values can be observed in the experimental data of NASA, see 3.

During the design of the launchers of the Apollo program, namely the Saturn V, NASA could not wait for the development of an analytical or numerical solution for predicting buckling loads of cylinders or to determine if such a methodology was even possible. Hence, they carried out a large test campaign with aerospace shells to derive an empirical lower bound of the knock-down factors to be applied to the linear stability predictions in order to obtain the maximum compression load a cylindrical shell could bear. This guideline is known as the NASA SP-8007 (Seide, 1969) and was in fact obtained based on the data already presented in figure 3. This guideline to obtain conservative buckling load predictions is still used nowadays in the preliminary design of critical structures such as space launchers.

It was also around the research effort to derive the NASA SP-8007 when the first ideas about introducing lateral probing appeared (Ricardo, 1967; Okubo et al., 1970). In the case of Ricardo and Okubo, the intention was to derive buckling loads under combined loading (compression and radial forces).

In the last decade of the XX century and the beginning of the XXI, with the advancement of computational capabilities, there have been developments in the direction of moving away from purely empirical methods. Two main approaches have appeared, both of them based on the extensive application of commercial finite element codes. The first one consists of the application of statistical design based on the application of imperfections that are generated either from real scans of cylindrical shells (Arbocz and Starnes, 2002) or synthetically (Elishakoff et al., 1996). The second approach consists of the application of worst-case imperfections with a low number of parameters to determine the minimum load a cylindrical shell can bear prior to manufacturing without resorting to destructive testing. In this second approach, lateral loads are used as imperfections (Castro et al., 2013) or dimples (Wullschleger, 2006). However, neither of the two approaches has led to a conclusion on how to determine the buckling load of a cylindrical shell accurately without resorting to its destructive testing.

In the last years, NASA is trying to develop new knock-down factor guidelines (Haynie and Hilburger, 2010; Hilburger, 2012). The direction followed in this case is based on the compilation of real imperfections because they are oriented towards a very specific geometry (Hilburger et al., 2012). To this end, NASA has been carrying a very ambitious test and analysis program based on the spare hardware form the Space Shuttle program (see figure 4) and the replication of the test via detailed finite element models. This work has been done under the umbrella of the Shell Knock-Down Factor project (Hilburger et al., 2018; Hilburger, 2018; Lovejoy and Hilburger, 2013; Lovejoy et al., 2018).

(a) Cylindrical test article with the speckle pattern required by a digital image correlation system to track deformation in real time during the loading sequence of an axial compression test

(b) Space shuttle heritage stiffened cylindrical shells. These section belong to the un-pressurized section of the main fuel tank of the vehicle

Figure 4 – Test set up and specimens used in the NASA shell buckling knock-down factor experimental buckling program

On the experimental side, the most notable development has been the vibration correlation technique proposed initially by Singer (Weller et al., 2002). The vibration correlation technique measures the natural frequencies of the corresponding structure as a function of the applied pre-load. Experimentally, it requires an acoustic excitation to visualize the variation of the natural frequencies of the cylindrical shell. This technique has also been investigated recently by DLR (Franzoni et al., 2019; Arbelo et al., 2014b) and Technion (Abramovich, 2021) in subscale specimens. The application of these techniques hinges in the dynamic excitation of the complete structure while it is being compressed. Nevertheless, the complex experimental set up associated with this technique makes it unpractical for its implementation in applications relevant for engineering.

0.0.3 Shell buckling: A new approach

Understanding the behaviour and stability of cylindrical shells is the focus of this research with a special focus on the prediction of the maximum axial compression force a cylindrical shell is able to bear prior to collapse. This collapse load is normally referred to as the spontaneous

buckling load or more plainly buckling load. As presented so far throughout this introduction, this seemingly simple question of how much load a cylindrical shell can carry has remained unanswered. In fact, to this date it is not possible to predict the buckling load of an engineering relevant cylindrical shell without recurring to destructive testing of the shell under study (Calladine, 1995).

On the analytical and numerical sides, the successful prediction of the buckling load of a cylindrical is directly not possible if the imperfections present are unknown. In fact, when standard linear theory is used to compute the stability threshold of cylindrical shells under compression, it significantly over-predicts it. The only feasible path to this date to predict the buckling load of a cylindrical shell without destructively testing it is hence building a very precise finite element model and performing a virtual test of it.

In the current research, a novel approach to study cylindrical shells and their behaviour at the onset of stability is discussed. This is done with the aim of predicting buckling loads for realistic cylindrical shells in a non-destructive manner. This new approach is based on the dynamical systems methodology used to study turbulence and shear flows transition in the field of fluid mechanics. Using this approach, cylindrical shells are modelled as a dynamical system of which equilibrium solutions, also referred to as fixed points, are calculated. Following the concepts of the dynamical system approach, the stability of each of those fixed points is studied to understand the behaviour of the system.

The dynamical system description of cylindrical shells allows for the modelling of their stability behaviour as a finite amplitude perturbation problem with a full non-linear description. This fact allows to define a set of perturbed states, that if the perturbation is removed will return to the unperturbed fixed point. The set of all possible perturbed states that satisfy this conditions define the basin of attraction associated with each fixed point.

The extension of the basin of attraction can be evaluated by perturbing the corresponding fixed point until it becomes unstable. The extension of the basin of attraction becomes smaller as the axial compression load exerted on the cylindrical shell increases, i.e. as the shell approaches the buckling point. In fact, there is a load level where the fixed point can only be infinitesimally perturbed that coincides with the maximum load the cylindrical shell can bear. This is the spontaneous buckling load or simply the buckling load.

The description in the state space of cylindrical shells as a dynamical system and the different features mentioned in the previous paragraph have a corresponding representation that can be assessed experimentally. The experimental representation of the fact that the basin of attraction shrinks as the axial load is increased is the creation of stability landscapes. Stability landscapes are the experimental representation of a single direction from the fixed point to the boundary of the basin of attraction in state space. An example of a stability landscape can be seen in figure 5 together with its key features.

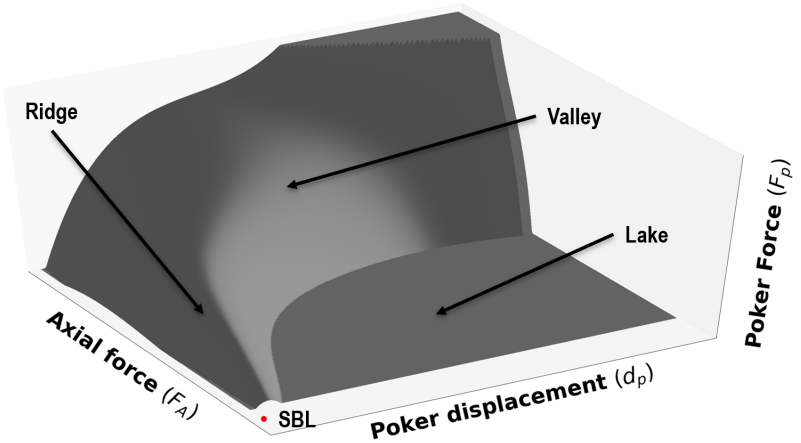

Figure 5 – Example of a stability landscape.

The most relevant feature of the stability landscapes for the current research is the ridge, more precisely the line connecting the points at the top of it. The top of the ridge extrapolates towards the point where the stability landscape vanishes. i.e. the buckling load of the cylindrical shell. This fact is the property of stability landscapes that will be investigated during the current research to propose a potential non-destructive testing procedure for cylindrical shells.

Part I Background and Methods

1 Shell theory for axially loaded cylinders

In this chapter we review the classical tools to derive the elastic response of shells. Specifically, we discuss shell theories and the different kinematic relationships between physical deformations and mechanical strains. The aim is to motivate the utilization of a certain strain-displacement model suitable for the calculations that will be carried out subsequently. Furthermore, a classic buckling analysis of a cylindrical shell will be presented to demonstrate the classic approach to estimate the buckling load of a cylindrical shell. This stability analysis is relevant due to the large influence that the linear buckling eigen-modes have had in the study of cylindrical shell buckling. The final section of this chapter will provide an insight into energy-based methodologies to numerically approximate solutions of shell equations as well as the techniques used to construct these approximations.

Shells have played a prominent role in the development of different aerospace engineering feats. In the process leading to the successful development of flight hardware several variants of structural analyses are essential. These analyses need to verify the structural integrity and stability of the different components present in the structure of the complete vehicle. Hence, models are needed to describe or approximate the elastic response of shells accurately under the presence of external loads. These models are required to predict the deformations and stresses present in the different components under their respective loading conditions. These internal stresses or strains need to be verified against the appropriate allowable values to demonstrate that a vehicle is able to undertake its mission. Due to the extensive use of shells in different aerospace crafts, there have been many attempts to model and construct analytical expressions that capture and accurately describe the elastic response of shells.

The main approaches to derive different strain-displacement models have been the application of geometric principles to infer admissible deformations and kinematic relations of the strains present in a certain shell (Timoshenko, 1964; Love, 1888, 1927; Kirchhoff, 1850) and the asymptotic reduction of 3D elasticity and variational formulations based on energy minimization (Hornung and Velčić, 2015; Lewicka et al., 2010). These approaches have certain advantages and limitations that will be shown later in the chapter. Each model has a range of validity regarding the kinematics that they can describe and approximate. These model

limitations specially restrict maximum displacements and rotations that can be describe accurately.

The fact that different cylindrical shell strain-displacement approximations or theories have associated different ranges of validity enables the possibility to select one or another depending on the analysis that needs to be carried out. As an example, if the stress of a shell is to be predicted far away from its linear stability threshold, a linear Kirchoff-Love strain-displacement approximation will describe accurately the kinematics of the problem. However, if an analysis requires to model the deformation of a cylindrical shell in the deep post-buckling regime, a strain approximation based on the Sander-Budiansky-Koiter strain-displacement approximation will be required.

Displacement-strain relationships together with a stress-strain relationship and force balance describes the response of a shell. The force balance should consider a general loading affecting the cylindrical shell. The equilibrium condition can be stated in the most general form by applying equation 1.1 to a cylindrical shell. In equation 1.1, $\underline{\mathbf{b}}$ represents the body forces, the term $\rho\underline{\ddot{\mathbf{u}}}$ the effect of inertia and $\underline{\boldsymbol{\sigma}}$ the internal stresses present in a solid as a reaction to the applied loading.

$$\nabla \cdot \underline{\boldsymbol{\sigma}} + \underline{\mathbf{b}} = \rho\underline{\ddot{\mathbf{u}}} \tag{1.1}$$

However, a force balance in the form of 1.1 applied to a cylindrical shell is not practical to study structures like cylindrical shells. This equilibrium is not practical to study cylindrical shells due to the fact that in this kind of structural components the thickness is orders of magnitude smaller than the other characteristic lengths. In fact the most common approach to study cylindrical shells is to study them as 2D entities in space with an associated parameter to represent the thickness (Niordson, 1985).

A well established practice (Timoshenko, 1964) to derive an expression of force balance in a cylindrical shell is to take a representative segment of a cylindrical shell, isolate it and identify all the forces acting on it. All these forces are required to be in equilibrium with the rest of the cylindrical shell via the internal reactions. The graphical representation of this equilibrium is a free body diagram. An illustration of all the forces involved is presented in the schematic shown in figure 1.1. Under equilibrium conditions, the internal strains and hence the stresses are related to the geometric deformations via the strain-displacement relationships. These strain-displacement relationships are obtained from different approximations of the asymptotic reduction of 3D elasticity.

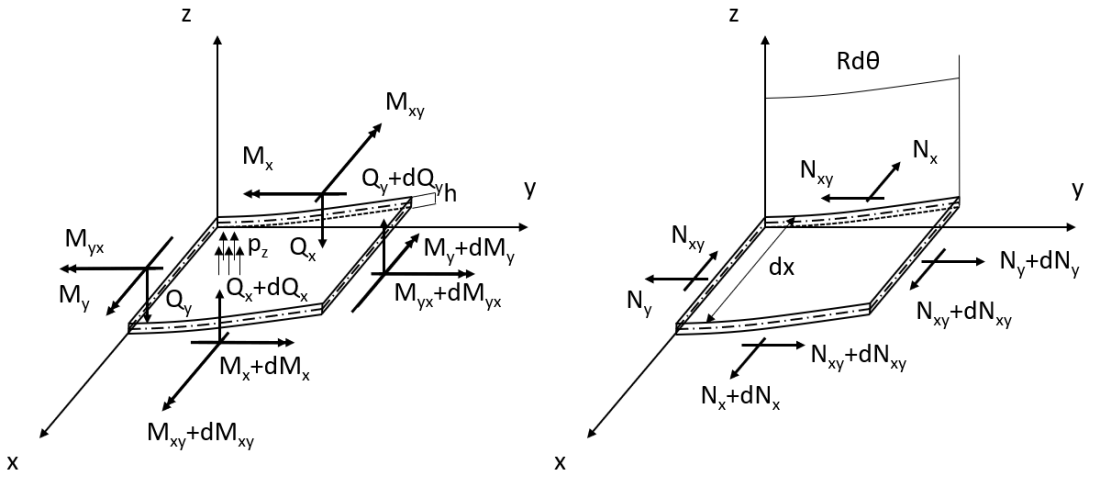

Figure 1.1 – Complete set of internal forces present in a representative shell element as a reaction of a generic external force.

There is an alternative variational approach to derive equilibrium equations. This approach consists of applying Hamilton's principle (Sanders, 1959) to a portion of a cylindrical shell. In this approach, a general expression containing the contributions of the different strains to the internal work is obtained. This expression of the internal work needs to be equal to the external work done by the external forces. In this expression the different strain approximations are included. The outcome is exactly the same as in the case where a force equilibrium is created from a free body diagram. Hence, it is an arbitrary choice to select one approach or another. The free body diagram approach will be used.

1.0.1 Cylindrical shell force balance

In the derivation of the shell model a change of coordinates is introduced. The change of coordinates reads as follows $x = x$, $y = R\theta$ being θ the azimuthal coordinate in the cylinder and $R = z$ where R is the nominal radius of the cylindrical shell (Doyle, 2001). This change of coordinates transforms all the components from a Cartesian coordinate system to a coordinate system where the cylinders becomes a surface with intrinsic curvature.

After introducing the change of coordinates, the first step in the derivation of the shell equations is to state the force equilibrium of the free body diagram depicted in figure 1.1. Equation 1.2 represent the force equilibrium along the x axis while equation 1.3 represent the force equilibrium along the azimuthal direction y. Equation 1.4 is the out of plane equilibrium considering the external load depicted in figure 1.1. In equations 1.2 to 1.4, N_{aa} represents the corresponding stress resultant aligned with coordinate a. N_{ab} represents the shear stress resultant oriented from coordinate a to b. The same nomenclature is applied to the moment

resultants M_{aa} and M_{ab}.

$$\frac{\partial N_x}{\partial x} + \frac{\partial N_{xy}}{\partial y} = 0 \tag{1.2}$$

$$\frac{\partial N_y}{\partial y} + \frac{\partial N_{xy}}{\partial x} = 0 \tag{1.3}$$

$$\frac{\partial Q_x}{\partial x} + \frac{\partial Q_y}{\partial y} + N_x \frac{\partial^2 w}{\partial x^2} + 2N_{xy} \frac{\partial^2 w}{\partial x \partial y} + N_y \frac{\partial^2 w}{\partial y^2} = -p_z \tag{1.4}$$

Taking moments around the x and y axis equations 1.5 and 1.6 are obtained.

$$\frac{\partial M_x}{\partial x} + \frac{\partial M_{xy}}{\partial y} = Q_x \tag{1.5}$$

$$\frac{\partial M_y}{\partial y} - \frac{\partial M_{xy}}{\partial x} = Q_y \tag{1.6}$$

Equations 1.5 and 1.6 express the equilibrium equation along the z axis as a function of stress and moments resultants as shown in equation 1.7

$$\frac{\partial^2 M_x}{\partial x^2} + 2\frac{\partial^2 M_{xy}}{\partial x \partial y} + \frac{\partial^2 M_y}{\partial y^2} = -\left[p_z + (N_x + P_0)\frac{\partial^2 w}{\partial x^2} + N_x y \frac{\partial^2 w}{\partial x} \partial y + N_y \left(\frac{\partial^2 w}{\partial y^2} + \frac{1}{R} \right) \right] \tag{1.7}$$

In equation 1.4, P_0 represents a uniform compression stress resultant, a compression force per unit length. The p_z in equation 1.7 represents a radial pressure distribution normal to the surface of the cylindrical shell. This represents a particular loading condition that will be of interest in the current research. The boundary conditions assumed for the cylindrical shell are clamped at both ends.

Once the force equilibrium is stated, an expression to relate the loading to the deformations is needed. This relationship of the different stress and moment resultants to the strains (ϵ) and curvatures (κ) is shown in equations 1.9 to 1.14 via the material characteristics and the thickness of the cylindrical shell h. The constitutive model of the material assumes a material model where the behaviour is isotropic and linear elastic (Lemaitre (2001)). The focus of the current research is oriented towards the mathematical models used to describe deformations and non-linearities in cylindrical shell from the geometric point of view. Hence, the material model is selected as simple as possible. The isotropic linear elastic model selected only uses 3 parameters, E (Young's Modulus), ν (Poisson's ratio) and G (Shear modulus), where only two

of them are required to define the third, 1.8.

$$G = \frac{E}{2(1+\nu)} \tag{1.8}$$

$$N_x = \frac{Eh}{1-\nu^2}\left(\epsilon_x + \nu\epsilon_y\right) \tag{1.9}$$

$$N_y = \frac{Eh}{1-\nu^2}\left(\epsilon_y + \nu\epsilon_x\right) \tag{1.10}$$

$$N_{xy} = \frac{Eh}{2(1+\nu)}\left(\epsilon_{xy}\right) \tag{1.11}$$

The moment resultants are related to curvature as follows:

$$M_x = \frac{Eh^3}{12(1-\nu^2)}\left(\kappa_x + \nu\kappa_y\right) \tag{1.12}$$

$$M_y = \frac{Eh^3}{12(1-\nu^2)}\left(\kappa_y + \nu\kappa_x\right) \tag{1.13}$$

$$M_{xy} = \frac{Eh^3}{2(1+\nu)}\left(\kappa_{xy}\right) \tag{1.14}$$

Inserting the different strain-displacement approximations in equations 1.9 to 1.14 is how the different shell models are included. The different strain-displacement expressions include the characteristic kinematics, the contributions of the different displacement components, of each shell theory.

An additional feature introduced in the equilibrium equations is the Airy stress potential ϕ. The Airy stress potential is used to simplify the two equations of in-plane equilibrium (1.2 and 1.3) to a single equation with

$$N_x = \frac{\partial^2\phi}{\partial y^2} \tag{1.15}$$

$$N_y = \frac{\partial^2\phi}{\partial x^2} \tag{1.16}$$

$$N_{xy} = \frac{\partial^2 \phi}{\partial x \partial y} \tag{1.17}$$

This stress potential is defined according to equations 1.15 to 1.17. The Airy stress potential exists due to the fact that the internal forces can be derived as a potential from equation 1.1 in the absence of inertial forces (Reddy, 2013). The Airy potential implies that the equilibrium equations are directly satisfied in the case when no body forces are applied (Airy, 1863).

1.1 Linear theory of cylindrical shells

In this section the linearized strain-displacement that are valid for small displacement are considered.

The application of this approximation is valid under the following assumptions. The deformations present in the cylindrical shell are small in comparison to the shell thickness and the sections of the cylindrical shell remain perpendicular to the line defining the mid-surface of the cylindrical shell under bending. This last point meaning that cross-sections that originally were perpendicular to the mid-plane of the shell remain so after deformation. This limitation in the shear deformation is acceptable for thin cylindrical shells. However, for cylindrical shells with a larger thickness, this assumption is not valid (Reissner, 1945). The shell theory resulting from these hypotheses was derived in the 19^{th} century independently by Love (Love, 1888, 1927) and Kirchhoff (Kirchhoff, 1850; Kirchhoff and Hensel, 1883).

Implementing the considerations stated in the previous paragraph leads to the strain-displacement relationships presented in expressions 1.18 to 1.20. These equations represent the strain-displacement relationships of the Kirchhoff-Love shell theory that have seen a very wide utilization to deal with linear analysis of shells (Gibson, 1965; Timoshenko, 1964).

$$\epsilon_x = \frac{\partial u}{\partial x} \tag{1.18}$$

$$\epsilon_y = \frac{\partial v}{\partial y} + \frac{w}{R} \tag{1.19}$$

$$\epsilon_{xy} = \frac{\partial u}{\partial y} + \frac{\partial v}{\partial x} \tag{1.20}$$

for the in-plane strains and

$$\kappa_x = \frac{\partial^2 w}{\partial x^2} \tag{1.21}$$

$$\kappa_y = \frac{\partial^2 w}{\partial y^2} \tag{1.22}$$

$$\kappa_{xy} = \frac{\partial^2 w}{\partial x \partial y} \tag{1.23}$$

for the curvatures.

This shell theory or strain-displacement approximation, as it was mentioned before, is suitable for cases where the displacements and rotations are small. The range of validity of this shell theory makes it not suitable to predict the behaviour of shells at the onset on instability or the collapse of cylindrical shell. This being due to the fact that more significant displacements and rotations are involved in this case (Hutchinson, 2016). This theory is useful to study linear problems that arise typically in stress analysis as shown in (Megson, 2007).

1.2 Non-linear shell theory of cylindrical shells

Elasticity is intrinsically non-linear due to the kinematics of the deformations of a solid. The deformation that a body undergoes changing the location of one point from its initial position to a final position leads to a term in each component of the strain tensor that is non-linear (Landau and Lifshitz, 1970). The definition of each of those terms of the strain tensor in 3D is the one shown in equation 1.24. In this expression, i, k are the different combinations of x, y and z.

$$\epsilon_{ik} = \frac{1}{2}\left(\frac{\partial u_i}{\partial x_k} + \frac{\partial u_k}{\partial x_i} + \frac{\partial u_i}{\partial x_i}\frac{\partial u_i}{\partial x_k}\right) \tag{1.24}$$

The non-linear term present in each component of the stress tensor 1.24 is neglected in applications where the deformations are small. However, in order to deal with a problems like the one of predicting the collapse of cylindrical shells, the geometrically non-linear behavior of elasticity can not be neglected. In this case the magnitude of the deformations, displacements and rotations involved are too big to not consider the non-linear contribution in the strain tensor.

1.2.1 Donnell-Mustari-Vlasov

This approximation of the strain-displacement relationships that includes non-linear effects is the so called Donnell-Mustari-Vlasov (DMV) approximation. It is the lowest complexity non-linear approximation due to the fact that it includes a single non-linear term on the strain-displacement relationships. Other approximations include more involved non-linear terms (Reddy, 2007).

The DMV shell theory was derived by Donnell, Mushtari and Vlasov (Donnell, 1933; Mushtari and Galimov, 1961; Vlasov, 1958) independently in the US and the USSR during the 20^{th} century. The DMV approximation of the strain-displacement relation of cylindrical shells has seen very wide application (Audoly and Pomeau, 2010; Howell et al., 2009; Chien, 1944a,b).

The DMV approximation is able to cope with small strains so linear elastic material models can be applied. In addition to that, the deformations need to be short wavelength due to the approximation of the curvatures and not exceed the order of magnitude of the shell thickness (Hutchinson and Thompson, 2017; Budiansky, 1968). Regarding rotations, the slope in the displacement field should remain small, meaning that $\partial w/\partial x << 1$ (Amabili, 2003, 2008). The Kirchoff-Love hypothesis should hold (Kirchhoff and Hensel, 1883; Love, 1888), meaning that the shell section must remain straight after the deformation occurs.

The strain-displacement relationships of DMV are presented in equations 1.25 to 1.30. Note that the non-linear term appears in the in-plane strains while the curvatures remain linear functions of the radial displacement of the cylindrical shell. The non-linear terms are a quadratic function of the radial displacement w with no non-linear terms involving the in-plane displacements u and v.

$$\epsilon_x = \frac{\partial u}{\partial x} + \frac{1}{2}\left(\frac{\partial w}{\partial x}\right)^2 \tag{1.25}$$

$$\epsilon_y = \frac{\partial v}{\partial y} + \frac{w}{R} + \frac{1}{2}\left(\frac{\partial w}{\partial y}\right)^2 \tag{1.26}$$

$$\epsilon_{xy} = \frac{\partial u}{\partial y} + \frac{\partial v}{\partial x} + \frac{\partial w}{\partial x}\frac{\partial w}{\partial y} \tag{1.27}$$

$$\kappa_x = -\frac{\partial^2 w}{\partial x^2} \tag{1.28}$$

$$\kappa_y = -\frac{\partial^2 w}{\partial y^2} \tag{1.29}$$

$$\kappa_{xy} = -2\frac{\partial^2 w}{\partial x \partial y} \tag{1.30}$$

Once the strain-displacement relationships are available, the next step is to update the equilibrium equations to consider the loading and boundary conditions of interest. The boundary conditions are clamped at both ends. The loading presented in figure 1.1 is simplified to consider as external forces only an axial compression load, a stress resultant (P_0) and a radial

pressure distribution (P_R) that for practical reasons will be represented by a Gaussian distribution. A Gaussian distribution was selected due to the ease to control the location, area and intensity of the maximum. Furthermore, a normal distribution satisfies all the requirements of continuity that are needed to not affect the solution of the equations. A presion distribution is included because in chapter 2 the DMV equations with an identical loading scheme will be used to study cylindrical shell buckling.

Equation 1.31 represents the equilibrium along the axial direction, equation 1.32 represents the equilibrium along the tangential direction and 1.33 the equilibrium in the radial direction. Sub-indices x and y denote derivatives with respect to x and y, respectively.

$$N_{x,x} + N_{xy,y} = 0 \tag{1.31}$$

$$N_{y,y} + N_{yx,x} = 0 \tag{1.32}$$

$$D\Delta^2 w + w_{,xx}(N_x + P_0) + w_{,yy}N_y + 2w_{,xy}N_{xy} - \frac{1}{R}N_y + P_R(x,y) = 0 \tag{1.33}$$

In the current research, the DMV approximation is considered sufficient. Namely because of the following reasons:

- The shells under study are sufficiently slender. The ratio of thickness over radius is smaller than 20 Amabili (2003).
- The DMV strain-displacement approximation describes the intrinsic non-linear behaviour of elasticity. It captures the non-linear behaviour of shells. These statements are only correct in the case the deformations are small.
- The range of deformations where the current research will focus, the pre-buckling regime, is within the range of validity of this approximation (Amabili, 2003). Pre-buckling deformations are in the order of the shell thickness.
- More complex approximations will not provide additional accuracy in describing the pre-buckling deformations. Higher-order models are used to cope with larger displacements associated with post-buckling (Hutchinson, 2016). This regime will not be studied in the current research.

The aim of this section was to provide a justification for the selection of the DMV approximation and the equations to be used in subsequent chapters. A more through justification of the model is provided in (Ciarlet, 1980),(Ciarlet and Paumier, 1986).

Although the DMV approximation of the strain-displacement relationships is used in the current research, a more complex approximation will be presented in the next section as an

example. The intention of presenting a more complex strain-displacement approximation is to show how additional complexity is added beyond the DMV one to model the non-linear behaviour of cylindrical shells when larger displacements and rotations are present. The main application of this more complex model is the study of the collapse of cylindrical shells beyond the pre-buckling regime.

1.2.2 Sanders-Budiansky-Koiter Shell theory

The Sanders-Budiansky-Koiter (SBK) approximation differs from the non-linear strain-displacement relationship proposed by the DMV model in that it retains higher order terms from the asymptotic reduction. This approximation was proposed in very similar forms by Sanders (1959), Budiansky (1968) and Koiter (1966). The strain-displacement relationships from the SBK approximation are presented in equations 1.34 to 1.39

$$\epsilon_x = \frac{\partial u}{\partial x} + \frac{1}{2}\left(\frac{\partial w}{\partial x}\right)^2 + \frac{1}{8}\left(\frac{\partial v}{\partial x} - \frac{\partial u}{\partial y}\right)^2 \tag{1.34}$$

$$\epsilon_y = \frac{\partial v}{\partial y} + \frac{w}{R} + \frac{1}{2}\left(\frac{\partial w}{\partial y}\right)^2 + \frac{1}{8}\left(\frac{\partial u}{\partial y} - \frac{\partial v}{\partial x}\right)^2 \tag{1.35}$$

$$\epsilon_{xy} = \frac{\partial u}{R\partial\theta} + \frac{\partial v}{\partial x} + \frac{\partial w}{\partial x}\left(\frac{\partial w}{\partial y} - \frac{v}{R}\right) \tag{1.36}$$

$$\kappa_x = -\frac{\partial^2 w}{\partial x^2} \tag{1.37}$$

$$\kappa_y = -\frac{\partial^2 w}{\partial y^2} + \frac{\partial v}{\partial y^2} \tag{1.38}$$

$$\kappa_{xy} = -2\frac{\partial^2 w}{\partial x \partial y} + \frac{1}{2R}\left(3\frac{\partial v}{\partial x} - \frac{\partial u}{\partial y}\right) \tag{1.39}$$

The SBK approximation has been used by different authors (Ciarlet, 2000; Yamaki, 1984; Amabili, 2003) to explore the limits of the different strain-displacement approximations. They verified that the DMV strain-displacement model becomes inaccurate beyond the pre-buckling regime. One of the most important application of this shell theory are commercial finite element codes like Abaqus (Dassault Systèmes Simulia Corp, 2011) that incorporate this approximation on the $2D$ elements. This code has been successfully used not only to predict buckling of shell structures, but also to trace the evolution process of the collapse of cylindrical shells deep in the post-buckling regime as shown in (Hilburger et al., 2018).

1.2.3 Derivation of non-linear shell theory from the Γ limit of energy functionals of 3D elasticity

A well established process to derive the different strain-displacement approximations that model the behaviour of cylindrical shells is based upon a formal asymptotic reduction from 3D non-linear elasticity. This asymptotic reduction leads to a model consisting of a 2D manifold in 3D with a parameter to model the thickness of the cylindrical shell. However, in the application of the asymptotic reduction process, there is the possibility to only retain certain contributors depending on the behaviour that is to be captured (moderate rotations, moderate strain, large rotations etc.). This leads to different strain-displacement approximations from the ones presented in subsections 1.2.1 and 1.2.2.

In recent years, a new approach for the derivation of the 2D non-linear strain-displacement approximation from 3D-elasticity has been developed in the applied math community (Hornung and Velčić, 2015), (Lewicka et al., 2010). A complete derivation of the DMV model is presented in (Hornung and Velčić, 2015). It is based on the application of Γ convergence (Braides, 2002) in the limit when a geometric dimension of the solid, the thickness of the shell in this case, tends to a very small value in comparison with the other characteristic dimensions. Furthermore, imposing the assumption of small strains and rotations, the DMV model is obtained (Hornung and Velčić, 2015; Lewicka et al., 2010). An introduction to Γ convergence and the practicalities of this technique is given in Maso (1993).

The fact that via a different approach the same expressions for capturing the non-linear behaviour of cylindrical shells can be obtained shows that the model used, DMV in this case, is a reliable tool for modelling the behaviour of cylindrical shells.

1.3 Classic stability analysis of cylindrical shells

The existing deviation between the buckling loads predicted by linear stability theory and the values obtained in compression tests of cylindrical shells is the motivation for the current research about the collapse of cylindrical shells. This discrepancy was realized very early on and initially it was thought that the source for the discrepancy between analytical predictions and the experiments could be attributed to an incorrect formulation of the shell models. This hypothesis was shown to be incorrect by Koiter (1945) in line with the initial suggestion of von Karman (Von Karman and Tsien, 1941).

In spite of the work of Koiter (1945), there are sources still claiming that wrong modeling is the source of the deviation between predictions and experiments (Hart-Smith, 2015). Beyond this last source, there is a well established consensus that the main reason of the deviation between the theoretical predictions and experiments are geometric imperfections, deviations from the ideal geometry of the cylindrical shell. In fact, in the last years, high-fidelity finite element models based on the SBK shell strain-displacement approximation managed to accurately predict the buckling load of non-ideal structures made out of cylindrical shells (Hilburger et al.,

2018) and Kosztowny (2021)). These models included the exact shape and imperfections of these cylindrical shells as well as the load introduction imperfection present at the boundary conditions.

Classical stability analysis remains relevant for two reasons. The first one is that the predictions made in the past have shaped the thinking of the structural engineering community about cylindrical shell buckling. These include the buckling load predictions and classical global eigen-modes that affect the complete domain of the cylindrical shell. These so-called global eigen-modes in the form of checkerboard patterns and other fully periodic solutions led researchers to not think about the possibility and relevance of localized solutions. This has changed recently as for example the work of Kreilos (Kreilos et al., 2016) demonstrates. The second reason is the fact that the results of the classical stability analysis are the ones used as reference to express the results of any buckling analysis or test of real shells. Hence, it is important to understand how this reference value is derived.

In this section, an overview about how the early methods used to approximate buckling loads will also be provided. These are early methods not based on numerical methodologies, like the finite element method. However, they were sufficient to predict the stability of cylindrical shells and provide early insights about the accuracy of the partial differential equations describing cylindrical shells.

1.3.1 Analytical stability prediction

A closed analytical solution for the derivation of the buckling load of a cylindrical shell via stability analysis can only be obtained for simply supported boundary conditions. These boundary conditions are detailed in equations 1.42 to 1.45. The linearized equations using the Donnell approximation read as shown in expressions 1.40 and 1.41. Here the a summary of the calculation is presented. For a complete overview of the procedure, the work of (Timoshenko, 1985) should be visited.

$$\frac{1}{Eh}\nabla^4\phi = -\frac{\partial^2 w}{\partial x^2}\frac{1}{R} \tag{1.40}$$

$$D\nabla^4 w = N_x\frac{\partial^2 w}{\partial x^2} + 2N_{xy}\frac{\partial^2 w}{\partial x \partial y} + N_y\frac{\partial^2 w}{\partial y^2} + \frac{1}{R}\frac{\partial \phi}{\partial x^2} \tag{1.41}$$

There are 4 boundary conditions required to solve the system of differential equations composed by equations 1.40 and 1.41. These boundary conditions are presented in equations 1.42 to 1.45. They are to be imposed at $x = 0$ and $x = L$, where x is the axial coordinate of the cylindrical shell of radius R and length L. The field w is the radial displacement in the complete cylindrical shell and ϕ the Airy stress potential as defined in expressions 1.15 to 1.17. $D = Eh^3/12(1-\nu)$ is the bending stiffness of the shell, where E is the Young's modulus of the

material, h the thickness of the cylindrical shell and ν the Poisson's ratio of the material.

$$w(x=0) = w(x=L) = 0 \tag{1.42}$$

$$v(x=0) = v(x=L) = 0 \tag{1.43}$$

$$\frac{\partial^2 w(x)}{\partial x^2}_{x=0} = \frac{\partial^2 w(x)}{\partial x^2}_{x=L} = 0 \tag{1.44}$$

$$\frac{\partial^2 \phi}{\partial y^2}_{x=0} = \frac{\partial^2 \phi}{\partial y^2}_{x=L} = 0 \tag{1.45}$$

Once the equations describing the system have been introduced together with the required boundary conditions, it is possible to proceed with their solution. The next step in the solution is to insert an ansatz for $w(x,y)$ and $F(x,y)$ that satisfies the simply supported boundary conditions described in equations 1.42 to 1.45. The following ansatz for $w(x,y)$ and $F(x,y)$ satisfies them.

$$w(x,y) = w_{mn} \sin\left(\frac{m\pi x}{L}\right) \cos\left(\frac{ny}{R}\right) \tag{1.46}$$

$$\phi(x,y) = \phi_{mn} \sin\left(\frac{m\pi x}{L}\right) \cos\left(\frac{ny}{R}\right) \tag{1.47}$$

Note that the expressions for the ansatz of equations 1.46 and 1.47 are fully periodic trigonometric functions with w_{mn} and ϕ_{mn} constant. This ansatz does not allow for any completely localized solution to occur.

Introducing equations 1.46 and 1.47 into the equilibrium equations 1.40 and 1.41 with the variables α and β defined as follows with m and n being the wave number of the corresponding eigen-mode in axial and azimuthal directions

$$\alpha = \frac{m\pi}{L} \tag{1.48}$$

$$\beta = \frac{n}{R} \tag{1.49}$$

leading to an eigen-value problem of the form presented in equation 1.50

$$N_x \, sin(\alpha x) sin(\beta y) = 0 \tag{1.50}$$

where N_x is

$$N_x = \frac{Eh^3}{12(1-\nu^2)} \frac{(\alpha^2+\beta^2)^2}{\alpha^2} + \frac{Eh}{R^2} \frac{\alpha^2}{(\alpha^2+\beta^2)^2} \tag{1.51}$$

and the critical value for N_x is the minimum

$$N_{x\,cr} = \min\left(\frac{Eh^3}{12(1-\nu^2)} \frac{(\alpha^2+\beta^2)^2}{\alpha^2} + \frac{Eh}{R^2} \frac{\alpha^2}{(\alpha^2+\beta^2)^2} \right) \tag{1.52}$$

Differentiation of equation 1.52 with respect to $\frac{(\alpha^2+\beta^2)^2}{\alpha^2}$ leads to the result that N_{cr} is a minimum for the following

$$\frac{(\alpha^2+\beta^2)^2}{\alpha^2} = \frac{2\sqrt{3(1-\nu^2)}}{hR} \tag{1.53}$$

Introducing 1.53 in 1.52 and considering that the resultant N_{cr} can be converted into stress by dividing it by the thickness of the cylindrical shell, the classical result for the buckling stress of a cylindrical shell is obtained. It is shown in equation 1.54. This is the classical result used to compute the linear stability threshold of an axially loaded cylindrical shell.

$$\sigma_{cl} = \frac{1}{\sqrt{3(1-\nu^2)}} \frac{Eh}{R} \tag{1.54}$$

The critical stress can be converted to an equivalent load by multiplying it by the cross-section of the cylindrical shell $2\pi Rh$, leading to equation 1.55.

$$P_{cl} = \frac{2\pi}{\sqrt{3(1-\nu^2)}} Eh^2 \tag{1.55}$$

Equations 1.54 and 1.55 do not consider the length of the cylinder. This means that these equations have a limited range of validity. Namely, in the case of very slender cylindrical shells, buckling will occur in a similar way to the traditional column Euler buckling. Furthermore, cylindrical shells that are too short will not be able to accommodate deformations with the characteristic length predicted. Batdorf derived an expression to consider the influence of the length of the cylinder, see equation 1.56 (Batdorf, 1947; Batdorf et al., 1947; Weller et al., 2002).

Where Z is the Batdorf parameter.

$$Z = \frac{L^2}{Rh}\sqrt{1-\nu^2} \tag{1.56}$$

The Batdorf parameter is a better metric to characterize the geometry of cylindrical shells due to the fact that for identical R/t it has been shown that the predicted buckling load varies for different lengths of the cylindrical shell (Wagner et al., 2019). However, in applications with moderate length, R/t is still the most established parameter to characterize a shell. Due to the moderate length ($L/R < 10$) of the shell used in the current research, R/t will be used to characterize the different test articles.

1.3.2 Approximate solution

In the previous section, it was shown that to obtain an analytical closed solution of the shell equations, even in the linear case, it is only possible for very specific cases of boundary conditions: simply supported. Hence, in order to deal with non-linear shell approximations, cope with more complex strain-displacement relationships or more complex boundary conditions, approximate methods exist. These methods can approximate solutions of these more complex shell problems without recurring to fully numerical schemes like the finite element method.

The most used methodology to construct the approximate solutions for these more complex configurations is the Raleight-Ritz method. The finite element method has also been used. However, it has been applied to the partial differential equations in the complete domain of interest. This imposes restrictions on the domains that are acceptable. This finite element methodology is the base for the case where the domain is discretized in smaller subdomains as it will be discussed in chapter 3.

The Raleight-Ritz method is a variational method based on the minimization of the energy potential associated with an elastic system (Rayleigh, 1877; Ritz, 1908). In the case of the the cylindrical shells, the energy potential is associated with the strain energy. The Raleight-Ritz method constructs an approximation of the relevant fields (displacements in the case of cylindrical shells) in the form of a finite Fourier series as shown in expression 1.57 for a generic 1D case.

$$u(x) \approx \sum_{i=1}^{N_{ui}} u_i X_i(x) + X_0 \tag{1.57}$$

Where the Fourier modes $X_i(x)$ must satisfy the homogeneous boundary conditions imposed on the system, in this case a cylindrical shell, and X_0 is used to satisfy the in-homogeneous boundary conditions. The different approximations built for the displacements fields of the shell (u, v and w) need to be constructed in the form of double Fourier series. Namely because

of the two-dimensional nature of the domain used to describe a cylindrical shell.

$$u(x,y) \approx \frac{L}{R} \sum_{m=1}^{N_u} \sum_{n=1}^{N_u} u_{mn} \cos \frac{m\pi x}{L} \cos \frac{ny}{R} \tag{1.58}$$

$$v(x,y) \approx \frac{L}{R} \sum_{m=1}^{N_u} \sum_{n=1}^{N_u} v_{mn} \sin \frac{m\pi x}{L} \sin \frac{ny}{R} \tag{1.59}$$

$$w(x,y) \approx \sum_{m=1}^{N_u} \sum_{n=1}^{N_u} w_{mn} \sin \frac{m\pi x}{L} \cos \frac{ny}{R} \tag{1.60}$$

In 1.58, 1.59 and 1.60, m and n are the axial half-wave number and the circumferential wave numbers respectively and the Fourier coefficients. u_{mn}, v_{mn} and w_{mn} are the unknowns that need to be calculated in order to construct the approximated solution.

The procedure followed to construct the approximated solution by the Raleight-Ritz method consists of finding the state of deformation that minimizes the total potential energy of the system. This state of deformation corresponds to the stationary point of the system (energy minimum). This is practically implemented by differentiating the potential energy associated with the cylindrical shell with respect to the unknown Fourier coefficients of the approximations 1.58, 1.59 and 1.60 simultaneously. This action can be mathematically expressed as shown in equation 1.61, where δ represents the variation of the potential energy.

$$\delta\Pi = \frac{\partial \Pi}{\partial u_{mn}} = \frac{\partial \Pi}{\partial v_{mn}} = \frac{\partial \Pi}{\partial w_{mn}} = 0 \tag{1.61}$$

In the case of cylindrical shells, the potential Π under a compression force can be written as

$$\Pi = U_B + U_M + V_P \tag{1.62}$$

where U_B is the strain energy due to the bending, U_M represents the membrane strain energy and V_P the variation in potential due to the action of the compression force acting on the cylindrical shell. These terms can be expressed as a function of strains and the acting forces and moments as follows:

$$U_B = \frac{1}{2} \int_0^{2\pi R} \int_0^L (M_x \kappa_x + 2M_{xy}\kappa_{xy} + M_y \kappa_y) dx dy \tag{1.63}$$

$$U_M = \frac{1}{2} \int_0^{2\pi R} \int_0^L (N_x \epsilon_x + 2N_{xy}\epsilon_{xy} + N_y \epsilon_y) dx dy \tag{1.64}$$

$$V_P = -\int_0^{2\pi R}\int_0^{L} N_0 \frac{\partial u}{\partial x} dx dy \tag{1.65}$$

Once these expressions of the potential are stated, the next steps are guided towards obtaining a system of equations where we can introduce the different derivatives of the approximation functions. In order to do this, it is required firstly to express the different moment and stress resultants as a function of the strains through the constitutive laws. Secondly to introduce the displacements trough the strain-displacement relationships. At this point, the derivatives of the approximations 1.58, 1.59 and 1.60 can be included and a system to derive the Fourier coefficients can be built using 1.61.

The Rayleigh-Ritz semi-analytical procedure has found some application in recent years as an alternative to finite elements analysis (Castro et al. (2015) Castro and Donadon (2017)). The motivations behind this were mainly two. Firstly, the semi-analytical Rayleigh-Ritz is computationally faster, at comparable accuracy, than commercial finite element codes (Castro et al. (2015)). Secondly, the search for alternative solvers to commercial finite element codes. However, there are limitations to this procedure that in some problems will force the utilization of those commercial codes. This is the case of complex geometries where the approximations of the field variables can not be constructed via Fourier series.

1.4 Conclusions

In the current chapter different shell approximations have been shown. These different approximations consists of different strain displacement relationships that represent the kinematics of existing shell models. Among the presented models the DMV approximation has been selected as a sufficiently accurate description. The main reasons are:

- The shells under study are sufficiently slender.
- The DMV strain-displacement approximation describes the non-linear behaviour of shells in the case of small deformations.
- The range of deformations where the current research will focus, the pre-buckling regime, are in the order of the shell thickness.
- Deformation beyond the onset of stability will not be studies.

Hence, the DMV model is the approximation that will be used for the theoretical work of chapter 2 about the dynamical system approach applied to buckling of cylindrical shells.

2 Dynamical systems approach applied to cylindrical shell buckling

A dynamical system is a mathematical description of the evolution of a physical system over time $f(\mathbf{u}, T)$. The system is characterized by the state vector $\mathbf{u}$ for any given time. The description and study of the behaviour of physical systems as a dynamical system is known as the dynamical system approach.

The applications of the dynamical system approach has become a relevant tool to study physical systems. In fact, it has seen very wide spread application as a methodology to explain the underlying physics of different phenomena. The dynamical systems approach has been used to study many different physical systems ranging from the relatively simple double pendulum (Strogatz, 1994) to complex pattern formation systems described by non-linear partial differential equations (Burke and Knobloch, 2007; Knobloch, 1986b,a) and even galaxy dynamics (Yılmaz and Güdekli, 2021).

The dynamical systems approach connects to key research questions in the field of engineering in the description of complex system governed by non-linear partial differential equations. As an example, the dynamical systems approach has been applied to uncover the physical phenomena underlying one of the most challenging research questions in the engineering world: turbulence (Jiménez, 2018).

In the research on turbulence, via the application of the dynamical systems approach and its ideas, a new conceptual description has arisen. The seemingly disordered patterns present in turbulent flows can be explained as a trajectory connecting different invariant solutions of the corresponding dynamical system (Reetz et al., 2019). In this conceptual description, specific invariant solutions or equilibrium states exist for specific values of control parameters and these states and the associated invariant manifolds and eigen-directions dictate how the system evolves in time (Azimi and Schneider, 2020).

2.1 From turbulence to cylindrical shell buckling

Cylindrical shells are structurally stable under axial compression up to a critical value of the loading force, above which they abruptly collapse in a buckled state. The classical approach to estimate the load at which this collapse occurs is based on the linear stability analysis of the unbuckled loaded state. Considering the unbuckled state as an equilibrium solution of the dynamical system, and the axial load as the control parameter, an estimate of the buckling load is obtained as the critical value of the loading force above which infinitesimal radial perturbations exponentially grow driving the (linearised) dynamics to the buckled state (see figure 2.1a)

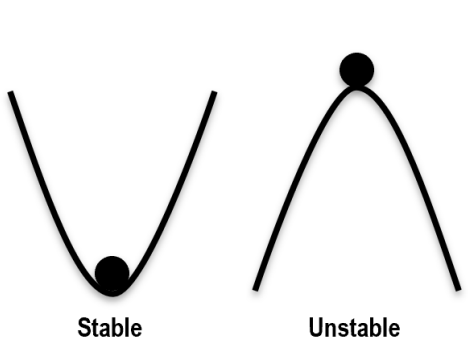

(a) Graphical description of the traditional approach to stability.

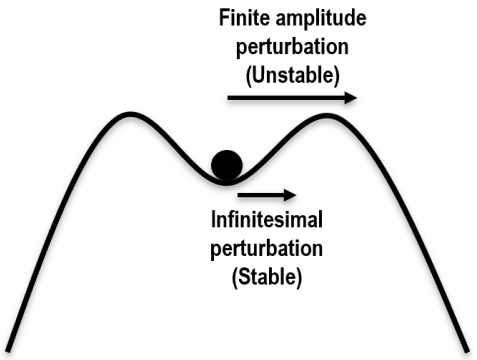

(b) Graphical description of the finite amplitude perturbation approach to stability.

Figure 2.1 – Graphic description of the different approaches to understand stability discussed in this research work

However, the theoretical prediction obtained via linear stability analysis has been shown to be an overestimate of the actual buckling load measured in experiments (Seide, 1969), see figure 3. In the experiments performed by NASA (Seide, 1969), it was shown that the transition from the unbuckled state to the buckled one occurs at loads that are smaller than the critical value predicted by linear stability theory. Furthermore, the buckling loads of nominally identical shells vary for each specimen. The discrepancy between the results from linear stability analysis and the experimental measures lies in the sensitivity of the transition point (buckling load) to the specific geometrical imperfections of each cylindrical shell (Koiter, 1945). Note that geometric imperfections are not considered by the standard analytical linear stability analysis.

Structural imperfections of the cylindrical shells, for which the value R/h is a proxy (the thinner is the shell, the more challenging is to manufacture a geometrical perfect shell) are then responsible for lowering the stability threshold above which the unbuckled state is triggered. These observations are summarised in figure 2.2, where the bifurcation diagram is shown. The black curve represents the end-to-end displacement of a perfect shell as a

function of the axial load. The unbuckled state of a perfect shell represented by the solid black line is linearly stable for values of the axial load from zero to the buckling load F_A, and unstable beyond it, at which point the system transitions to the buckled state via a backward bifurcation. The effect of the imperfections is to reduce the stability range of the base state, shifting the linear stability threshold down towards lower values of load F_A. The stochastic nature of imperfections thus makes in principle necessary a full characterisation of each shell and its imperfections to determine the buckling load. Making therefore the prediction of buckling a challenging task.

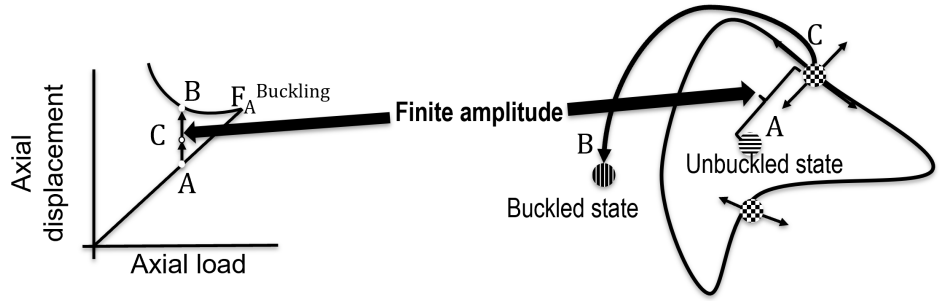

Figure 2.2 – Conceptual depiction of basin of attraction of a perfect shell and its relationship to the axial load versus displacement curve characteristic of a cylindrical shell.

Interestingly, a similar scenario can be observed in other physical systems, more specifically in the transition to turbulence of many subcritical shear flows. Analogously to the critical buckling load, the transition from the laminar to the turbulent regime is characterised in fluid flows by a critical value of the Reynolds number (Re) [1]. This critical value can be estimated by means of linear stability analysis of the laminar state, represented by the steady solution of the Navier-Stokes equations describing the flow physics. However, as for the buckling problem, the predictions of the critical Reynolds number obtained from linear stability analysis are far from capturing the actual laminar-turbulent transition process of many flow systems.

Considering, for example, the plane Poiseuille flow system in a channel geometry (the flow between two infinite parallel planes driven by a fixed pressure gradient), the numerical solution of the Orr-Sommerfield problem, obtained from the linearisation of the Navier-Stokes equations, yields a critical value of the Reynolds number $Re_{cr} = 5772$ (Orszag, 1971), approximately five times larger than the values at which transition to turbulence has been experimentally observed (Davies et al., 1992). Even more remarkable is the case of the plane Couette flow systems (fluid motion between two infinite parallel planes where one is stationary and the other one has a constant motion) or the pipe flow system. For these cases, the laminar solution is linearly stable for all Reynolds numbers.

In all the fluid examples mentioned above, transition to turbulence can be explained as the result of a finite amplitude perturbation of the linearly stable laminar state. As shown in figure

[1] The ratio between inertial and viscous forces

2.3a, when the laminar state of a pipe flow is perturbed with a finite amplitude disturbance, injecting a perpendicular flow jet of amplitude A_{jet} in a perfect pipe, it is possible to identify at each value of the control parameter Re, a critical perturbation amplitude below which instabilities decay (blue dots in figure 2.3a) and above which turbulence is sustained (red dots in figure 2.3a). In other words, at a given value of the Reynolds number, both states, the laminar one (linearly stable) and the turbulent one, can be observed depending on the amplitude of the disturbance introduced in the system.

The surprising similarity between the results obtained from pipe flow experiments (figure 2.3a) and those obtained from shell buckling experiments (figure 2.3b) suggests a connection between the linear stability threshold of an imperfect shell, due to imperfections, and the critical perturbation amplitude necessary to trigger buckling in a perfect shell for a given sub-critical value of the axial the load.

Considering the bifurcation diagram shown in figure 2.2, this translates into the identification of the critical non-linear amplitude perturbation at each load $F_A < F_{A\,buckling}$ which allows the transition from the unbuckled base state to the buckled one. Owing to the similarities between laminar-turbulent transition in fluid mechanics and shell buckling, we believe that a deeper insight onto the latter problem can be achieved by means of a dynamical system approach, transferring theoretical and numerical tools already used for the non-linear analysis of the Navier-Stokes equations to the elastic shell theory.

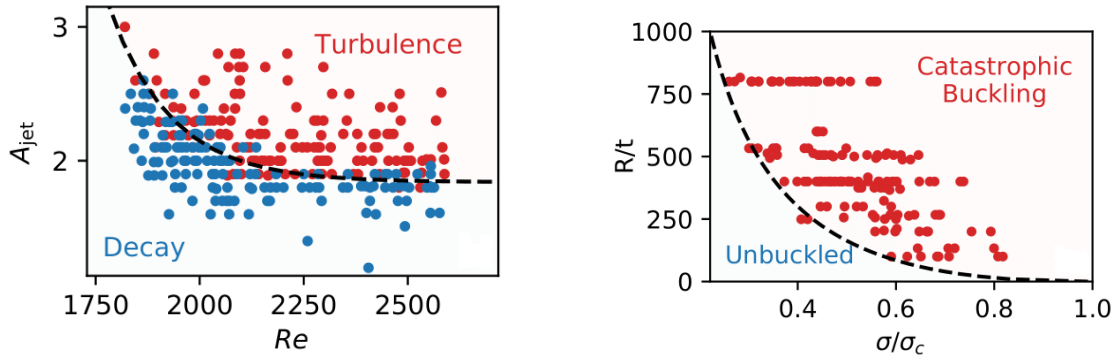

(a) Disturbance amplitudes that triggered the transition from laminar to turbulent flow from the experiments performed by Darbyshire and Mullin (Darbyshire and Mullin, 1995) (Mullin, 2011)

(b) Data from compression test carried out by NASA in the $60's$ showing the buckling load of each of the cylindrical shells tested Seide (1969). The R/t is a proxy for imperfections.

Figure 2.3 – Analogy between turbulence transition in shear flows and cylindrical shell buckling.Virot et al. (2017)

Given the aforementioned similarities between cylindrical shell buckling and some fluid systems, it might be obvious to study them with the same tools, i.e. using the dynamical systems approach. However, this has not been the case and the dynamical systems approach has not been applied as a general framework in the field of solid mechanics or to cylindrical

shell buckling in particular. Traditionally, buckling or collapse of cylindrical shells has been studied instead as the attempt to predict the maximum load that a given cylindrical shell with a certain imperfection shape and intensity can bear (Wullschleger, 2006; Hühne et al., 2008; Deml and Wunderlich, 1997). In practice, this means that the most accepted approaches to derive the buckling load of a cylindrical shell are two. A first one where a linear stability analysis is performed in the ideal geometry neglecting the influence of imperfections. A second one where an envisaged potentially critical imperfection is included on the ideal geometry and either a real or an *in silico* compression experiment (Simulation) is performed to obtain the maximum load the cylindrical shell can bear (Wagner et al., 2016; Kriegesmann et al., 2016; Khakimova et al., 2014) including the mentioned imperfection.

2.2 Dynamical systems and cylinder shell buckling

The great advance in computational power over the past two decades, enabled the possibility of describing many non-linear problems as high-dimensional dynamical systems and characterising their fully non-linear solutions, theretofore not accessible. The field that benefited the most of these developments is without any doubt represented by transitional turbulent flows where dynamical system theory allowed to establish a connection between the emergence of turbulence and chaos theory.
A fluid flow is normally described by a three-dimensional velocity field $\mathbf{u}$ whose evolution is constrained to satisfy the Navier-Stokes equations and some given boundary conditions

$$\dot{\mathbf{u}} = NS(\mathbf{u}) \quad + \quad b.c. \tag{2.1}$$

where $NS(\mathbf{u})$ is the nonlinear Navier-Stokes operator. From a dynamical system point of view such a system can be described in its state space rather than in the three-dimensional physical space. Defining the state space as the space where each point represents a possible solution of the governing equations plus boundary conditions, the temporal evolution of the state vector $\mathbf{u}$ under the action of a time operator $f^t(\mathbf{u})$ can be seen as a trajectory among these solutions. After an initial transient is passed the long term dynamics of the system is controlled by the steady solutions $\mathbf{u}^*$ for which the left-hand side of (2.1) vanishes or equivalently satisfies

$$\sigma f^t(u^*) - u^* = 0 \tag{2.2}$$

up to a symmetry operation σ . These type of solutions, referred to as *invariant solutions*, can be of different types, from simple fixed points for which the left-hand side of (2.1) vanishes point-wise in time, to periodic orbits for which equation (2.2) is satisfied for a specific value of $t = T$ (with T period of the orbit) to more complex solutions.

Many of these solutions have been already found in several flow systems in the past 20 years yielding a much deeper understanding of the mechanistic underpinning of transitional turbulent flows: from the Nagata solution in plane Couette flow (Nagata, 1990), to the spatially

localised solutions in plane Couette flow and pipe flow (Schneider and Eckhardt, 2006), and several others (Kawahara et al., 2012) including solutions of non-Newtonian fluid systems (Page et al., 2020).

Within the dynamical system framework the unbuckled state is represented in the state space as a fixed point solution, and it is characterised by a basin of attraction. The boundary of the basin of attraction separates initial conditions that decay to the base state from those that buckle. Often referred as *edge of chaos*, the basin boundary is represented by a co-dimension one manifold whose size varies with the prescribed axial load (see figure 2.4). On this manifold many non-linear fixed points are embedded. These invariant states, called *edge states*, are characterised by a single unstable direction and belong to the basin of attraction of the unbuckled state.
With the aim of characterising the critical perturbation amplitude that drives the system to the buckled state we then need to estimate the size of the basin of attraction for varying loading force, and this can be done computing and characterising the invariant states on the basin boundary, specifically the edge states, and studying how they change when changing the load.

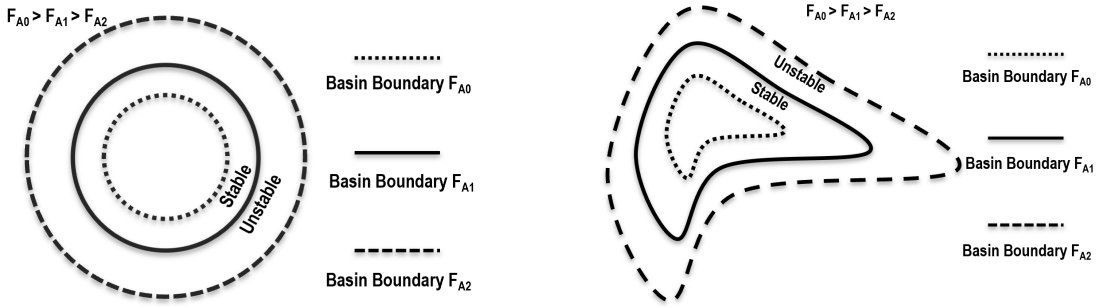

(a) Conceptual depiction of basin of attraction of a perfect shell

(b) Conceptual depiction of the basin of attraction of an imperfect shell

Figure 2.4 – Basin of attraction conceptual description for the case of a perfect and an imperfect shell.

2.2.1 Dynamical system description of cylindrical shell buckling

The description selected to describe the cylindrical shells uses the DMV approximation because it is accurate enough to represent the cylindrical shell for the reasons outlined in the previous chapter. The DMV shell description captures the geometrical non-linear strain-displacement relationship for the case of a cylindrical shell allowing for the fully non-linear description of the different states. The equilibrium equations of the DMV approximation are presented in equations 2.3 and 2.4. Equation 2.3 represents the in-plane force balance that has been simplified to a single equation thanks to the application of Airy stress function. Equation 2.4 represents the force balance in the out-of-plane directions. These equations have as a reference a pre-buckling state of a uniformly expanded cylinder that has been pre-

compressed with an axial force P_0 and has a constant radial displacement w_0 making the total displacement $w_{total} = w + w_0$.

$$\frac{1}{Eh}\Delta^2\phi = \frac{1}{R}w_{,xx} - \frac{1}{2}[w,w] \tag{2.3}$$

$$D\Delta^2 w + \frac{1}{R}\phi_{,xx} - [w,\phi] + P_0 w_{,xx} = 0 \tag{2.4}$$

The bracket from equations 2.3 and 2.4 is defined as follows:

$$[A,B] = A_{,xx}B_{,yy} + A_{,yy}B_{,xx} - 2A_{,xy}B_{,xy} \tag{2.5}$$

Using the Airy stress function ϕ to simplify to a single equation the in-plane force balance yields the expression given in equation 2.3. Where E is the Young's modulus and h is the thickness of the shell. D is the bending stiffness of the cylindrical shell. It is equal to $Eh^3/12(1-\nu)$ where ν is the Poisson's ration of the material.

$$\frac{\partial^2\phi}{\partial x^2} = N_{yy}\ ,\ \frac{\partial^2\phi}{\partial y^2} = N_{xx}\ ,\ \frac{\partial^2\phi}{\partial x\partial y} = -N_{xy} \tag{2.6}$$

The system of equations based on the DMV non-linear shell description defined by equations 2.3 and 2.4 can be posed as a dynamical system of the form presented in equations 2.7 and 2.8 by including the dynamic viscous forces.

In the dynamical system describing the cylindrical shell, the second order in time term has been neglected. The stability of fixed points is not modified by the second order inertial term if the first order viscous damping is present. Hence, the inertial contribution can be neglected and it can be assumed that the over-damped dynamics will be studied.

$$\frac{1}{Et}\Delta^2\phi - \frac{1}{R}w_{,xx} + \frac{1}{2}[w,w] = 0 \tag{2.7}$$

$$D\Delta^2 w + P_0 w_{,xx} + \frac{1}{R}\phi_{,xx} - [w,\phi] = -\delta w_{,t} \tag{2.8}$$

The dynamical system described by equations 2.7 and 2.8 can also include a radial forcing function $P(x,y)$ as shown in equation 2.9.

$$D\Delta^2 w + P_0 w_{,xx} + \frac{1}{R}\phi_{,xx} - [w,\phi] + P(x,y) = -\delta w_{,t} \tag{2.9}$$

This radially acting forcing function has not been included in the initial description of the dynamical system because the system of interest is the cylindrical shell under uniform compression. However, in order to perturb linearly stable fixed points and characterise their associated basins of attraction, this radial forcing is required. Furthermore, using this radial forcing, a very relevant equilibrium point of the system has been obtained. This especial equilibrium point will be discussed in section 2.3.

The boundary conditions used for the solution of the dynamical system are defined by equations 2.7 and 2.9 are periodic boundary conditions in the azimuthal direction. In the longitudinal direction, the boundary conditions used are clamped at the shell structure ends. Meaning in this case that the field and its first derivative in the normal direction are zero for the deviation from the pre-compressed state (w).

2.2.2 Numerical implementation

The aim is to compute equilibria of equations 2.7 and 2.8 and characterize their stability. The solutions scheme for the system makes use of an in-house developed code CYBUCK. CYBUCK relies on a high-order finite differences solver following the algorithm proposed by (Fornberg, 1998). This software was developed for the work presented by Kreilos in (Kreilos and Schneider, 2017). In the current research, CYBUCK has been used as a tool to explore the state space and understand the behaviour of cylindrical shells.

The studies carried out using CYBUCK are the search of fixed points in the system, parametric continuation studies, time integration and stability. A continuation study consists of the search of fixed points in the dynamical system for a varying parameter. In the case of the dynamical system used to define the cylindrical shell, the control parameter used is the axial pre-load P_0. A continuation procedure means finding the equilibrium points of the system for a changing control parameter. Time integration shows the evolution of the system in time. Lastly, with the stability feature of CYBUCK, the spectrum of the different fixed points can be characterized.

2.3 Fixed points and their role in cylindrical shell buckling

The determination of the critical amplitude perturbation which triggers buckling in a perfect shell, requires to determine the size of the basin of attraction of the unbuckled state. This can be done computing the invariant states of equations 2.7 and 2.8 that are embedded on its basin boundary. These states will be first constructed numerically for a fixed load and then parametrically continued in the axial force to characterise the variations of the critical perturbation amplitude as a function of the axial compression load.

Unstable equilibria of cylindrical shells

The initial localised solution consisting of a single dimple was built in the following manner. Firstly, an axial compression load P_0 was prescribed. In a second step, after applying the axial compression, a localised radial pressure distribution $P(x, y)$ was applied similar to a radial probe. Then, while leaving constant the compression force, the value of the radial pressure distribution was varied in a continuation procedure. The continuation procedure varies the pressure distribution resultant and finds the corresponding equilibrium states of the system for each value of the pressure.

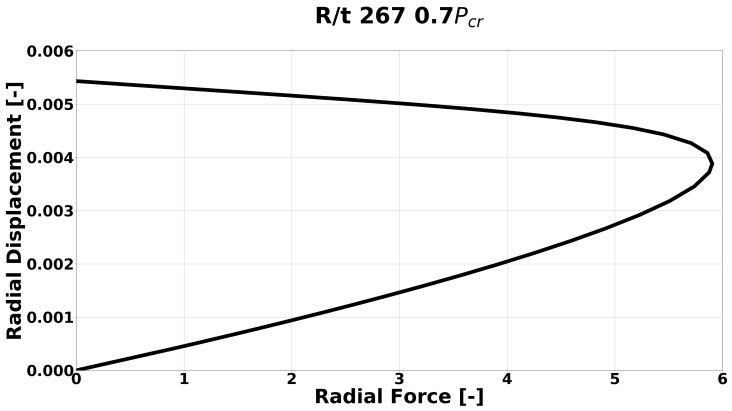

(a) Non-dimensional poking curves used to construct the initial edge state associated considering the geometrical properties of the 7.5oz can with a continuation procedure of the integrated lateral pressure.

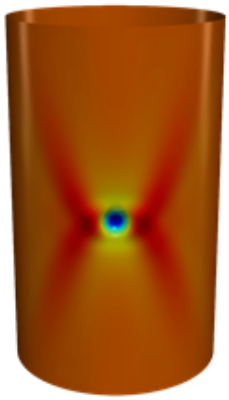

(b) Edge state of the 7.5oz can

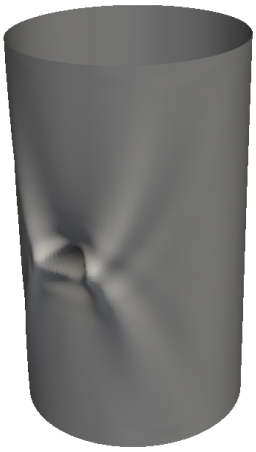

(c) Single unstable eigen mode from the edge state of the 7.5oz can

Figure 2.5 – Construction of the edge state for the 7.5oz can geometry. The pre-load considered in this case is 70% of the critical buckling load.

The continuation of the integrated pressure field of the radial pressure distribution grows up to a maximum. After this maximum the radial displacement increases while the total force of the pressure field decreases until in becomes 0 as shown in figure 2.5a. In this continuation procedure, at the point where the radial load vanishes, the radial displacement field sustains an inward displacement in the form of a localised dimple (See figure 2.5b). This is an equilibrium point of the dynamical system under a uniform compression load P_0 and no radial force. This equilibrium point although it has been calculated using equation 2.9 it is also a fixed point of the dynamical system defined by equations 2.7 and 2.7. The stability analysis of the single dimple fixed point from figure 2.5b has a single unstable eigen-mode. This means that the single dimple unstable fixed point is an edge state of the system.

An alternative technique to construct the single dimple unstable fixed point is edge tracking. This method consists of creating a bisection between two states that are known to bound the basin boundary. The state in between these two initial states is a state on the edge or basin boundary (Kreilos and Eckhardt, 2012). This technique was demonstrated initially for the dynamical system describing the cylindrical shells in (Kreilos and Schneider, 2017).

The technique to construct the single dimple edge state via probing is a numerical correlation of the experimental work that will follow in upcoming sections. Probing is a technique that can be implemented in the experiments while edge tracking has a more challenging implementation in an experimental set up.

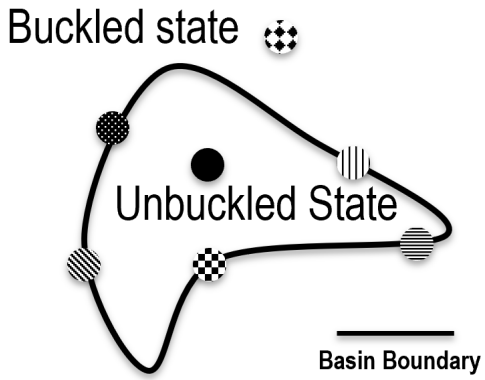

(a) Graphical depiction of the basin of basin of attraction of a shell showing the basin boundary where a large variety of un-stable fixed points exists

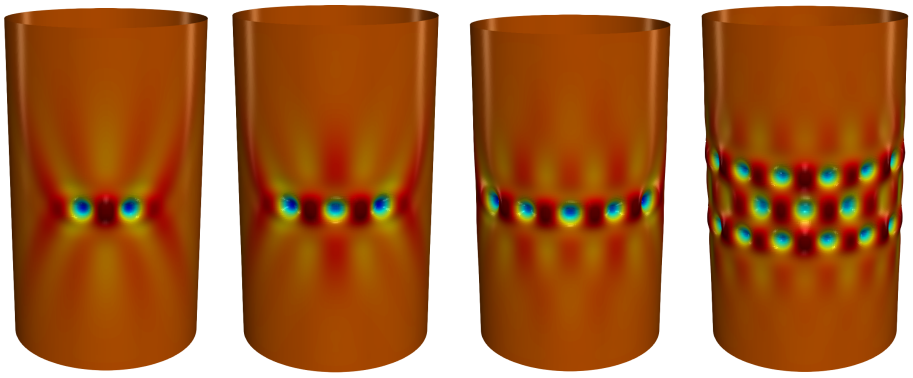

(b) 2 dimple solution built by assembly of individual dimples

(c) 3 dimple solution built by assembly of individual dimples

(d) 5 dimple solution built by assembly of individual dimples

(e) 17 dimple solution built by assembly of individual dimples

Figure 2.6 – Example of the complexity of unstable equilibria that may lay in the basin boundary separating the un-buckled state from the buckled state. All these un-stable fixed points have been calculated for identical compression force, 70% of the critical one.

Using as a minimal unit the localized dimple of the edge state, is possible to construct other unstable fixed points that may lay in the basin boundary. The solutions shown in the 3D plots of figure 2.6 have been obtained using this construction technique. These fixed points are potential candidates to be unstable equilibria on the basin boundary, i.e. the edge.

The construction technique used to obtain the fixed points from figure 2.6 consists in creating an initial conditions for a Newton search based on the original single dimple solution. The core structure of the single dimple field is cut and placed in a field a number of times and this artificial field is used as an initial condition for a Newton search. This process is shown schematically for the case of the 2 dimple solution in figure 2.12.

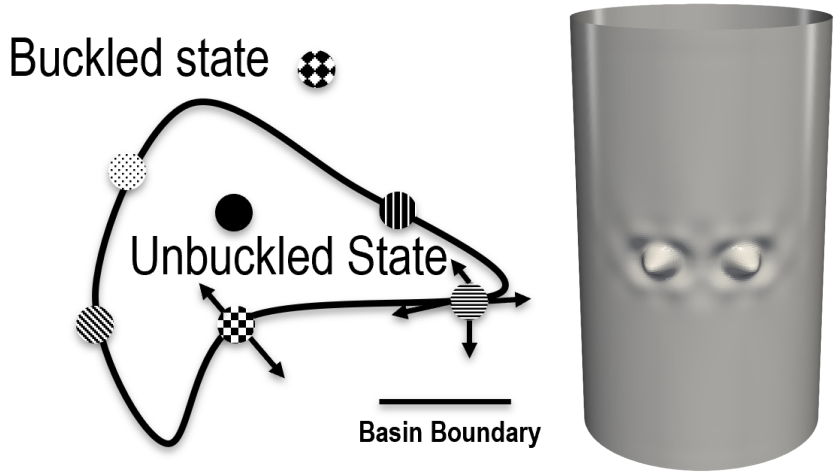

(a) Graphical description of states on the edge and associated eigen modes represented by the arrows

(b) Example of most unstable eigen-mode of a 2 dimple solution.

Figure 2.7 – Illustration of states on the edge or basin boundary and example one of the 3 unstable eigen-modes associated with a 2 dimple state. There is always one unstable eigen-mode associated with each individual localized structure plus a series of all the possible combinations.

The complex arrangements of dimples from figure 2.6 are unstable equilibrium solutions of the shell equations. However, in order to confirm that these states are in the basin boundary, there is a verification that needs to be performed.

The approach to discern whether the solutions from figure 2.6 are embedded in the basin boundary or not consists of deriving the spectrum of the corresponding solution, find the most unstable one and perturb the fixed point ($\mathbf{u}$) in opposite direction of the basin boundary as graphically depicted in figure 2.7a with the most unstable eigen-mode ($\mathbf{u}*$). The final step in the verification about whether the solution is part of the basin boundary or not is to perform a forward time integration of the perturbed solutions ($\mathbf{u}+\epsilon\mathbf{u}*$ and $\underline{\mathbf{u}}-\epsilon\mathbf{u}*$). In this forward time integration, the solution perturbed toward the unbuckled state ($\mathbf{u}-\epsilon\mathbf{u}*$) should decay while the one perturbed towards the buckled state ($\mathbf{u}+\epsilon\mathbf{u}*$) should move toward the buckled state, developing additional structures. In the first case the strain energy should tend to 0 while in the second it should grow as shown in figure 2.9a. A graphical depiction of the two time integrations is shown in figure 2.8. The upper row corresponds to the dashed line of figure 2.9a, the two dimple structures vanishes. The lower row corresponds with the solid line of figure 2.9a. The two dimple structures grows and starts to develop additional structures.

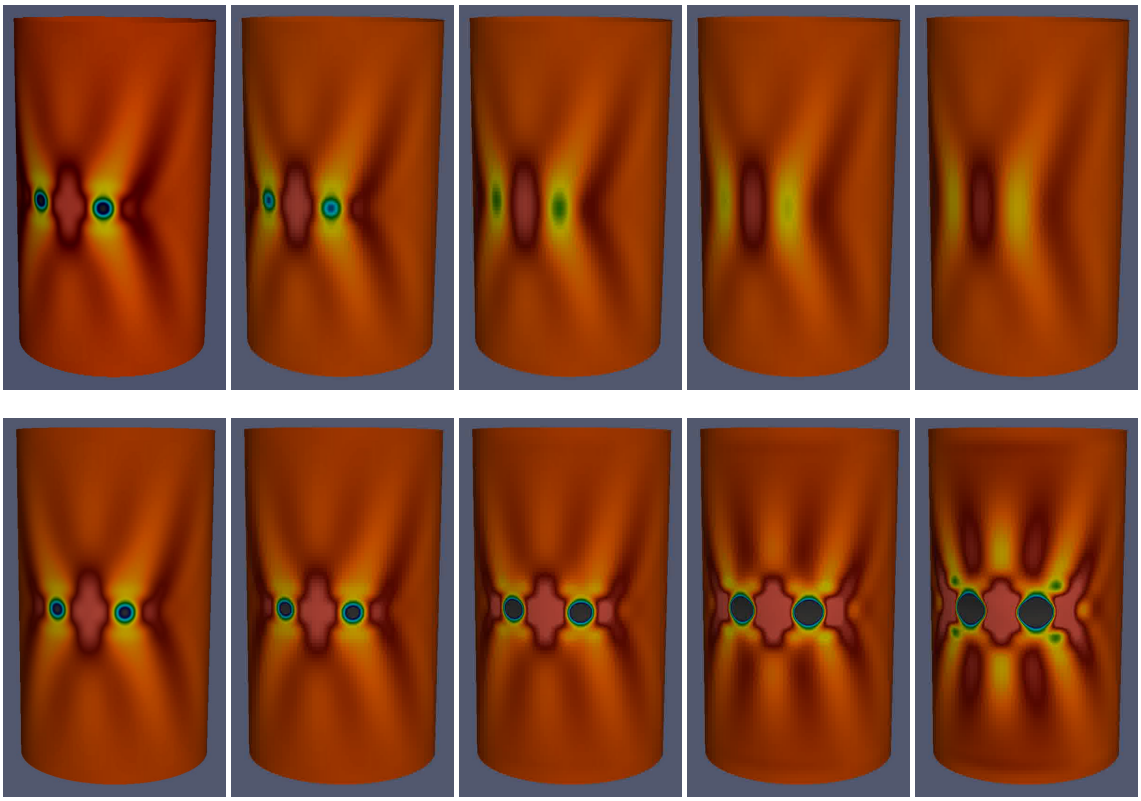

Figure 2.8 – Snapshots of the forward time integration of the perturbed field. The upper row corresponds to the direction towards the basin of attraction of the un-buckled state. The lower row corresponds to the forward time integration of the direction towards the buckled state.

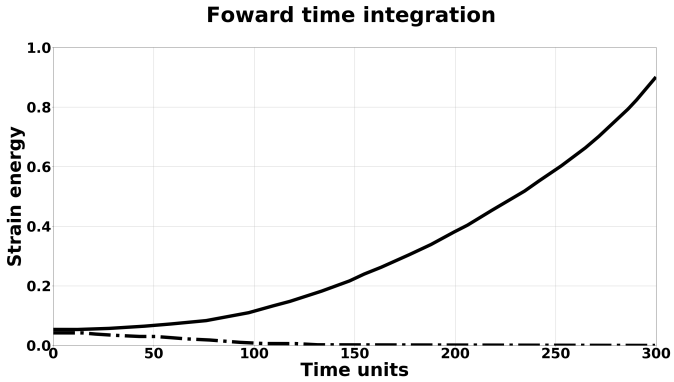

Figure 2.9 – Evolution of the strain energy of the forward time integration of the perturbed solutions. The solid one in the direction of the buckled state and the dashed one in the direction of the unbuckled state.

Snaking in cylindrical shells

Once the initial localised solution with a single dimple is obtained, it is possible to follow a continuation procedure on the compression load parameter P_0. The additional fixed points found following this continuation procedure allow to explore the change of the state space structures as a function of axial load supported by the DMV shell equations. Under decreasing axial load, the continuation procedure unveils a series of localised solutions similar to an arrangement of dimples where additional localised structures develop through different bifurcations. The branch containing an odd number of localised features emerging from the single dimple solution can be observed in figure 2.10 in blue. This branch of solutions was initially calculated by Kreilos and published in Kreilos and Schneider (2017). The structure of spikes that follows the growth of localised structures is a feature of dynamical systems called snaking (Champneys, 1998; Hunt et al., 2000).

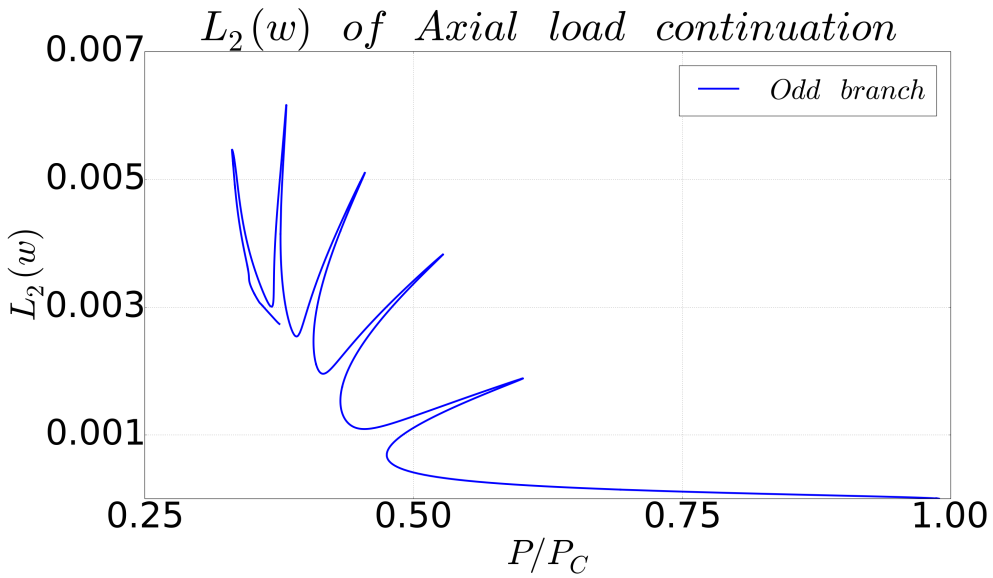

Figure 2.10 – Reproduction of the snaking curve calculated by Kreilos and Schneider (2017). This branch is referred as the odd branch of the snaking due to the fact that there is an odd number of dimples present in each invariant solution.

In the initial work by Kreilos and Schneider (2017), it was already discovered that the fixed points of the dynamical system describing the cylindrical shell undergo snaking. Figure 2.10 reproduces the so-called odd branch of the snaking. Due to the symmetries in the system, it was hypothesised that the localised solutions behave similarly to the Swift-Hohenberg equation as it is the case in many other physical systems (Burke and Knobloch, 2007). If this is the case the cylindrical shell dynamical system should have a state space similar to the schematic of figure 2.11. Following this hypothesis about the similarity of behavior of cylindrical shells and Swift-Hohenberg, the next feature to be searched for is the second branch of the snaking. Meaning that a search for an additional branch with similar localised

structures but with an even number of features, i.e. dimples.

The starting point for this search of the even branch of the snaking is the original edge state found with a single dimple. In order to build the simplest solution with an even number of features, two of the single dimples can be put together and used as an initial condition for a Newton search. Practically, this means to take the field with a single dimple that is known to be an invariant solution of the system, include two dimples in a new field and use this initial field as initial condition for CYBUCK to find a new fixed point.

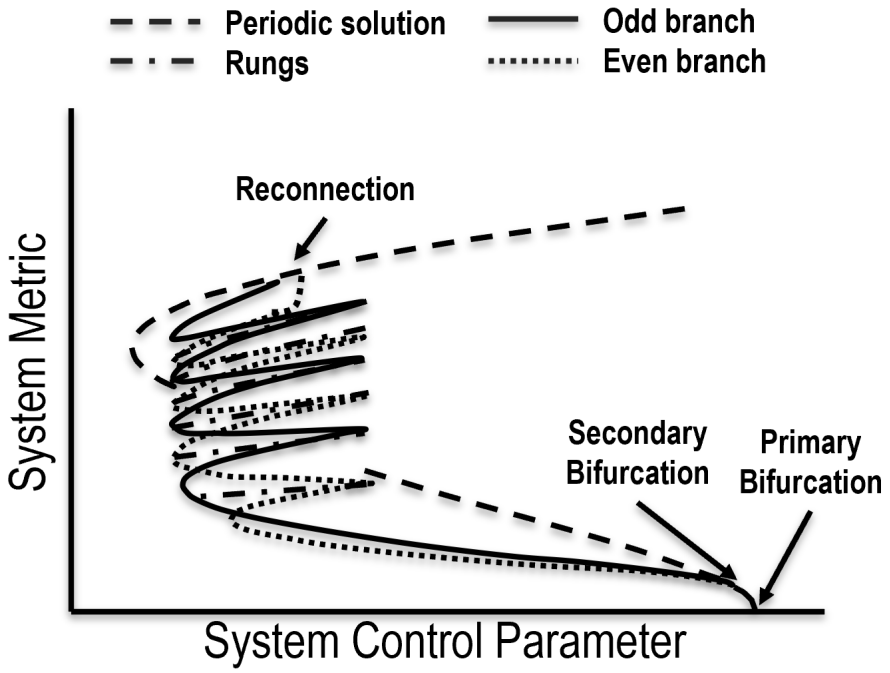

Figure 2.11 – Sketch depicting the typical state space diagram of the Swift-Hohenberg equation with quadratic and cubic non-linearity. Note that the odd and even branches emerge in a secondary bifurcation from the fully periodic solution.

This process required a number of iterations to find the correct spacing between dimples that would first lead to an invariant solution of the system and second to a solution that would undergo snaking. In figure 2.12 this process is illustrated showing the initial developed single dimple fix point, the patterned dimple structure from the single dimple fix point and the final converged 2 dimple solution. This 2 dimple solution was calculated for the same load parameter and then continued in axial load parameters toward the primary bifurcation at higher load. The continuation also followed towards a lower load level. In this second continuation the 2 dimple solution underwent homoclinic snaking as seen in the odd branch of the snaking.

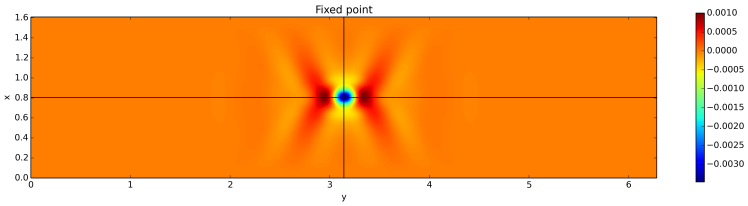

(a) 2D representation of the single dimple solution

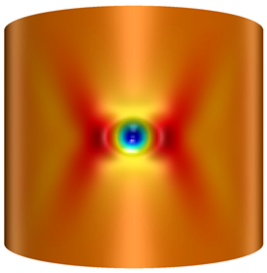

(b) 3D representation of the single dimple solution

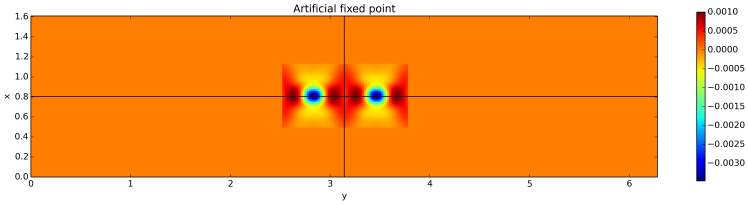

(c) Initial condition of the 2 dimple solution consisting of 2 single dimples tilled together

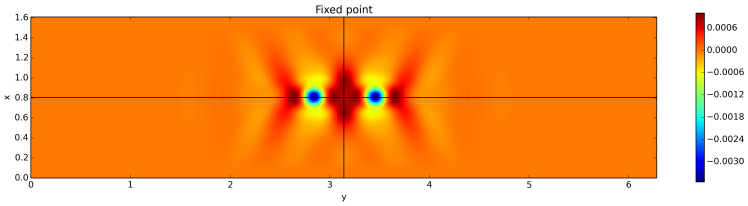

(d) 2D representation of the converged 2 dimple solution

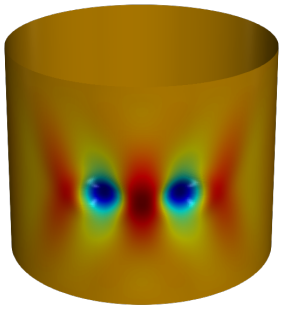

(e) 3D representation of the converged 2 dimple solution

Figure 2.12 – Schematic representation of the construction of the 2 dimple unstable equilibrium.

Under the continuation of the axial force towards lower values, the localised solution undergoes a series of bifurcations. The system underwent a series of saddle node and pitchfork bifurcations leading to the creation of additional structures. The role of these specific bifurcations will be explained later. The branch with an even number of features emerging from the double dimple solution can be observed in figure 2.13. The fact that the second branch with even number of localised structures is also present in the system confirms that the system behaves similarly to a traditional physics model. The Swift-Hohenberg equation with squared cubic non-linearity (SH23). The characteristic state space of SH23 is shown in figure 2.11.

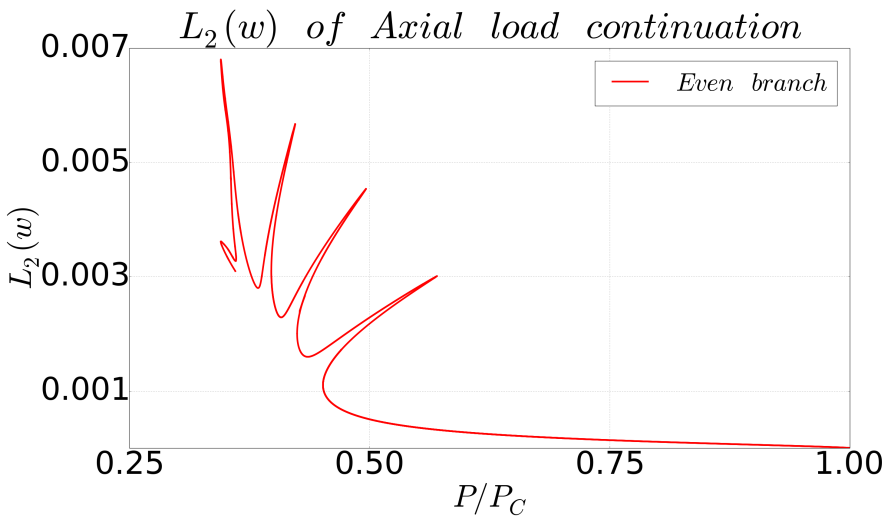

Figure 2.13 – Additional branch containing the solutions with even number of dimples

The phase space diagrams presented in figures 2.10, 2.13 and 2.15 show the evolution of the L_2 norm of the radial displacement associated with each invariant solution as a function of the normalized axial compression load.

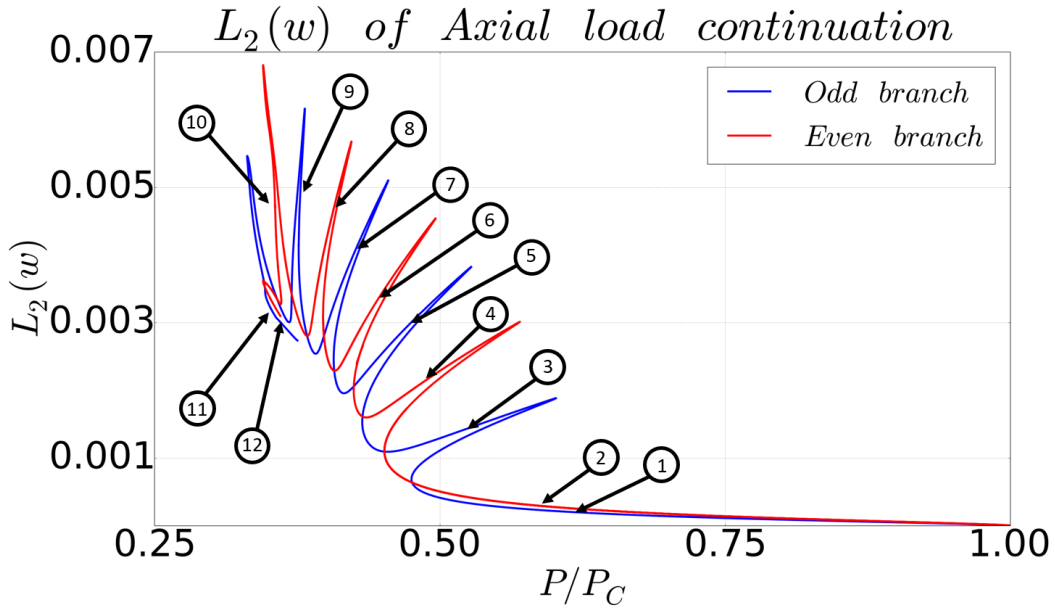

Figure 2.15 – Combination of the branches with odd an even number of features showing a snaking diagram. The number included in the plot refer to the 3D deformation of figure 2.14

It was mentioned earlier that bifurcations are the mechanism for the creation of additional structures in the system. In the case of the cylindrical shell, the bifurcation that is responsible

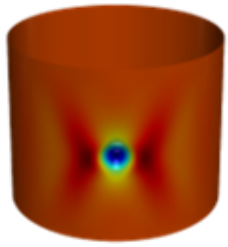

(a) Figure corresponding to point 1

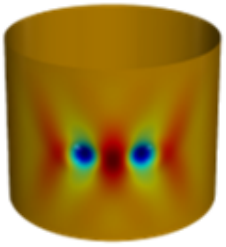

(b) Figure corresponding to point 2

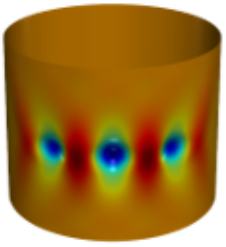

(c) Figure corresponding to point 3

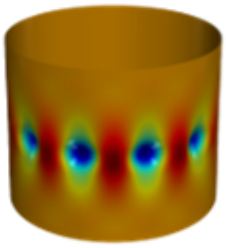

(d) Figure corresponding to point 4

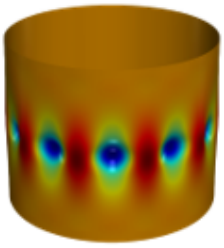

(e) Figure corresponding to point 5

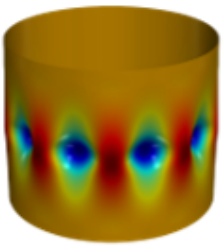

(f) Figure corresponding to point 6

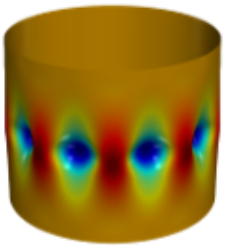

(g) Figure corresponding to point 7

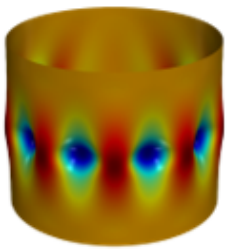

(h) Figure corresponding to point 8

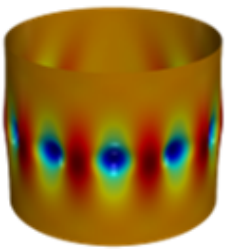

(i) Figure corresponding to point 9

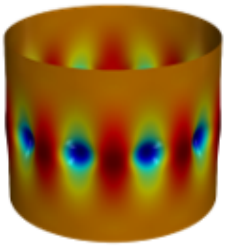

(j) Figure corresponding to point 10

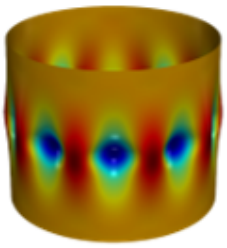

(k) Figure corresponding to point 11

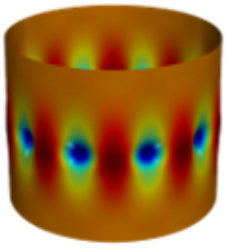

(l) Figure corresponding to point 12

Figure 2.14 – Fixed points along the even and odd branches of the snaking. The numbers in the sub-captions refer to the numbers used in the annotations of figure 2.15

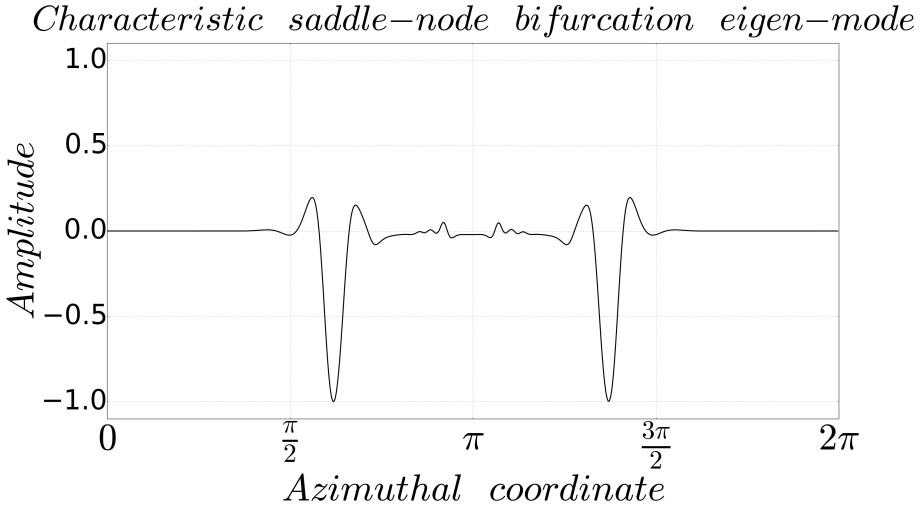

(a) Cross-section of the eigen-mode associated with the first saddle node bifurcation.

for the growth of additional structures on the sides of the existing dimples are saddle node bifurcations. This kind of bifurcations can be identified evaluating the spectrum associated with each fixed point. At the moment when an eigen-mode becomes unstable and the associated displacement field suggests the addition of new structures to the existing ones, the system has undergone a bifurcation. In the case of the saddle node bifurcation the eigen-mode is fully symmetric and adds new structures at the extremes of already existing ones in the corresponding fixed point.

An additional bifurcation identified studying the spectrum of the snaking curves are pitchfork bifurcations. These phenomena lead to the creation of new structures that are not symmetric in this case. This guarantees the existence of an additional feature that is also present in the Swift-Hohenberg model, rung states. These states are non-symmetric fixed points that are in between the even and odd branches. The succession of these non-symmetric states form connections between the odd and the even branch as shown in figure 2.11. These connections between the even and odd branches of the snaking forms a structure of ladders that has also been reported for different systems Schneider et al. (2010). In figure 2.18, the result of the initial rung state emerging from the single dimple solution is shown. The non-symmetric field is also displayed in the 3D plot of the same image.

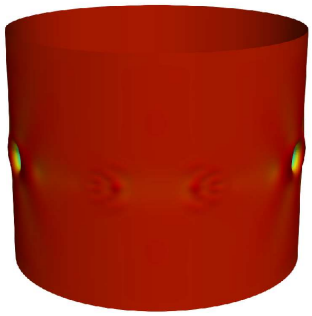

(b) Front view eigen-mode associated with the first saddle node bifurcation.

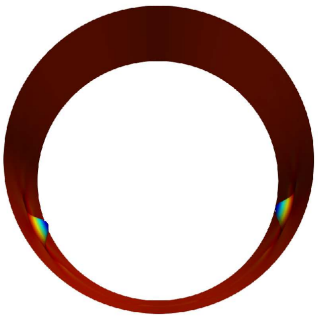

(c) Top view eigen-mode associated with the first saddle node bifurcation.

Figure 2.16 – Summary of the results used to identify the first saddle node bifurcation of the even branch, the transition between 2 to 4 dimples. In the saddle node bifurcation the symmetry is preserved. It is a mechanism that adds localized structures to the train of localized dimples in the mid section of the cylindrical shell

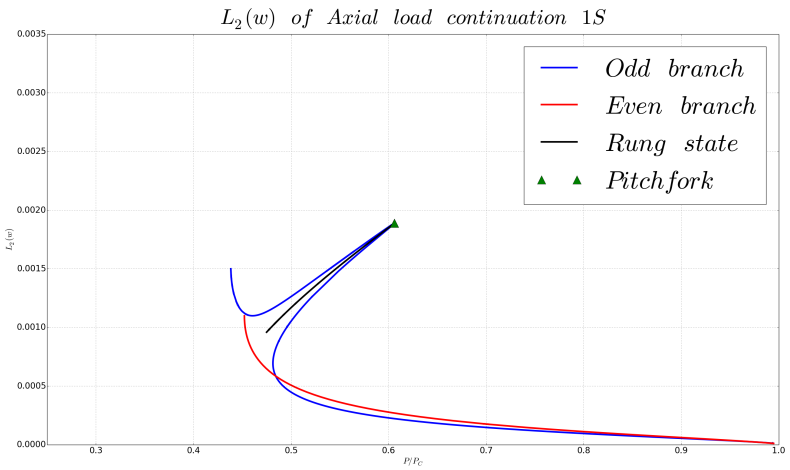

(a) Partial rung state.

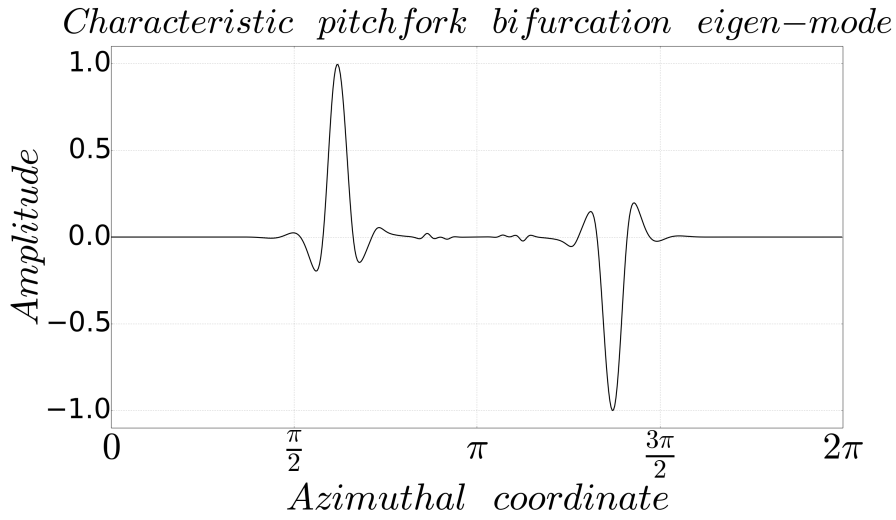

(a) Front view eigen-mode associated with the first saddle node bifurcation.

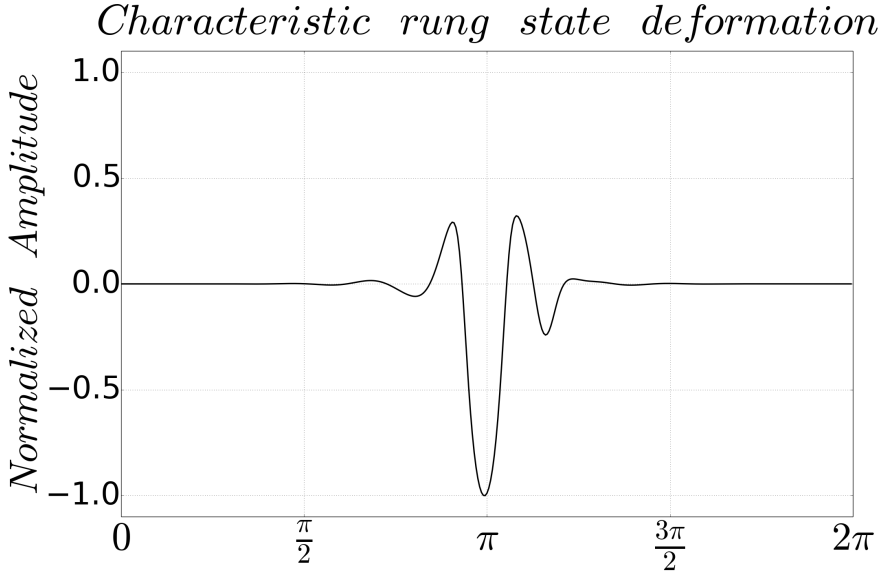

(b) Cross-section of the displacement field associated with the rung state

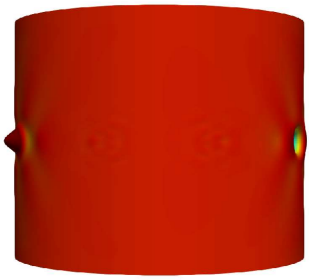

(b) Front view eigen-mode associated with the first saddle node bifurcation.

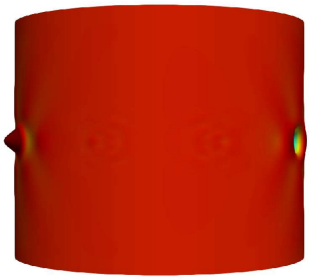

(c) Top view eigen-mode associated with the first saddle node bifurcation.

Figure 2.17 – This is a pitchfork bifurcation. In this bifurcation the symmetry is not preserved. It is a mechanism to add localized structures to the train of localized dimples in the mid section of the cylindrical shell only on one side. This is the sign that rung states are present in this system

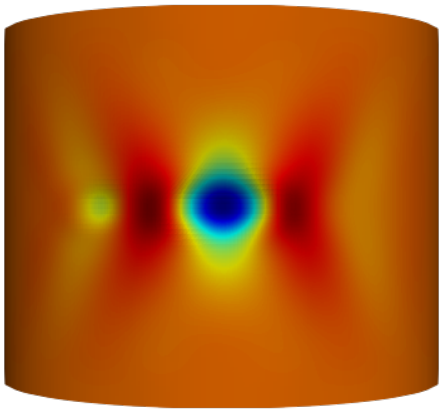

(c) Front view eigen-mode associated with the first saddle node bifurcation.

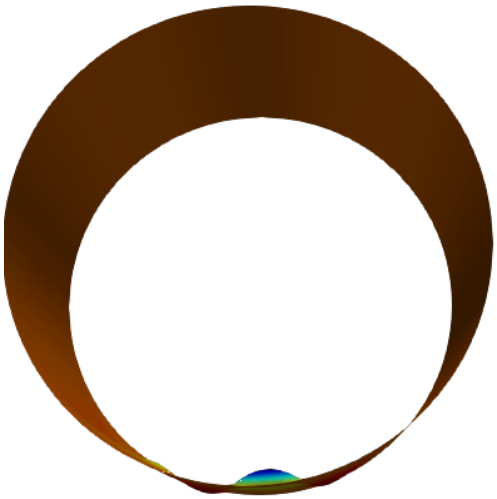

(d) Top view eigen-mode associated with the first saddle node bifurcation.

Figure 2.18 – This is the 3D representation of the initial rung state. The run state emerges from a symmetry breaking bifurcation that allows the creating of additional structures only in one front.

This last feature completes a picture that shares a lot of similarities with the Swift-Hohenberg equation with quadratic and cubic non-linearity ($SH23$) Burke and Knobloch (2006). Cylindri-

cal shell can only behave similarly to SH23 due to symmetry reasons in the field characterising the systems. In cylindrical shells, radial displacement is not the same weather it happens inwards or outwards. Hence the similarity with the Swift-Hohenberg equation with cubic and quintic non-linearity ($SH35$). This last version of the Swift-Hohenberg equation posses additional features that have not been found in the case of the cylindrical shell. Namely, the two additional branches of localized solutions that should emerge from the primary bifurcation for the $SH35$ Houghton and Knobloch (2011).

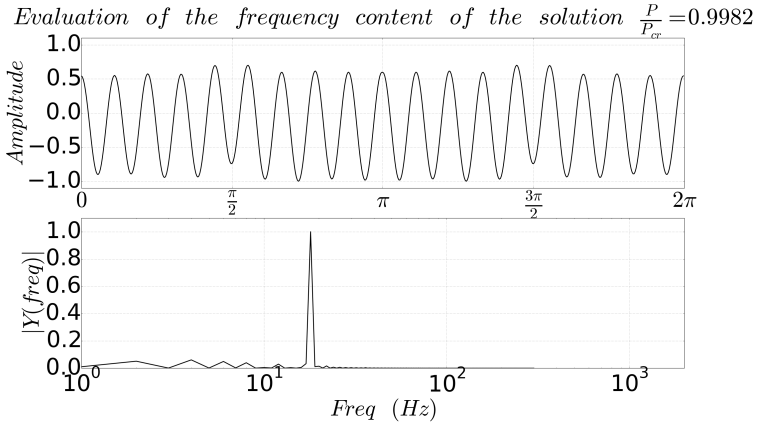

(e) The upper graph of the plot represents the mid section of the last invariant solution obtained via continuation on the load parameter towards higher axial load. The lower one is a Fourier transform of the upper graph showing the frequency content of the solution along the azimuthal direction.

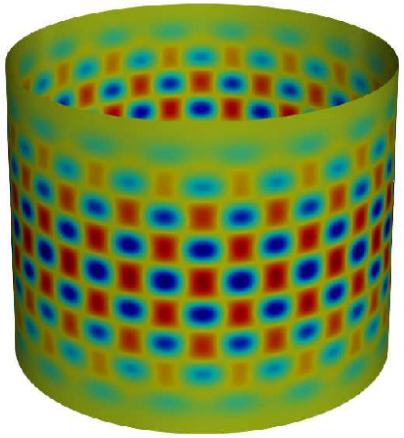

(f) 3D view of the nearly periodic invariant solution

Figure 2.19 – Summary of the nearly periodic solution found during the continuation in load towards higher value of axial load.

The continuation procedure used to obtain the snaking curves for values of decreasing axial load was also followed in the direction of increasing load. In this direction, the aim was to find

an additional feature present in physical systems that behave similarly to the Swift-Hohenberg model, the full periodic branch that should emerge close to the primary bifurcation.

The radial displacement field of the fixed point of figure 2.19f is very similar in terms of morphology to the fully periodic eigen-modes reported in the literature (Koiter, 1945). The secondary bifurcation emerging from the fully periodic solution was not found. This is a deviation form the picture of the SH23. The secondary bifurcation where the two snaking branches emerges must exist. However, the numerical scheme used during the current research had difficulties resolving the region where the bifurcation should occur.

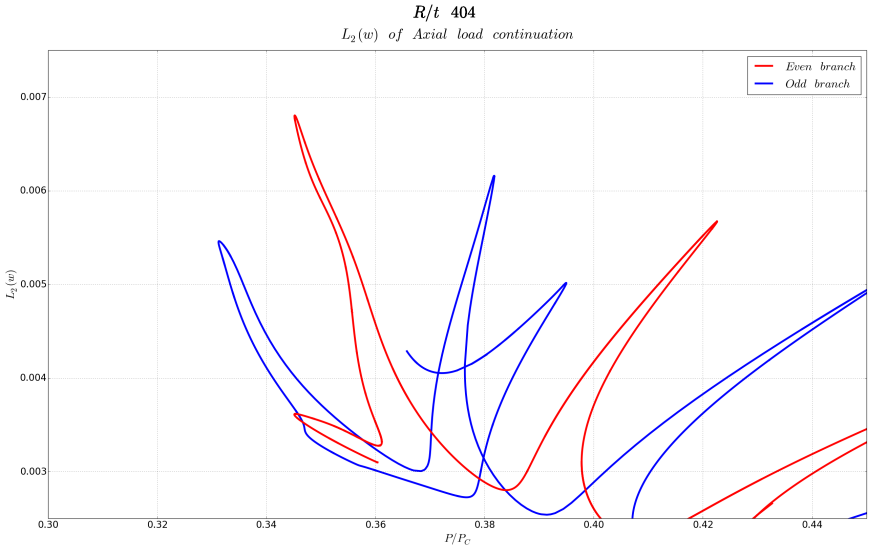

(a) State space representation of the final part of the continuation of the odd and even branch of snaking towards lower axial load

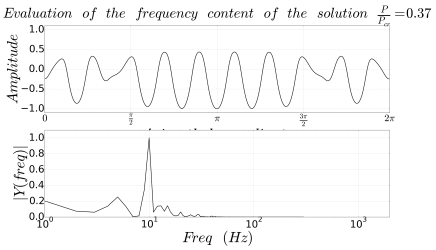

(b) Evaluation of frequency content of the last invariant solution of the odd branch

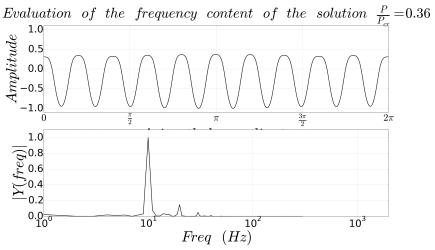

(c) Evaluation of frequency content of the last invariant solution of the even branch

Figure 2.20 – Summary of the results of the continuation towards lower loads approaching to a nearly periodic state.

The snaking branches in the original SH23 system reconnect to the periodic state. However, in the case of the cylindrical shell this does not occur. The continuation towards lower load develops a set of dimples that cover the complete cylinder

This different behaviour is possibly linked to the fact that the selected parameter of the geometry does not allow for the domain to accommodate the required dimples.

2.4 Conclusions

In this chapter, a dynamical system description of a cylindrical shell based on the DMV approximation has been introduced. The concepts from turbulence research have been applied to obtain fixed points of the this dynamical system and study the stability of the different fixed points obtained during the current research. The buckling of cylindrical shells has been studied as a finite amplitude perturbation characterising partially the basin of attraction of the system. The concept of basin of attraction has been introduced. An approach to create fixed points based in probing has been demonstrated. This probing technique is the numerical analogy of the probing probing technique that will be used experimentally to explore the extension of the basin of attraction in chapter 5.

The basin of attraction shrinks as the compression load increases, until vanishing at the critical buckling load. This last point is the link between dynamical systems theory and experiments. Hence, the basin of attraction and its potential as a predictive tool of buckling loads will be explored in chapters 5 and 6.

On the numerical side, a new set of features of the dynamical system describing cylindrical shells have been found during the current research. These new dynamical system features describing cylindrical shells resemble features in the Swift-Hohenberg with quadratic and cubic non-linearity. Namely, the even branch of the snaking, a rung state and an almost periodic state close to the primary bifurcation parameter.

3 Finite Elements applied to the prediction of cylindrical shell buckling

The finite element method is the numerical scheme that lies at the foundation of many tools used to solve partial differential equations. In fact it is the numerical method of choice of the main commercial codes used in the field of solid mechanics in general and to study the collapse of cylindrical shells in particular. The key advantages of the finite element method are its flexibility to adapt to complex domains, cope with complex load cases and deal with systems with over constrained boundary conditions (Liu, 2003; Bathe, 2014a).

The ability to cope with complex geometries is the most relevant advantage that sets apart finite element based analyses from analytical methods or other numerical schemes like spectral methods. Analytical solutions can only provide a closed form solution for a small group of very simple geometries and boundary conditions. In fact these boundary conditions are often idealized and can not be exactly replicated in reality. In the case of other numerical methods, like spectral methods (Gottlieb and Orszag, 1977), regular simply connected domains are required.

Tools based on the finite element method have seen a widespread utilization in industry and are the main tool of the structural engineers to analyse the mechanical response of any structure. In the case of the current research, the study of the collapse of cylindrical shells, the main advantages of using finite elements are two:

- The possibility to adapt to any complex geometry in 3D space including geometrically imperfect cylindrical shells
- The capability to capture realistic boundary conditions, loading imperfections and complex loading schemes as in physical experiments

The first one is key for the study of realistic imperfect systems. The possibility to adapt to any complex geometry allows the inclusion of complex geometrical imperfections and loading schemes. The geometrical imperfections are deviations form the ideal geometry that make

the system under study closer to reality. The complex loading scheme allows the inclusion of load cases that combine different loads as it occurs in reality.

The second capability listed allows to study numerically the same system that can be tested in an experimental set up. The control over the boundary conditions is very important to capture accurately the physics of the different systems that can be studied with finite elements. Namely the sensitivity that some systems like cylindrical shells present to any deviation from the ideal conditions.

The basic pictorial and simplified idea of the finite element method is the following one. A complex domain representing the system under study is discretized by smaller regular patches. In these smaller patches is where the solid mechanics problem of interest is solved locally constructing approximations of the displacement fields (Zienkiewicz, 2013). A more formal description of finite element method is is the following one: The strong form of the governing equations modelling a system can be expressed in an equivalent weak formulation that together with a set of local approximation functions are used to build estimations of the solutions of the problem in a discretized domain (Fish, 2013).

The finite element formulations described in this section are presented following the displacement-based approach instead of the force-based approach. The difference between the two approaches is the fields that are approximated. In the displacement-based formulation the displacements are approximated while in the force-based one the stress fields are approximated. The displacement formulation is more convenient because the compatibility conditions required at element level in terms of displacements and rotations can be determined directly from the displacement field (Bathe, 2014b). This formulation is the one used in commercial finite elements codes like Abaqus or NASTRAN.

In section 3.1 the basic numerical scheme of the linear finite element method will be presented. Section 3.2 illustrates the non-linear finite element schemes and their basic functionalities to include geometrical non-linearity. The sections presenting the mathematical descriptions are included to demonstrate technicalities of the different finite element formulations used in the current research. The references used as resources in sections 3.1 and 3.2 are (Fish, 2013; Crisfield, 1981; Liu et al., 2008; Bathe, 2014b). These references provide much deeper insight in the topic of finite element analysis than what is presented here. In addition to the technical description about how finite elements work, details will be provided about how to practically carry out an accurate finite element analysis to predict the collapse of cylindrical shells.

3.1 Linear Finite Elements

In the linear finite element formulation, the key underlying assumption about displacement and rotations is that they are assumed infinitesimally small. Hence, the effect of deformations does not affect the stress state of the system under study (Crisfield, 1981). This linear behaviour refers to the geometry. In the case of the material, the behaviour will be also considered as

linearly elastic.

The first step required to implement the finite element method is the derivation of the weak formulation of the corresponding problem under study. The weak formulation is more commonly referred to principle of virtual work (W) in solid mechanics (Fish, 2013)

$$\delta W = 0 \tag{3.1}$$

The virtual work principle is to be applied to an arbitrary elastic body that represents a $3D$ portion of a solid. In this arbitrary piece of solid, the work performed by a set of virtual displacements $\delta\underline{\mathbf{u}}$ times the forces applied need to be equal to the work of the internal stresses times the internal strains. The internal stresses at the boundaries of the 3D element are given by the Couchy stress tensor σ_{ij}

$$\sigma_{ij}\begin{Bmatrix}\sigma_{11} & \sigma_{12} & \sigma_{13}\\ \sigma_{21} & \sigma_{22} & \sigma_{23}\\ \sigma_{31} & \sigma_{32} & \sigma_{33}\end{Bmatrix} \tag{3.2}$$

The fact that $\sigma_{ij} = \sigma_{ji}$ makes 3.2 a symmetric matrix with only 6 independent components. Consequently, it is possible to express the stress components in vector notation:

$$\sigma_{ij}^{T} = [\sigma_{11}, \sigma_{22}, \sigma_{33}, \sigma_{12}, \sigma_{23}, \sigma_{31}] \tag{3.3}$$

The internal virtual strains have the same symmetries as the stress components and can also be expressed in vector notation:

$$\delta\epsilon_{ij}^{T} = [\delta\epsilon_{11}, \delta\epsilon_{22}, \delta\epsilon_{33}, \delta\epsilon_{12}, \delta\epsilon_{23}, \delta\epsilon_{31}] \tag{3.4}$$

The virtual work principle applied to a portion of a 3D elastic body is then:

$$\int_V \delta\epsilon_{ij}^{T}\sigma_{ij}\, dV = \int_V \delta\underline{\mathbf{u}}^{T}\,\mathbf{b} dV - \int_{A_\sigma} \delta\underline{\mathbf{u}}^{T}\mathbf{t}\, dA_\sigma \tag{3.5}$$

where **b** represents the body forces acting on the volume of the 3D element and **t** represents the traction forces at the boundaries. In order to obtain the total virtual work of the body, the integrals from equation 3.5 need to be extended to the complete body. In order to do that, a summation covering the complete body is required. This summation extended to the

complete body is

$$\sum_{1}^{n}\int_{V}\delta\epsilon_{ij}^{T}\sigma_{ij}\,dV=\sum_{1}^{n}\int_{V}\delta\underline{\mathbf{u}}^{T}\,\mathbf{b}dV-\sum_{1}^{n}\int_{A_\sigma}\delta\underline{\mathbf{u}}^{T}\mathbf{t}\,dA_\sigma \tag{3.6}$$

In 3.6, n represents the number of elements used to discretize the complete solid. The stress term on the left hand side of 3.6 can be expressed as a function of the strain times a material related matrix **M**. Under the assumption that the material behaves linearly and in an isotropic manner, all the components of that matrix are constant leading to the linear stress-strain relation

$$\sigma_{ij}=\mathbf{M}_{ij}\epsilon_{ij} \tag{3.7}$$

Once the stress term in the left hand side has been expressed as a function of the strains,

$$\sum_{1}^{n}\int_{V}\delta\epsilon_{ij}^{T}\mathbf{E}\epsilon_{ij}\,dV=\sum_{1}^{n}\int_{V}\delta\underline{\mathbf{u}}^{T}\,\mathbf{b}dV-\sum_{1}^{n}\int_{A_\sigma}\delta\underline{\mathbf{u}}^{T}\mathbf{t}\,dA_\sigma \tag{3.8}$$

the expression for the virtual work is only a function of deformations.

Equation 3.8 represents the virtual work performed by a virtual displacement in global coordinates on a complete body. At this point it is important to remember that the aim is to obtain the nodal displacements at the level of the element 3.8 and then assemble the contribution of all the finite elements present in the body. Hence a relationship between global strains and local displacements ($\underline{\mathbf{u}}_L$) following equation 3.9.Furthermore an expression to link the global displacement ($\underline{\mathbf{u}}$) with the local ones ($\underline{\mathbf{u}}_L$) is also needed, this is done following equation 3.10. These relationships are provided by the matrices **B** and **N**. **B** is the so-called strain matrix and **N** is the shape functions matrix. The shape functions are polynomial expressions used to approximate the displacements within each individual element (Liu, 2003).

$$\epsilon_{ij}=\mathbf{B}\underline{\mathbf{u}}_L \tag{3.9}$$

$$\underline{\mathbf{u}}=\mathbf{N}\underline{\mathbf{u}}_L \tag{3.10}$$

$$\sum_{1}^{n}\int_{V}\delta\underline{\mathbf{u}}_L^{T}\mathbf{B}^{T}\mathbf{E}\mathbf{B}\underline{\mathbf{u}}_L\,dV=\sum_{1}^{n}\int_{V}\delta\underline{\mathbf{u}}_L^{T}\mathbf{N}\,\mathbf{b}dV-\sum_{1}^{n}\int_{A_\sigma}\delta\underline{\mathbf{u}}_L^{T}\mathbf{N}\mathbf{t}\,dA_\sigma \tag{3.11}$$

Equation 3.11 can be simplified by taking out the common factor $\underline{\mathbf{u}}_L^T$ into equation 3.12

$$\sum_1^n \int_V \mathbf{B}^T \mathbf{E} \mathbf{B} \underline{\mathbf{u}}_L \, dV = \sum_1^n \int_V \mathbf{N}\, \mathbf{b} dV - \sum_1^n \int_{A_\sigma} \mathbf{N} \mathbf{t} \, dA_\sigma \tag{3.12}$$

After the elimination of the virtual displacements, a system of linear equation is obtained in the form of equation 3.13

$$\mathbf{K} \underline{\mathbf{u}}_L = \underline{\mathbf{p}} \tag{3.13}$$

where $\mathbf{K}$ and $\underline{\mathbf{p}}$ are defined according to 3.14 and 3.15

$$\mathbf{K} = \sum_1^n \int_V \mathbf{B}^T \mathbf{E} \mathbf{B} \, dV \tag{3.14}$$

$$\underline{\mathbf{p}} = \sum_1^n \int_V \mathbf{N}\, \mathbf{b} dV - \sum_1^n \int_{A_\sigma} \mathbf{N} \mathbf{t} \, dA_\sigma \tag{3.15}$$

$\mathbf{K}$ in equation 3.14 is the global stiffness matrix of the problem and $\underline{\mathbf{p}}$ in equation 3.15 is the load vector.

3.2 Non-linear Finite Elements

The buckling event of a cylindrical shell and the large displacements and rotations associated with it invalidate the assumptions underlying the linear finite element formulation which requires infinitesimal displacements and rotations. The deformations and rotations are large enough so the state of deformations influences the internal stress state of the cylindrical shell (Crisfield, 1981). In addition to geometry-induced non-linearity, there are other sources of non-linearities in solid mechanics as it was mentioned in section 3.1. These additional sources for non-linear behaviour are not going to be explored in this section. If the reader would like to get information about material-induced non-linearities, (Hutchinson J.W., 1970) offers a good insight into this topic. Following the statement of section 3.1, the material behaviour will be considered linear elastic also in this section.

The main source contributing to the non-linear behavior of the collapse of cylindrical shells is largely attributed to geometric imperfections (Babcock, 1983). Geometric imperfections are deviations form the ideal geometry of the cylindrical shells. In the current research, the imperfections considered consist of radial deformations. The presence of geometric imperfections leads to larger radial deformations than in the case of perfect cylindrical shells. Hence, a method to consider the influence of this pre-buckling deformation is required in

order to accurately predict when buckling occurs. The approach to capture this non-linear behaviour in the non-linear finite element method formulations is the inclusion of the tangent stiffness matrix (Crisfield, 2012).

The presence of the tangent stiffness matrix implies that the complete stiffness matrix in the case of non-linear finite elements has two components. A tangent stiffness matrix and a linear stiffness matrix. The tangent stiffness matrix captures the effect on the deformed geometry of the loaded cylindrical shells. Hence, it is a function of the state of deformation and encodes information about the loading. The linear stiffness matrix describes the rigidity of the cylindrical shell in an unloaded state. This means that the constant stiffness matrix of the linear finite element formulation (K) is the addition two stiffness matrices, a first one constant (K_l) and a second one that depends on the loading (K_{nl}).

$$[K_l + K_{nl}]\underline{\mathbf{u}} = \mathbf{p} \tag{3.16}$$

Following a similar approach to the previous section with linear finite elements, a derivation of the non-linear version of the method is shown. The derivation presented will be a brief introduction of how the methodology works and how the key features of the non-linear behaviour of a geometrically non-linear problem are included in the non-linear finite element formulation. In order to gain a better understanding about the details of this formulation, (Crisfield, 1981) provides a complete overview.

There are different formulations that are used for the derivation of the non-linear finite element algorithm. The commercial finite element code Abaqus uses the updated Lagrangian formulation (Dassault Systèmes Simulia Corp, 2011). Other formulations that are commonly used are the total Lagrangian and corrotational formulations (Crisfield, 1981).

The main differences between these formulations is the reference state that is used along the iterative process to reach the final configuration. In the case of the total Lagrangian formulation it is the initial unloaded state, while in the case of the updated Lagrangian it is the previous computed equilibrium state. In the case of the corrotational formulation, it is a local coordinate system that moves with the element is used. In this coordinate system the element can be considered to behave linearly. This last fact makes the corrotational formulation suitable to deal with large displacements that do not imply large local strains or curvatures (Crisfield, 1981).

Abaqus is the tool used for the finite element calculations of this work. Hence, the derivations of the non-linear finite elements will be done following the updated Lagrangian formulation.

The solution strategy in non-linear finite element problems follows an incremental scheme. This incremental scheme acts via the inclusion of a pre-factor acting on the loading that varies from 0 to 1. This pre-factor acts as a "knob" where 0 corresponds to no load and 1 corresponds to the complete loading being applied. Hence in order to apply a loading completely a number

of intermediate problems or steps for increasing values of the pre-factor need to be solved. The pre-factor acts as a control parameter to introduce the loading. In cylinder shell buckling the pre-factor is applied to either the prescribed end to end displacement of the cylindrical shell or the applied axial compression load.

In the updated Lagrangian formulation the state of the next step $(t+1)$ can be expressed as a function of the set of displacements to be solved at the current state (u) plus the contribution of the previous completed step (u_t).

$$u_{t+1} = u_t + u \tag{3.17}$$

where the displacement u is the unknown part to be calculated to obtain the next step u_{t+1} using as a reference the already calculated one u_t. The fact of using the previous state as a reference state makes the construction of the strain displacement depend only on derivatives of u. In the case of the updated Lagrangian formulation the non-linear strain metric used is the Green strain tensor:

$$\epsilon_t = \frac{1}{2}\left[\left(\frac{\partial \mathbf{u}_t}{\partial \mathbf{x}}\right) + \left(\frac{\partial \mathbf{u}_t}{\partial \mathbf{x}}\right)^T + \left(\frac{\partial \mathbf{u}_t}{\partial \mathbf{x}}\right)^T \left(\frac{\partial \mathbf{u}_t}{\partial \mathbf{x}}\right)\right] \tag{3.18}$$

The Green strain tensor defined in 3.18 can be split in two different parts, a linear and a non-linear one:

$$\epsilon = \epsilon_{Linear} + \epsilon_{Non-linear} \tag{3.19}$$

The stresses at each state (as well as the displacement field u) can also be expressed in the same way:

$$\sigma_{t+1} = \sigma_t + \sigma \tag{3.20}$$

As in the linear formulation, in the non-linear one the virtual work principle is also applied. The virtual work expression in the case of the updated Lagrangian formulation reads:

$$\int_{i\,V} \sigma \delta_i \epsilon_i dV + \int_{i\,V} \sigma \delta_i \eta_i dV + \int_{i\,V} S_i \delta_i \epsilon_i dV + \int_{i\,V} S_i \delta_i \eta_i dV = \delta_i W_{ext} \tag{3.21}$$

In this expression the term

$$\int_{i\,V} S_i \delta_i \eta_i dV \tag{3.22}$$

is neglected. This simplification is made because $\eta_i << \epsilon_i$. η_i is the product of the partial derivatives representing the non-linear part of the strain while ϵ_i represents a first order derivatives in the linear part of the strain-displacement relationship. Additionally, the stress is expressed as a function of the material properties times the strain.

$$\sigma_t = C\epsilon_t \tag{3.23}$$

Thus the expression for the virtual work 3.21 can be rewritten as

$$\int_{tV} \sigma \delta_t \epsilon_{Non-Linear\ t} + \int_{tV} C\epsilon_{Linear\ t} \delta_t \epsilon_{Linear} dV = \delta_t W_{ext} - \int_{tV} \sigma \delta_t \epsilon_{linear} dV \tag{3.24}$$

at step t.

The virtual work as stated in equation 3.24 is referred to displacements in a global coordinate system. These global displacements need to be expressed in the local nodal coordinates applying the shape function matrix N in the same way it was done in the linear formulation.

$$\underline{\mathbf{u}} = \mathbf{N}\underline{\mathbf{u}}_L \tag{3.25}$$

And similarly for the virtual displacements.

$$\delta\underline{\mathbf{u}} = \mathbf{N}\delta\underline{\mathbf{u}}_L \tag{3.26}$$

After transforming the global displacements to the local coordinate system displacement via the shape functions matrix N, a similar transformation needs to be applied to the strains. They need to expressed as a function of the local displacement and that is done, as in the case of the linear finite element formulation, via matrix $\mathbf{B}$ as shown in equation 3.27.

$$\epsilon = \mathbf{B}\underline{\mathbf{u}}_L \tag{3.27}$$

And similarly for the virtual strains.

$$\delta\epsilon = \mathbf{B}\delta\underline{\mathbf{u}}_L \tag{3.28}$$

A key benefit of the updated Lagrangian formulation is that it does not include any reference to the initial state of deformations. Hence, the variation of the linear and non-linear part of the strain does not contain any term related to the initial state. This fact simplifies the variation of

the linear part of the strain as shown in equation 3.29.

$$\delta_t \epsilon_{Linear} = \frac{1}{2}\left[\left(\frac{\partial \delta \mathbf{u}}{\partial_t \mathbf{u}}\right) + \left(\frac{\partial \delta \mathbf{u}}{\partial_t \mathbf{u}}\right)^T\right] \tag{3.29}$$

It has the same effect for the variation of the non-linear part of the strain as presented in 3.30.

$$\delta_t \epsilon_{Non-linear} = \frac{1}{2}\left[\left(\frac{\partial \delta \mathbf{u}}{\partial_t \mathbf{x}}\right)^T \left(\frac{\partial \mathbf{u}}{\partial_t \mathbf{x}}\right) + \left(\frac{\partial \mathbf{u}}{\partial_t \mathbf{x}}\right)^T \left(\frac{\partial \delta \mathbf{u}}{\partial_t \mathbf{x}}\right)\right] \tag{3.30}$$

Considering expressions 3.29 and 3.30, a transformation following expressions 3.31 to 3.34 can be implemented to represent the displacement in the local coordinates frame.

$$\left[\frac{\partial u_i}{\partial_t x_j}\right] = \mathbf{B}_l \underline{\mathbf{u}}_L \tag{3.31}$$

$$\left[\frac{\partial \delta u_i}{\partial_t x_j}\right] = \mathbf{B}_l \delta \underline{\mathbf{u}}_L \tag{3.32}$$

$$\left[\frac{\partial u_i}{\partial_t x_j}\right] = \mathbf{B}_{nl} \underline{\mathbf{u}}_L \tag{3.33}$$

$$\left[\frac{\partial \delta u_i}{\partial_t x_j}\right] = \mathbf{B}_{nl} \delta \underline{\mathbf{u}}_L \tag{3.34}$$

This transformation enables us to write the expression for the virtual work as a function of local deformations:

$$\int_{tV} \mathbf{B}_{nl}^T [\sigma_{ij}] \mathbf{B}_{nl} dV + \int_{tV} \delta \underline{\mathbf{u}}_L^T B_l^T C_t B_L \underline{\mathbf{u}}_L dV = \int_{tV} \delta \underline{\mathbf{u}}_L^T \mathbf{b} dV + \int_{tA_\sigma} \delta \underline{\mathbf{u}}_L^T N^T t_t dA_\sigma - \int_{tV} B_L^T \sigma_{ij} dV \tag{3.35}$$

Equation 3.35 can then be expressed in compact form:

$$[K_l + K_{nl}] \underline{\mathbf{u}}_L = p_t - f_t \tag{3.36}$$

with

$$K_l = \int_{tV} B^T C B dV \tag{3.37}$$

$$K_{nl} = \int_{tV} B_{NL}^T \sigma_{ij} B_{NL} dV \tag{3.38}$$

$$p_t = \int_{tV} N^T b dV + \delta \underline{\mathbf{u}}_L^T \int_{tA_\sigma} N^T t_t dA_\sigma \tag{3.39}$$

$$f_t = \int_{tV} B^T \sigma_{ij} dV \tag{3.40}$$

Where K_l is the linear part of the tangent stiffness matrix. K_{nl} is the non-linear contribution to the tangent stiffness matrix. Note that the tangent stiffness matrix is the key difference between the linear and non-linear formulations. It encodes the influence of the change of geometry due to the loading. p_t represents the external loading and f_t corresponds to the internal forces reacting to the external loading.

3.3 Predicting the buckling load of cylindrical shells with finite element tools

State-of-the-art commercial codes like Abaqus are commonly used in industrial and research applications to predict the maximum load cylindrical shells can carry before they collapse or become unstable. A commercial code is a tool that can provide the estimation of these loads and their associated displacement fields. However, there are many details of the analysis that need to be considered to obtain physically representative and reliable results. The system to derive the buckling load of a cylindrical shell consists of the shell to be studied constrained in all degrees of freedom at both ends with the exception of the axial degree of freedom at one of the ends. At the end where the axial degree of freedom is not constrained, a load is then applied in the form of a force or a displacement until collapse occurs.

The first step to define when buckling occurs is the definition of an observable metric that provides relevant information about the status of the system under study. A variable that is able to show if a cylindrical shell has undergone buckling or not. In cylindrical shell buckling the main observable metric used to identify buckling events is the reaction force that a cylindrical shell exerts while being compressed. The axial reaction force increases as higher compression load is applied and shows a sudden drop once the maximum axial compression load associated with a buckling event is reached. An example with two curves of axial reaction force as a function of axial displacement is presented in figure 3.1. These curves are referred to as end-shortening curves. The end-shortening curves present the axial reaction force as a function of the displacement of the top part of the cylindrical shell as it shrinks due to the applied force.

In figure 3.1 there are two curves, a dashed one and a dotted one, for two axially compressed finite element models of realistic cylindrical shells including geometric imperfections. The

dashed line shows a single drop in force while the doted line features a first mild drop in reaction force followed by a final abrupt one. The curve with a single drop represents a single global buckling event, since after that first drop the cylindrical shell is not able to bear any higher load. In the case with the two drops, the mild one occurs first, i.e. for a lower axial displacement. It corresponds to a local buckling event. While the second drop, the abrupt one, corresponds to the global buckling event that dictates the maximum load bearing capacity of the shell. A local buckling event is identified as a drop in the end-shortening curve after which the cylindrical shell can withstand a higher load than the one that triggered the local buckling event itself. Physically, local buckling can be identified by the appearance of a dimple that remains localized until the global buckling event. Physically, global buckling can be identified by the sudden appearance of an arrangement of dimples that cover the complete cylindrical shell.

The utilization of the axial compression force to identify buckling events is very convenient because it allows to directly compare results of simulations and data from experiments. This is the case because the same metrics can be observed directly in numerical models as well as experiments. Experimentally, the radial displacement is also used to understand if the maximum compression load a cylindrical shell can bear has been overcome. Practically this is done via the application of strain gauges or digital image correlation (DIC) (Weller et al., 2002). In the case of the extensometers they are placed opposed to each other, one in the interior face of the cylindrical shell and the other in the exterior. Once the readings from the two diverge buckling has occurred. In the case of the DIC it is more obvious. The characteristic large dimple pattern emerges after the critical load is overcome and it is reported by the DIC system.

The shortcomings of using the radial displacement to identify buckling and correlate numerical models with experiments is that the imperfection present in the shell needs to be known. This is required not only to get a good correlation but also to understand where to place the extensometers to sample the results. Hence, the reaction force is the most suitable approach to identify a buckling event in cylindrical shells.

The previous paragraph implicitly assumed that the buckling load is obtained from a geometrically non-linear compression analysis. However, there is another approach to estimate the buckling load of a cylindrical shell. This approach consists in performing linear stability analysis using as a reference the un-loaded state. The linear stability analysis approach without including pre-buckling deformations provides an ideal load that cannot be reached in reality. It is a useful measurement to compare the effect of imperfections with respect to the case of the cylindrical shell with no imperfection. However, it lacks the capability to provide a reliable buckling load estimate for practical purposes on its own. If combined with a geometrically non-linear analysis to provide a loaded base state, then linear stability becomes an option to predict buckling. This option will be discussed later in the chapter.

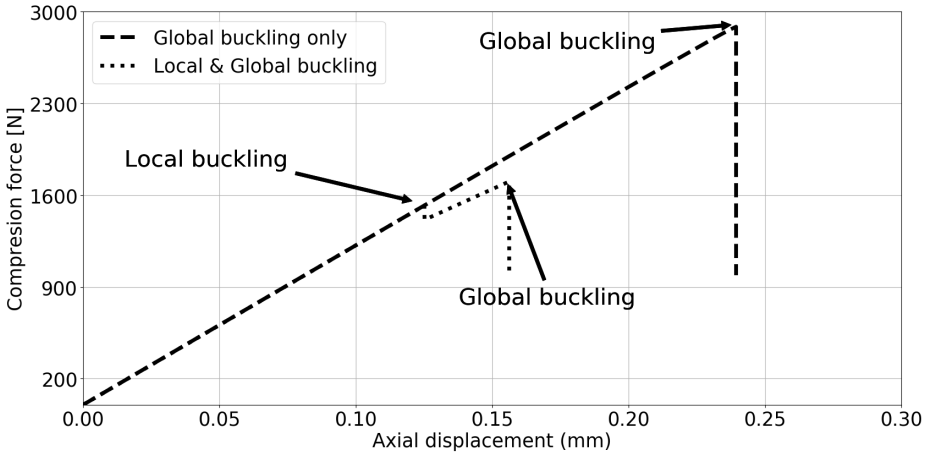

Figure 3.1 – End shortening curves obtained from a geometrically non-linear solution using the Newton solver of Abaqus. The curves show two different phenomenology of the buckling process. The dashed line represents a case where only a global buckling event exists. The dotted line represents the case where a local instability occurs before the global buckling event.

3.3.1 Linear stability analysis around the unloaded state

Historically, the first approach to derive the maximum load a cylindrical shell can carry was to perform linear stability analysis (Von Karman et al., 1940). The prediction of buckling loads based on linear stability analysis provides an overestimation of the load carrying capacity of real cylindrical shells (Koiter, 1945).

Linear stability analysis around the unloaded state of cylindrical shells with the finite element method yields an eigen-value problem. This eigen-value problem aims at finding the point where the stiffness matrix of the system becomes singular. The path to this eigen-value problem is going to be presented in this section. A more detailed derivation can be found in the different references used as support for the one presented herein (Liu, 2003; Bathe, 2014b).

$\underline{\mathbf{F}}$ in equation 3.41 represents the vector of forces acting on a cylindrical shell for an equilibrium state $\underline{\mathbf{u}}^\star$. $K(\lambda)$ is the stiffness matrix associated with state $\underline{\mathbf{u}}^\star(\lambda)$ that encodes information about the loading state. λ loading parameter that is used to control the applied load.

$$\underline{\mathbf{F}} = K(\lambda)\underline{\mathbf{u}}^\star \tag{3.41}$$

The condition for the cylindrical shell to become unstable is that the stiffness matrix $K(\lambda)$ becomes singular for a certain λ. The stiffness matrix can be approximated as a Taylor

expansion in the form of

$$K(\lambda) = K_0 + \lambda \frac{\partial K(\lambda)}{\partial \lambda} \tag{3.42}$$

where only linear terms are retained. $\partial K(\lambda)\ /\partial\lambda$ is the so called tangent stiffness matrix K_t. Thus, the above expression can be rewritten as

$$K(\lambda) = K_0 + \lambda K_t \tag{3.43}$$

where K_0 is the stiffness matrix of the base state. In this section, the base state is the unloaded state K_0 hence the components of K_0 are the stiffness components associated with each degree of freedom of each individual element.

Therefore, in order to find the value of λ where the stiffness matrix becomes singular the eigen-value problem

$$det(K_0 + \lambda K_t) = 0 \tag{3.44}$$

needs to be solved.

This is the standard eigen-value problem solved by commercial software packages like Abaqus (Dassault Systèmes Simulia Corp, 2011).

The eigen-value problem is based on the assumption that a linear extrapolation of the loading scheme of the problem is sufficiently accurate. This is the issue of using standard linear stability analysis to predict buckling loads of real shells. It is a linear extrapolation of a non-linear problem. Hence, this imposes a limit on how accurately the prediction can be if the linearization occurs using as a reference state one that is far away from the point where the system becomes unstable. However, if the reference state is close enough, within the range of validity of the linear approximation, then linear stability analysis remains a valid tool to predict when cylindrical shell becomes unstable.

3.3.2 Quasi-static non-linear analysis

In the derivation of the non-linear finite element algorithm it was mentioned that non-linear systems are solved in an incremental manner. The approach followed to implement this incremental solution strategy is realized by a scalar parameter that pre-multiplies the loading in order to apply it progressively. This parameter is increased until the complete load is implemented and at each increment of the process an equilibrium solution is obtained. In the case of the commercial code Abaqus, this parameter is associated to a *pseudo-time* that acts

as the parameter that varies the loading parameter from 0 at the beginning of the analysis to 1 at the end of it.

The numerical scheme to solve this kind of problems is the Newton-Rapshon method. This method consists of the construction of a first order Taylor expansion around the known state i and approximating the $i+1$ based on a linear approximation.

The implementation of this algorithm is the following. Given a certain state defined by $\underline{\mathbf{u}}^i$. If this state is a solution, an equilibrium point, this state must satisfy the condition that the work performed by external forces ($\underline{\mathbf{p}}$) is identical to the work performed by internal forces ($\underline{\mathbf{f}}$) leading to a residual $\underline{\mathbf{r}}$ equal to 0

$$\underline{\mathbf{r}} = \underline{\mathbf{p}} - \underline{\mathbf{f}} = 0 \tag{3.45}$$

The Taylor expansion for the residual for the next step can be written as shown in equation 3.46

$$\underline{\mathbf{r}}(\underline{\mathbf{u}}^{i+1}) = \underline{\mathbf{r}}(\underline{\mathbf{u}}^i) + \left[\frac{\partial \underline{\mathbf{r}}(\underline{\mathbf{u}}^i)}{\partial \underline{\mathbf{u}}^i}\right] \underline{\mathbf{u}}^i \tag{3.46}$$

with 3.45 in 3.46 we obtain

$$\frac{\partial \underline{\mathbf{f}}}{\partial \underline{\mathbf{u}}} \underline{\mathbf{u}} = \underline{\mathbf{p}} - \underline{\mathbf{f}} \tag{3.47}$$

where

$$\frac{\partial \underline{\mathbf{f}}}{\partial \underline{\mathbf{u}}} = K_T \tag{3.48}$$

K_T is referred as the tangent stiffness matrix at point i.The tangent stiffness matrix is the Jacobian matrix (Brothers et al., 2014). The approximation for the step $i+1$ can be obtained as shown in equation 3.49.

$$K_T^i \underline{\mathbf{u}}^i = \underline{\mathbf{p}} - \underline{\mathbf{f}} \tag{3.49}$$

The output produced by equation 3.49 is an approximation. This approximation is based on a set of values of nodal displacements that needs to be updated until a certain criteria or tolerance is met to consider the solution accurate enough. The most common metric to determine if the approximated solution is accurate enough is the residual r. Ideally, the residual r should be 0 but in reality this is not possible and it is set to a low enough value that can be considered 0. In case the residual r is not within the specified tolerance, the Newton-Rapshon procedure undergoes successive iterations until the value of r is within the specified tolerance.

Loading strategy

An important aspect in the prediction of the buckling load of a cylindrical shell are the loading conditions. Namely, if an analysis is performed under load control conditions, meaning that a compression load is prescribed, or displacement control conditions, meaning that a compression displacement is prescribed. Under any of these two loading conditions, the value of the buckling load must remain the same because it is a feature of the system. Furthermore, the initiation of buckling and the associated displacement field should remain similar for the same reason. The displacement field at the onset of instability will be used to define a buckling mode showing the initial state of deformations at the initiation of buckling. This is done by subtracting from the displacement field of the first equilibrium state after the buckling load the displacement field of the equilibrium state at the buckling load.

The possibility to define the buckling mode at the onset of instability is very important especially in chapter 6 because it will be used to understand how buckling initiates in cylindrical shells. Hence, it will be verified whether there is any difference in this buckling mode depending on the loading strategy and the most suitable loading strategy to derive it.

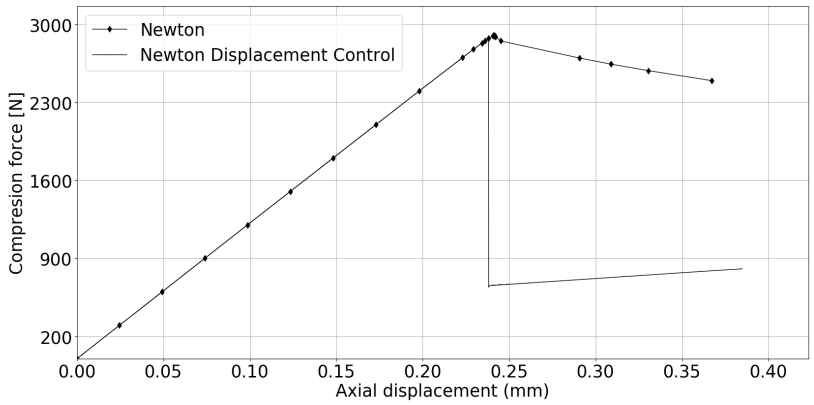

Figure 3.2 – Geometrically non-linear solution using Abaqus inbuilt Newton solver for different loading conditions. The system used for this analysis is a perfect cylindrical shell with an R/h of 283 and a length of 107 millimeters. The boundary conditions used in the analysis are clamped at both ends of cylindrical shell. The clamped boundary conditions suppress all degrees of freedom in the unloaded end and all degrees of freedom with the exception of the axial one on the loaded end. The axis of the cylindrical shell are aligned with the Z axis of the analysis allowing axial displacement once the load is applied. In the load control case the maximum load capability is $2899N$ and in the case of the displacement control case the maximum load capability is $2873N$. The relative difference is below 1%

In figure 3.2 the end shortening curves of the analysis of a cylindrical shell under compression obtained with the Newton solver of Abaqus are shown. The two different curves correspond to the cases of load controlled and displacement controlled loading. The curve with the sudden

drop in the compression load is the displacement controlled one. The prediction obtained with both loading strategies is in very good agreement. The deviation between both case is only $26N$, less than 1%.

Figures 3.3 and 3.4 show the radial displacement plots at onset of instability and the buckling for load controlled conditions and displacement controlled conditions respectively. The radial displacement plot of the buckling mode is obtained by subtracting to the radial displacement fields of the first equilibrium state that is obtained immediately after the maximum compression force reached the radial displacement field at the maximum compression force the shell can bear. This buckling mode shows the location where buckling starts. It removes the pre-buckling deformations and only shows the structures that appear after the onset of instability.

The deformation patterns in figures 3.3a and 3.4a are very similar in terms of morphology although in the case of the load controlled conditions the deformations are more evenly distributed. Regarding the buckling modes from figures 3.3b and 3.4b, the morphology of the eigen-mode varies between the two loading conditions. However, in both cases the larger displacements tend to accumulate in the vicinity of the locations where the boundary conditions are applied. The reason for more extended deformation in the load controlled case is the fact that the first loading step after the onset of instability is deeper in the post buckling regime. At the onset of stability the stiffness matrix becomes singular and large displacements can be reached with no force increase. This only occurs in the case of load controlled loading conditions and it is the reason to use displacement controlled boundary conditions. The information about the transition towards a buckled state is more precise in the case of the displacement controlled loading strategy.

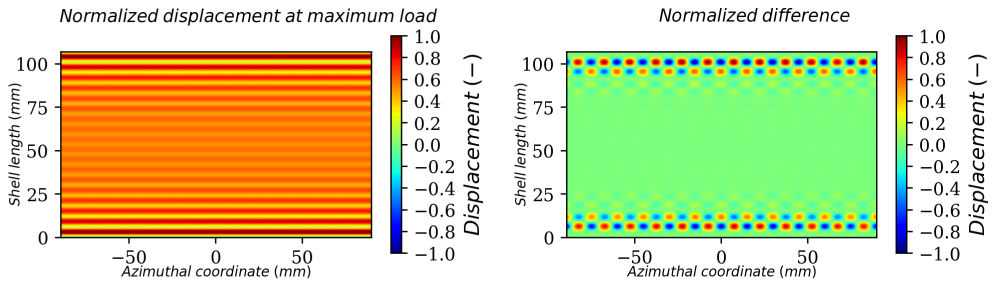

(a) Maximum radial displacement plot under load controlled conditions

(b) Buckling-mode at the onset of instability under load controlled conditions

Figure 3.3 – Displacement fields associate with the load controlled loading newton simulation of Abaqus. Each field, has been normalized with the maximum radial displacement of them.

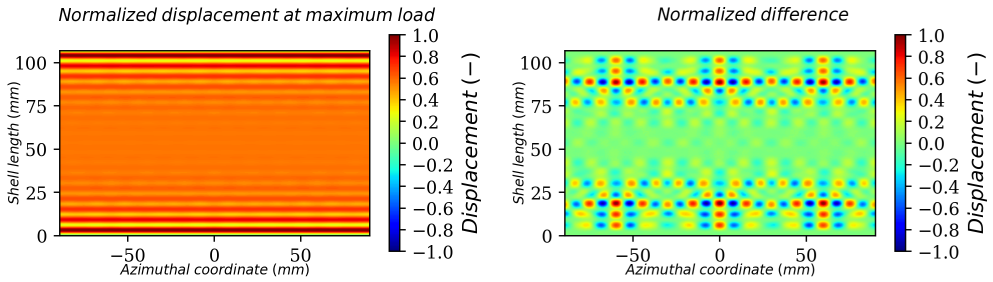

(a) Maximum radial displacement plot under displacement controlled conditions

(b) Buckling-mode at the onset of instability under displacement controlled conditions

Figure 3.4 – Displacement fields associate with the displacement controlled loading newton simulation of Abaqus. The fields have been normalized with the maximum radial displacement of each of them.

3.3.3 Quasi-static arc-length analysis

The arc-length method is a step forward from the standard Newton-Raphson method in the sense that it allows to follow unstable solution paths that include snap-through and snap-back phenomena like the ones sketched in figure 3.5. The arc-length method allows to deal with situations where the stiffness matrix of the system under study becomes singular unlike the Newton-Rapshon method. A classical case of this behaviour is the complete path followed by the joint of two rods of arbitrary length with a force or displacement pushing at this joint. Depending on the length of the rods, they will follow a behaviour similar to one of the sketches from figure 3.5. This path cannot be computed with a traditional Newton-Raphson method. In fact, if the solution of this problem is attempted using the Newton-Raphson method, the trajectory followed by the solutions will be the one described by a dashed line in the sketches of figure 3.5. The limit and turning points located where the dashed lines begin in figures 3.5a and 3.5b, respectively, can not be passed by the Newton method. At those points, the stiffness matrix associated with the problem becomes ill-conditioned in their vicinity and becomes singular at exactly those points (Jorabchi and Suresh, 2011; Müller, 2007).

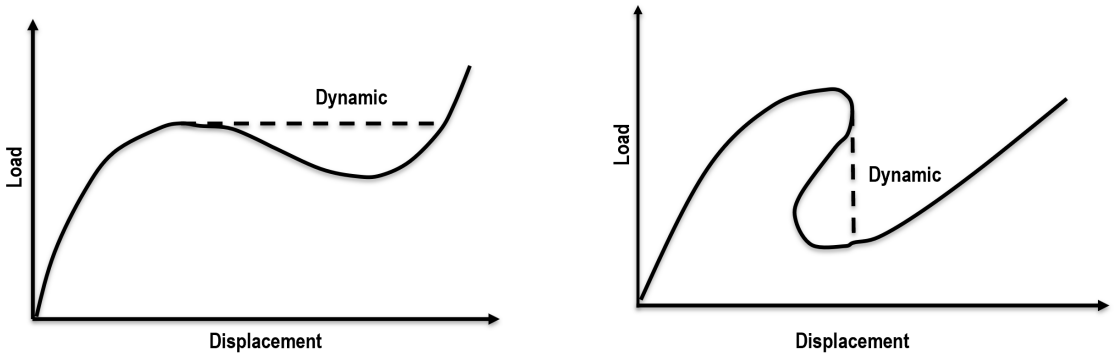

(a) Snap through example.

(b) Snap back example.

Figure 3.5 – Snap through and snap back examples to illustrate the cases where the arc-length method is to be used. (Crisfield, 1981)

The implementation of the arc-length method algorithm is similar to the one of the Newton-Rapshon method. If any given state is a solution of a system, it must satisfy the condition that the external work is identical to the internal one. This condition leads to a residual $\underline{\mathbf{r}}$ equal 0 as in the case of the Newton-Rapshon method.

$$\underline{\mathbf{r}} = \underline{\mathbf{p}} - \underline{\mathbf{f}} = 0 \tag{3.50}$$

In the case of the arc-length, the loading f is applied incrementally by a pre-factor λ that is 0 for no load and 1 once the complete loading has been applied. Hence, $\underline{\mathbf{f}}$ in 3.50 is a function of λ that is used to move towards the final loading condition in an incremental manner so the expression in 3.50 can be written as shown in equation 3.51.

$$\underline{\mathbf{r}} = \underline{\mathbf{p}} - \lambda\underline{\mathbf{f}} = 0 \tag{3.51}$$

The residual r is a function of the state $\underline{\mathbf{u}}$ and the pre-factor λ ($r(\underline{\mathbf{u}}, \lambda)$). This means that the residual r will also be affected by the same issues of the tangent stiffness matrix mentioned before. It will become rank deficient at the point where the system becomes unstable.

$$\underline{\mathbf{r}}(\underline{\mathbf{u}}, \lambda) = \underline{\mathbf{p}} - \lambda\underline{\mathbf{f}} = 0 \tag{3.52}$$

In order to avoid the stiffness matrix of the problem becoming rank deficient, Riks introduced the idea of including the pre-factor λ as an additional variable. In the arc-length method, the pre-factor λ controlling the loading becomes another variable to solve for (Crisfield, 1981; Riks, 1979). Due to the fact that there is an additional variable to solve for an additional equation, it is required to keep the number of equations equal to the number of unknowns. This additional

new equation is the arc-length that should provide the intersection with the trajectory of solutions of the system. This arc-length can be expressed in incremental form as shown in equation 3.53 (Crisfield, 1981).

$$a = (\Delta \underline{\mathbf{u}}^T \underline{\mathbf{u}} + \Delta\lambda^2 \underline{\mathbf{f}}^T \underline{\mathbf{f}}) - \Delta l^2 = 0 \tag{3.53}$$

Where Δl is the fix radius of the desired intersection. Considering the new equation 3.53 together with equation 3.50, the enhanced system of equations can be solved by applying the Newton-Rapshon method. In section 3.3.2 it was shown that the Newton-Rapshon method is implemented based on a Taylor series truncated up to the linear term. In this case the Taylor series expansion is to be applied to equation 3.52 and 3.53. The truncated Taylor series for these equations can be expressed as shown in equations 3.54 and 3.55, where the sub-index 0 refers to the previous known state and the sub-index 1 refers to following one.

$$\underline{\mathbf{r}}_1 = \underline{\mathbf{r}}_0 + \frac{\partial r}{\partial \underline{\mathbf{u}}}\delta\underline{\mathbf{u}} + \frac{\delta r}{\partial\lambda}\delta\lambda = \underline{\mathbf{r}}_0 K_T \delta\underline{\mathbf{u}} - \underline{\mathbf{f}}\delta\lambda \tag{3.54}$$

$$a_1 = a_0 + 2\Delta\underline{\mathbf{u}}^T\delta\underline{\mathbf{u}} + 2\Delta\lambda\delta\lambda\underline{\mathbf{p}}^T\underline{\mathbf{p}} \tag{3.55}$$

Equations 3.54 and 3.55 can be combined and solved for $\delta\lambda$ and $\delta\underline{\mathbf{u}}$, after setting r_1 and a_1 to 0, as shown in equation 3.56.

$$\begin{pmatrix}\delta\underline{\mathbf{u}}\\ \delta\lambda\end{pmatrix} = -\begin{bmatrix}K_T & -p\\ 2\Delta\underline{\mathbf{u}}^T & 2\Delta\lambda p^T p\end{bmatrix}^{-1}\begin{pmatrix}\delta r_0\\ a_0\end{pmatrix} \tag{3.56}$$

In equation 3.56, the matrix in the square brackets remains non-singular even when K_T is singular. This is the key feature that makes the arc-length method a tool capable of following equilibrium paths that are not possible with other approaches like the pure Newton-Rapshon method. Riks algorithm is the one implemented in the commercial solver used in this research Abaqus (Riks, 1979; Crisfield, 1981; Ramm, 1981).

Loading strategy

As in the previous section about the use of the Newton-Raphson solver of Abaqus, the impact of the two different loading strategies in the buckling load prediction is studied. The aim is to know if there is any difference in the predicted buckling load or behaviour that could impact the application of the arc-length to study the collapse of cylindrical shells.

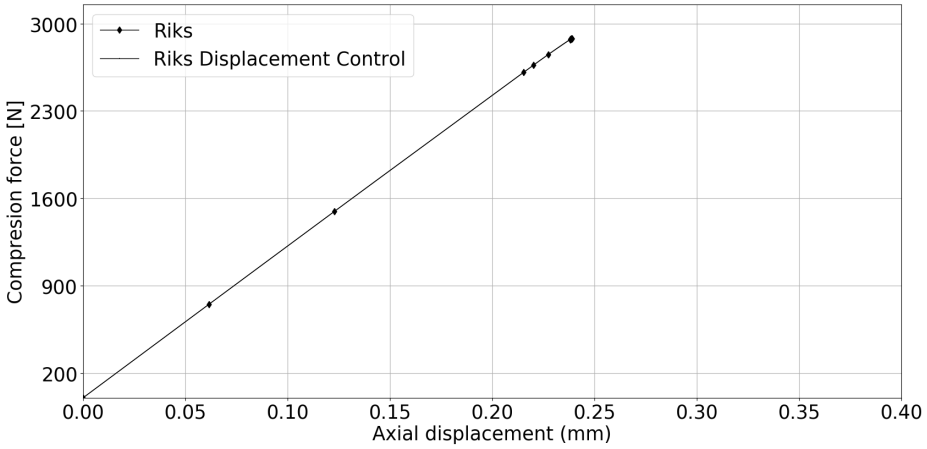

Figure 3.6 – Geometrically non-linear solution using Abaqus arc-length solver for different loading conditions. In the load control case the maximum load capability is $2881N$ and in the case of the displacement control case the maximum load capability is $2864N$, the deviation is $18N$. The system used to carry out is the same used to derive the end shortening curves of figure 3.2

Figure 3.6 contains the end shortening curves for the load and displacement controlled cases. In this case both curves are exactly on top of each other. The end shortening curves from figure 3.6 illustrate one of the shortcomings of the application of the arc-length algorithm as a solution strategy, the identification of the point where buckling occurs. This is due to the difficulty to pass the bifurcation point compared to the Newton-based algorithm of the previous section.

A second limitation of the application of the arc-length algorithm to obtain the buckling load is its lack of correlation with real experiments. Buckling of cylindrical shells is a sub-critical backward bifurcation (Champneys et al., 2019) that can be followed numerically with the arc-length algorithm but can not be accessed experimentally during the compression test usually employed to derive the buckling load of a cylindrical shell experimentally. Hence, the correlation between numerical studies and experiments is only possible up to the primary bifurcation provided no local buckling event occurs before reaching this point.

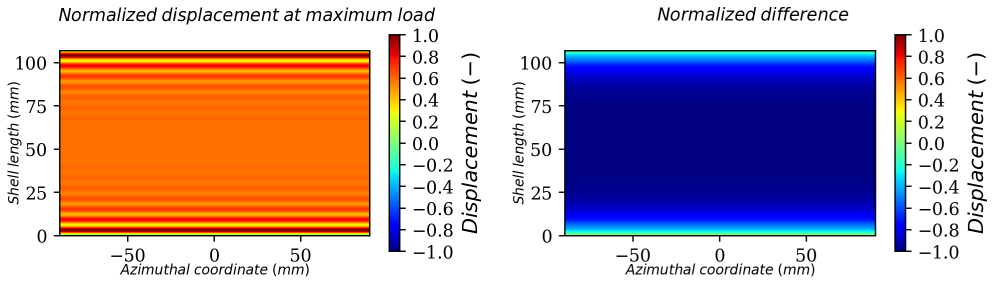

(a) Maximum radial displacement plot under load controlled conditions

(b) Buckling-mode at the onset of instability under load controlled conditions

Figure 3.7 – Displacement fields associate with the load controlled arc length simulation of Abaqus. The fields have been normalized with the maximum radial displacement of each of them.

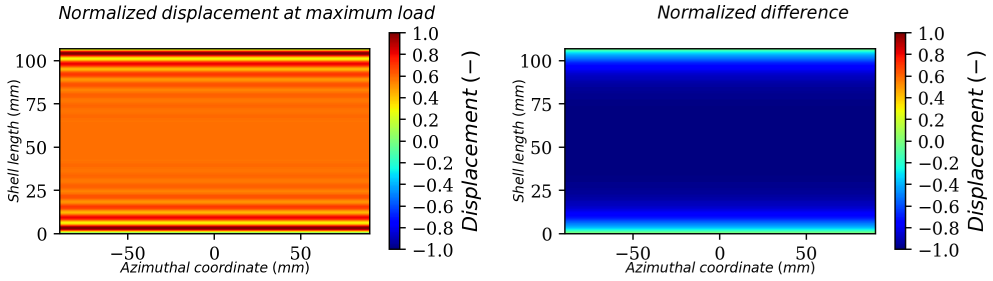

(a) Maximum radial displacement plot under displacement controlled conditions

(b) Buckling-mode at the onset of instability under displacement controlled conditions

Figure 3.8 – Displacement fields associate with the displacement controlled arc length simulation of Abaqus. The field have been normalized with the maximum radial displacement of each of them.

The fields from figures 3.7 and 3.8 represent the maximum radial displacement and eigenmode. In this case they are identical because in the case of the arc-length algorithm the path followed by the solution is identical independently of the loading configuration used. However, due to the impossibility of following these paths in experiments, the arc-length will not be used as a solution strategy in the different analysis of this research.

3.3.4 Dynamic explicit analysis

Shell buckling in reality is a dynamic event. In fact, the development of the characteristic buckling pattern that occurs once the onset of instability is overcome has a characteristic time in the order of milliseconds. Hence, the dynamic part beyond the onset of instability certainly involves the effects of inertia that a quasi-static simulation does not include. A particular case where dynamics might play an important role is the case where local buckling is present

during the compression loading of a cylindrical shell. In this specific situation the effect of inertia might be a contributor to trigger global buckling from this initial localized buckling event due to the contribution of inertial forces.

The time evolution of a cylindrical shell is described by the equation of motion of the form of equation 3.57.

$$M\underline{\ddot{\mathbf{u}}} + C\underline{\dot{\mathbf{u}}} + K\underline{\mathbf{u}} = \underline{\mathbf{p}} \tag{3.57}$$

Where M represent the mass matrix, C the damping matrix, K the stiffness matrix and p the external forces acting on the system.

The differential equation posed in 3.57 can be solved by direct time integration methods (Bathe, 2014b). These methods are based on satisfying the equilibrium of the system considering the inertia and damping terms not at all time but at discrete time steps. This means that in order to find a solution for certain elapsed time T, this time period (T) is divided in a certain number of intervals N leading to a solution step ΔT equal to T/N. One approach used to solve this kind of problem relies upon explicit methods, where the accelerations and velocities present in the system can be calculated by central differences as shown in equations 3.58 and 3.59. In this case the initial condition of the system in terms of velocity and acceleration needs to be known:

$$\underline{\ddot{\mathbf{u}}}^n = \frac{\underline{\mathbf{u}}^{n+1} - 2\underline{\mathbf{u}}^n + \underline{\mathbf{u}}^{n-1}}{\Delta t^2} \tag{3.58}$$

$$\underline{\dot{\mathbf{u}}}^n = \frac{\underline{\mathbf{u}}^{n+1} - \underline{\mathbf{u}}^{n-1}}{2\Delta t} \tag{3.59}$$

Introducing equations 3.58 and 3.59 in equation 3.57 for step n the displacements for the next time step can be obtained as presented in equation 3.60. This can be done under the assumption that the values for step n and $n-1$ are available.

$$\left(\frac{1}{\Delta t^2}M + \frac{1}{2\Delta t}C\right)\underline{\mathbf{u}}^{n+1} = p - f + \frac{2}{\Delta t^2}M\underline{\mathbf{u}}^n - \left(\frac{1}{\Delta t^2}M - \frac{1}{2\Delta t}C\right)\underline{\mathbf{u}}^{n-1} \tag{3.60}$$

The key to use this solution scheme is to have well defined initial conditions. In this case the initial condition that needs to be known corresponds to the initial state $n = 0$ and the previous one, $n = -1$ that are calculated following equation 3.61

$$\underline{\mathbf{u}}^{n-1} = \underline{\mathbf{u}}^n - \Delta t\underline{\dot{\mathbf{u}}} + \frac{\Delta t^2}{2}\underline{\ddot{\mathbf{u}}} \tag{3.61}$$

These explicit solvers can cope with large systems at a very low effort per time increment due to the simplicity of the algorithm.They are efficient in terms of time, the computational time

per step is short. However, the central difference procedure is conditionally stable depending on the size of the time increment. The most common limitation used to pick the largest stable time increment is shown in equation 3.62, known as a Courant–Friedrichs–Lewy condition.

$$\Delta t \leq \eta \frac{L_{min}}{c_d} \tag{3.62}$$

Where L_{min} is the minimum distance between nodes in the mode, c_d is the dilatational wave speed of the material and η is a characteristic speed in the problem being solved. η is the speed related to the problem under study. The dilatational wave speed is

$$c_d = \sqrt{\frac{E(1-\nu)}{\rho(1+\nu)(1-2\nu)}} \tag{3.63}$$

In equation 3.63 E is the Young's modulus of the material and ν the Poisson ratio.

Loading strategy

In the case of a dynamic analysis, the loading strategy is more important than in the quasi-static analysis described in the previous sections. This is due to the fact that in the case of the dynamic analysis the characteristic time imposed by the presence of inertia and the presence of inertia itself can affect the evolution and initiation of buckling. One example of this is the triggering effect that local buckling might have to induce global buckling due to the inertia of the section affected by the local buckling event. A second example is the loading rate. Due to the presence of a damping term in the dynamics, a high loading rate will stiffen the response of the cylindrical shell. Hence, explicit simulations expand the range of parameters to control and study in order to perform an accurate prediction of the buckling load of a cylindrical shell.

Figure 3.9 shows the end-shortening curves for the two loading strategies. In these end-shortening curves, the one associated with load controlled loading conditions does not reach the same maximum load as the displacement controlled one. This discrepancy is caused by the fact that the load increment for the solution did not match the exact same value. The reason for this is the resolution in terms of loading required, the load increment would need to become smaller so they can achieve the same value in both curves. The time increment is too small in the load control with respect to the time scale of the buckling process.

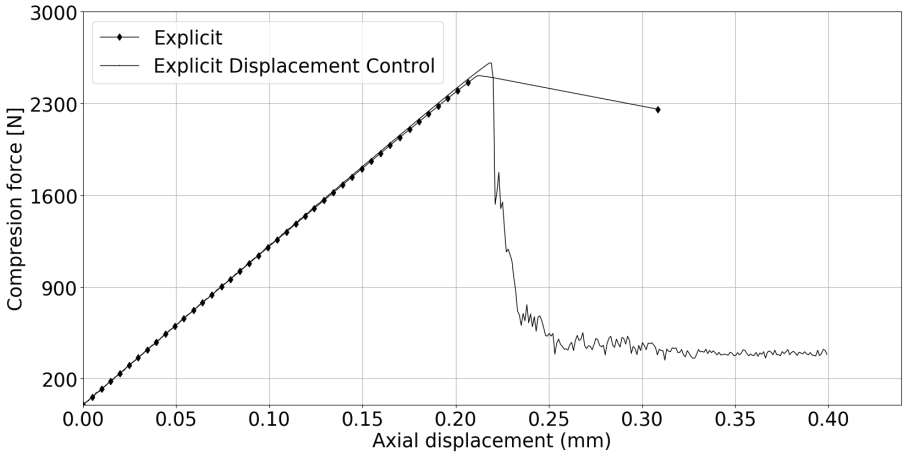

Figure 3.9 – Geometrically non-linear solution using Abaqus explicit solver for different loading conditions.In the load control case the maximum load capability is $2512N$ and in the case of the displacement control case the maximum load capability is $2608N$

This is a limitations of the load controlled loading scheme in a dynamic simulation in particular to match the results of the displacement controlled loading scheme. The loading increments have to be very small to avoid missing the exact moment when buckling occurs. This detail together with the large computation effort required makes dynamic simulations not a practical tool to study a broad range of parameters. However, a dynamic simulation is the closest one to reality when describing the complete buckling process.

Figures 3.10 and 3.11 show the radial displacements plots at the maximum axial load together with the buckling mode. In this case, the differences are more significant than in the previous sections. The reason for this deviation is the increment size relative to the characteristic time of the event being modelled, collapse of a cylindrical shell.

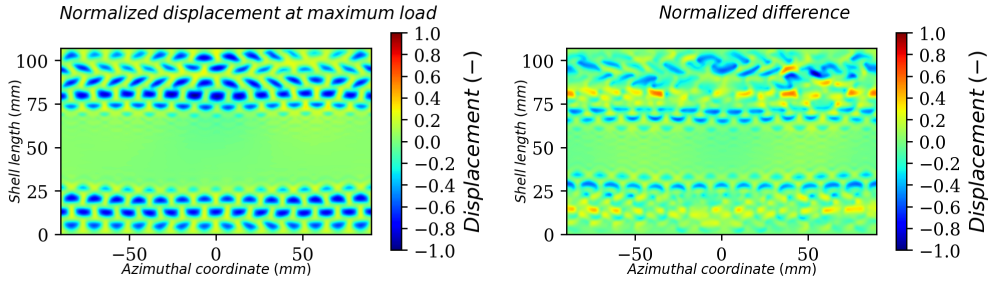

(a) Maximum radial displacement plot under load controlled conditions

(b) Buckling-mode at the onset of instability under load controlled conditions

Figure 3.10 – Displacement fields associated with the load controlled explicit simulation of Abaqus. The fields have been normalized with the maximum radial displacement of them.

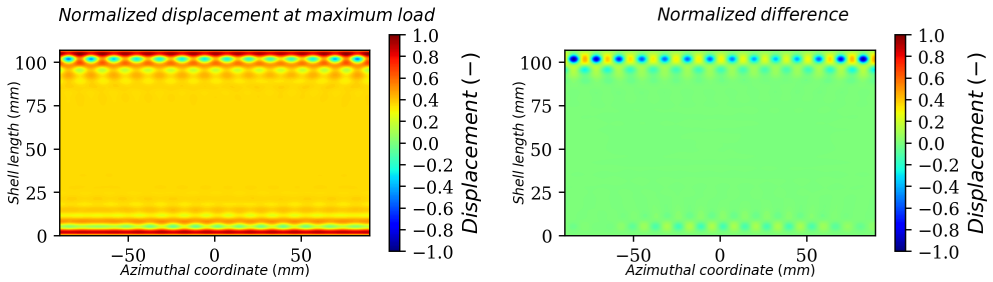

(a) Maximum radial displacement plot under displacement controlled conditions

(b) Buckling-mode at the onset of instability under displacement controlled conditions

Figure 3.11 – Displacement fields associated with the displacement controlled explicit simulation of Abaqus. The fields have been normalized with the maximum radial displacement of them.

In the case of the load control loading scheme, the time increment is in the order of magnitude of the characteristic time that the buckling process needs to develop through the complete cylindrical shell. Hence, the difference between the different fields is due to the fact that the comparison is not being done for the equivalent conditions of compression force. The load controlled case is much deeper into the post-buckling regime due to the highly dynamic nature of the buckling event. As mentioned before, this issue would require a very short time increment to accurately capture the buckling. The short time increment required would make the computational time impractical. The simulation would require a large number of increments to be computed even if the computational cost of each of those time increment is low.

3.3.5 Finite element solution strategies conclusions

Table 3.1 summarizes the buckling loads obtained by the different loading conditions and solution strategies. The differences between the quasi-static cases are below 1%. In the case of the dynamic simulations, the deviation is higher between the different loading strategies, approximately 3%. In the comparison between the quasi-static solutions and the dynamic ones the deviation is higher, roughly 13%. The linear buckling prediction using linear extrapolation from the unloaded base state matches very closely the values predicted by the non-linear quasi-static solutions. This is expected due to the fact that the shell used in these analyses is an ideal one and has a linear behaviour up to the buckling point.

Two main reasons motivate the choice of a given finite element method for predicting shell buckling in this work: the sensitivity of the dynamic simulations to small variations of the time step and the fact that the information of interest is the maximum buckling load prior to the buckling event. The most suitable solutions strategy to determine the buckling load of a cylindrical shell is then a quasi-static solver. Namely the Newton-Rapshon one under displacement control loading conditions. The arc-length is considered not suitable due to the

non-physical behaviour shown by this solutions when compared to experiments.

Solver	Loading strategy	Predicted Buckling load (N)
Newton	Controlled displacement	2873 N
Newton	Controlled load	2899 N
Arc-length	Controlled displacement	2864 N
Arc-length	Controlled load	2881 N
Dynamic explicit	Controlled displacement	2608 N
Dynamic explicit	Controlled load	2512 N
Linear buckling	—	2902 N

Table 3.1 – Buckling load predicted by the most representatives solvers

The different buckling load predictions have been done for an ideal geometry. In this case the buckling load predicted by the linear stability analysis linearizing around the unloaded state manages to predict the buckling load. If the linear stability analysis would be performed with an imperfect shell, the prediction would be less accurate.

In the next section it will be shown how additional factors influence the behaviour of cylindrical shells. Namely, flexible boundary conditions and pre-buckling deformations.

3.4 Additional factors influencing cylindrical shell buckling

In addition to the loading conditions and the different solvers that can be used to predict buckling loads of cylindrical shells, there are other aspects to consider. Among those, the primary ones are the boundary conditions of the model and the pre-buckling deformations. Other features like material properties variability is not considered due to its minimal impact.

3.4.1 Flexible Boundary Conditions

The boundary conditions at the constrained ends of the cylindrical shells influence the overall buckling behaviour of cylindrical shells under compression(Babcock, 1983; Weller et al., 2002). Furthermore, to compare numerical analysis with real experiments, boundary conditions should be thoroughly studied to understand how they might affect the final result.

In the current research this impact has been very clear due to the fact that most of the experimental work has been carried out with commercial beverage cans. Cans offered a very repeatable and accessible population that allowed carrying out buckling tests on statistically relevant populations. However, these cans have conical ends that showed evident deformations during the experimental work.

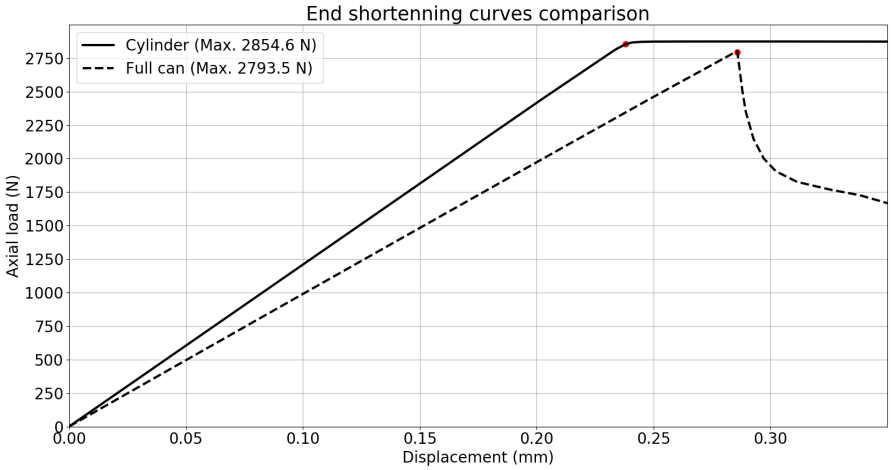

Figure 3.12 – End shortening curves comparing the behaviour under compression load of a complete can and an equivalent straight cylinder. The boundary conditions at the end of the complete can is fully clamped with the 6 degrees of freedom of each node constrained at the bottom and 5 degrees of freedom constrained at the top with only the degree of freedom aligned with the axial direction free to allow the loading to take place. In the equivalent cylinder the boundary conditions are the same. The rest of parameters are the same in both cases.

Hence, the study of the influence of the boundary conditions was a key point that needed to be addressed. Particularly, the influence of the boundary conditions in shells that are similar to the ones used in the experimental work of the current research. The approach followed was to compare the behaviour of a complete can and a simplified cylinder. The simplified cylinder had the length of the straight section of the can. This is the approximation that has been used to perform the numerical experiments. The end-shortening curves of the complete can and the simplified equivalent cylinder can be seen in figure 3.12. The flexibility of the boundary conditions of the complete can played a role in the overall stiffness, making the can significantly softer than the equivalent cylinder. However, the presence of the conical ends in the can did not affect significantly ($< 1\%$) the load bearing capacity of the shell. Furthermore, the collapse occurred in the straight section of the can represented in the equivalent cylindrical shell. In the post-buckling regime, the load controlled analysis of the simplified cylinder just gets an infinite displacement. In the case of the full can the conical ends act as a limit.

3.4.2 Pre-Buckling Deformations

The second relevant additional factor influencing the buckling load of cylindrical shells are pre-buckling deformations. In this section it will be shown how the pre-buckling deformations influence the actual buckling load of a cylindrical shell and the shift in the eigen-mode shape associated with it. This study is only relevant for linear stability analysis. Namely, in this

section it will shown how linear stability analysis around points closer to the buckling load provide different estimations of it. This is due to the fact that as the loading approaches the critical buckling load the linearization extrapolates to different points.

It is a well known fact that pre-buckling deformations affect the maximum load a cylindrical shell can carry. Deviations of around 15% have been reported in the literature (Brush et al., 1975). The reason for this deviation in buckling load is not including the non-linear contribution to the pre-buckling deformation in the base state (Koiter, 2008; Thompson, 1969) in analytical solutions or in the tangent stiffness matrix (Drew and Pellegrino, 2002) in the case of finite elements.

A less known fact is the shift in shape of the eigen-mode that becomes unstable as the pre-load is increased. The analysis used to demonstrate this mode shift is a linear stability analysis performed using different reference states with increasing levels of pre-load. The reference pre-loaded state will consist of a non-linear solution using the Newton solver of Abaqus. The analysis is performed in a cylindrical shell corresponding to the straight section of a can. This straight section corresponds with a cylindrical shell that is 107 mm long and has an R/h of 263 with a thickness of 0.105 μm. The boundary conditions are clamped in the same way as described in the previous sections. The outcome of this analysis can be seen in figures 3.13 to 3.22.

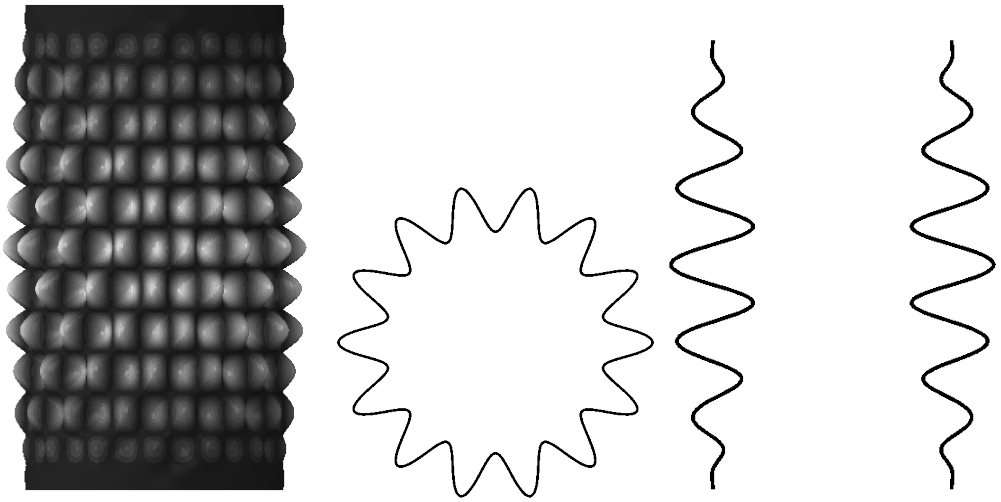

(a) Linear buckling eigen-mode displacement field

(b) Section at half height of the shell

(c) Section at the middle plane of the shell

Figure 3.13 – Linear buckling mode and sections of a perfect cylinder with no pre-load effect considered

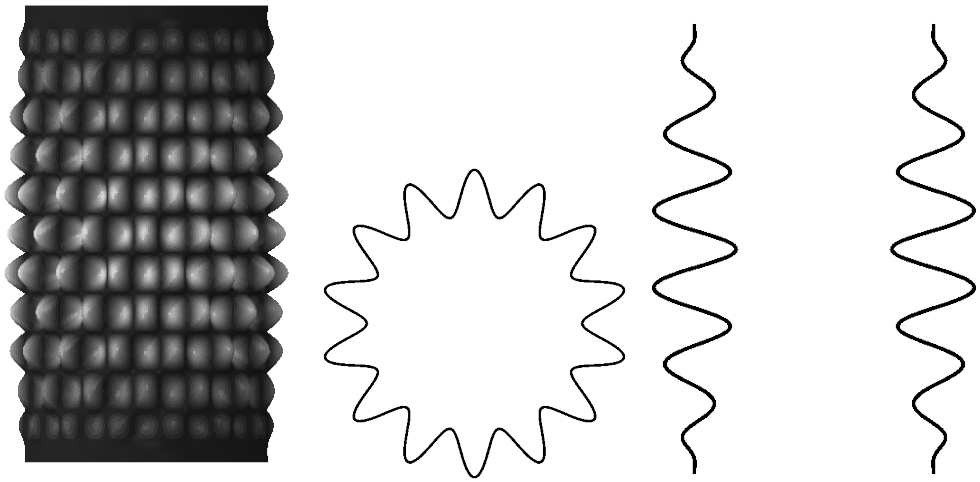

(a) Linear buckling eigen-mode displacement field

(b) Section at half height of the shell

(c) Section at the middle plane of the shell

Figure 3.14 – Linear buckling mode and sections of a perfect cylinder with 1000N pre-load effect considered

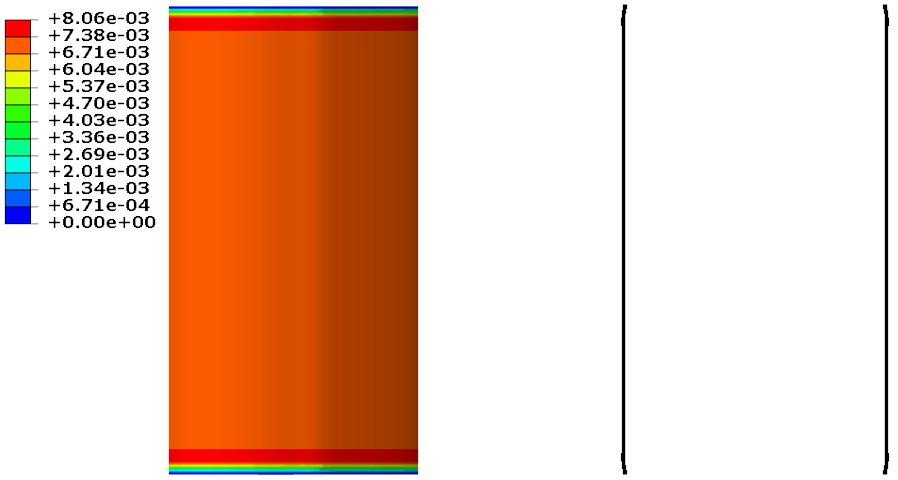

(a) Radial displacement displacement field

(b) Section of the radial displacement field amplified 50 time with respect to reality

Figure 3.15 – Radial displacement corresponding to an axial compression load of 1000 N. The maximum value is 8.06 10^{-3} mm and it is located near the nodes where the boundary conditions are enforced at the top and the bottom of the shells.

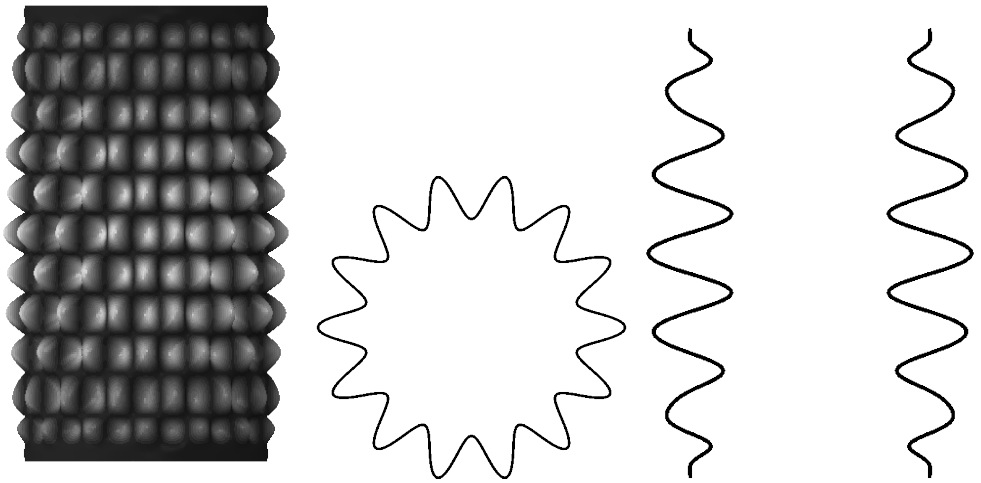

(a) Linear buckling eigen-mode displacement field

(b) Section at half height of the shell

(c) Section at the middle plane of the shell

Figure 3.16 – Linear buckling mode and sections of a perfect cylinder with 1500N pre-load effect considered

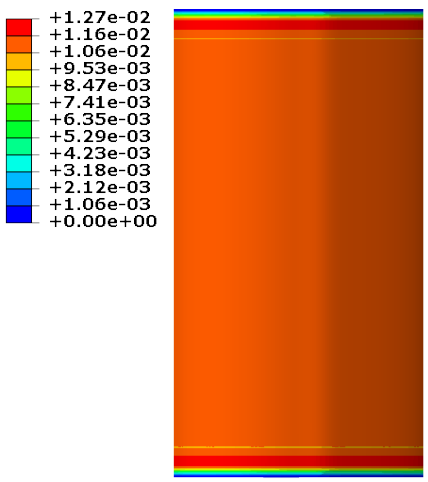

(a) Radial displacement displacement field

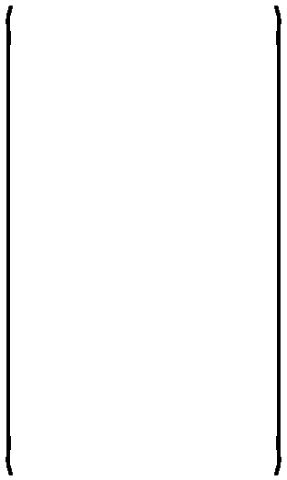

(b) Section of the radial displacement field amplified 50 time with respect to reality

Figure 3.17 – Radial displacement corresponding to an axial compression load of 1500 N. The maximum value is 1.27 10^{-2} mm and it is located near the nodes where the boundary conditions are enforced at the top and the bottom of the shells.

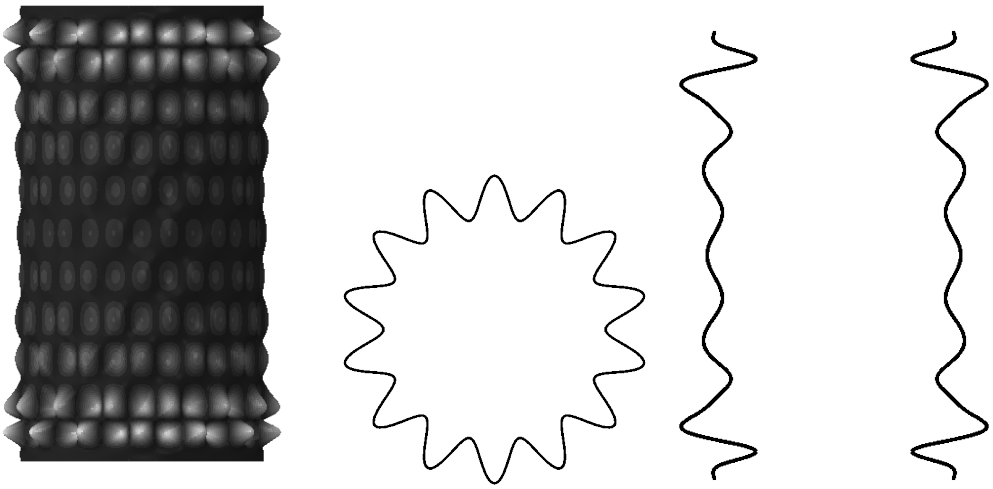

(a) Linear buckling eigen-mode displacement field

(b) Section at half height of the shell

(c) Section at the middle plane of the shell

Figure 3.18 – Linear buckling mode and sections of a perfect cylinder with 2000N pre-load effect considered

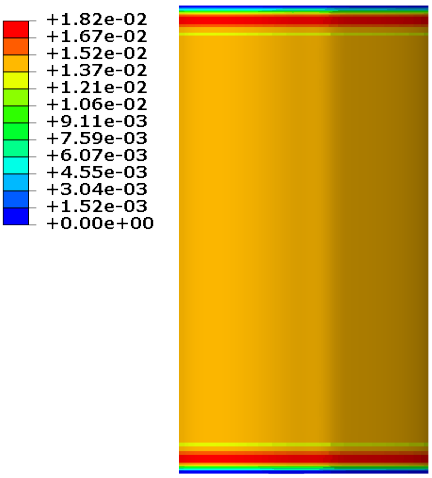

(a) Radial displacement displacement field

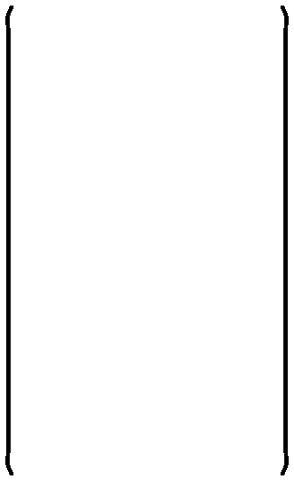

(b) Section of the radial displacement field amplified 50 time with respect to reality

Figure 3.19 – Radial displacement corresponding to an axial compression load of 2000 N. The maximum value is 1.82 10^{-2} mm and it is located near the nodes where the boundary conditions are enforced at the top and the bottom of the shells.

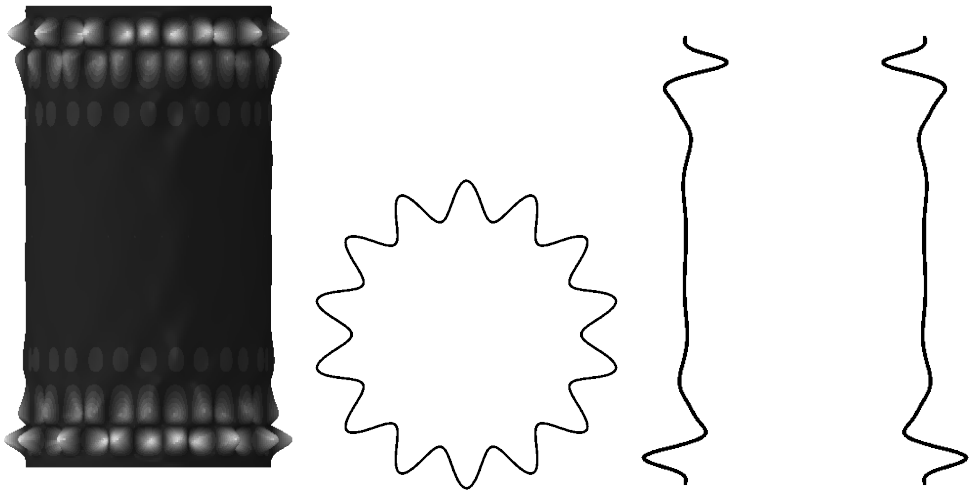

(a) Linear buckling eigen-mode displacement field

(b) Section at half height of the shell

(c) Section at the middle plane of the shell

Figure 3.20 – Linear buckling mode and sections of a perfect cylinder with 2500N pre-load effect considered

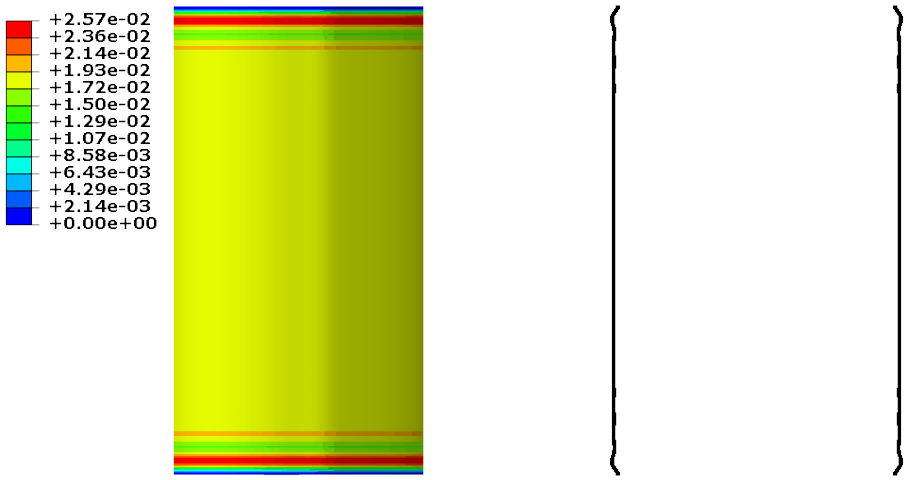

(a) Radial displacement displacement field

(b) Section of the radial displacement field amplified 50 time with respect to reality

Figure 3.21 – Radial displacement corresponding to an axial compression load of 2500 N. The maximum value is 2.57 10^{-2} mm and it is located near the nodes where the boundary conditions are enforced at the top and the bottom of the shells.

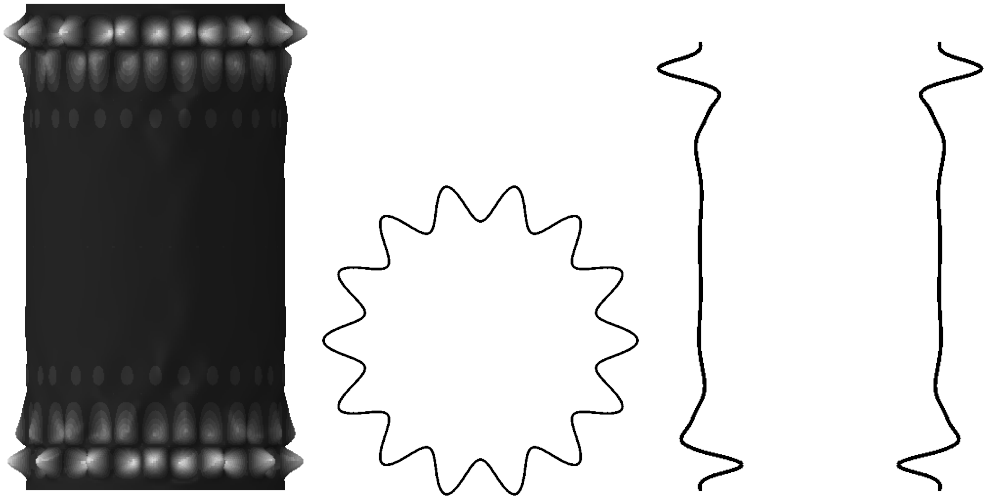

(a) Linear buckling eigen-mode displacement field

(b) Section at half height of the shell

(c) Section at the middle plane of the shell

Figure 3.22 – Linear buckling mode and sections of a perfect cylinder with 2650N pre-load effect considered

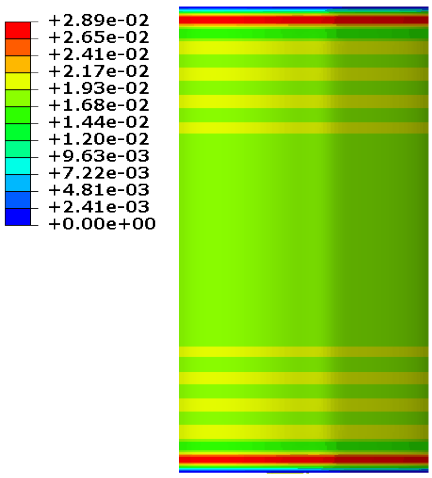

(a) Radial displacement displacement field

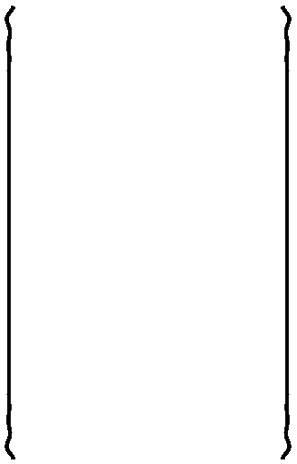

(b) Section of the radial displacement field amplified 50 time with respect to reality

Figure 3.23 – Radial displacement corresponding to an axial compression load of 2650 N. The maximum value is 2.89 10^{-2} mm and it is located at the nodes near where the boundary conditions are enforced at the top and the bottom of the shells.

In figures 3.13 to 3.22 the evolution of the lower eigen-mode is shown. There is a shift in the shape of the eigen-mode from a regular checkerboard pattern in the case with no pre-load

(Figure 3.13) to a boundary dominated one as the pre-load increases (Figure 3.22).

3.5 Practical aspects of predicting buckling loads of cylindrical shells

The aim of this section is to summarize the practical aspects and lessons learnt during the current research about how to reliably predict buckling loads of cylindrical shells. The main tool used to predict buckling loads of cylindrical shells in the current research is the commercial finite element code Abaqus. Hence, the practical details will be referred to this software.

The four options that Abaqus offers for predicting buckling loads of cylindrical shells are the utilization of the Newton-Rapshon, the arc-length, the dynamic explicit solvers and the combination of the Newton solver with a linear stability analysis sufficiently close to the buckling load. Among these four options, the most suitable one for practical applications is the one based on the Newton-Raphson solver. Namely because of the following points:

- Capability to capture the geometrical non-linearity.
- Capability to replicate entire experimental setups.
- Computationally cost-effective.

The arc-length is less suitable than the Newton solver because it can not replicate real testing conditions. The arc-length solver follows the unstable paths of solutions admissible by the system. These unstable paths are not accessible in real loading conditions during an axial compression experiment.

The explicit solver is very fast per iteration. However, due to limit on the size of the time increment dictated by the stability of the solver, a large number of time steps are required. Hence, explicit solvers end up requiring a long time to complete the analysis, making them computationally expensive in terms of time.

The option of using a linear stability analysis whit a previous Newton-based analysis is convoluted. It involves applying a sufficiently high pre-load that should be as close as possible to the buckling load via a Newton solver analysis and performing a linear stability analysis afterwards. It is more efficient to perform the complete analysis with a Newton solver until the buckling load is reached.

Beyond the points listed as benefits, there are details on the Newton-Rapshon solver of Abaqus that require careful selection in order to perform accurate predictions of the buckling load of a cylindrical shell. These parameters are the stepping and the stabilisation scheme. The stepping represents the subdivisions in fictitious time units that Abaqus uses to increase the loading progressively during the analysis. The stabilization scheme is a numerical method used by the solver to stabilize the solution at points where the stiffness matrix becomes close

to singular. Practically it introduces a damping term that uses the nodal displacements from the two previously converged steps and the fictitious time units associated between these two steps to avoid having a singularity (Dassault Systèmes Simulia Corp, 2011).

The stepping needs to be kept small enough so no buckling event is missed. Hence a maximum step size is to be established by an exploratory study of this parameter. It should be remembered that the step size is linked to the loading increment and that the solutions of the system found are for each of these load increments. Hence if a step (loading increment) is too large, it is possible that the exact loading where a local buckling occurs is not computed and the local buckling event can go unnoticed. The minimum and maximum step sizes used successfully during the current research to pass the buckling point and not miss any local buckling event are $1x10^{-12}$ and $1x10^{-2}$ respectively.

The stabilization needs to be kept as small as possible so as not to affect the physics of the system under study. In fact, a parametric study is required as in the case of the maximum stepping allowed in order to identify the minimum value that allows the computation to overcome discontinuities like snap-through or buckling events. As mentioned before, the introduction of the damping term modifies the physics of the problem due to the fact that it dissipates energy through an artificial mechanism. The approach to identify the maximum level of stabilisation allowed is to increase the damping factor used while controlling the level of energy dissipated. The energy dissipation should remain below 2% of the total energy present in the system under analysis (Drew and Pellegrino, 2002). The specific stabilization scheme used during this research has been the prescription of a damping factor. The value of the damping factor used is $2x10^{-7}$. During the current research the application of this value never led to a energy dissipation greater than 2%.

An additional relevant parameter to control in the computation of the buckling load of cylindrical shells is the element sized used, i.e. the density of the spatial discretization. This is a critical parameter to be able to capture the different deformation patterns that emerge during the buckling process of cylindrical shells. An approach to derive this is a parametric study with decreasing element size until the variation of the buckling load obtained stops varying below a certain threshold. However, there is a characteristic length that avoids the lengthy parametric study, $0.5\sqrt{Rh}$ (Wullschleger, 2006). Where R represents the shell radius and h its thickness.

The key parameters to perform an accurate buckling load prediction of a cylindrical shell with the Newton solver of Abaqus are therefore summarized in table 3.2.

3.6 Conclusions

In this chapter the finite element implementation used to analyze structural mechanics problem have been introduced. The finite element code used in the current research, Abaqus, has been evaluated to select the most suitable approach to deal with geometrically non-linear problems, particularly collapse of cylindrical shell. Among the different options the the solvers

Solver Parameter	Parameter Value
Maximum Damping Factor	$2x10^{-7}$
Minimum Step Size	$1x10^{-12}$
Maximum Step Size	$1x10^{-2}$
Maximum element size	$0.5\sqrt{Rh}$

Table 3.2 – Summary of modelling related and solver parameters used during the current research and recommended to perform accurate predictions of the buckling load of cylindrical shells

available in Abaqus, the most suitable strategy has been to use the Newton solver under displacement control conditions to determine the real buckling load of cylindrical shells. The newton solver required lower computational time than the other options while maintaining the accuracy. The displacement control loading strategy was selected because the buckling point is more evident.

The utilization of the newton solver with s displacement controlled loading strategy will be used to determine the buckling load of cylindrical shells required in the current research.

;

Results Part II

4 Localised nature of cylindrical shell buckling

Remark: This chapter is largely inspired by an article under preparation titled *"Holes, a geometric imperfection view in the context of cylindrical shell buckling"*

It is well-known that geometric background imperfections, specifically deviations from the ideal geometry of a cylinder in the radial direction, reduce the maximum axial compression load a cylindrical shell can sustain before it buckles and collapses. In many relevant engineered shell structures, spatially distributed geometric background imperfections coexist with additional localized features that will further degrade the load-carrying capacity. We thus combine an extensive experimental study with FEM simulations to investigate how localized defects represented by a drilled hole interact with geometric background imperfections in setting the load-carrying capacity of cylindrical shells. Introducing amplitudes for both interacting imperfection types, we show that there is no cumulative degrading affect of both, but that, depending on the relative amplitudes, either localized defects or the background control the buckling load. These observations suggest a path towards quantitatively comparing the strength of different imperfections and can inform the design of shell structures.

4.1 Introduction

Shells are one of the most weight-efficient structural concepts available in engineering. Without the exceptional strength-to-weight ratio of shell structures, spaceflight would likely remain a mere dream. However, the beneficial mechanical characteristics of shells come with a major engineering flaw; it is notoriously difficult to predict the maximum load-bearing capability of shell structures under compression. Linear stability analysis provides a prediction for the critical load at which a shell buckles and collapses, but in reality, shells fail at much smaller loads. This drastic reduction in the failure load compared to its linear prediction is a general feature of shell structures and is especially pronounced for highly symmetric geometries, including spheres and cylinders. The deviation between predicted and observed failure loads in compressed shells is primarily caused by the presence of geometric imperfections (Von Karman

and Tsien, 1941; Koiter, 1945). In addition, other types of imperfections such as non-perfect loading conditions, residual stresses, pre-buckling deformations and material imperfections contribute to the reduction in the load-carrying capacity relative to the theoretical prediction. However, it was demonstrated by Babcock (Babcock, 1983) that the main reason for the observed reduction of buckling loads in shells is indeed the presence of geometric imperfections, as initially highlighted by Koiter (Koiter, 1945) and von Karman (Von Karman and Tsien, 1941).

In the 1960's, following the advancement of rocketry, the need to reliably predict the buckling load of axially loaded cylindrical shells became a priority for agencies like NASA. Extensive experimental test campaigns, summarized in Fig. 4.1a, evidenced the stochastic nature of buckling loads caused by stochastically varying realizations of imperfections that result in nominally identical shells buckling at different loads. In view of the stochastic nature of imperfections, predicting the buckling load of an individual shell was considered practically impossible. Consequently, a conservative empirical lower bound for the distribution of buckling loads was defined and codified as a design guideline; the NASA SP-8007 (Seide, 1969). This guideline remains the basis of shell design until today. Perhaps motivated by the renewed interest in space travel, there is a recent thrust by NASA, headed by Hilburger (Hilburger, 2018), to derive less conservative yet reliable criteria for estimating minimal buckling loads of shells. The recent approach to improve design guidelines aims to capture the characteristic imperfections induced by different manufacturing methodologies in finite elements models, numerically compute buckling loads for these characteristic imperfections, and extrapolate the simulation results to new designs. In addition to these recent application-driven programs, also novel fundamental research on shell buckling conducted at TU Delft, EPFL, Harvard, Bristol, and others (Uriol et al., 2020; Yang and Pezzulla, 2020; Groh and Pirrera, 2019) indicates that understanding the buckling of shells remains an important issue and a subject of great interest in structural engineering.

The manufacturing process of shells creates a background of smooth deviations from the ideal geometry stochastically distributed over the entire shell (Gardner et al., 2018; Lovejoy et al., 2018). These geometric background imperfections including their spatial correlations set the buckling load of the individual shell. However, shell structures may also have, or in some cases require, additional localized imperfections in the form of dimples or holes. The interactions of stochastic background imperfections with additional localized ones are not well-understood, and only the interaction between multiple deterministic defects has been very recently studied for spheres(Yang and Pezzulla, 2020; Arbelo et al., 2014a,b).

There is evidence that local imperfections can act as nucleation points that localize the initiation of buckling (Esslinger, 1970; Abramian et al., 2020). Even in shells without intentionally engineered dimples or holes, buckling is typically initiated at a single location, as directly shown by high-speed images obtained by Esslinger (Esslinger, 1970). Based on transferring the Southwell method (Southwell, 1932) to shells, Craig et al. (Craig and Duggan, 1973) suggested that the locations where buckling is initiated are characterized by minimal stiffness with respect to lateral deformations and maximal deviations from the ideal cylindrical geometry.

The local response to laterally-induced deformations has recently also led to a description of stability properties of axially loaded cylinders by so-called stability landscapes (Virot et al., 2017). These have allowed predicting the spontaneous buckling loads even for individual defected shells (Abramian et al., 2020). Similar approaches have been successfully applied to spherical shells without defects (Hutchinson and Thompson, 2018). Additional evidence that local properties of the shell contribute to controlling the buckling load of compressed cylinders is provided by the identification of dynamically unstable dimple-like equilibrium solutions of the Donell-Mushtari-Vlasov shell equations (Kreilos and Schneider, 2017), whose existence was confirmed by finite element computations (Groh and Pirrera, 2019). These localized equilibria define critical perturbations to induce buckling for subcritically loaded shells.

Observations that global background imperfections strongly affect buckling loads while the buckling process is initiated locally suggest that both localized and distributed background imperfections together control when a compressed cylinder buckles. Previous studies have, however, focused only on either engineered localized or randomly distributed background imperfections. Here, we study the interactions of coexisting localized and distributed background imperfections. In a combined experimental and numerical study, we investigate the impact of introducing a round hole in an imperfect cylindrical shell with background imperfections. On the experimental side, we extend surveys by Toda (Toda, 1974, 1983) and Starnes (Starnes, 1972) from the $70's$ and $80's$, who investigated the effect of introducing a hole of increasing size in a small number of very high-quality Mylar shells. For two out of the three studied specimens, the data replicated in Fig. 4.1b clearly suggests that the hole significantly affects the buckling load only if its radius a exceeds a characteristic length scale given by the geometric mean of the cylinder radius and the shell thickness $a \gtrsim \sqrt{Rt}$. The remaining dataset shows no clear threshold in hole size.

Here, we experimentally study the buckling of an extended ensemble of aluminum shells, consisting of 470 different specimens with varying realizations of background imperfections. The large set of cylindrical shells allows us to test whether there is indeed a universal critical hole size beyond which the hole affects the buckling load, or whether the size at which a hole starts to affect the buckling load depends on the specifics of the background imperfections. The experiments show no clear significance of the characteristic $\sqrt{Rt}$ scale. Presumably, due to large variations in the background imperfections of commercial aluminum shells, the experimental data thus remains inconclusive. To disentangle the combined effects of hole size and background imperfections, we thus introduce an amplitude for the background imperfections. We measure buckling loads as a function of the hole size and the amplitude of randomly-generated background imperfections in a numerical study. Based on 550 buckling calculations, we demonstrate that the introduced background imperfection amplitude modifies the statistics of buckling loads. To isolate the deterministic aspects of the interaction between the hole size and the background imperfections, we choose a fixed realization of background imperfections, only varying their amplitude. For a fixed background imperfection amplitude, the buckling load shows a transition as a function of hole size. As in the data by

Toda and Starnes (Toda, 1974, 1983; Starnes, 1972), the hole only controls the buckling load if it exceeds a critical size. However, this critical size is not universal but depends on the amplitude of background imperfections. Consequently, the ratio of the hole size and the characteristic amplitude of background imperfections determines whether the background or the localized imperfection controls the buckling load. Only for specific background imperfection amplitudes, the critical hole size is given by $\sqrt{Rt}$.

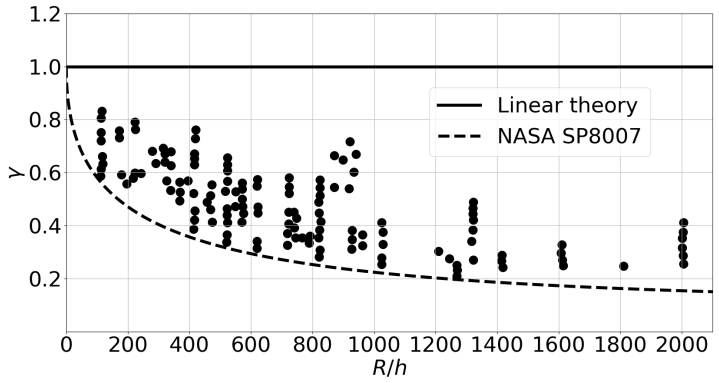

(a)

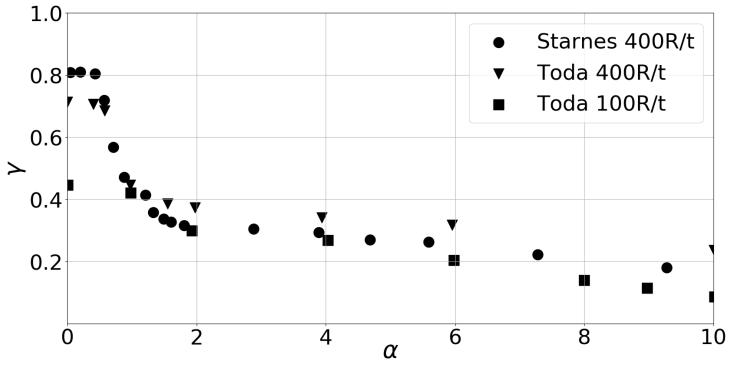

(b)

Figure 4.1 – **a)** Experimental data of buckling loads of aerospace shells tested for the creation of the $NASA\ SP-8007$ design guideline (Seide, 1969) in the late $60's$. The knock-down factor $\gamma = P_{crit.}/P_{theory}$ measuring the ratio of the buckling load relative to its linear theory prediction as a function of the radius-to-thickness ratio R/t is presented. The data shows significant deviations from the linear theory ($\gamma = 1$) and stochastic variations that led to the empirical design rule (dashed curve). **b)** Historical data about the effect of holes on the buckling load of cylindrical shells. The knock-down factor γ is shown as a function of the hole radius a normalized by the geometric mean of the shell radius and thickness, $\alpha = a/\sqrt{Rt}$ Lekkerkerker (1965). Only three shells manufactured out of Mylar that allowed buckling without undergoing damage were used in these experiments and a new, bigger hole was subsequently implemented after each test. Two datasets suggest a possible transition at $\alpha \approx 1$. Data from (Toda, 1974, 1983; Starnes, 1972).

4.2 Experimental study

(a)

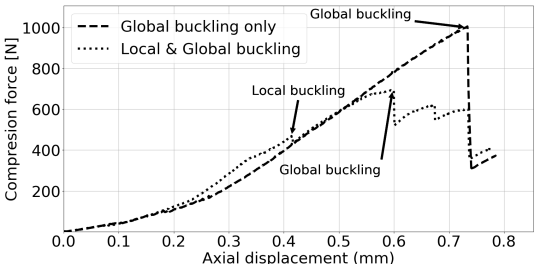

(b)

(c)

Figure 4.2 – **a)** The experimental setup consisting of a biaxial testing machine described in detail elsewhere (Virot et al., 2017; Abramian et al., 2020). **b)** Typical end-shortening curves obtained for shells with different hole sizes under axial loading. Two types of behavior are observed. The first is a single sharp drop in the force indicating a single catastrophic global buckling event beyond which the shell cannot carry the pre-buckling load. Alternatively, there can be multiple drops indicating initial local buckling events followed by a subsequent global buckling event. After the local buckling event, the shell can carry a load higher than the local buckling threshold. Whether a specific shell shows local buckling depends on the individual specimen with its distinct imperfections. We, however, observe that shells with holes of a smaller size tend to only show global buckling, while larger holes tend to promote local buckling events. **c)** Characteristic deformation patterns observed in the post-buckling regime of the test specimens for different hole radii, ranging from $0.4mm$ (top left), $0.8mm$ (top left), and $2.1mm$ (bottom left) to $3.4mm$ (bottom right). We typically observe a shorter pattern wavelength for the specimen with smaller holes.

Table 4.1 – Parameters of the 470 shells tested within the experimental campaign. For the given geometry, the empirical NASA SP 8007 design rules suggests a knock-down factor (KDF) of 0.44.

Hole radius	α	Sample size	Average buckling load (N)	Standard deviation (N)	Average KDF
$a = 0\ mm$	0	80	986.9	219.9	0.34
$a = 0.4\ mm$	0.46	80	953.2	145.3	0.32
$a = 0.5\ mm$	0.48	80	923.6	198.6	0.31
$a = 0.6\ mm$	0.69	80	955.7	186.3	0.32
$a = 0.8\ mm$	0.92	80	973.2	162.9	0.33
$a = 1.2\ mm$	1.38	30	931.6	154.3	0.32
$a = 1.6\ mm$	1.85	30	914.4	137.4	0.31
$a = 2.1\ mm$	2.42	30	864.2	68.4	0.29
$a = 3.0\ mm$	3.46	30	761.8	44.7	0.26
$a = 3.4\ mm$	3.92	30	754.9	78.1	0.26

4.2.1 Experimental setup

In the current experimental campaign, we study the buckling load of aluminum soda cans. Specifically, we consider $7.5oz$ coke cans available in the American market. These shells, with a thickness of $t = 105\mu m$ and a radius $R = 28.6mm$ have been studied previously (Virot et al., 2017; Abramian et al., 2020). Holes of a given radius were manually drilled at the mid-plane of the straight cylindrical section of length $L = 107mm$. Additional radial deformations were minimized by using high drill speeds and a minimal applied force. Following the initial proposal by Lekkerkerker (Lekkerkerker, 1965), we normalize the hole radius by the geometric mean of the cylinder radius and the shell thickness. This yields the non-dimensional hole size $\alpha = a/\sqrt{Rt}$, where a is the radius of the hole, R is the radius of the shell, and t is the shell thickness. The same re-scaled hole radius α has been considered in previous studies on the influence of holes on the buckling behavior of shells (Starnes, 1972, 1970; Toda, 1983; Van Dyke, 1965). The experimental setup consists of a custom-designed compression testing machine manufactured by ADMET. The machine can apply a compression load of up to 2200 N with a displacement and force resolution of 20 μm and 0.1 N respectively. We perform standard displacement-controlled tests. The axial vertical stage reduces the end-to-end distance until the maximum compression force is reached and the shell buckles. Compression loads and end-shortenings are recorded continuously. Thereby end-shortening curves like those presented in figure 4.2b are measured for each of the 470 individual shells that have been tested.

4.2.2 Experimental test results

The end-shortening-curve for each shell indicates a maximum axial load beyond which the shell fails. This catastrophic failure is referred to as global buckling (Weller et al., 2002; Haynie

and Hilburger, 2010) and the maximum force defines the buckling load of the specific shell. For some specimen, end-shortening-curves also present a local drop in force but subsequently, higher loads can be applied without the shell failing; this behavior is called local buckling. Examples of end-shortening curves for two shells showing either global buckling only, or a local buckling event preceding global buckling are shown in figure 4.2b.

Buckling loads for all 470 tested shells are measured and shown in figure 4.3 as a function of the hole size α. For each tested hole size, the distribution of buckling loads is characterized by its mean and standard deviation. Table 4.1 summarizes the entire collected data.

The ensemble average of the buckling loads varies by approximately 30%, ranging from 986.9 N for $\alpha = 0$ to 754.9 N for $\alpha = 4$. Significantly larger variations by more than 200% have been observed for the standard deviation, which ranges from 219 N for $\alpha = 0$ to 78.1 N for $\alpha = 4$. While the data in figure 4.3 and table 4.1 clearly indicates a strong influence of the hole size on the statistical distribution of buckling loads, no clear threshold behaviour, as reported in previous works, can be identified within the studied range of α values. We also observed an increasing probability for local buckling events for larger α.

The data by Toda (Toda, 1974, 1983) and Starnes (Starnes, 1972) clearly suggests the presence of a threshold at $\alpha = 1$. In contrast to the present study, those data sets do not refer to an ensemble of many nominally identical shells but were obtained for a single specimen manufactured from Mylar. For the same shell, the size of the hole was varied. Those tests followed the sequence: elastically buckle the shell, un-buckle the shell and drill a new hole for the explored range of values of α. Moreover the Mylar shells chosen for those earlier experiments (Toda, 1974, 1983; Starnes, 1972) show knock-down factors reaching 0.7, which is considerably higher than the average knock-down of 0.34 characterizing the aluminum shells studied here. The lower knock-down factor of the shells tested here suggests that on average, the aluminum shells are significantly more damaged and have more background imperfection than the pristine Mylar shells used by Toda and Starnes, but they are likely more representative of many commonly used shell structures.

While the statistics of buckling loads for the tested aluminum shells shows clear variations with α indicating the hole size to significantly alter the load-carrying capabilities, no apparent transition at a specific value of α is visible in the data shown in figure 4.3. We attribute the lack of a threshold to larger background imperfections that together with the hole set the buckling load of each individual shell specimen. In order to disentangle the influence of the hole from statistically varying background imperfections in shells with larger background imperfections typical of many engineering situations, we conduct a numerical study where we systematically investigate the interaction between a background imperfection and a localized hole defect. Numerical *"in-silico"* experiments allow us to control the relative strength of the hole defect compared to background imperfections, and to characterize the interactions between those. Since background imperfections result from uncontrolled details of the shell's manufacturing process, a systematic variation of background imperfections in lab experiments would not be

feasible.

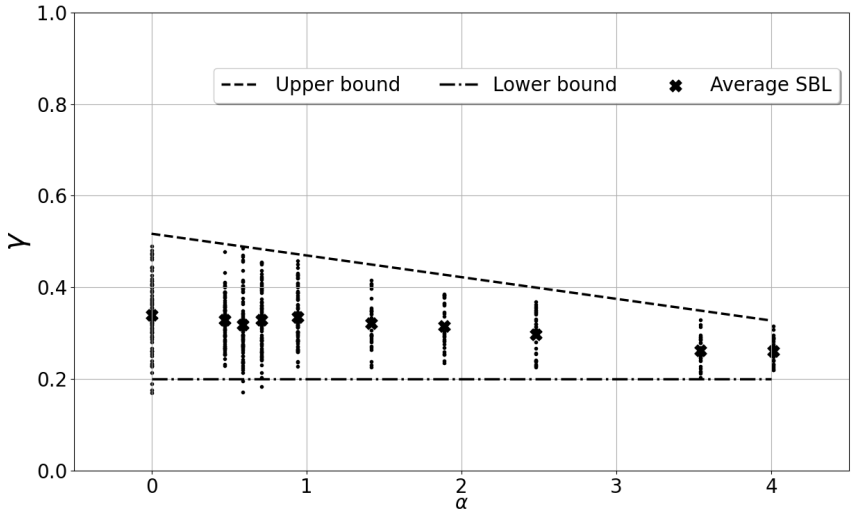

Figure 4.3 – Complete data set of the experimental campaign studying the variations of the buckling load with increasing hole size for the natural background imperfections present in aluminum soda cans. For fixed $\alpha = a/\sqrt{Rt}$ with hole radius a, shell diameter R and shell thickness t, all specimens have nominally the same geometry but buckle at different loads measured in terms of the knock-down factor γ. These variations are attributed to different realizations of the (in general unknown) background imperfections.

4.3 Numerical study

To investigate the interaction of a hole with background imperfections, we set up a suitable finite element model. We thereby aim to systematically test whether a critical hole size beyond which the hole controls the buckling load exists. Finite element models have been successfully applied in the past to analyze shells with holes (Brogan and Almroth, 1970; Almroth and Holmes, 1972). We consider either perfect cylinders or perfect cylinders with imperfections, subject to fully clamped boundary conditions applied to all the nodes of both ends of the shells. To mimic parallel end-plates in the experiment, the nodes on the upper end satisfy a multi-point constraint and are free to move in axial direction by a common displacement defining the end-shortening of the shell. The line-integral of the stress resultant over the circumference at the top end is set to the applied axial force. The considered cylinder geometry replicates the straight section of the commercial cans used in the experiments, as detailed in table 4.2.

Table 4.2 – Geometric characteristics of the shell used in the creation of the Abaqus finite element model. These dimensions correspond to the straight cylindrical section of the $7.5oz$ cans tested in the experiment.

Parameter	Value
Radius	28.6 mm
Thickness	105 μm
Length	107 mm
R/t	274
L/R	3.74

We discretize the cylinder geometry using Abaqus' parabolic pre-integrated shell elements $S8R$ with 6 degrees of freedom (DOF) associated with each node. The strain approximation used in the formulation of the $S8R$ element is based on the Koiter-Sanders-Budiansky shell theory (Dassault Systems Simulia Corp., 2018) in a fully Lagrangian framework. This formulation is suitable for small-strains and large rotations(Sanders, 1959). The material response is modeled as Hookean and isotropic with the representative material parameters detailed in table 4.3.

Table 4.3 – Mechanical characteristics of the material

Parameter	Value
Alloy	$H-19$
Young modulus	69 GPa
ν	0.33
Yield stress	200 MPa

To obtain sufficiently resolved numerical solutions, elements should be smaller than the characteristic length in circumferential direction $0.5\sqrt{Rt} \approx 0.86mm$ (Wullschleger, 2006). We consequently choose elements with a characteristic length of $0.8mm$, which translates into 225 elements in the circumferential direction. An aspect ratio close to one sets the number of elements in the axial direction and yields nearly perfectly square elements. For this grid resolution, additional refinement tests show no variation in the buckling load for shells without holes, validating the numerical model including the chosen resolution. Implementing holes of varying diameters requires a refined mesh close to the hole that transitions to the near-square background mesh. The topological constrains imposed by the hole necessitates the use of a non-ideal element shape; in the transition area elements with high aspect ratios and skewness

need to be used. Such mesh geometries may cause numerical artifacts and spurious results. The accuracy of numerical results is therefore confirmed by checking the robustness of a solution with respect to small parameter perturbations. If a solution is robust, infinitesimal parameter variations lead to infinitesimal variations of the buckling load, while spurious solutions show non-smooth dependence on small parameter variations.

4.3.1 Numerical model justification and background imperfections

A numerical analysis based on the entire geometry of a commercial 7.5 oz coke can is possible but computationally very expensive. Here, we thus consider the simplified system of a pure cylinder, neglecting the conical parts at the top and bottom of the can. We consider the simplified geometry is justified and allows comparisons to experiments for the following three reasons:

1. The deformations of the conical section within a can are very small compared to the cylindrical section prior to the global buckling point so that the cylindrical section is effectively loaded subject to the same clamped boundary conditions considered in the numerical model.

2. In our experiments, buckling is always confined to the cylindrical section of the can suggesting that differences in boundary conditions have negligible effects.

3. The eigenmode associated with the linear stability threshold, evaluated with the Abaqus Lanczos solver, is virtually indistinguishable for both geometries, as shown in figure 4.4.

The simplified cylinder has an associated eigenvalue of 2902 N and 0.23784 mm for the load and displacement control, respectively. The eigenvalue of the simplified cylinder is used as the reference throughout the study to calculate the knock-down factors of the non-perfect cylinders and to non-dimensionalize the end-shortening.

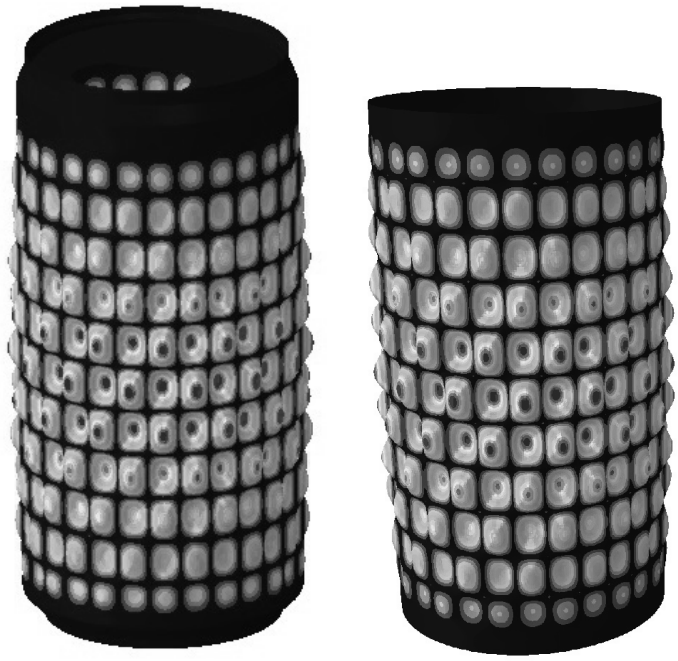

(a) (b)

Figure 4.4 – Comparison of the critical eigenmode of the complete can **a)** and the simplified cylinder **b)** representing the straight section of the can. In both cases the structure of the eigenmode is identical with 28 azimuthal and 11 axial half waves respectively. The critical eigenvalue of the can and the cylinder differ by only 2%.

To replicate the behaviour of real defected shells such as those studied experimentally, background imperfections need to be included in the numerical model. The aim is to emulate non-local defects that cover the complete surface, with a spatial structure similar to the ones surveyed at NASA Langley in the Space Shuttle legacy hardware (Gardner et al., 2018; Lovejoy et al., 2018). Non-local random imperfections have been implemented in finite element-based numerical analysis of buckling before (Hansen, 1977; Elishakoff et al., 1987; Roorda and Hansen, 1972), either as the only imperfection or in combination with local defects (Schenk and Schuëller, 2007). Background imperfections have been traditionally implemented using either uncorrelated random distributions or randomized linear combinations of trigonometric functions (Koiter, 1945) to perturb the location of nodes radially away from the ideal cylinder geometry. These approaches led to valuable insights into the statistical impact of a random background, but both traditional implementation approaches also have significant disadvantages. The uncorrelated random model is nonphysical as the imperfections lack the smoothness of background imperfections present in real shells. The alternative randomized linear combination of trigonometric functions preserves smoothness but requires arbitrarily choosing a large number of parameters. To overcome the limiting disadvantages and combine the advantages of the two traditional methodologies, we here introduce Random Gaussian Correlated (RGC) imperfections. RGC imperfections retain the stochasticity of uncorrelated

random imperfections and preserve the smoothness of a randomized linear combination of trigonometric functions while minimizing the number of arbitrary parameters to be selected to only three.

Technically, the imperfections are implemented as follows. We introduce preferred axial and azimuthal correlation length scales by spatially filtering an initially uncorrelated random deformation field with a Gaussian filter. That means, we define a radial displacement field $dw(z,\theta)$ relative to the perfect cylinder with axial and azimuthal coordinates $z \in [0,L]$ and $\theta \in [0,2\pi]$, respectively:

$$dw(z,\theta) = C \int_0^L \int_0^{2\pi} \kappa(z-z',\theta-\theta')\eta(z',\theta')\,dz'\,d\theta' \,. \tag{4.1}$$

Here η is a (spatially) uncorrelated and centered Gaussian random function with $\langle \eta(z,\theta)\eta(z',\theta')\rangle \propto \delta(z-z',\theta-\theta')$ and $\langle \eta \rangle = 0$. The kernel

$$\kappa(z,\theta) = \exp\left(-\frac{z^2}{\lambda_z^2} - \frac{\theta^2}{\lambda_\theta^2}\right) \tag{4.2}$$

has a Gaussian form and sets an axial and azimuthal length scales $\lambda_z = L/n$ and $\lambda_\theta = 2\pi/m$ corresponding to the integer values of n and m, respectively. Together with the scaling factor C these two integer values constitute the three parameters controlling the RGC imperfections. Technically, we evaluate the convolution in equation 4.1 using 2D Fourier transforms together with the convolution theorem, as commonly done in filtering applications (Garcia and Stoll, 1984). Throughout this study, we set $n = 2$, and $m = 4$, so that only the maximum deviation from the ideal geometry is to be selected. This maximum deviation is denoted by β, a non-dimensional parameter that expresses the maximum deviation for the ideal geometry in terms of the thickness of the shell. For each realization of the Gaussian correlated random noise, we thus adjust the scaling factor C such that

$$\beta = \max(|dw|)/t \,. \tag{4.3}$$

The resulting background imperfection is smooth and random, as shown in detail in figure 4.5.

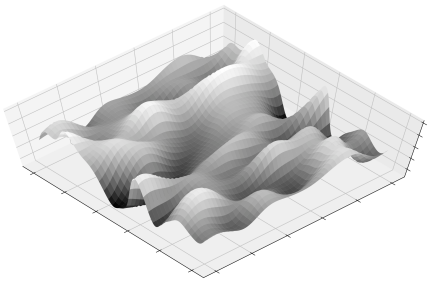

(a)

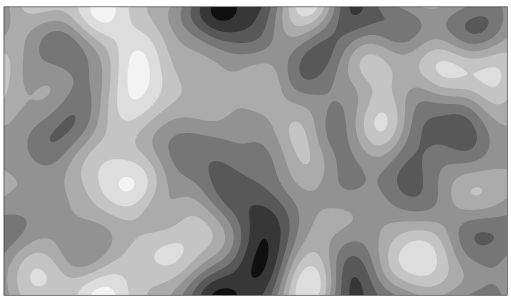

(b)

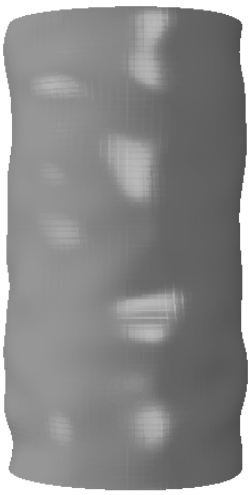

(c)

Figure 4.5 – **a)** 3D visualization of a characteristic RGC imperfection. The field defines a stress free radial displacement applied to the nodes of the FE model. **b)** 2D visualization of a characteristic imperfection showing the random nature of the arrangement of smooth dimples. **c)** Example of the FE model. The random self correlated imperfection has been amplified for visualisation purposes.

To characterize the reduction of buckling loads for varying amplitudes of the background imperfections and in order to determine a value of β, for which the numerical model captures the behaviour of the experimentally tested shells, we carry out a large number of *in-silico* experiments for shells with background imperfections but without a hole defect. Figure 4.6b shows the spontaneous buckling loads of ensembles of shells for prescribed β, ranging from 0.25 to 5.0. For each value of β, 50 unique realizations of an RGC background imperfection were constructed and numerical buckling tests performed. Figure 4.6a shows a set of typical end-shortening curves obtained at different imperfection amplitudes β.

The data clearly indicates a reduction in average buckling load with increasing imperfection amplitude; the average knock-down factor varies from above 0.9 for $\beta = 0.25$ to a value below 0.2 for $\beta = 5$. At $\beta = 2$, we obtain an average knock-down factor very close to the one of the experimentally tested commercial cans with no holes, as shown in Table 4.1.

A detailed inspection of the end-shortening curves shown in figure 4.6a reveals that for $\beta = 1$, the behavior is very similar to the one expected from a perfect shell, showing a single large drop in load when the global buckling threshold is reached. However, this shell, with $\beta = 1$, already exhibits a substantially reduced load-bearing capability compared to a shell without defects. For values of β ranging from 2 to 3, end-shortening curves reveal the likely emergence of local buckling events preceding the global buckling and a further reduced load-bearing capability. The curves corresponding to values of $\beta = 2$ and $\beta = 3$ have the same slope as the one for $\beta = 1$, which indicates an identical stiffness until the first buckling event. For $\beta = 4$ and $\beta = 5$, the behavior changes significantly compared to the other end-shortening curves. The stiffness is noticeably reduced, and the characteristic drop in the global buckling becomes significantly smaller. At $\beta = 5$ almost no drop characteristic of a catastrophic buckling event remains. Consequently, at $\beta = 4$ and $\beta = 5$, no characteristic dynamic buckling behavior with mostly unchanged stiffness followed by sudden loss of stability is observed. This behaviour suggests that beyond a certain amplitude of background imperfections, cylindrical shells no longer exhibit a dynamic buckling event, while they retain a residual load-bearing capability of approximately 20% of that of the perfect shell.

The random realizations of the RGC imperfection yields a stochastic distribution of buckling loads for fixed amplitude β, as evidenced by the data displayed in Fig. 4.6b. Thus, the numerical model replicates the stochastic nature of the experimental test data in Figs. 4.5 and 4.3, albeit with smaller standard deviation. The lower bound of the experimentally observed buckling loads both with and without a hole defect corresponds to a knock-down factor of approximately 0.2 (Fig. 4.3), which is very close to the knock-down factor the numerical data asymptotes to, when the amplitude of background imperfections is increased. This suggests that the ensemble of experimentally tested shells contains realizations with large enough amplitude so that the residual load-bearing capability of shells is reached. The numerical data with controlled imperfection amplitude, shows that the average buckling load decreases monotonically as a function of β. Initially it drops linearly until it levels off around $\beta = 2$ and asymptotes towards a fixed value. Consequently, the maximum amplitude of the background

imperfection β indeed controls the average buckling load. For small enough values of β, the distribution remains broad, while for large enough values of β, the distribution significantly narrows.

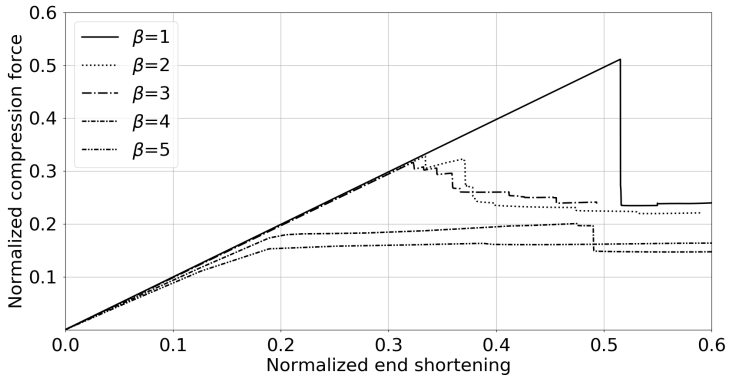

(a)

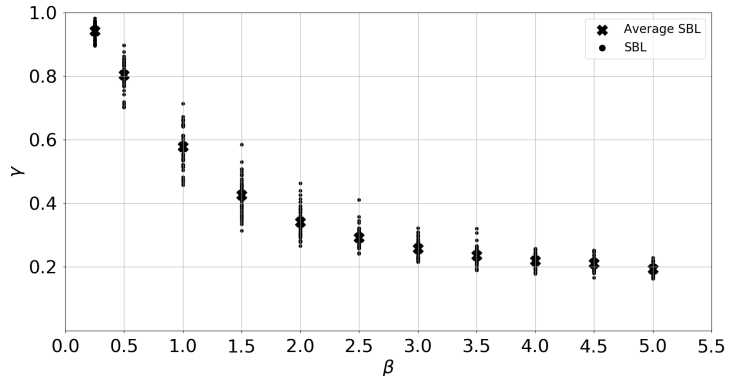

(b)

Figure 4.6 – **a)** Characteristic end shortening curves for varying values of the background imperfection amplitude β. **b)** Numerical data showing the influence of the amplitude in the RGC imperfection on the buckling load of the shell.

4.3.2 Interaction of background imperfections with a localized defect

We have shown that introducing specific random background imperfections in a numerical FEM model reproduces the stochastic nature of buckling loads observed in experiments. We have moreover introduced an amplitude parameter for the background imperfections that allows controlling their strength. To investigate the interaction of those background imperfections with localized hole defects, we now introduce holes of varying size in the numerical model. Varying both the size of the hole, characterized by its re-scaled radius α and the amplitude of background imperfections β, independently allows us to investigate

under which conditions either the hole or the background imperfections control when the shell buckles.

Holes in a perfect cylinder: Using the mesh parameters discussed above, we first introduce a hole of radius a at the midsection of a perfect cylinder. In figure 4.7a representative end-shortening curves of the finite element analysis of the perfect cylinder, $\beta = 0$, with a hole of varying size given by $\alpha = a/\sqrt{Rt}$ are presented. As expected, introducing a hole defect has a downgrading effect on the maximum load that the cylinder can sustain before global buckling occurs. For small holes with $\alpha \leq 2$, only global buckling occurs, while for larger holes with $\alpha > 2$ local buckling occurs before the global buckling event. The presence of the hole does not affects the stiffness of the shell before buckling. For the studied hole sizes up to $\alpha = 4$ all shells retain a residual load-bearing capability of approximately $600N$, equivalent to a knock-down factor of 0.2, suggesting the existence of a minimum load that all shells of a certain geometry can carry independently of the size of the hole defect.

To investigate the impact of the hole defect on the loaded shell and gain information on the location where buckling is initiated, we visualize the deformation of the loaded shell at the buckling load for different hole sizes. The radial deformation is shown in the contour plots of figure 4.6b. As expected, due to the fact that the hole defect breaks rotational symmetry of the perfect cylinder, even for the smallest hole sizes, the initiation of buckling occurs at the hole and then propagates through the complete shell.

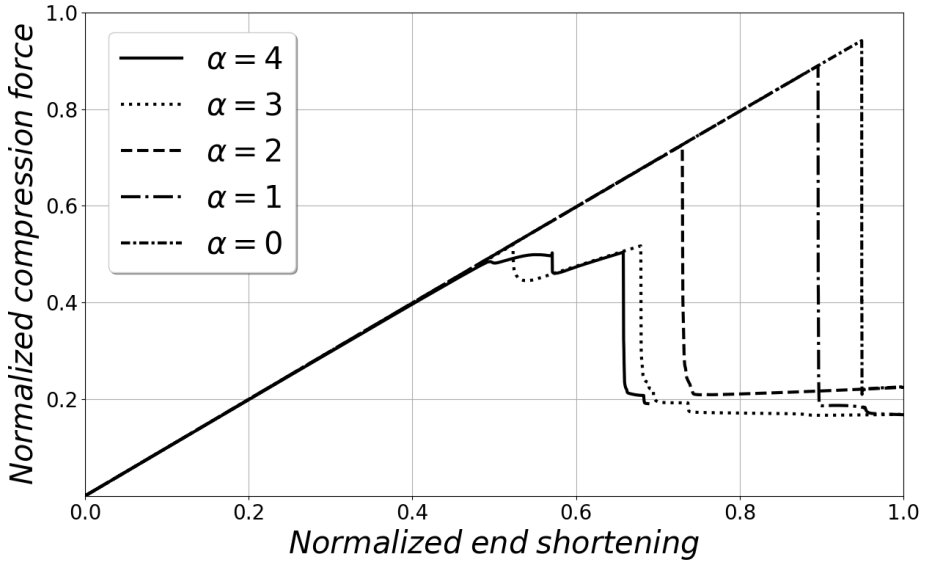

(a)

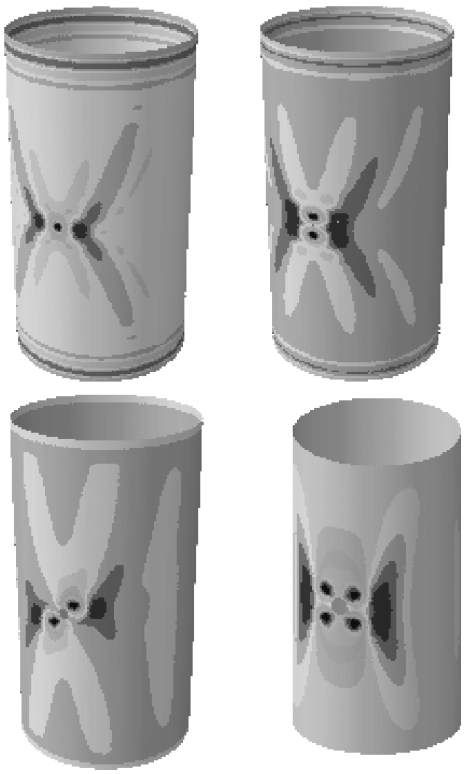

(b)

Figure 4.6 – Buckling behavior of a perfect shell ($\beta = 0$) with a hole of varying size. **a)** Representative end-shortening curves of the perfect shell for different hole sizes given in terms of the rescaled radius α. **b)** Representative contour plots of radial displacement fields at the onset of global buckling for a perfect shell with different hole sizes. α grows from left to right and from top to bottom. The hole sizes in the shells are $0.8mm$ and $1.6mm$ for the first 2 shells, and $4.2mm$ and $6.8mm$ in the case of the last 2. The grayscale was selected to show the deformation contours of each individual shell qualitatively.

Holes interacting with background imperfections: For the perfect cylinder without background imperfections, even a very small hole defect acts as the only and thus dominant imperfection controlling at which load and location the shell buckles. To explore the interaction of a hole defect with background imperfections, we now consider a cylinder that contains both a hole defect and background imperfections whose relative strength can be varied. Instead of considering an ensemble of different realizations of the RGC background imperfections, we select a single realization and scale its amplitude. We thus consider a deterministic system with two control parameters, the hole size α and the amplitude of background imperfections β, which can be varied independently.

The computed knock-down factor for the background imperfection amplitude ranging from $\beta = 0$ (perfect cylinder) to $\beta = 2$ and hole size ranging from $\alpha = 0.25$ to approximately $\alpha = 2.5$ is shown in Fig. 4.7. In the absence of background imperfections, i.e. $\beta = 0$, the buckling

load decreases almost linearly with hole size, until at $\alpha \approx 2$ a plateau is reached. For non-zero background imperfection amplitudes and small hole sizes, the buckling load is independent of the hole size α but varies with β, suggesting that the background imperfections control when the shell buckles. As the hole size increases, there is a β-dependent critical value of α, beyond which the buckling load becomes dependent on α and – for intermediate background imperfection amplitudes – approximately follows the $\beta = 0$ trend. For the largest studied background imperfection amplitudes, $\beta = 1.5$ and $\beta = 2$, the presence of the hole does not affect the buckling load of the shell for any value of α within the studied range. However, for values of β between $\beta = 0.25$ and $\beta = 1$, two regimes coexist. For holes below a critical size, $\alpha < \alpha_{\text{crit}}$, the shells are insensitive to the presence of the hole, while for $\alpha > \alpha_{\text{crit}}$ shells become senstitve to the presence of the hole and approximately behave as if background imperfections were absent. This behaviour suggests that there is a critical hole size below which the background imperfections control when the shell buckles, while for larger holes the localized defect acts as dominant imperfection. However, contrary to the observations by Toda and Starnes (Starnes, 1972; Toda, 1974, 1983), the critical hole radius is not universal and given by $\sqrt{Rt}$, but depends on the amplitude of background imperfections.

In order to determine the critical hole size α_{crit} as a function of background imperfection amplitude β, we normalize each computed knock-down factor $\gamma(\alpha, \beta)$ by the knock-down factor for the smallest studied hole size $\gamma(\alpha_{min} = 0.25, \beta)$. As shown in Fig. 4.8, extrapolation allows to clearly determine the value of α_{crit} beyond which the hole defect further degrades the buckling load of a shell. The obtained values are compatible with a linear fit (Figure 4.8 inset), implying that the critical hole size is approximately proportional to the amplitude of the background imperfections.

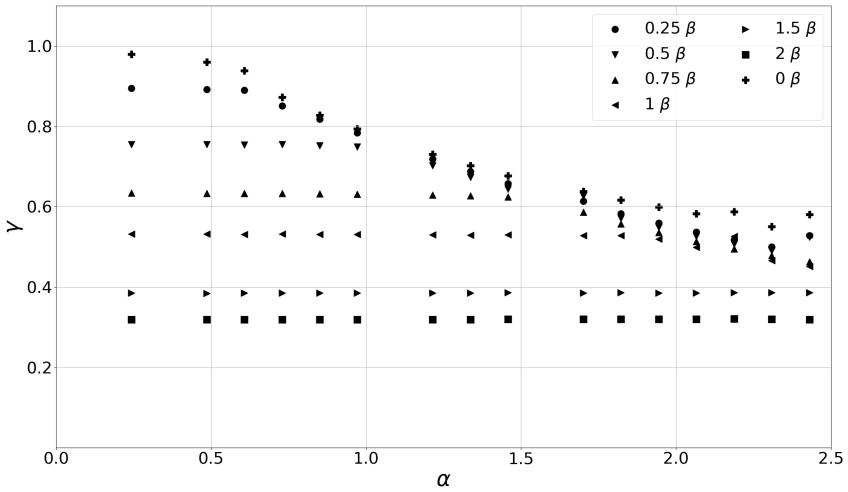

Figure 4.7 – Influence of the hole size (α) on the global buckling load for different imperfections amplitudes (β).

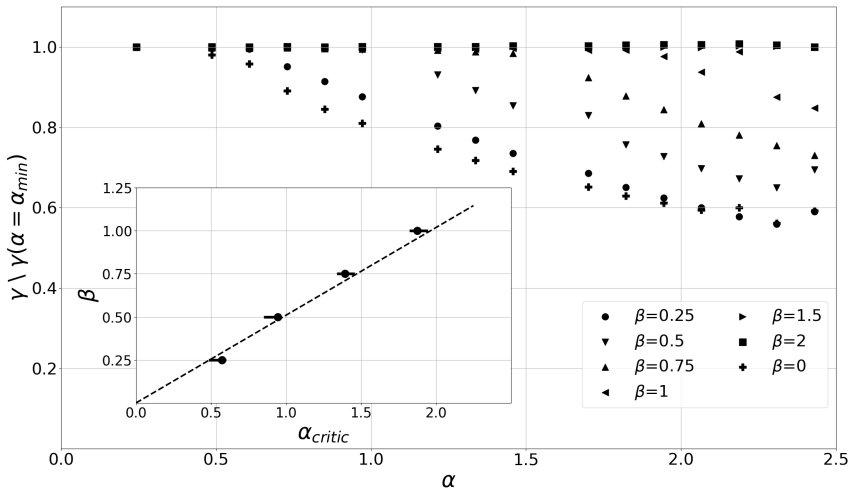

Figure 4.8 – Re-normalization of the data from figure 4.7 by the smallest α. For each β the critical α_{crit} beyond which the hole defect further degrades the load-carrying capacity can be extracted. α_{crit} and the background imperfections amplitude β are approximately proportional (inset).

4.4 Discussion

Within an extensive campaign combining experiments and FEM simulations, we have studied how unavoidable geometric background imperfections and localized hole defects interact to set the buckling load of an axially loaded cylindrical shell. Experimental buckling tests of 470 commercial aluminum shells with hole defects of varying size indicate that the hole size affects the distribution of knock-down factors within the ensemble of nominally identical specimens. While the lower-bound of the distribution with $\gamma \approx 0.2$ does not depend on the hole size, the highest knock-down factors observed within each distribution decrease as a function of hole size (Fig. 4.3). In combination, an increased hole size leads to a reduced mean knock-down factor. However, unlike in previous studies based on exceptionally high-quality shells, no clear threshold in the hole size beyond which the hole defect affects the buckling load has been observed. Specifically, no evidence of a threshold at a hole radius of $\sqrt{Rt}$, or equivalently $\alpha = 1$, was found.

To complement the experimental campaign, FEM simulations were carried out. Gaussian filtering of uncorrelated noise allowed us to include realistic random background imperfections in the model, and to define an adjustable amplitude β, measuring the maximal radial deviation from the perfect geometry in units of the shell thickness. Numerical buckling tests for 550 realizations of random background imperfections without a hole defect, reveal stochastic distributions of buckling loads. The distributions for a fixed imperfection amplitude are narrower than those observed for the experimental shells where amplitudes are unknown,

and strongly depend on β (Fig. 4.6b). As the imperfection amplitude is increased, the mean knock-down factor first decreases almost linearly with the imperfection amplitude, before it levels off at a residual load-carrying capacity of $\gamma \approx 0.2$, the same value also observed as the lower bound in the experimental tests.

To investigate the interaction of background imperfections and a hole defect of varying size, we include a hole in the numerical model, consider a fixed realization of the background imperfections, and compute the buckling load for the now deterministic system as a function of independently varied hole size α and background imperfection amplitude β (Fig. 4.7). Withing the tested hole sizes and for background amplitudes up to $\beta = 1$, two distinct regimes are observed. Below a critical hole size α_{crit}, the knock-down factor is independent of the hole size, indicating that the background imperfection controls the buckling load. For holes larger than the critical value, the knock-down factor depends on α and becomes approximately independent of the background imperfection amplitude, indicating that now the hole defect controls when the shell buckles. Consequently, the knock-down factor is not given by a superposition of the degrading influence of background imperfections and an additional degrading factor due to the hole defect. Instead, the clearly separated regimes suggest that either the background imperfections or the localized hole defect provide the dominant imperfection and control the buckling load.

Unlike suggested by previous studies (Starnes, 1972; Toda, 1974, 1983), the critical hole size is not universal and given by the geometric mean of the shell radius and thickness $\sqrt{Rt}$, or $\alpha_{crit} = 1$, but depends on the amplitude of background imperfections with the data suggesting that the critical hole size is proportional to the background imperfection amplitude β (Fig. 4.8). This is compatible with the observation that for a perfect shell, the limit $\beta \to 0$, even the smallest hole defect will act as the only and thus obviously dominant defect degrading the knock-down factor.

These results are not only relevant for understanding the specific interaction of local and distributed imperfections in an axially loaded cylindrical shell, but also suggest a more general framework for comparing the 'strength' of different types of imperfections. There is no obvious norm that characterizes how large imperfections are. Introducing amplitudes for two interacting imperfection types, here smooth geometric background imperfections and a localized hole defect, and identifying thresholds for when one of them dominates, allows to compare their strength.

Based on the observation that their respective amplitudes determine whether the background or the hole control the buckling load, we can interpret the experimental buckling data for commercial aluminum shells (Fig. 4.3). Here background imperfections are a result of the manufacturing, transport and handling processes so that not only the spatial structure but also amplitude of the background imperfections is randomized. As the critical value for α depends on the randomly varying background imperfection amplitude, no clear threshold is observed. Moreover, a comparison of the average knock-down factor below $\gamma = 0.4$ to the

β- resolved numerical data, suggests that for most specimens the background imperfections are so large that the hole has no substantial influence on the buckling load. The lower bound within the measured distributions of knock-down factors is compatible with the asymptotic value found for large background imperfection amplitudes in the absence of hole defects. This behaviour clearly suggests that the background imperfections control the buckling load and explains a lower bound that remains independent of the hole size. The realizations of background imperfections with the lowest amplitudes within each distribution however enter the hole-size dependent regime in which the hole defect dominates. Consequently, the hole defect degrades the highest knock-down factors within each distribution and leads to the observed maxima decreasing as a function of α. Thus, the experimental data supports our conclusion, that there is no superposition or additive degrading effect due to localized hole defects and geometric background imperfections but that both interact with the stronger imperfection dominating and controlling the buckling load.

The experiments by Starnes (Starnes, 1972) and Toda (Toda, 1974, 1983) were using a single shell with one specific realization of (unknown) background imperfections. These results are thus comparable to our deterministic investigation albeit without control and variation of the background imperfection amplitude. For their pristine shells, they report a knock-down factor without any hole of close to $\gamma = 0.8$. Within our numerical model using random gaussian correlated imperfections, this knock-down factor translates into an equivalent background imperfection amplitude of $\beta \approx 0.5$. Remarkable, with the approximately linear dependency of the critical hole size (Fig. 4.8 inset), we get $\alpha_{crit} \approx 1$, precisely as reported by Starnes and Toda. Although the shells used in previous experiments differ slightly in geometry, with $R/t = 400$ as opposed to $R/t = 274$ studied here, and despite the analysis being based on a specific realization of background imperfections, this calculation suggests that the observation of a critical hole size with $\alpha_{crit} = 1$ was likely a coincidence and is only valid for the specific background imperfections of the tested shells.

4.5 Conclusions

In summary, we do not observe a universal significance of the scale $\sqrt{Rt}$ for the critical size of a hole beyond which it degrades the load-carrying capacity of an axially loaded cylindrical shell. Instead, the hole will control the buckling load when it is the strongest or dominating imperfection. Whether this is the case depends on how strong other coexisting background imperfections are in comparison, implying a critical hole size that depends on the strength of the geometric background imperfections. The interaction of a localized hole defect with background imperfections is not simply described by a superposition of degrading effects due to both. But the stronger imperfection will have a dominant effect. Comparing the relative strength of different imperfections remains an open problem. However, the existence of clear threshold when both interacting imperfections are assigned independent amplitudes suggests a path towards quantitatively comparing the strength of different imperfections.

5 Predicting global buckling of cylindrical shells via stability landscapes

Remark: All published experimental data from section 5.2.1 has been published in (Abramian et al., 2020). The data was collected by the author of this thesis using control scripts for the bi-axial-test machine, developed by the author.

In chapter 4 it has been shown that the buckling behaviour of cylindrical shells is modified by localized defects. It was also shown that the modification of the buckling load is not only dependent on the localized defects but also on the background long range imperfections.

The fact that the presence of background imperfections influences the buckling load of cylindrical shells, even in the presence of large localized imperfections, does not undermine the importance of the local properties of shells to control buckling or infer information about their stability. The buckling load of cylindrical shells is influenced simultaneously by both kinds of imperfections, local and global.

The effect of long range global imperfection in the buckling load of cylindrical shells under the presence of any localized imperfection suggest a complex interaction. The expected behaviour would be that for a strong enough local imperfection the background imperfections would have no effect and vice-versa. In order to understand this complex behaviour, a suitable methodology to explore the stability of cylindrical shells at different locations is required. The capability to explore different locations is important to understand the influence of the background imperfections that cover the complete cylindrical shell.

Due to the catastrophic nature of the buckling event in cylindrical shells, this methodology will have to be able to provide information about the stability of a cylindrical shell without risking triggering its collapse. Furthermore, this methodology will have to be able to provide information about the stability behaviour of the shell in a large number of locations to capture the influence of the background imperfections in combination with localized ones.

A methodology that satisfies the requirements mentioned above is based on stability landscapes. This approach allows for a local evaluation of the properties of a cylindrical shell.

Furthermore, stability landscapes encode information about the stability of the cylindrical shell without triggering collapse (Abramian et al., 2020; Virot et al., 2017; Thompson and Sieber, 2016).

The stability landscape is a surface defined in a three dimensional space spanned by the axial load at which the different measurements are performed, the displacement of a poker used to probe the surface of the cylindrical shell in the radial direction and the reaction force of the shell opposing the deformation induced by the poker.

Stability landscapes extrapolate to a vanishing point as the axial load is increased. This feature enables the utilization of stability landscapes to predict the maximum load a cylindrical shell can bear. This last possibility will be explored in this chapter

The only property that stability landscapes do not satisfy is the capability to provide information about the complete shell. However this can be changed by successively building stability landscapes at different locations to learn about the stability properties of a cylindrical shell in multiple locations. Practically, this means that stability landscapes will have to be constructed at different locations. A sufficient number of locations will have to be investigated to achieve a degree of certainty about the fact that there is a point or area in the cylindrical shell where the buckling load extrapolation is correct. This is an option that will also be explored in this chapter.

In chapter 2 the dynamical systems description of cylindrical shells was introduced together with the idea of the basin of attraction linked to each fix point of the system. Stability landscapes are the experimental methodology to explore the extension of the basin of attraction. They are the link between the theoretical description of cylindrical shell buckling as a finite amplitude problem and experiments.

In state space, an stability landscape corresponds to the exploration under a finite amplitude perturbation of one of the possible directions leading to the basin boundary. There are infinite directions to be explored, these directions correspond with different shapes of the finite amplitude perturbation used. In the current research a single poker is the perturbation that is going to be used to explore the basin of attraction of each stable fix point. A fix point on the dynamical systems corresponds with a stable configuration of a cylindrical shell under a compression load.

5.1 Predictions via numerically obtained stability landscapes

In order to use the stability landscapes as a predictive tool, it is important to verify their ability to provide an accurate estimation of the buckling load of a cylindrical shell non-destructively at the compression load where the stability landscape vanishes. The approach followed to demonstrate that stability landscapes are able to extrapolate to the correct buckling load once the right location is found is to perform an experiment in the most controlled manner possible.

Due to the stochastic nature of the imperfections present in real cylindrical shells and the known sensitivity to imperfections of cylindrical shells, the most suitable experiments are numerical ones (also known as *in-silico* experiments). These numerical experiments will be based on finite element analyses following the recommendations from chapter 3.

5.1.1 FEM applied to stability landscape derivation

The main reason to use numerical experiments is the fact that in simulations it is possible to control all the different aspects that have an effect on the final result. The main aspects to be controlled in the case of cylindrical shells are geometric imperfections, non-ideal boundary conditions or imperfections in the loading conditions. In simulations it is possible to remove all the aforementioned real world features, implement perfect boundary conditions, use perfect load introduction and implement at the same time engineered imperfections in a controlled fashion. This last feature can be used to carry out a parametric study to understand the influence of an imperfection for nominally identical conditions.

In-Silico test procedure

The sequence for the simulation to verify the predictive capability of stability landscapes is to prescribe a certain load below the maximum the cylindrical shell can bear and probe radially the shell retrieving the radial displacement of the probe as well as the radial reaction force exerted by the shell on the probe. The plot of radial force as a function of radial displacement is a poking curve. A very useful feature of these simulations is that it allows a destructive test to be carried out to obtain the maximum load the cylindrical shell can bear prior to the extraction of the stability landscapes. This fact is very useful to understand the different load levels to include in the derivation of the stability landscapes through successive poking curves. Namely, it allows to discern the levels of pre-load that can be applied to construct stability landscapes without triggering buckling.

Regarding the location where to derive the stability landscape, the most reasonable position is the point where the nucleation of buckling takes place. This location is the position where the variation in radial force becomes zero at the moment where the collapse of the cylindrical shell begins. Furthermore, a suitable point should be as far away as possible from the boundary conditions to avoid any influence of them (Mikulas et al., 2011) and localized in the azimuthal direction. In order to fulfil these conditions, the best is to introduce a controlled imperfection at the location where the probing will take place.

On the modelling side, the finite element model used in the simulations consists of a shell that is probed with an infinitely rigid poker at different axial loads making use of a contact tracing algorithm inbuilt in the commercial finite element software Abaqus. At each of the axial loads a poking curved is built by extracting the radial reaction exerted by the shell as the poker moves radially via a prescribed displacement. This process is repeated for increasing

axial loads to build a complete landscape. An illustration of the finite element model including a cylindrical shell and the poker is shown in figure 5.1.

The solver used for these *in-silico* experiments is the Newton-based one from Abaqus. This is the most suitable solver for practical applications as discussed in chapter 3. It allows for the solution of geometrically non-linear problems. Furthermore, it is able to cope with different bifurcation scenarios via the utilization of different stabilization techniques as shown in chapter 3. These stabilization techniques are not used during the extraction of the landscapes because no singularity of the stiffness matrix occurs. The stabilization techniques are only used in this chapter to obtain the maximum load bearing capability of the cylindrical shell. This load is needed to guarantee that the pre-load induced in the cylindrical shell for the extraction of the landscape is not greater than the load bearing capability of the cylindrical shell under study. The solver control values are the one specified in chapter 3.

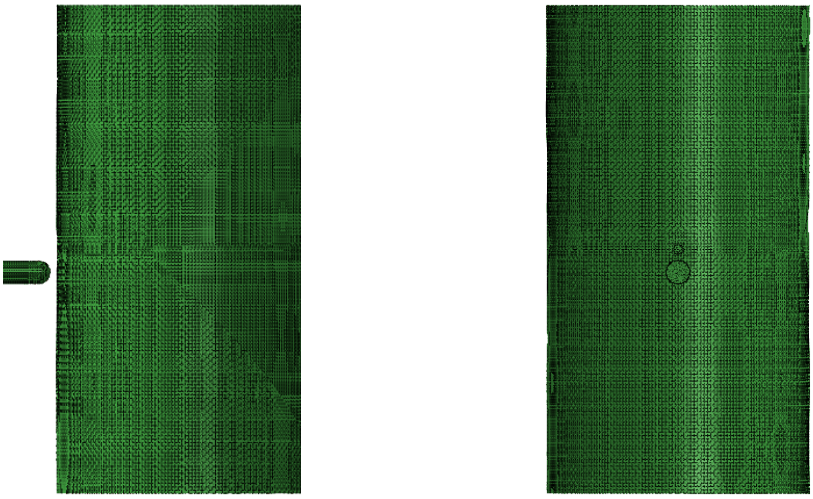

(a) Side view finite element model including the cylindrical shell and the poker

(b) Front view finite element model. The poker is located $5mm$ below the hole used as a local imperfection to nucleate buckling

Figure 5.1 – Example of the finite element model used for the creation of the stability landscapes. The model includes 2 bodies, the shell and the poker that is used as a probing device. The shell is modelled with parabolic pre-integrated S8R elements. The poker is modeled with 3D tetrahedral elements with infinite stiffness. The interaction between the poker and shell is done using the friction less penalty contact algorithm of Abaqus. The complete solution ,consisting a pre-loading step and a probing step, is done using the Newton solver of Abaqus.

Numerically derived stability landscapes

A set of stability landscapes obtained using the numerical approach previously described are shown in figure 5.3 for different localized imperfection sizes. In the case of the landscapes in figure 5.3 the localized imperfections are holes of various sizes ranging from 0.8 mm to 3.2 mm. The landscapes show the same features discovered empirically (Virot et al., 2017). The main feature is the ridge, this feature corresponds to the section where the poking forces grows up to a level to then decrease down to zero for a fix axial load. The relevance of the ridge feature comes from the fact that the point where it vanishes corresponds with the maximum compression load a cylindrical shell can bear. This load is referred as the spontaneous buckling load (SBL).

The data points in the lines projected in the axial force / poking force (F_A/F_p) plane in figure 5.3 are the elements used to extrapolate to the corresponding maximum load a certain cylindrical shell can carry: the buckling load prediction. These curves are shown independently in figure 5.4. The curves used for the extrapolation follow the maxima of the stability landscape feature referred as the ridge according to (Virot et al., 2017). In figure 5.4 the extrapolation curves predict the buckling load of the cylindrical shell. The deviation between the different predicted buckling loads and the actual ones is below 1%. As a side note, the influence of the hole in the local stiffness becomes significant as the hole size grows. In the case of the smallest two hole sizes, 0.8mm and 1mm, the local stiffness sensed by the poker does not change through the extrapolation curve.

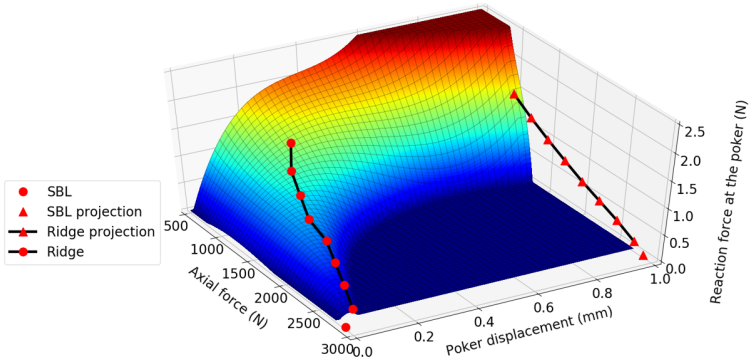

(a) Stability landscape for
a perfect shell with hole of 0.8 mm

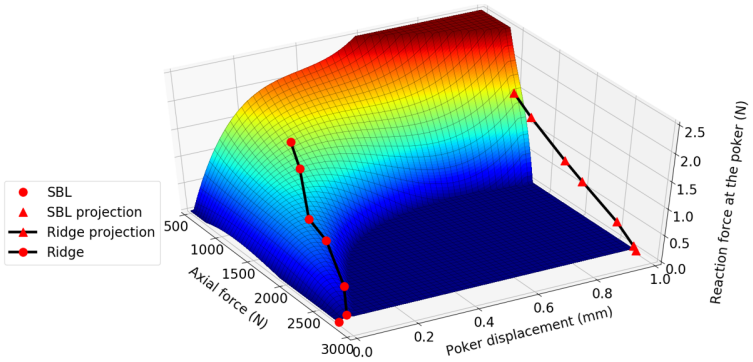

(b) Stability landscape for
a perfect shell with hole of 1 mm

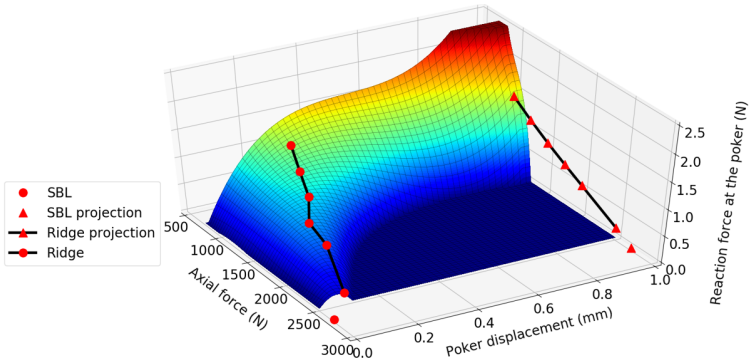

(c) Stability landscape for
a perfect shell with hole of 1.2 mm

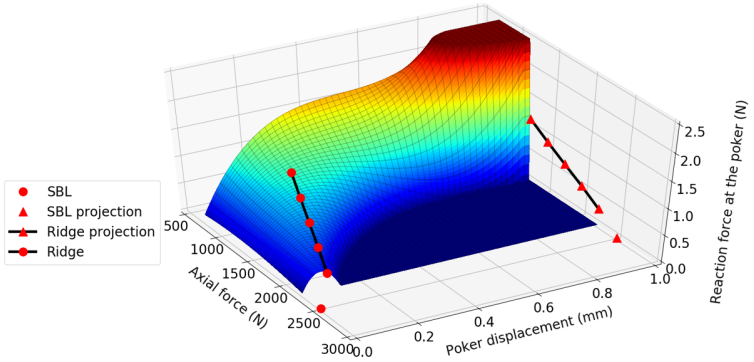

(d) Stability landscape for
a perfect shell with hole of 1.6 mm

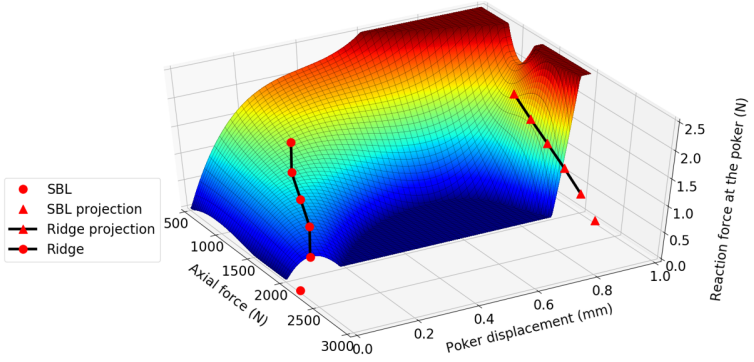

(e) Stability landscape for
a perfect shell with hole of 2.4 mm

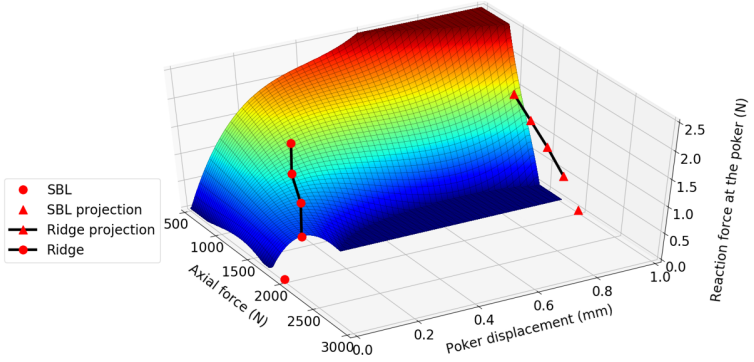

(f) Stability landscape for
a perfect shell with hole of 3.2 mm

Figure 5.3 – Numerically derived stability landscapes for the geometry of $7.5oz.$ coke can containing a hole of different sizes. The poking location for the construction of the different stability landscapes is located 5mm below the hole. Note how the maximum of the ridge decreases as the axial load increases enabling the extrapolation for the buckling load of each cylindrical shell. The X axis represents the compression load applied (F_A). The Y axis represents the distance the poker has moved in contact with the shell (D_p). The Z axis represents the reaction force exerted by the cylindrical shell on the poker as the poker moves radially (F_p).

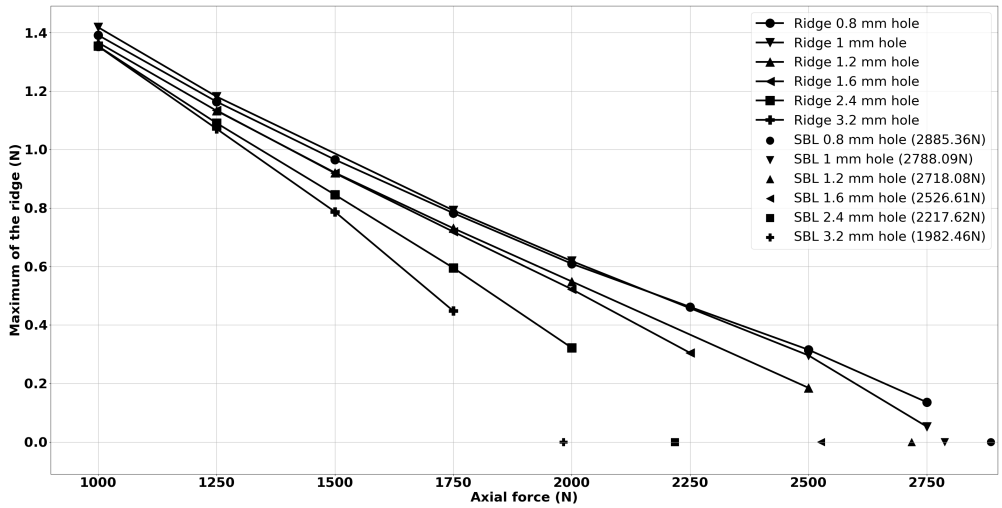

Figure 5.4 – Extrapolation results for a cylindrical shell with a hole of different sizes and no additional background imperfections. The boundary conditions in the cylindrical shell are fully clamped with the exception of the axial degree of freedom at the opt that is left free to allow the loading to take place. The buckling loads predicted via extrapolation in all the cases are accurate. The criteria used to accept a prediction as accurate is to present a deviation below 5%

Conclusions

Stability landscapes derived numerically can provide an accurate prediction of the maximum load bearing capability of a perfect cylindrical shell with a localized imperfection. This has been verified for the case in which a localized engineered imperfection in the form of a hole is the only imperfection. Similar results have been reported in the case of spherical shells (Abbasi et al., 2021).

5.2 Predictions via experimentally obtained stability landscapes

In section 5.1 the suitability of stability landscapes to extrapolate to the buckling load of a cylindrical shell was shown in a set of *in silico* experiments. In this section the aim is to replicate the same procedure but with real cylindrical shells experimentally. The experimental work in this research is oriented towards performing a series of test campaigns to demonstrate how stability landscapes if used at the right location of a cylindrical shell are able to predict buckling as shown numerically in section 5.1.

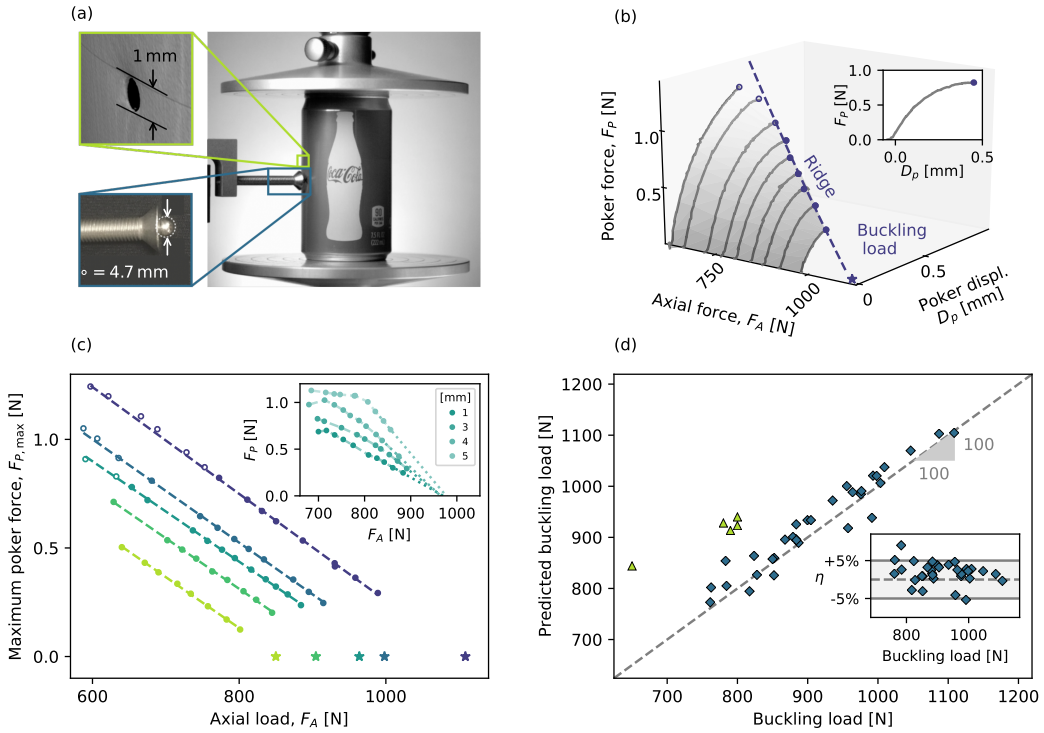

Figure 5.5 – Summary of the results published in Abramian et al. (2020) where the work from the current research was included. Sub-figure (a) described the configuration of the poking experiments. Sub-figure (b) shows the creation of a so-called ridge. Sub-figure (c) shows ridges for shells with nominally identical geometry but different background imperfections. Sub-figure (d) shows a summary of all the data.

The experiments were performed using the same set up described in chapter 4. It employs an uni-axial ADMET machine with the addition of a new feature: a radial actuator. This radial actuator has a force measurement set up at the tip. This force measuring set up is composed by a round poker that comes in contact with the cylindrical shell and a force sensor in the form of a S-type load cell. The poker is used to probe the cylindrical shells via a prescribed radial displacement.The force readings from the load cell are used to build the poking curves that compose the stability landscapes. A close image of the poker can be seen in the top left part of figure 5.5.

The experimental work of this chapter is divided in three test campaigns. A first one where the idea of predicting buckling load with stability landscapes was tested. A second more extensive campaign was carries out to clarify the influence of using a dimpled hole instead of a hole as localized imperfection. A third campaign was conducted to study the complete area around the localized imperfection to understand the buckling load predictive capability of stability landscapes.

5.2.1 1st Test campaign: Stability landscapes of dimpled holes

The configuration selected for the cylindrical shell corresponds, as in the previous chapter, to the $7.5oz.$ coke can present in the American market. These cylindrical shells have a straight section that is 107 mm long. The wall thickness of the straight section of the shell is 0.105 mm and the radius is 28.6 mm. The cylindrical shells contain a localized imperfection in the shape of a 1 mm hole, placed in the middle of the straight section. The probing of the cylindrical shell is done $5mm$ below the center of this hole.

The dimension of 1 mm for the hole diameter was selected so the average buckling load of shells remained unaffected while providing a location for a relevant noticeable imperfection. The fact that a 1 mm hole will not affect the average buckling load was obtained experimentally in chapter 4.

The results obtained in this test campaign are presented in figure 5.5. In a high percentage, the tests were successful (Deviation smaller than 5 % between prediction and actual buckling load), meaning that the buckling load of the corresponding cylindrical shell could be predicted accurately. On the opposite side, there were a few experiments that provided wrong extrapolations of the actual buckling load. These experiments that provided wrong predictions are considered failures. Hence based on these definitions, it is possible to specify a success rate via dividing the number of successful tests by the total number of experiments that yielded a buckling load prediction. In the number of experiments that yielded a buckling load prediction are included the correct predictions and the wrong predictions.

The fact that there was a high success rate in predicting the actual buckling load of cylindrical shells was not unexpected. In fact, the prediction based on the dynamical system theory and the finite element models predicted that this would be the case. Furthermore, looking at how the imperfections of real shells look like (See figure 5.6), the relevance and presence of the hole is evident. The hole is located at the central blue dot that appears in all the cylindrical shells from figure 5.6. The area covered by the hole and the deviation suggest that although the hole was selected because of the single parameter nature of its morphology, its implementation was more complex than that.

In reality the creation of the hole induced a dimple of a size considerably larger than the intended 1 mm diameter of the hole. Hence, in this case the induced defect need to be considered a dimpled hole and not a simple hole at location. This imperfection is a more relevant, stronger imperfection than the bare hole and it is believed to have an impact in the predictions provided by the stability landscapes created in its vicinity. This last fact will be tackled in the next section.

Specimen ID	**Buckling load** (N)	**Buckling load prediction (N)**	**Deviation** (N/%)	**Accurate prediction** ✓ / ✗
Can №1	761	773	12/1.62	✓
Can №2	762	803	40/5.27	✓

Can №3	783	854	71/9.00	✓
Can №4	785	805	20/2.56	✓
Can №5	817	794	22/2.74	✓
Can №6	828	826	2/0.29	✓
Can №7	824	863	40/4.83	✓
Can №8	852	825	27/3.21	✓
Can №9	849	858	8/0.95	✓
Can №10	853	861	8/0.96	✓
Can №11	868	895	27/3.13	✓
Can №12	884	895	11/1.22	✓
Can №13	879	901	21/2.44	✓
Can №14	888	889	2/0.18	✓
Can №15	884	924	40/4.53	✓
Can №16	905	934	28/3.13	✓
Can №17	900	934	34/3.75	✓
Can №18	936	971	35/3.75	✓
Can №19	958	918	39/4.10	✓
Can №20	956	999	43/4.47	✓
Can №21	965	988	22/2.30	✓
Can №22	978	990	12/1.26	✓
Can №23	977	984	7/0.74	✓
Can №24	992	938	54/5.45	✓
Can №25	1004	1006	2/0.22	✓
Can №26	999	1029	20/2.05	✓
Can №27	993	1020	27/2.73	✓
Can №28	1010	1037	27/2.69	✓
Can №29	1047	1070	22/2.15	✓
Can №30	1088	1002	14/1.32	✓
Can №31	1109	1005	4/0.39	✓
Can №32	649	842	193/29.68	✗
Can №33	780	925	145/18.61	✗
Can №34	790	910	120/15.16	✗
Can №35	800	920	120/14.96	✗
Can №36	801	940	139/17.34	✗

Table 5.1 – Buckling load of the poking experiments carried out with a hole of $1mm$ and the additionally induced dimple from the drilling process. This work was performed as a part of the current research and was published in Abramian et al. (2020)

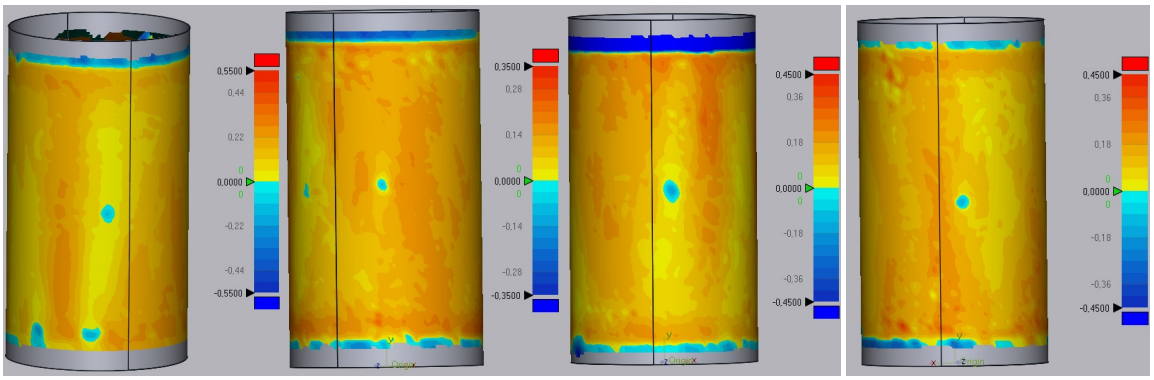

(a) Scan of specimen A

(b) Scan of specimen B

(c) Scan of specimen C

(d) Scan of specimen D

Figure 5.6 – Deviation from the ideal geometry present in real shells. The contour plots show the complexity of the imperfections present in shells. The shell are nominally identical however the deviations in the form of imperfections makes them unique. The maximum deviations are in the order of 2 to 3 times the thickness of the shell, $0.105mm$

Note that in the case where the landscapes were built around a dimpled hole there was a high success rate regarding the capability to predict buckling of cylindrical shell. The success rate achieved is approximately 86%. This success rate is defined as the ratio between the test that predicted the buckling load of cylindrical shells correctly and the total number of test expressed in percentage form. The data from this test campaign is summarized in table 5.1.

The high rate of success achieved in this first experimental test campaign was a strong evidence of the capability of stability landscapes to predict buckling loads of cylindrical shells in a non-destructive manner. However, the cases where the extrapolation provided an inaccurate prediction were not expected. In fact, according to the numerical models and the dynamical system-based theoretical prediction, the extrapolation should always provide an accurate estimation of the buckling load at the vanishing point of the stability landscape. The reason for this is the fact that a stability landscape always has an axial load where it vanishes. In fact, the success rate in the numerical model used to extrapolate the buckling load of cylindrical shells with a hole is 100% as it can be seen in figure 5.4.

5.2.2 2nd Test campaign: Stability landscapes of flat holes

Initially, high success rates of the prediction observed in preliminary studies described in section 5.2.1 could not be reproduced. It was eventually found that undocumented details on the hole drilling procedure had significant relevance. A second test campaign was carried out including carefully drilled holes instead of the dimpled ones used in the fist test campaign. In this second test campaign no dimple was induced during the drilling process because the drilling technique did not use pressure but very high rotational speed of the drill bit for drilling

the hole. The results from this second test campaign showed a lower success rate than those from the first campaign. The success rate dropped to 25% from the 86% obtained in the first test campaign. The reason for the variation in the success rate is thought to be the change of morphology between imperfections from dimpled holes to bare holes.

The results from this second test campaign are presented in table 5.2. In table 5.2 the dashed rows refers to poking experiments where the specimen failed before poking started. These specimens are not considered as a part of the population to define the success rate of the test campaign. Only specimens where a prediction of the buckling load was obtained are used to define the success rate.

Specimen ID	**Buckling load** (N)	**Buckling load prediction (N)**	**Deviation** (N/%)	**Accurate prediction** ✓ / ✗
C11906	944	1045	101/10.70	✓
C21906	1089	1494	405/37.19	✗
C31906	851	1112	261/30.67	✗
C41906	873	2814	1941/222.34	✗
C51906	1018	1651	633/62.18	✗
C61906	840	871	31/3.69	✓
C71906	910	2043	1133/124.51	✗
C81906	-	-	-	-
C12906	864	1305	441/51.04	✗
C22906	949	1162	213/22.44	✗
C32906	-	-	-	-
C42906	1005	1077	31/3.69	✓
C52906	820	1354	534/65.12	✗
C62906	-	-	-	-
C10907	1005	1077	72/7.16	✓
C20907	928	1034	106/11.42	✗
C30907	800	1354	554/69.25	✗
C40907	872	1005	133/15.25	✗
C50907	872	1598	726/83.26	✗
C60907	930	1226	296/31.83	✗
C11007	930	1069	139/14.95	✗
C21007	862	929	67/7.77	✓
C31007	-	-	-	-
C41007	803	1059	256/31.88	✗
C21307	864	1306	442/51.16	✗
C31307	905	1049	144/15.91	✗
C41307	1005	1077	72/7.16	✓
C51307	-	-	-	-
C61307	820	1354	534/65.12	✗
C11307	-	-	-	-

C21307	949	992	43/4.53	✓
C31307	-	-	-	-
C41307	864	1304	440/50.93	✗
C11607	-	-	-	-
C21607	-	-	-	-
C31607	-	-	-	-
C41607	858	1184	326/38.00	✗
C51607	-	-	-	-
C61607	-	-	-	-
C71607	916	991	75/8.19	✓
C81607	-	-	-	-
C91607	-	-	-	-
C101607	-	-	-	-
C121607	830	1091	261/31.45	✗
C121607	-	-	-	-
C131607	-	-	-	-
C141607	-	-	-	-
C11707	801	829	28/3.50	✓
C21707	-	-	-	-
C31707	929	976	57/5.06	✓
C41707	912	949	37/4.06	✗
C51707	-	-	-	-
C61707	845	943	98/11.60	✗
C71707	817	904	87/10.65	✓
C81707	-	-	-	-
C91707	-	-	-	-
C101707	-	-	-	-
C121707	-	-	-	-
C121707	-	-	-	-
C131707	1148	1269	121/10.54	✓
C141707	-	-	-	-
C101707	858	872	14/1.63	✓
C121707	833	1092	259/31.09	✗
C121707	815	972	157/19.26	✗
C131707	1000	1103	103/10.30	✗
C141707	-	-	-	-

Table 5.2 – Buckling loads and prediction of experiments carried out with carefully drilled holes with a $1mm$ diameter.

5.2.3 3rd Test campaign: The effect of distance in stability landscapes

The difference between a carefully drilled hole and a dimpled hole is their morphology. The geometry of both imperfections is different. However, under the visual inspection that each specimen of the different test campaigns underwent, the difference between imperfections, although noticeable, is only evident for a trained eye. In fact it is very striking that such a small difference has such a relevant impact in the results. This small difference in the imperfection realization shifted the success rate from 86% in the case of the dimpled hole (1^{st} test campaign) to 25% in the case of the carefully drilled or flat hole (2^{nd} test campaign). This is an evidence of how sensitive cylindrical shells are to small variations in their geometry.

The cases where the extrapolation did not provide an accurate prediction of the buckling load contradicts the behaviour predicted by the numerical models and the prediction of the dynamical systems theory model of the cylindrical shell. The theory says that the value of axial compression where the stability landscape vanishes marks the maximum compression load a cylindrical shell can bear. The main difference between these ideal models and the experiments is the existence of background long range imperfections. Hence, the research effort is directed towards understanding the influence of the long range background imperfections in the buckling load predicted by stability landscapes. This is done by sampling a grid of points around the local imperfection. The sampling of a grid of points around the local imperfection intends to show the variability in buckling loads as the distance from the local imperfection varies.

In order to understand further what makes the extrapolation work only for some cases, the best strategy was considered to be gathering more information around the probing locations as mentioned before. This is considered the most suitable strategy because extracting more landscapes at different spacial locations around the localized imperfection will show the dependency of the quality of the predictions as a function of the distance to the imperfection. Considering these details, the subsequent experimental campaign consisted of constructing stability landscapes in locations around the dimpled hole and attempt to understand how the extrapolations of the ridges of the stability landscape change around such a defect. This kind of experiment is only possible due to the non-destructive nature of the stability landscapes.

Motivated by the higher success rate of the dimpled hole, this configuration was selected to uncover why the extrapolation based on ridges works in some cases and does not in others. The testing procedure to build the different landscapes around the dimpled hole consisted of varying the axial and azimuthal coordinates to create a grid of locations where the buckling load was predicted. In each of these locations, a poking curve was extracted before the load was increased. Meaning that a mapping of the complete grid for each load increment was done before moving to the next increment of axial load. The maximum applied load was limited by the moment where a poking force lower than $0.2N$ was reached. This is a limit set based on the experience in the different test campaigns.

In practice, the sampling at multiple locations was done with an automatic rotating stage

that allowed for controlling the azimuthal location of the probing. The axial position was controlled with metallic shims placed below the shell to control the relative axial position of the local imperfection and the probing device. The utilization of shims to control the relative distance between the probing location and the localized imperfection meant that only locations below the localized imperfections could be explored. However, due to symmetry reasons an identical behaviour can be expected in locations placed symmetrically above the localized imperfection. The variation at symmetric locations was only performed in the azimuthal coordinate. The azimuthal coordinate locations to the right and left of the localized imperfection were explored.

The area of the shell where the grid for the procedure was implemented is represented by a cylindrical sector. This sector corresponds to a section of the shell covering 112° in the azimuthal coordinate with the hole centered in it and a 5 mmm length in the axial coordinate. The grid density is 13 points in the azimuthal direction and 4 in the axial direction. In the case of the azimuthal direction, the density is not homogeneous, with additional locations in the vicinity of the holes. Axially the are 4 locations evenly spaced. The exact locations are $-44°, -33°, -22°, -11°, -5°, 0°, 5°, 11°, 22°, 33°, 44°$ azimuthally and 2 mm, 3 mm, 4 mm and 5 mm axially. The data obtained in the different test is summarized in figures 5.7, 5.11, 5.15 and 5.19.

The tests were carried out with different 7.5oz coke cans, with a total population of 23 shells. Out of these test articles, only 4 survived the complete procedure. The other 19 failed at compression load increments.

In the 4 cases (Specimen A, B, C and D) that endured the complete procedure, the buckling load was obtained with a final destructive compression testing. In this test campaign, the shells were scanned prior to testing. The aim of this observation was to try to discover a potential correlation between existing imperfections and quality of the prediction. Figure 5.6 shows the scans of 4 cylindrical section of the coke cans with a dimpled hole that endured the complete testing sequence.

3rd test campaign: Specimen A

The data obtained in the case of specimen A shows a wide spread of values in the extrapolations provided by the different ridges. As the vertical distance increases, the extrapolation provided by all the ridges becomes less accurate. An additional trend in the data from specimen A seems to be that the further away from the dimpled hole in the azimuthal direction, the lower the accuracy of the buckling load prediction.

Figure 5.8 represents a map of the relative error of each extrapolation provided by the different ridges. In this figure, the general trends pointed out earlier remain true although there are exceptions where ridges constructed far away from the localized imperfection provide an accurate prediction. This behaviour suggests that there is not a perfect correlation between

distance to the hole and accuracy in the prediction.

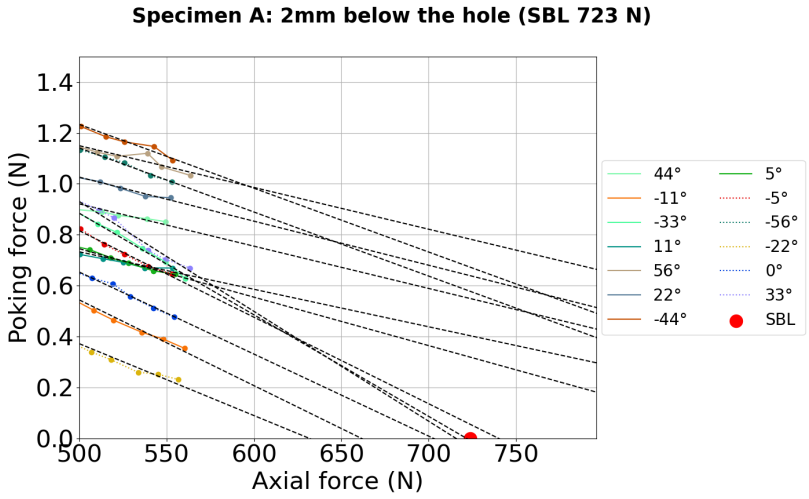

(a) Ridges for axial location 2 mm below the hole

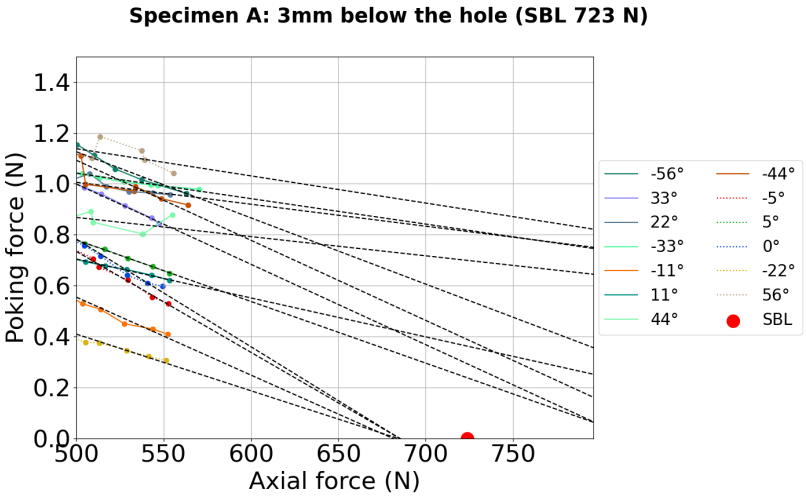

(b) Ridges for axial location 3 mm below the hole

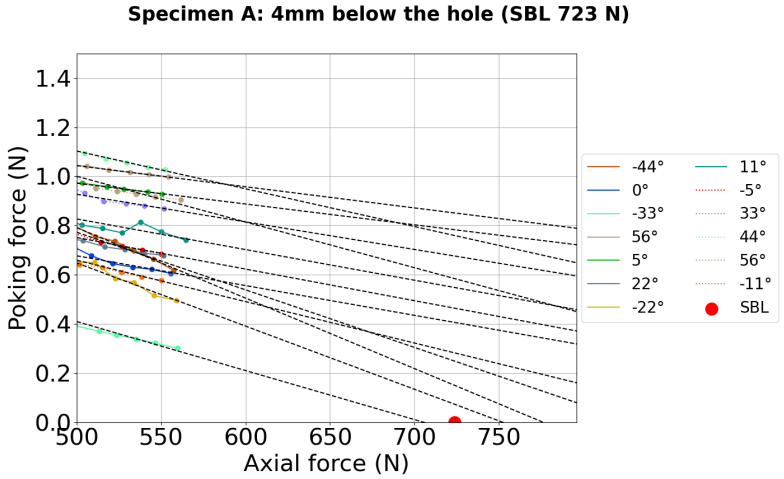

(c) Ridges for axial location 4 mm below the hole

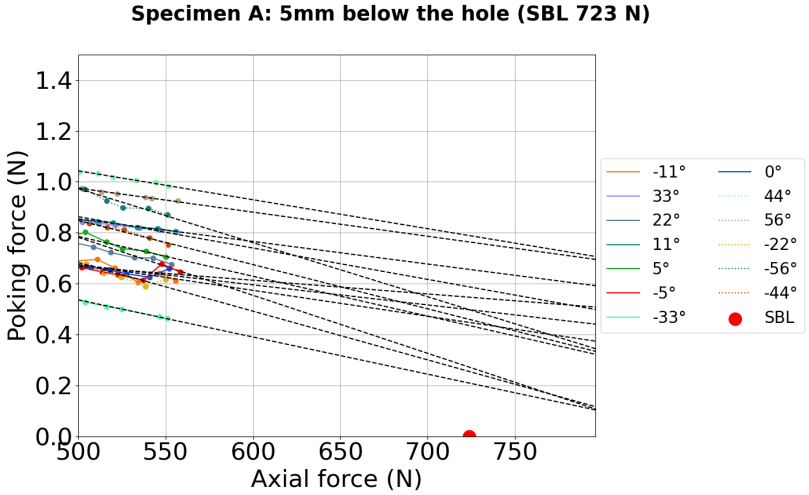

(d) Ridges for axial location 5 mm below the hole

Figure 5.7 – Summary of the ridges obtained at different locations azimuthally and axially probed in specimen A

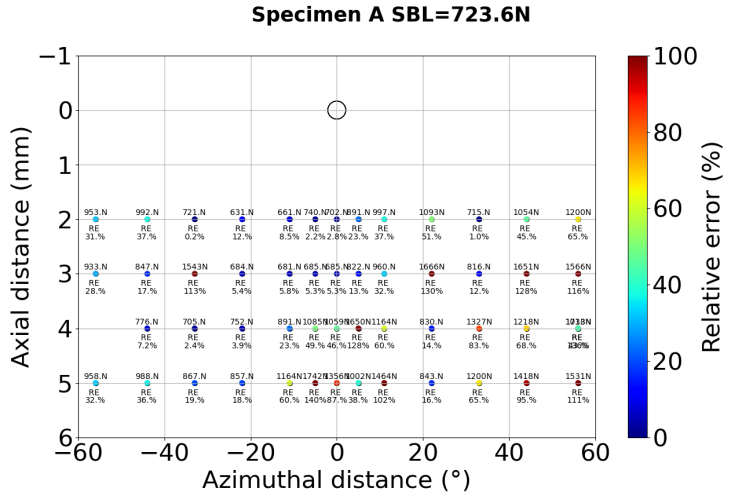

Figure 5.8 – Relative error maps for the different shells. The color coding is related to the accuracy of the prediction provided by the ridge derived at each specific location.

In order to show better the correlation between distance from the imperfection and accuracy of the prediction, the data from figure 5.8 was plotted as a function of the distance to the hole. Figure 5.9 shows this representation. In figure 5.9 there is not a clear evidence of the correlation between distance and accuracy of the prediction. There are accurate predictions far away from the localized imperfection as there are inaccurate predictions in the vicinity of the local imperfection.

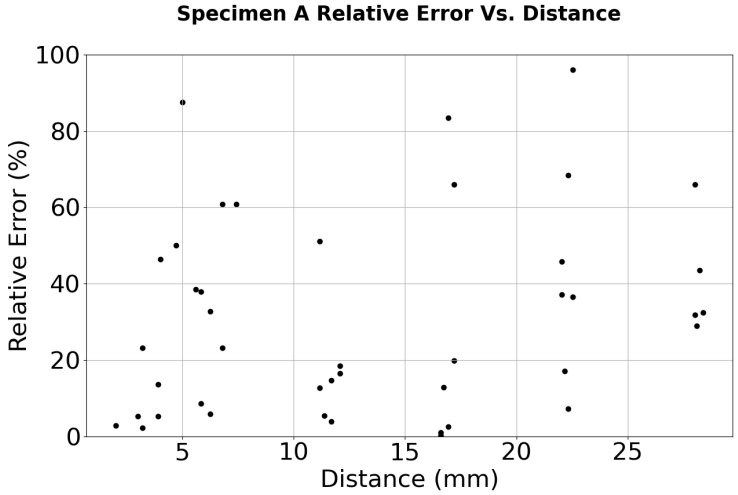

Figure 5.9 – Relative error of the buckling load prediction as a function of the distance to the dominant imperfection.

In the case of specimen A, only a few of the extrapolation curves in the vicinity of the imperfection provide an accurate approximation of the buckling load of the shell. Locations placed

at symmetrical azimuthal locations never provide the same extrapolation nor have the same stability landscapes as shown by their ridges. This is shown in figure 5.9.

The variability is a feature of the system and demonstrates first the influence of background imperfection and second the sensitivity of cylindrical shells to small variations in its geometry. The differences present in the ridges shows the wealth of information that a stability landscape encodes about each point of a cylindrical shell. In fact, it seems that each point in the shell has a very characteristic signature that makes each landscape unique for a combination of azimuthal and axial coordinates and compression load.

The end-shortening curve of specimen A displayed in figure 5.10 features a clear global buckling event at 723 N. Prior to the global event, there is a small drop in axial force at approximately 650 N. This local drop is linked to a local buckling event. The predictions from the extrapolations provided by the stability landscapes do not capture the local buckling event looking at the data summarized in figure 5.7. Only a single ridge provides an accurate estimation of the local buckling load in the case were the probing occurs 2 mm bellow the dimpled hole and $-22°$ away from it in the azimuthal direction. The slope in the ridges also shows a significant spread of values. The variation in the maximum forces reached by the ridges is very high for nominally identical compression loads.

A final remark about specimen A is that under the standard configuration of testing that provided a highly reliable load prediction (Single stability landscape constructed 5mm below the localized imperfection), the test of this shell would have provided a failed prediction. The load extrapolation for specimen A would have over-shot the real buckling load of the shell.

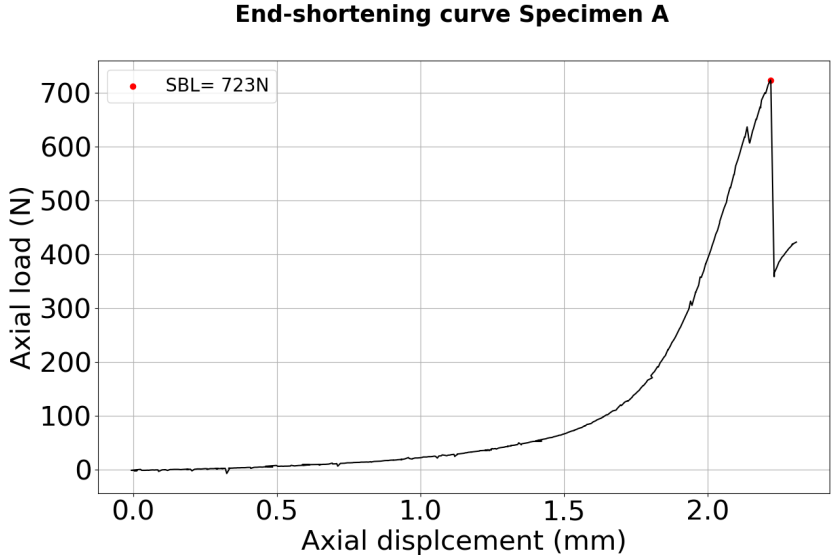

Figure 5.10 – End-shortening curve for specimen A. This specimen shows a local buckling event at 630 N before reaching the maximum compression force, the buckling load of this shell, of 723 N

3rd test campaign: Specimen B

Specimen B is the second shell that underwent the complete procedure. The obtained ridges are shown in figure 5.11.

The different extrapolation curves built based on the ridges from the individual landscapes of specimen B show a similar trend to the ones observed in the case of the specimen A. In both cases there seems to be a worse capability to predict the maximum load capability of a shell as the distance from a relevant imperfection grows. The slope in the ridges also seems to have a significant spread. However, in the case of Specimen B, the quality of the prediction is better. In the ridges of specimen B there seems to be two different clusters in the data. This is more clear in figures 5.12a to 5.11c, where one set of ridges extrapolate relatively well the buckling load while a second group predicts much higher buckling load values.

In the case of specimen B, a poking map summarising all the predictions and relative errors has been crated too. This second specimen features a stronger correlation with the distance to the defect when compared with specimen A. However, there are accurate predictions coming from ridges far away from the hole too. This becomes more evident in figure 5.13, where the relative error is plotted against the distance to the imperfection. Although in the case of specimen B the correlation between distance and accuracy of the prediction is better in comparison with specimen A, the correlation is not perfect. This is an additional evidence of the influence of the variable background imperfections.

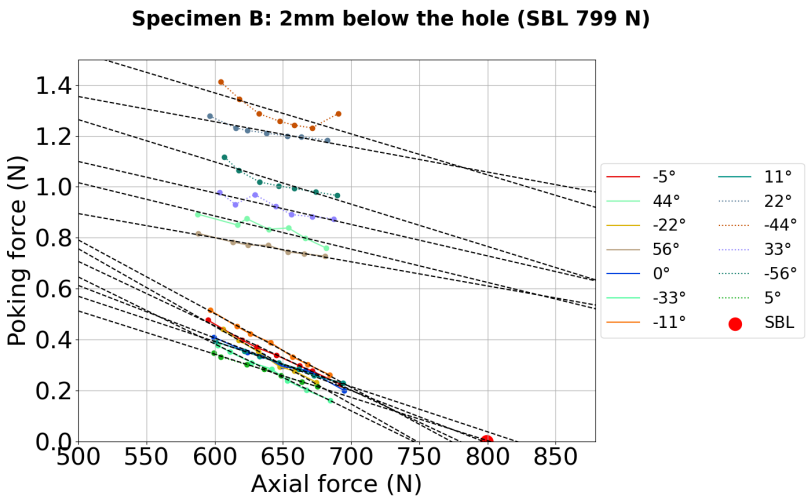

(a) Ridges for axial location 2 mm below the hole

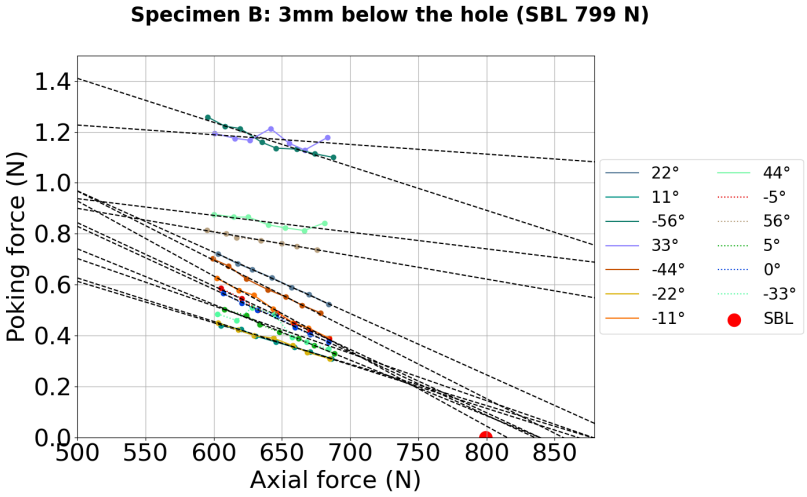

(b) Ridges for axial location 3 mm below the hole

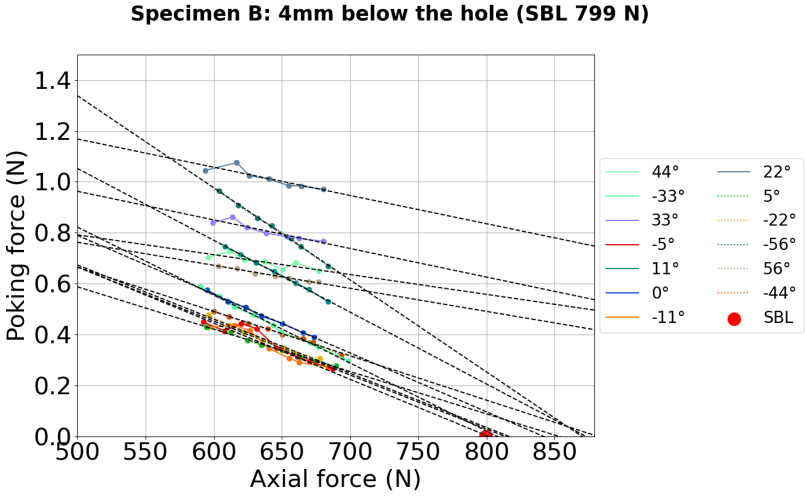

(c) Ridges for axial location 4 mm below the hole

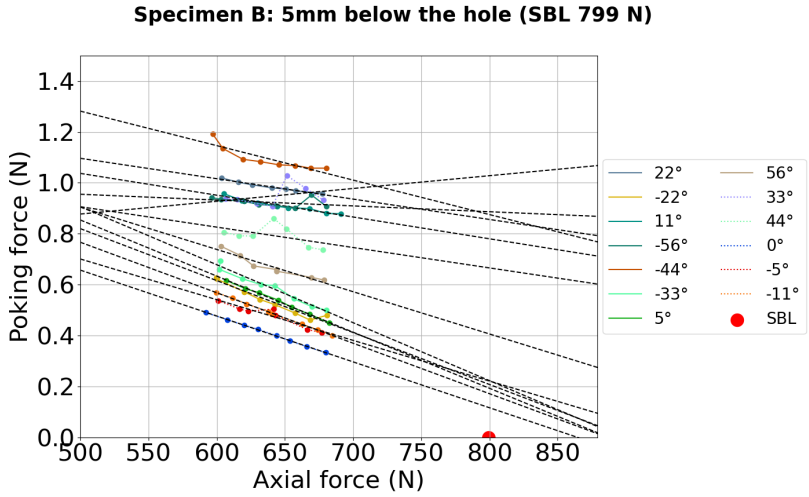

(d) Ridges for axial location 5 mm below the hole

Figure 5.11 – Summary of the ridges obtained at different locations azimuthally and axially probed in specimen B

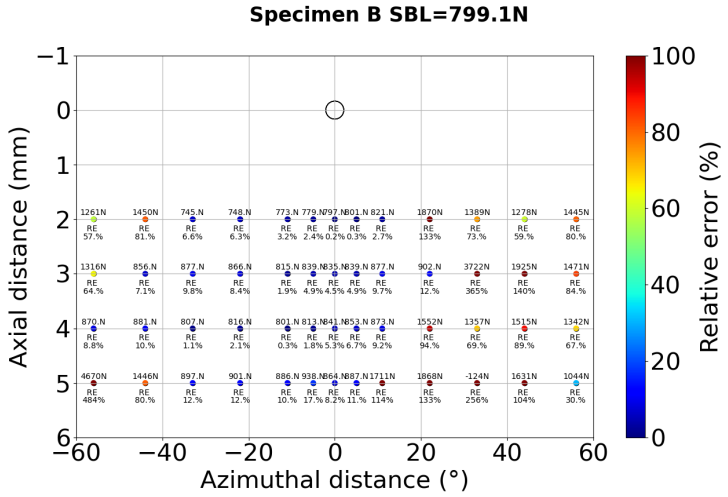

(e) Relative error map for can SH16b

Figure 5.12 – Relative error maps for the different shells. The color coding is related to the accuracy of the prediction provided by the ridge derived at each specific location.

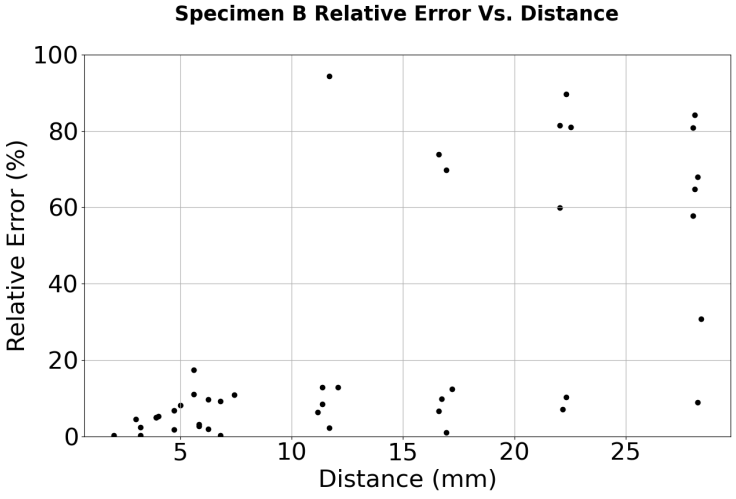

(a) Caption 2

Figure 5.13 – Poking maps for the different shells explored

The end-shortening curve presented in figure 5.14 for specimen B shows a clear global buckling event with no previous local buckling. In this case, the extrapolation of the buckling load for shell specimen B would have provided an accurate prediction under the nominal test conditions of a dimpled hole.

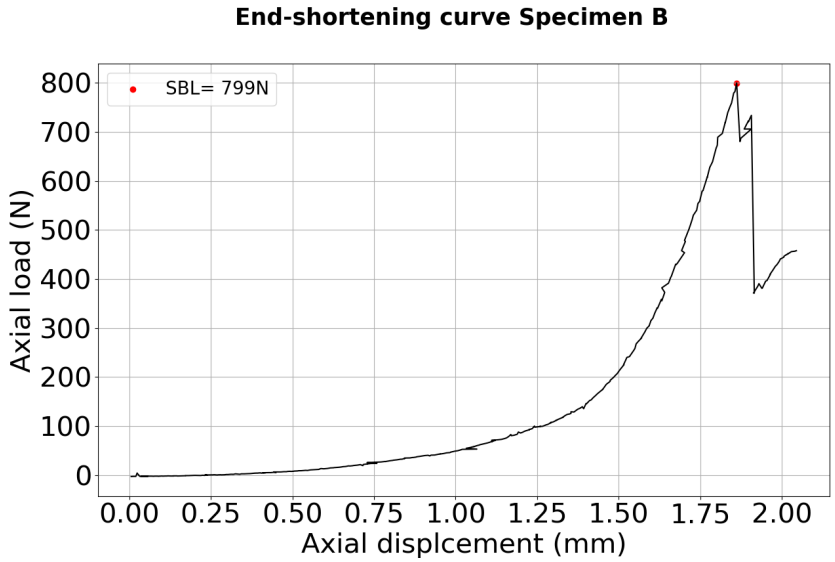

(a) End- shortening curve for specimen B

Figure 5.14 – End-shortening curve Specimen B

3rd test campaign: Specimen C

The third test article that underwent the test procedure completely was specimen C. The summary of the ridges constructed in the different locations is shown in figure 5.15.

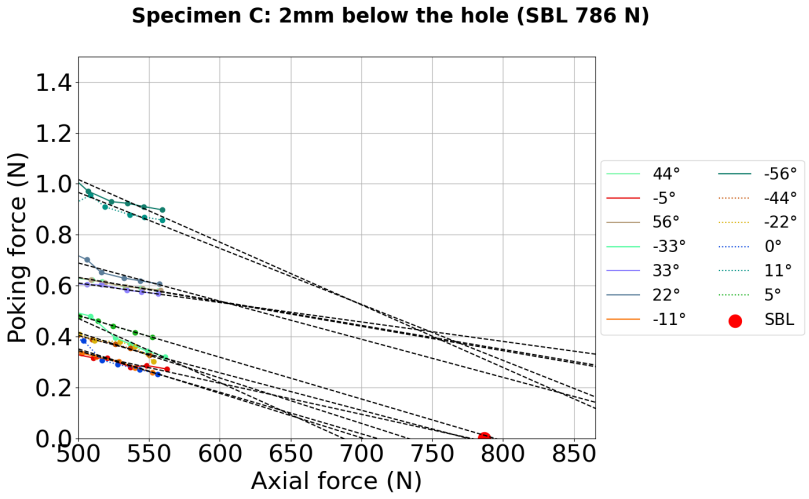

(a) Ridges for axial location 2 mm below the hole

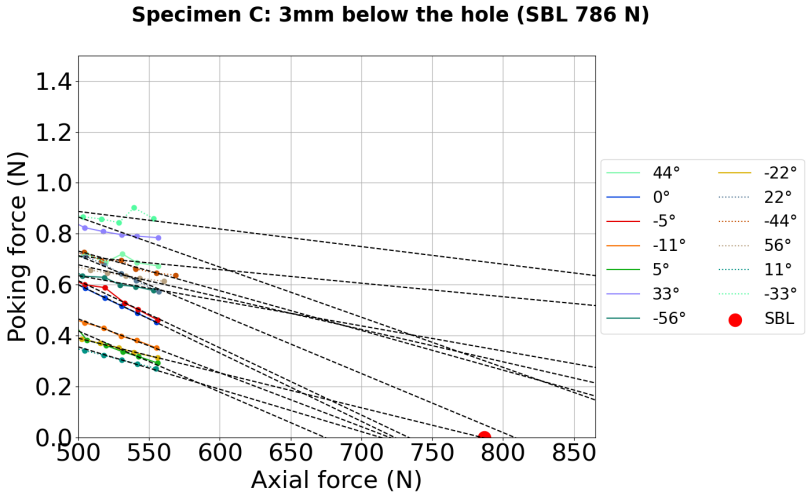

(b) Ridges for axial location 3 mm below the hole

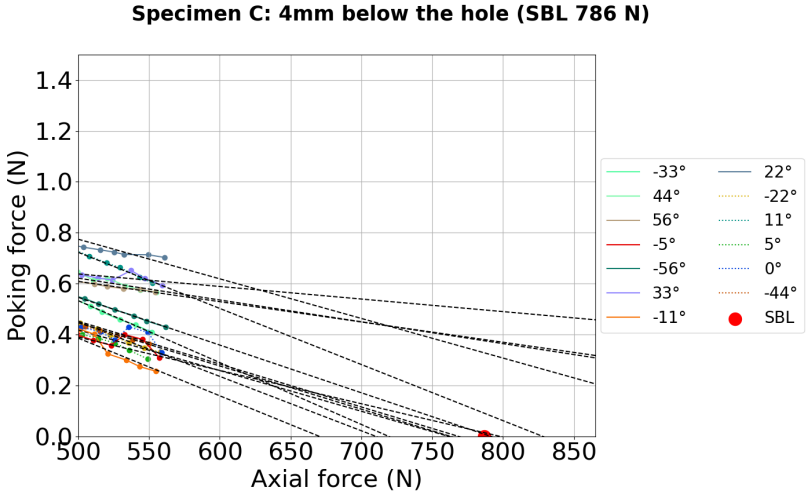

(c) Ridges for axial location 4 mm below the hole

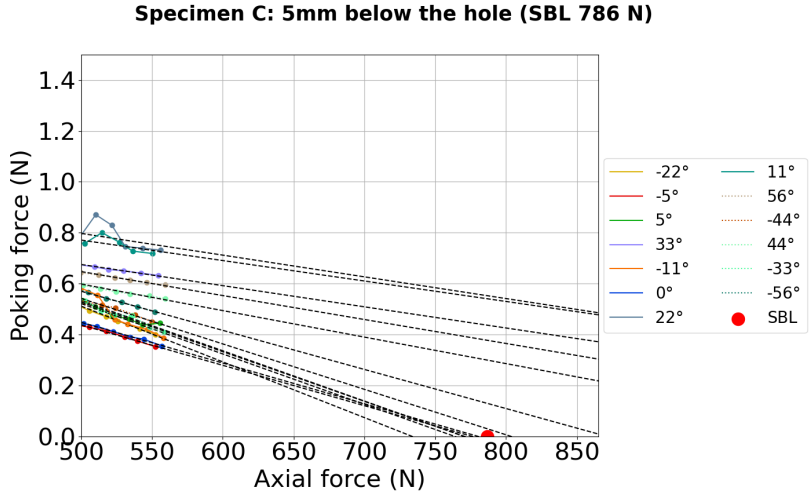

(d) Ridges for axial location 5 mm below the hole

Figure 5.15 – Summary of the ridges obtained at different locations azimuthally and axially probed in specimen C

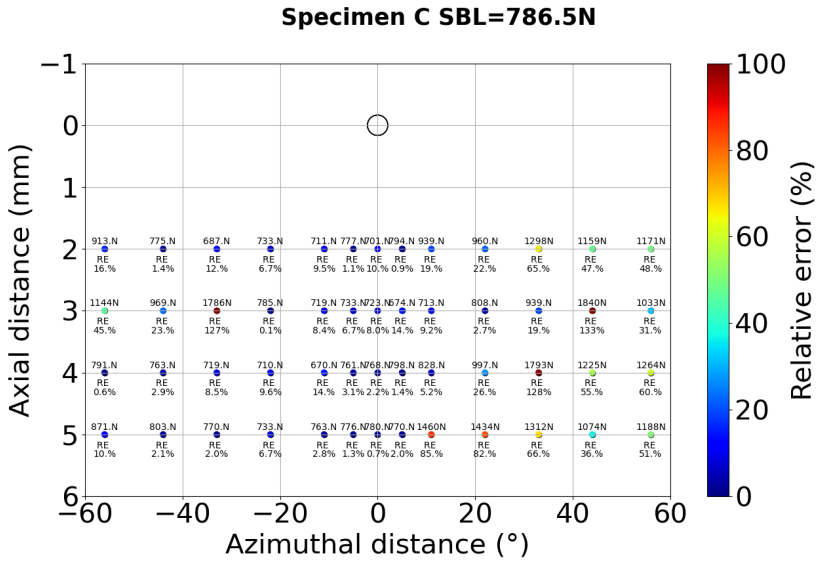

(e) Relative error map for can SH19b

Figure 5.16 – Relative error maps for specimen C. The color coding is related to the accuracy of the prediction provided by the ridge derived at each specific location.

The results from the probing data of specimen C show the same spread of extrapolations of the buckling load found in specimens A and B. The same trend related to the distance to the hole can also be observed in this case. The closer to the relevant imperfection, a hole in this case, the higher the probability to obtain a good approximation of the buckling load. Nevertheless, there also a small number of accurate predictions obtained away from the hole. The structure in the ridges of specimen C is closer to the structure in the ridges present in specimen A. i.e. there are not two distinct sets of ridges as it occurs with specimen B. The slopes of the ridges of specimen C show a similar variability to that found in the slopes of the ridges of specimen A.

The end-shortening curve of specimen C of the final destructive test presents a single drop in the axial force. This drop is associated the global buckling event. It is worthwhile noting the fact that there is no local buckling event previous to the final global one. This is a difference with respect to the behaviour observed for specimen A. This difference with respect to specimen A might be related to the fact that a significant number of ridges of specimen C predict a buckling load significantly lower than the one obtained in the final destructive test.

In the case of specimen C, a map summarising all the predictions has also been created. This map is displayed in figure 5.16. It becomes evident in this map that there are accurate predictions obtained far away from the localized imperfections as well as inaccurate ones that occur in the vicinity of the local imperfection. The lack of correlation between distance to the local imperfection and the quality of the prediction is shown more clearly in figure 5.17, where the relative error of the prediction is plotted as a function of the distance to the localized imperfection. The correlation between quality of the prediction and distance to the

local imperfection is more similar to the one shown by specimen A than by specimen B.

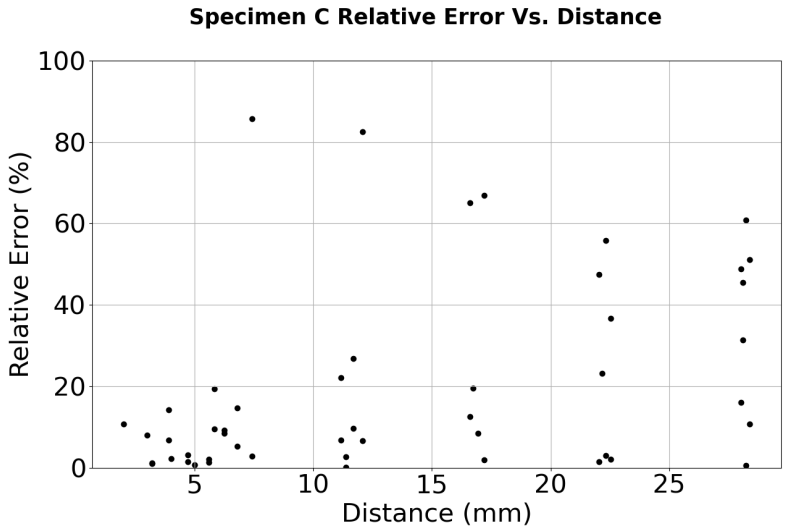

(a) Caption 2

Figure 5.17 – Poking maps for the different shells explored

In this case the testing of specimen C would have also provided a successful prediction of the buckling load of specimen C under the test procedure used in the 1^{st} and 2^{nd} test campaigns. The ridge obtained at 5 mm below the ridge and 0° delivered a very accurate prediction of the buckling load with a deviation of only 0.7% from the real buckling load.

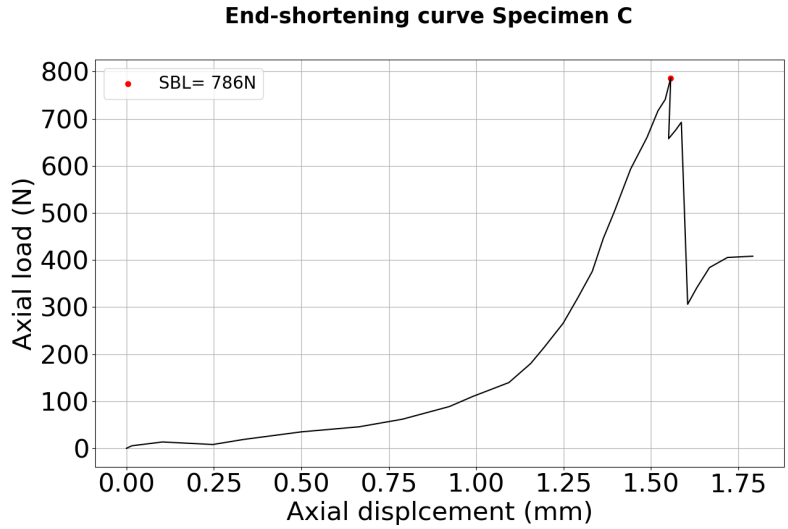

Figure 5.18 – End-shortening curve specimen C

Specimen C only presents a single drop in the end shortening curve as it can be observe in figure 5.18.

3rd test campaign: Specimen D

The fourth specimen that underwent the complete testing procedure is specimen D. In the case of this test article, the behaviour is very similar to the one featured by specimen B. There are two different clusters of ridges, which become evident in figures 5.20a, 5.20b and 5.19c. The first cluster interpolates to the right buckling load, while the second interpolates to a significantly higher one. Interestingly, the variation of the slope of the ridge as a function axial load is lower for the ridges that extrapolate to the wrong buckling load.

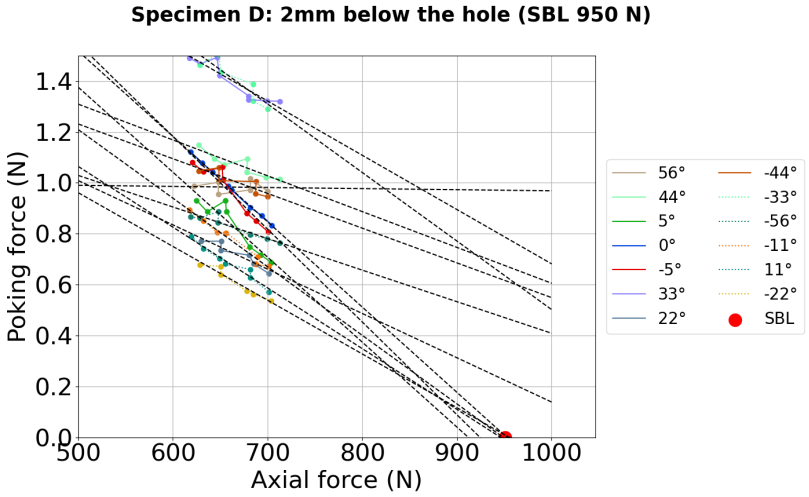

(a) Ridges for axial location 2 mm below the hole

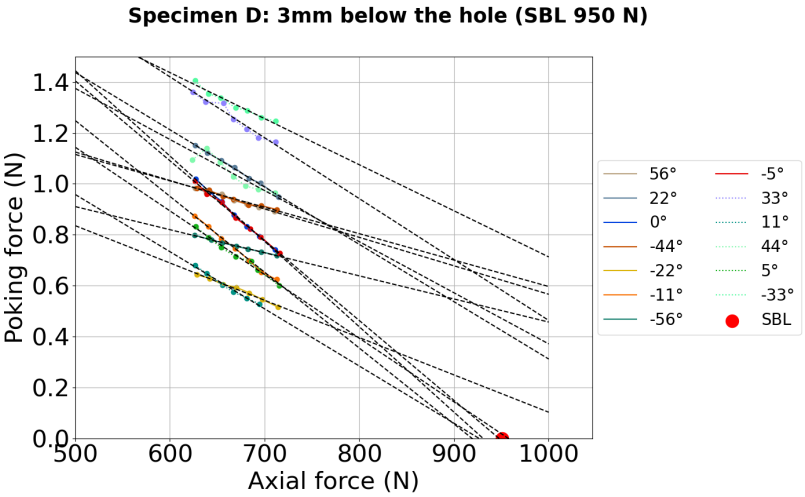

(b) Ridges for axial location 3 mm below the hole

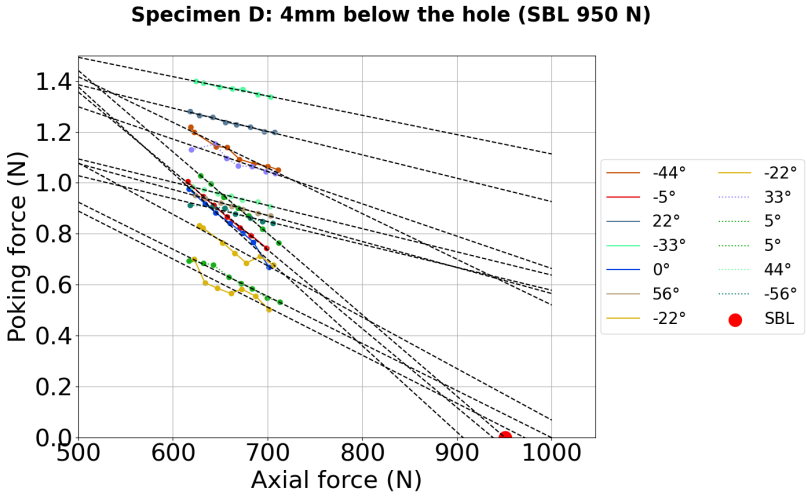

(c) Ridges for axial location 4 mm below the hole

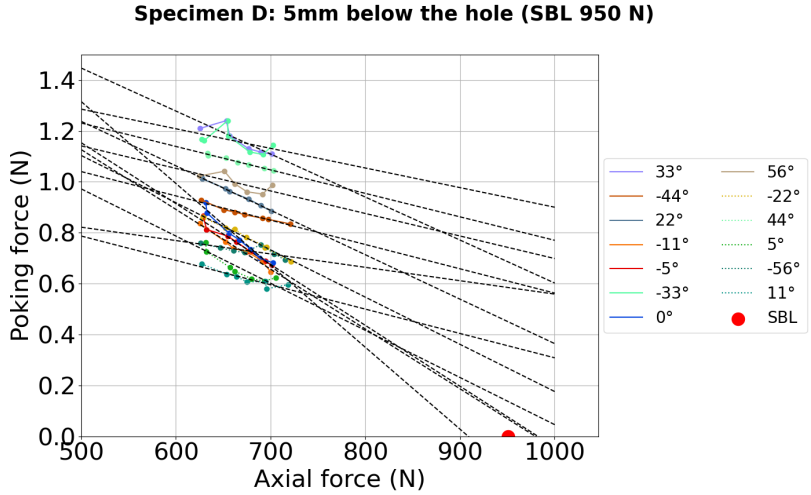

(d) Ridges for axial location 5 mm below the hole

Figure 5.19 – Summary of the ridges obtained at different locations azimuthally and axially probed in specimen D

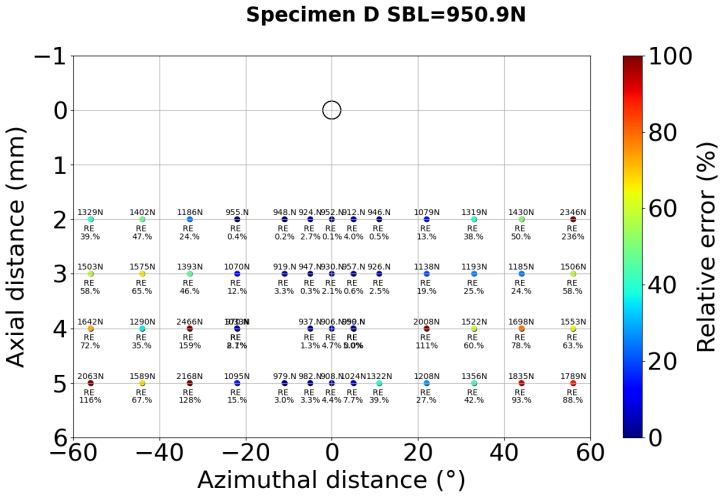

(e) Relative error map for can SH23

Figure 5.20 – Relative error maps for the different shells. The color coding is related to the accuracy of the prediction provided by the ridge derived at each specific location.

Specimen D has been included to show a third case where the standard testing procedure would have provided a good prediction. The standard procedure is the one were a single ridge was built 5 mm below the hole to extrapolate the buckling load of a shell.

Furthermore, in the case of specimen D there is better a correlation between distance to the local imperfection and the accuracy of the prediction. As for specimen B, a larger portion of the landscapes constructed near the local imperfections provide an accurate predictions when compared to specimen A. This decrease in accuracy for increasing distances to the imperfection occurring for specimen D can be assessed in the relative error map featured in figure 5.20.

Following the same approach as in the other specimens, the data from the relative error map has been plotted as an scatter graph. In this graph the relative error is plotted versus the distance to the local imperfection as shown in figure 5.21.

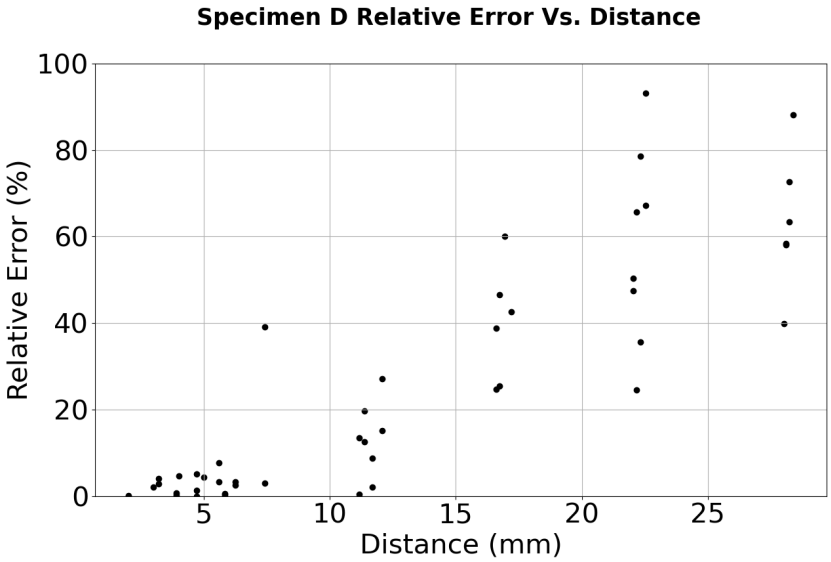

(a) Caption 2

Figure 5.21 – Relative error versus distance to the localized imperfection of the predictions of buckling load for specimen D.

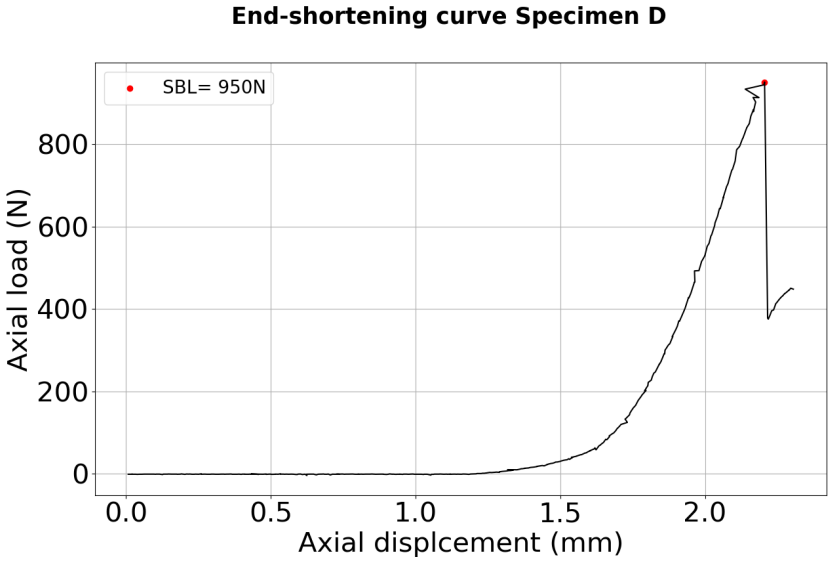

Figure 5.22 – End shortening curve for specimen D

Regarding the buckling behaviour of Specimen D, it is also characterised by a single global buckling event as shown in the end-shortening curve of figure 5.22

5.3 Conclusions

In the the current chapter a non-destructive method based on the construction of single stability landscapes was demonstrated numerically. The non-destructive methodology was tested in different test campaigns. It was found that the high success rate achieved in the numerical implementation was not achievable in experiments. The limitation of the methodology is linked to the reduced area sampled with the suggested non destructive testing methodology. Hence, an extension of the local probing technique of the current chapter is suggested for the next chapter. The suggested improvement consists in sampling multiple locations covering the complete shell.

5.3.1 Numerical predictions

Numerical-based stability landscapes are able to predict the buckling load of cylindrical shells with a hole of different sizes and no background imperfection. This finding opens new avenues for buckling research as it enables researchers to replicate complete test procedures of shells. Furthermore with the added value that an identical shell can be tested an infinite amount of times.

5.3.2 Experimental work: 1^{st} test campaign

Stability landscapes derived in the vicinity of a relevant local imperfection, a dimpled hole in this case, are able to predict the buckling load of a cylindrical shell with a high success rate (86%). Hence, stability landscapes revealed themselves as a useful tool to non-destructively test non-idealised cylindrical shells and predict their buckling load.

The fact that the success rate is not 100% means that the stability landscapes are a promising tool but it is not ready to be used as a reliable engineering tool to predict the buckling load of cylindrical shells.

5.3.3 Experimental work: 2^{nd} test campaign

In the 2^{nd} test campaign carefully drilled holes were used as local imperfections. In order to achieve more control in the implementation of the local imperfections the drilling technique was modified with respect to the technique used in the dimpled holes of the 1^{st} campaign. The key outcome from the the 2^{nd} test campaign is that the buckling predictions had a lower success rate 25% in comparison to the 86% obtained in the 1^{st} test campaign. Hence, the predictions provided by stability landscapes created at a location close to a weaker (Bare hole, 2^{nd} test campaign) localized imperfection have a lower predictive capability than the predictions arising from stability landscapes constructed close to s stronger local imperfection (Dimpled hole, 1^{st} test campaign) .

5.3.4 Experimental work: 3^{rd} test campaign

In the 3^{rd} test campaign it was observed that the relative error of the buckling load predictions as a function of the distance to the imperfection is not a monotonic function. There are accurate predictions of the buckling load that occur far away from the localized dominant imperfection as well as inaccurate ones obtained close to the imperfection.

Nevertheless, there is a higher density of accurate predictions in the vicinity of a dominant local imperfection imperfection.

6 Predicting buckling of imperfect cylindrical shells

The initial picture about the relevance of localised imperfections and local behaviour is more complex than anticipated in the case of real cylindrical shells. This has been made evident in the previous chapters, particularly in chapters 4 and 5. In chapter 4 it was shown that local and long range background imperfections can not and should not be disentangled. This fact makes the buckling load of a cylindrical shell a function of both kinds of imperfections. In chapter 5 the variations in accuracy of predictions around a dominant local imperfection and the varied success in predicting buckling showed that local imperfections play an important role but do not control buckling for every case.

This view where the buckling load of a cylindrical shell depends on the background and the local imperfections is not necessarily opposed to the experimental evidences about localisation shown in chapter 4. In fact, in the same chapter it was shown that local modifications of geometry can only modify the buckling process to a certain degree. The buckling load of cylindrical shells is affected by non-localised imperfections independently of the size of the local defect.

Furthermore, in chapter 5 it was shown that the local argument might not be as solid as claimed in Abramian et al. (2020). The buckling load predictions based on stability landscapes constructed at a proper location (near a dominant imperfection) are able to predict the spontaneous buckling load of a cylindrical shell with a very high degree of accuracy in most of the cases (Abramian et al., 2020; Virot et al., 2017). However, some cases still provided inaccurate predictions.

In the three experimental campaigns discussed in chapter 5, there were subsets of cases where the predictions of buckling loads delivered wrong values. The existence of these cases where stability landscapes provided inaccurate predictions forced us to investigate more deeply the phenomena occurring when a cylindrical shell undergoes a poking experiment. In essence, the aim would be to understand why the predictions work in some cases and do not work in others.

To that aim, a set of carefully controlled and monitored experiments would be the optimal tool. The experimental data from chapter 5, although very meaningful, required a large amount of samples and long testing periods. Hence, to be more time efficient and have access to carefully controlled and monitored experiments, the best approach is given by *in-silico* experiments. These experiments are similar to the ones from section 5.1.1, based on finite elements. In order to have meaningful *in-silico* experiments, a representative finite element model is required. It will be introduced in the next section.

6.1 Finite element analog of real cylindrical shells

This finite element model used in the present chapter includes realistic synthetic imperfections created following the approach to replicate real shell background imperfections presented in chapter 4. In addition to the background imperfection, a local one was introduced to have a geometrical configuration that resembled as much as possible the one of the shells experimentally tested, see chapter 5. Thus, a 1 mm diameter hole was used as a local imperfection and, around the hole, a 5 mm by 5 mm Gaussian dimple was introduced to replicate the geometry of the $1^s t$ test campaign of chapter 5. Hence, the final finite element model used in this chapter is a combination of the realistic model of the shell from chapter 4 and the model for the probing *in-silico* experiments of chapter 5. During the current research an Abaqus plug-in was created to automate the constructions of all the finite element models. The code can be found in appendix A.

In order to obtain a behaviour in the analog finite element model similar to that of the real test, a numerical study consisting of synthetic probing experiments of shells was carried out. In this *in-silico* experiments, a similar behaviour was obtained. i.e. in a subset of the specimens, the buckling loads were predicted accurately (specimens Ax in table 6.1), while in other cases the predictions were inaccurate (specimens Bx in table 6.1). A summary of these *in-silico* experiments can be seen in tables 6.1 and 6.2. The data presented in tables 6.1 and 6.2 is not the complete population of synthetic poking tests. The total population was 71 specimens, where only the 15 specimen A cases, shown in tables 6.1 and 6.2, provided successful predictions. Thus, the success rate was 21%.

The criteria to select this population of working predictions (specimens Ax) is to understand if there is a common factor between them. The smaller segment of the non-working ones (specimens Bx) are going to be used to find counter examples to challenge the hypotheses and try to explain why the predictions work or not work. The main outcome of the current research would be a non-destructive procedure to test cylindrical shells using stability landscapes. This procedure should ideally be based on one or several of the hypotheses formulated and tested in the upcoming sections provided their validity is confirmed.

Specimen ID	**Buckling load Displacement Control (N)**	**Buckling load Load Control (N)**	**Linear buckling prediction (N)**
Specimen A1	996	996	1067

Specimen A2	891	891	1102
Specimen A3	908	909	1035
Specimen A4	842	842	932
Specimen A5	832	832	830
Specimen A6	948	948	1180
Specimen A7	954	954	1087
Specimen A8	1192	1192	1648
Specimen A9	899	899	1134
Specimen A10	1007	1007	1259
Specimen A11	793	794	871
Specimen A12	829	829	900
Specimen A13	993	992	1201
Specimen A14	1071	1067	1152
Specimen A15	981	980	1074
Specimen B1	787	789	867
Specimen B2	826	825	819
Specimen B3	843	843	972
Specimen B4	728	729	757
Specimen B5	940	940	871

Table 6.1 – Buckling loads predicted by different methodologies. The values from the second column are derived via imposing an ever increasing compression force until the buckling point is reached. In the third column the axial compression is imposed via a displacement. In the last column the value correspond with the results of a linear stability analysis

Note that the linear buckling prediction using the unloaded state as a reference state provides a buckling load estimation that is larger than the real buckling load. However, there are cases where this does not happen. In the cases where the linear stability prediction under-predicts the buckling load, the end-shortening curves present a noticeable change of slope before the main collapse associate with the global buckling event. The slope of the end-shortening curves becomes smaller until the point of collapse is reached. This behaviour is in line with the explanation in chapter 3 about linear stability. Linear stability analysis around the unloaded base state is a good tool if the response of structure is linear. However, linear stability analysis breaks down or would need to use a reference base state closer to the maximum load to provide a reasonable prediction of the buckling load.

Specimen ID	**Buckling load** (N)	**Buckling load prediction (N)**	**Deviation** (N/%)	**Accurate prediction** ✓ / ✗
Specimen A1	996	1028	32/3.21	✓
Specimen A2	891	896	5/0.56	✓
Specimen A3	908	902	6/0.66	✓
Specimen A4	842	844	2/0.24	✓
Specimen A5	832	831	1/0.12	✓

Specimen A6	948	961	13/1.37	✓
Specimen A7	954	961	7/0.73	✓
Specimen A8	1192	1191	1/0.08	✓
Specimen A9	899	910	11/1.22	✓
Specimen A10	1007	1046	39/3.87	✓
Specimen A11	793	831	38/4.79	✓
Specimen A12	829	831	2/0.24	✓
Specimen A13	993	993	0/0.00	✓
Specimen A14	1071	1091	20/1.87	✓
Specimen A15	981	992	11/1.12	✓
Specimen B1	787	8095	7308/928.59	✗
Specimen B2	826	1500	674/81.60	✗
Specimen B3	843	∞	∞/–	✗
Specimen B4	728	1445	717/98.49	✗
Specimen B5	940	1180	240/25.53	✗

Table 6.2 – Buckling loads of the *in silico* experiments compared to the predicted values with the stability landscape extrapolations and the capability to accurately predict the maximum compression load the different cylindrical shells can carry. The success criteria to consider a prediction successful has been set to a maximum deviation of 5% between the prediction and the real buckling load. The ridges and extrapolations used in the prediction presented in this table can be seen in appendix B.

Considering the data presented in tables 6.1 and 6.2, the *in silico* experiments behave like the real experiments. Hence, the synthetic specimens are considered representative to explore the mechanism dictating why the buckling load prediction works in some cases and not in some other.

The current research has been done using the Abaqus commercial FE software. The utilization of this code allowed to access the different states of the shell and to operate with the radial displacement fields under different loading conditions. Hence, the utilization of the output from Abaqus was key to develop the framework used in this chapter to understand under which circumstances stability landscapes are able to provide accurate predictions of buckling loads. Furthermore, the capability to access different states of different analyses enabled the understanding of the contributions of the different loads to the radial deformation field that is used to characterise the state of the cylindrical shells under study.

The approach to find the mechanism behind successful predictions is based on proving or refuting a set of hypotheses based on observations of the synthetic experimental data. The main observable of the experimental data is the radial displacement at different stages of the *in silico* experiments. Using the radial displacements at the different stages of tests and correlating it with different features of the stability landscape, the validity of each hypothesis is investigated. The different hypotheses are presented and investigated in sections 6.2 to 6.6.

6.2 Correlation between Probing location & Buckling Mode

The first hypothesis about why predictions of buckling loads are successful or not is the following one: If the stability landscape is built at the location where buckling starts, the prediction of the buckling load will be successful.

The traditional view about buckling initiation is that the location where the maximum displacements occurs is the point of nucleation, i.e. the location where buckling starts (Hilburger, 2012). However, the correct approach to define where the buckling process begins is the location where deformations occur once the maximum compression load is overcome, not at the maximum load. The approach to visualize this variation of displacements is to subtract the displacement field at the maximum compression load to the displacement field of the next equilibrium point. This results in a radial displacement field that shows the initial growth of the spacial structures of the buckling process, i.e. the buckling mode.

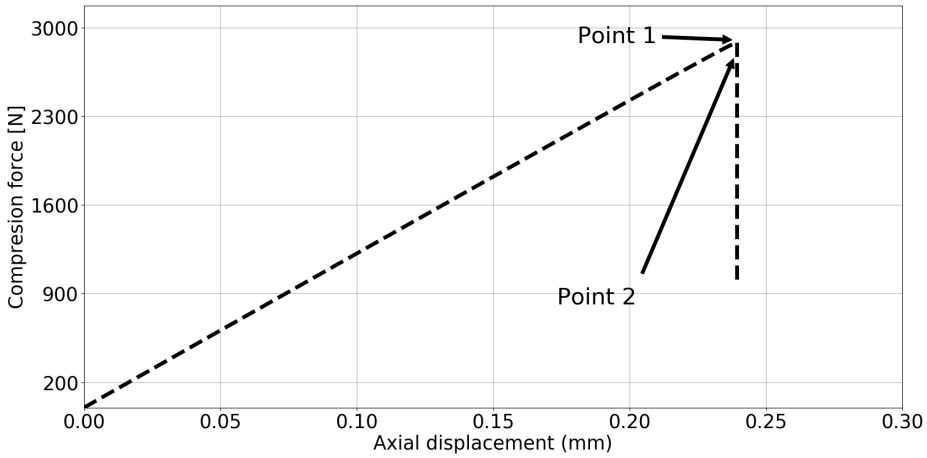

Figure 6.1 – Locations along the end shortening curve used for the construction of the buckling mode. At point the maximum compression load is reached and point 2 is the next converged step. The radial displacement at point 1 is subtracted from the radial displacement of point 2.

After defining the field that shows the buckling mode, it is important to verify that it remains independent of the loading strategy. This independence of the loading strategy is depicted in figure 6.2. In addition to this verification, one needs to introduce a normalization for the different fields so they can be compared. The field normalization selected is presented in section 6.2.1.

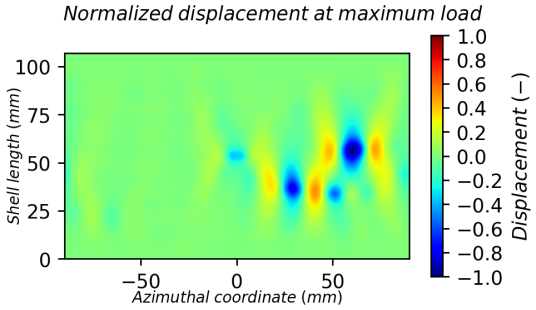

(a) Maximum radial displacement plot under load control conditions

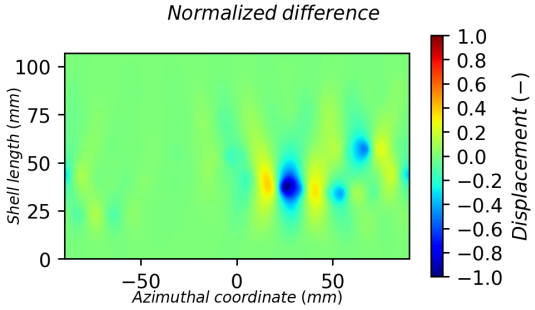

(b) $\hat{c}$ plot under load control conditions

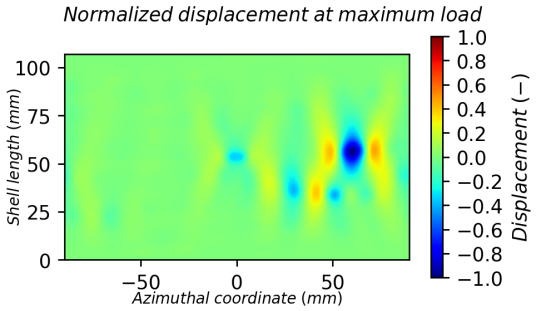

(c) Maximum radial displacement plot under displacement control conditions

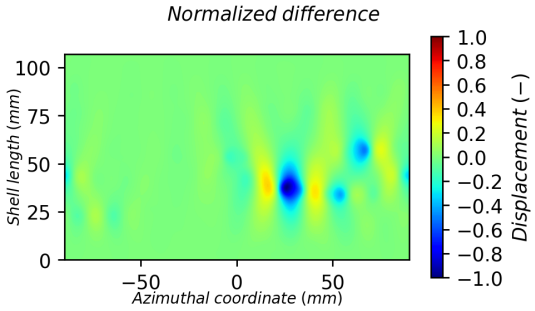

(d) $\hat{c}$ plot under load control conditions

Figure 6.2 – Radial displacement fields from the Specimen A5 shell showing that the maximum displacement fields and the buckling mode are identical for the two different loading strategies, load controlled and displacement controlled

6.2.1 Vector normalization

The radial displacement extracted form the finite element analysis w' can be expressed in terms of a selected length scale. w' is expressed using a reference length scale L of $1mm$. The selection of $1mm$ as a length scale facilitates the coupling between the post-processing that takes place outside of the finite element software and displacement fields obtained directly from it. The formal expressions relating the different length-related variables with respect to the selected length scale are presented in equations 6.1 and 6.2

$$\begin{aligned} w'(x', y') \\ w' &= Lw \\ x' &= Lx \\ y' &= Ly \end{aligned} \tag{6.1}$$

$$\begin{aligned} Lw &= w(x', y') \\ &= w(Lx, Ly) \\ w(x, y) &= \frac{w'(Lx, Ly}{L} \end{aligned} \tag{6.2}$$

Once the reference length scale is selected, the next step is to define a norm and a normalization for the different fields following equation 6.3.

$$||\,||_2 \,:\, w \longrightarrow ||w||_2 \in \mathbb{R} \tag{6.3}$$

In this case, the norm selected is a L_2 norm of the radial displacement fields w following equation 6.4.

$$||w||_2 = \sqrt{\iint_A w^2 \, dA} \tag{6.4}$$

$$||w||_2 = \sqrt{\langle w, w \rangle} \tag{6.5}$$

With an inner product of the field w as shown in equation 6.6 for a continuous and a discrete function on the left and right sides of the second equal sign, respectively.

$$\langle w_a, w_b \rangle = \iint_A w_a \, w_b \, dA = \frac{Area}{N\,M} \sum_{ij} w_{aij} \, w_{bij} \tag{6.6}$$

In 6.6 the $Area$ (A) can be computed as given in equation 6.7.

$$Area = (-\frac{\pi R}{L}, \frac{\pi R}{L}) \times (0, \frac{l}{L}) = (-a, a) \times (0, b) \tag{6.7}$$

Considering the definitions presented in equations 6.3 to 6.7 to obtain a norm of a field w equal to 1 expression 6.8 must be fulfilled.

$$||w \equiv 1|| = \sqrt{2ab} \stackrel{!}{=} \sqrt{\alpha \sum_{ij} w_{ij}^2} = \sqrt{\alpha \, N \, M} \tag{6.8}$$

The condition that fulfills expression 6.8 is to use a parameter α according to equation 6.9.

$$\alpha\, N\, M = 2ab \Leftrightarrow \alpha = \frac{2ab}{NM} \tag{6.9}$$

6.2.2 Probing location & buckling mode correlation

Let us define the field $\hat{c}$ as the normalized buckling mode of a cylindrical shell. The name of buckling mode was selected because of the difference between radial displacement fields used to construct $\hat{c}$. The difference between the radial displacement field associated with the maximum radial displacement minus the radial displacement field from the next converged after the maximum force is overcome determines the evolution of the buckling process.

Figure 6.3 shows the $\hat{c}$ field of specimen A7. This test article provided a successful prediction of the buckling load using the stability landscape methodology. The stability landscape was built in the 0, 48.5 point (see figure 6.3). Hence, there is a certain degree of correlation between probing location and buckling mode. The structures of the $\hat{c}$ overlap with the location of probing. This case where correlation is observed therefore supports the hypothesis stated at the beginning of the present section.

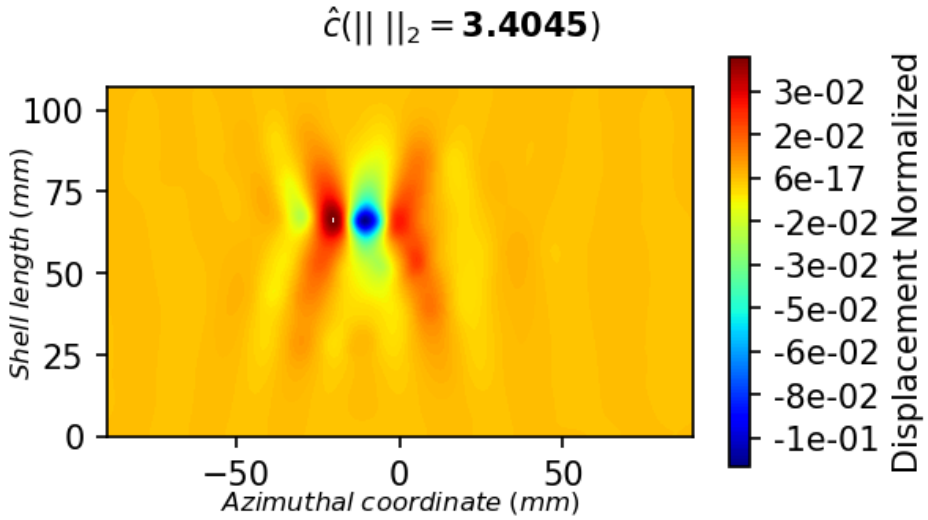

Figure 6.3 – $\hat{c}$ of specimen A7. The probing location and the buckling mode are spatially correlated in the case where the predictions are accurate.

Figure 6.4 shows the $\hat{c}$ field of specimen B1. In this case the stability landscape methodology provided an inaccurate prediction of the buckling load. The stability landscape was built a the $0°, 48.5$ point as well. Hence, there is no correlation between the probing location and the buckling mode. This case where no correlation is observed also supports the hypothesis stated at the beginning of section 6.2. In this case the prediction does not work and it should

not work because the correlation stated at the beginning of 6.2 is not fulfilled.

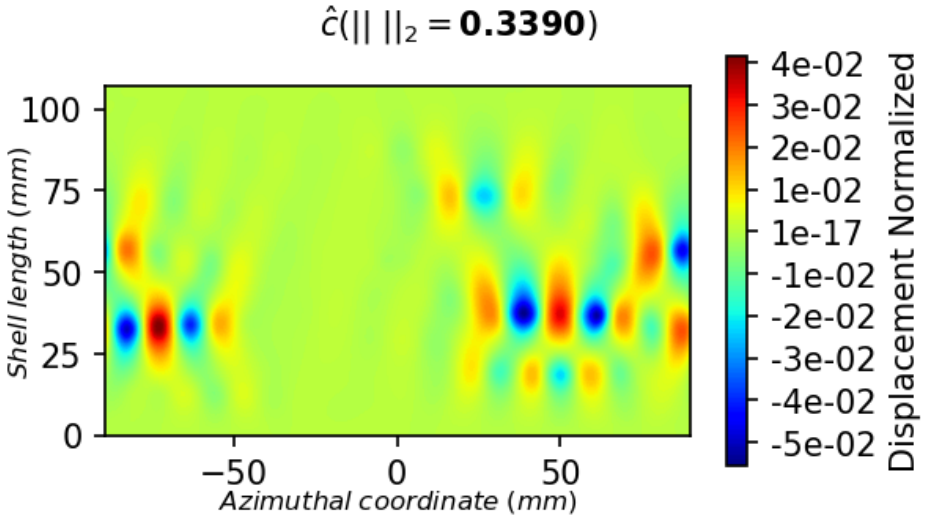

Figure 6.4 – $\hat{c}$ of specimen B1. The probing location and the buckling mode are not spatially correlated in the case where the predictions are not accurate.

Lastly, figure 6.5 shows the $\hat{c}$ field of specimen A11. For this specimen, an accurate prediction of the buckling load was obtained using the stability landscape methodology. The stability landscape was built in the $0°, 48.5$ point. However, there is no correlation between probing location and buckling mode. Thus, this case where no correlation is observed does not support the hypothesis stated at the beginning of section 6.2. In this case the prediction does not work but it should work for the hypothesis stated at the beginning of 6.2 to be fulfilled. Hence, this is a counter example that refutes the validity of the hypothesis stated at the beginning of this section.

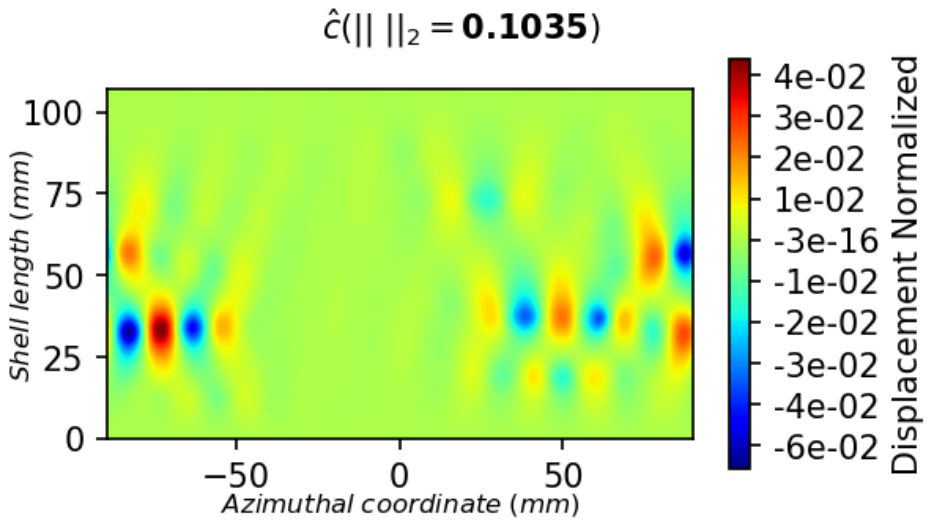

Figure 6.5 – $\hat{c}$ of specimen A11. The probing location and the buckling mode should be spatially correlated in the case where the predictions are accurate. However, in this case the correlation does not exists.

6.2.3 Conclusions

Two examples that motivated the hypothesis formulation about the correlation between probing location and buckling mode were shown in figures 6.3 and 6.4. However, a counter example to the hypothesis was found in specimen A11. The field $\hat{c}$ associated with this case is shown in figure 6.3. Therefore, the hypothesis that if the probing location and the buckling mode of a shell are correlated then a successful prediction based on stability landscapes can be provided is refuted.

6.3 Correlation between ridge variation & buckling mode

The second hypothesis about why predictions of buckling loads are successful or not reads as follows: If the buckling mode and the radial displacement field constructed from the difference between two consecutive maxima of two poking curves (ridge variation) are correlated, then the prediction of the buckling load will be successful.

6.3.1 Variation of radial displacement on the ridge

Let us consider $\mathbf{u}(\mathbf{F_A}, \mathbf{D_p^{max}}) - \mathbf{u}(\mathbf{F_A} - \Delta, \mathbf{D_p^{max}})$, the radial displacement field calculated between two consecutive points (F_A and $F_A - \Delta$) at the top of the ridge (D_p^{max}). This field represents the direction in which the vector used for interpolation evolves as a function of axial compression force. The resulting entity to evaluate the correlation is a radial displacement field. An illustration of this vector in a stability landscapes is shown in figure 6.6.

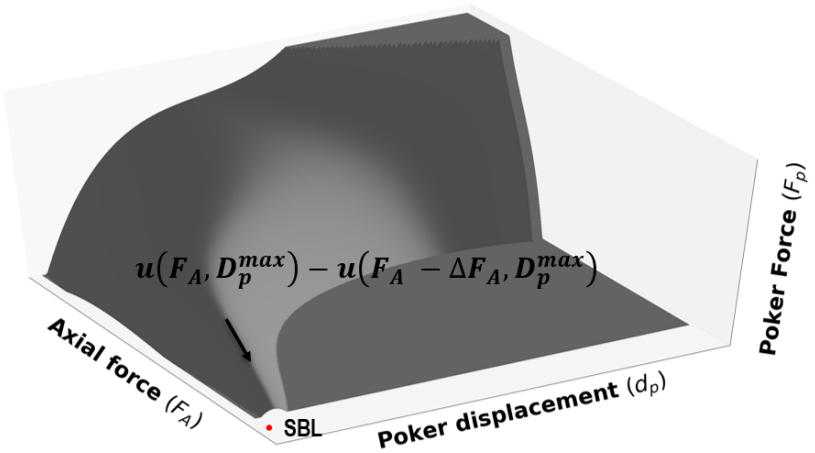

Figure 6.6 – Pictorial representation of the vector defining the variation of the radial displacement of a cylindrical between two consecutive poking curves at the point where the reaction of the poker is maximum, the ridge.

6.3.2 Correlations

The $u(F_A, D_p^{max}) - u(F_A - \Delta, D_p^{max})$ field of specimen A8 is displayed in figure 6.7. This case provided a successful prediction of the buckling load using the stability landscape methodology. The stability landscape was built in the $0°, 48.5$ point. Hence, there is a certain degree of correlation between the top of the ridge extrapolations and buckling mode. This case where correlation is observed therefore supports the hypothesis stated at the beginning of the current section.

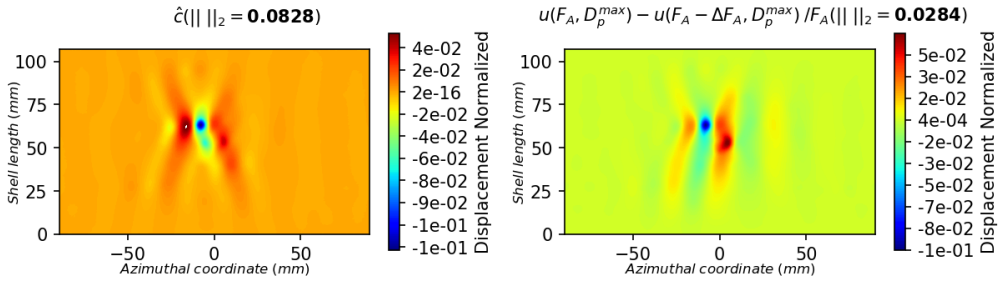

(a) Specimen A8 $\hat{c}$ buckling mode

(b) Specimen A8 $u(F_A, D_p^{max}) - u(F_A - \Delta, D_p^{max}$

Figure 6.7 – Example of fields that are spatially correlated supporting the hypothesis that when the buckling mode and the vector defined along the top of the ridge in figure 6.6 are correlated then predictions are successful. Specimen A8

Figure 6.8 shows the $u(F_A, D_p^{max}) - u(F_A - \Delta, D_p^{max})$ field of specimen B3. In this case, the stability landscape methodology yielded an inaccurate prediction of the buckling load. In this case there is no correlation between top of the ridge extrapolations and buckling mode. Hence,

this case where no correlation is observed supports the hypothesis stated at the beginning of section 6.3 as well since it provided an inaccurate buckling load prediction.

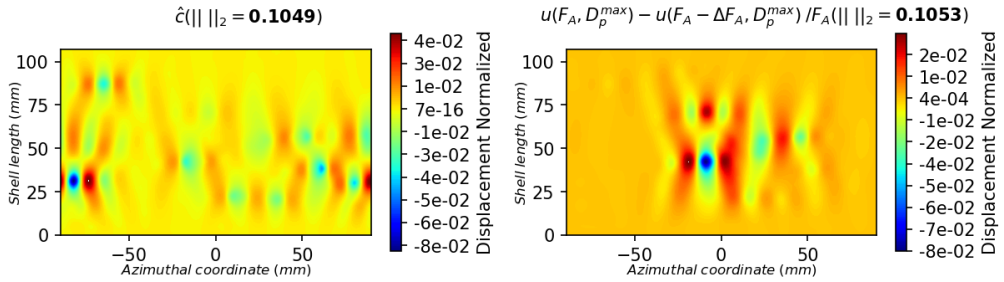

(a) Specimen B3 $\hat{c}$ buckling mode

(b) Specimen B3 $u(F_A, D_p^{max}) - u(F_A - \Delta, D_p^{max}$

Figure 6.8 – Example of fields that are not spatially correlated supporting the hypothesis that when the buckling mode and the vector defined along the top of the ridge in figure 6.6 are not correlated then predictions are not successful. Specimen B3

Figure 6.9 shows the $u(F_A, D_p^{max}) - u(F_A - \Delta, D_p^{max})$ and $\hat{c}$ fields of specimen A15. This case provided an accurate prediction of the buckling load using the stability landscape methodology. This case where no correlation is observed between the fields does not support the hypothesis stated at the beginning of section 6.3. In this case the correlation does not work but it should work for the hypothesis stated at the beginning of the section to be fulfilled. Hence, this case is a counter-example that refutes the validity of the hypothesis stated at the beginning of section 6.3.

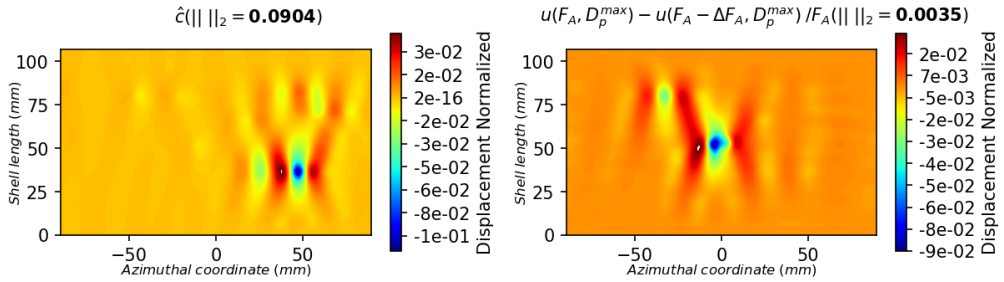

(a) Specimen A15 $\hat{c}$ buckling mode

(b) Specimen A15 $u(F_A, D_p^{max}) - u(F_A - \Delta, D_p^{max}$

Figure 6.9 – Example of fields that are not spatially correlated refuting the hypothesis that when the buckling mode and the vector defined along the top of the ridge in figure 6.6 are correlated then predictions are successful. Specimen A15

6.3.3 Conclusions

For this hypothesis about the correlation between the top of the ridge vector and buckling mode, two examples supporting it were shown in figures 6.7 and 6.8. Nevertheless, a counter

example to the hypothesis was found for specimen A15. The fields $u(F_A, D_p^{max}) - u(F_A - \Delta, D_p^{max})$ and $\hat{c}$ associated with this item are shown in figure 6.9. Therefore, the hypothesis that if the extrapolation of the tops of the ridge and the buckling mode of a shell are correlated then a successful prediction based on stability landscapes can be provided has been refuted.

6.4 Correlation between filtered ridge variation & buckling mode

The third hypothesis about why predictions of buckling loads are successful or not is the following one: If the buckling mode and the radial displacement field constructed from the difference between two consecutive maxima of 2 poking curves without the contribution of the pre-load deformation (filtered ridge variation) are correlated, then the prediction of the buckling load will be successful.

6.4.1 Variation of radial displacement along the ridge filtered

Let us define a new field $\hat{\mathbf{a}}$ as the radial displacement depicting the variation of the displacement field without the contribution of the base state deformations. The radial displacement field (u) can be constructed as the combination of the deformations due to the effect of the axial load ($\tilde{u}$) and the deformation caused by the poking ($\hat{u}$). The idea behind the third hypothesis studied herein is that the contribution of the deformations in the shell prior to the lateral probing ($\tilde{u}$) hide the effect of the deformations induced by the lateral probing ($\hat{u}$). Hence, the deformation coming just from the pre-load should be subtracted ($\tilde{u}$), i.e. filtered out. A graphical depiction of the emerging vector ($\hat{a}$) is displayed in figure 6.10.

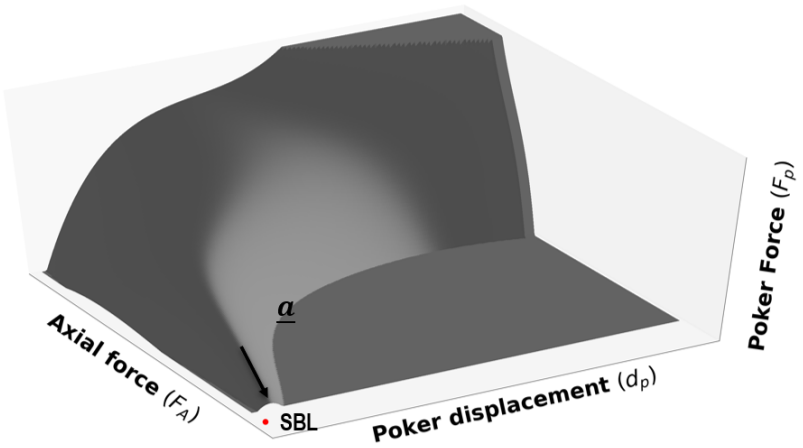

Figure 6.10 – Pictorial representation of the vector $\hat{a}$ representing the variation of radial displacement between two points at the top of the ridge subtracting the contribution of the initial pre-load in the radial displacement.

6.4.2 Correlations

Figure 6.11 shows the $\hat{c}$ and $\hat{a}$ fields of specimen A8. This case provided a successful prediction of the buckling load using the stability landscape methodology. In this case there is a certain degree of correlation between the top of the ridge extrapolations without the contribution of the pre-load deformations and the buckling mode. Hence, this case where correlation is observed and provides an accurate prediction supports the hypothesis stated at the beginning of the present section.

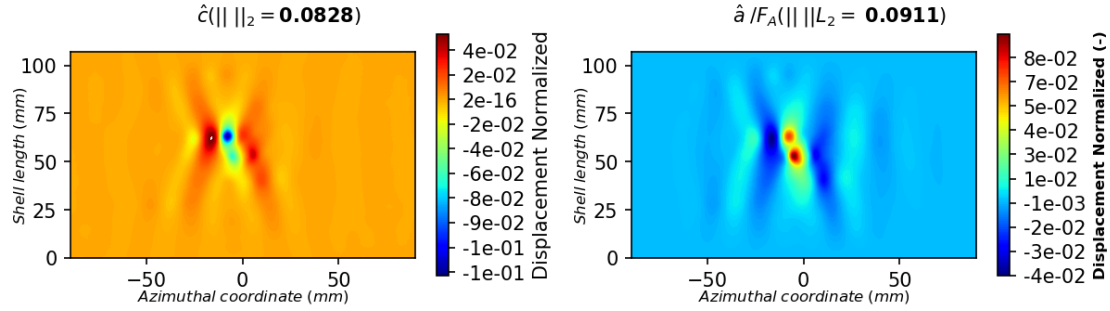

(a) $\hat{c}$ (b) $\hat{a}$

Figure 6.11 – Example of fields that are spatially correlated supporting the hypothesis that when the buckling mode and the vector defined along the top of the ridge in figure 6.10 are correlated then predictions are successful. Specimen A8

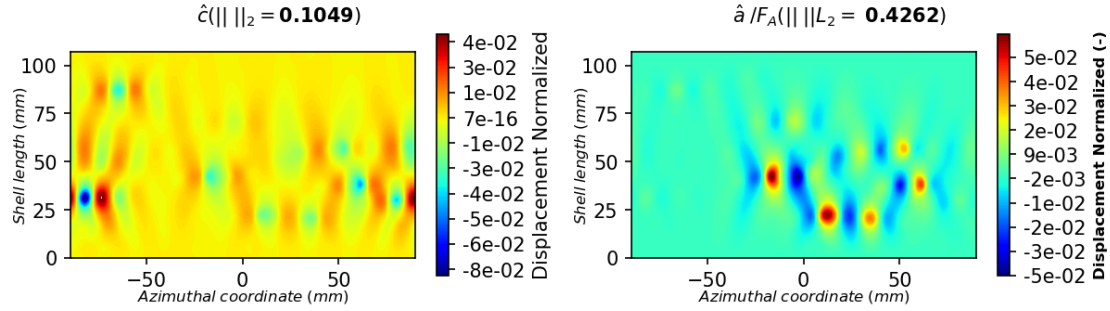

(a) $\hat{c}$ (b) $\hat{a}$

Figure 6.12 – Example of fields that are not spatially correlated supporting the hypothesis that when the buckling mode and the vector defined along the top of the ridge in figure 6.10 are not correlated then predictions are successful. Specimen B3

The $\hat{c}$ and $\hat{a}$ fields of specimen B3 are depicted in figure 6.12. This case provided an inaccurate prediction of the buckling load using the stability landscape methodology. In this case there is no correlation between the top of the ridge extrapolations without the contribution of the pre-load deformations and the buckling mode. Therefore, this case where correlation is not observed and an inaccurate prediction is obtained also supports the hypothesis studied in

this section.

Finally, figure 6.13 displays the $\hat{c}$ and $\hat{a}$ fields of specimen A15. This case provided an accurate prediction of the buckling load based on the stability landscape methodology. However, in this case there is no correlation between the top of the ridge extrapolations without the contribution of the pre-load deformations and the buckling mode. This case where correlation is not observed and provides a successful prediction does not support the hypothesis stated at the beginning of section 6.4.

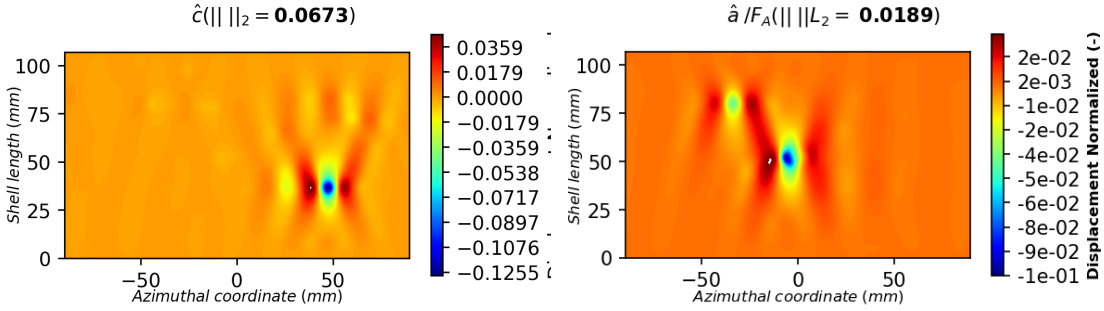

(a) $\hat{c}$ (b) $\hat{a}$

Figure 6.13 – Example of fields that are spatially not correlated refuting the hypothesis that when the buckling mode and the vector defined along the top of the ridge in figure 6.10 are correlated then predictions are successful. Specimen A15

6.4.3 Conclusions

In the present section two examples that supported the hypothesis formulation about the correlation between the top of the ridge vector without the pre-load radial deformations and buckling mode were shown in figures 6.11 and 6.12. However, a counter-example to the hypothesis was found in specimen A15. The fields $\hat{c}$ and $\hat{a}$ associated with this case are depicted in figure 6.13. The hypothesis that if the extrapolation of the tops of the ridge without the contribution of the pre-load deformation and the buckling mode of a shell are correlated then a successful prediction based on stability landscapes can be provided was refuted.

6.5 Correlation between filtered ridge variation & ridge orthogonal probing

The fourth hypothesis about why predictions of buckling loads are successful or not reads as follows: If the field associated with vector $\hat{a}$ and the field arising from the difference between two points at the top of a poking curve with constant axial pre-load are correlated, then the prediction of the buckling load will be successful.

Variation of radial displacement at the top of the ridge for constant pre-load

Let us consider $\hat{b}$, the new vector introduced to evaluate the correlation from the present hypothesis. It is a field containing the radial displacement depicting the variation of the radial displacement field perpendicular to the ridge. Namely the variation in the radial displacement field existing between the converged solutions of the *in-silico* experiments immediately before and after the maximum of one of the poking curves. A poking curve is constructed with the radial force obtained during the probing of the shell at a fix compression load. In each of the points of a poking curve, there is a unique radial displacement field associated to it. A graphical representation of the direction described by field $\hat{b}$ is shown in figure 6.14.

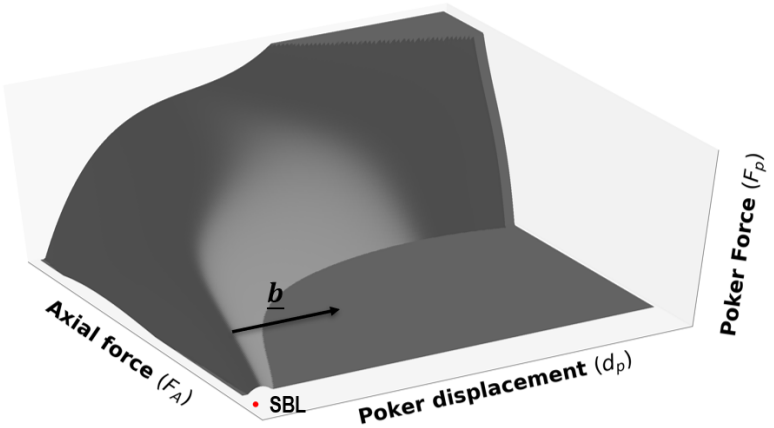

Figure 6.14 – Pictorial representation of the vector containing the information about the variation in radial displacement between two points before and after the top of the ridge for a certain poking curve.

6.5.1 Correlations

Figure 6.15 shows the $\hat{a}$ and $\hat{b}$ fields of specimen A3. This case provided a successful prediction of the buckling load using the stability landscape methodology. In this case there is a certain degree of correlation between the top of the ridge extrapolations without the contribution of the pre-load deformations and the field orthogonal to the ridge associated with $\hat{b}$. This case where correlation is observed and a successful buckling load prediction is obtained supports the hypothesis stated at the beginning of the present section.

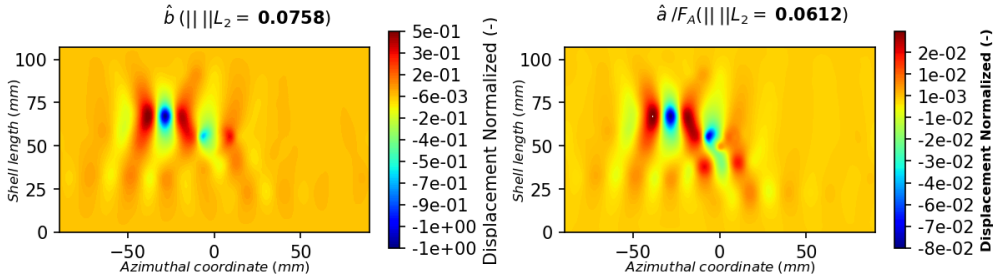

(a) $\hat{b}$ (b) $\hat{a}$

Figure 6.15 – Example of fields that are spatially correlated supporting the hypothesis that when $\hat{a}$ and $\hat{b}$ are correlated then predictions are successful. Specimen A3

Figure 6.16 shows the $\hat{a}$ and $\hat{b}$ fields of specimen B1. This case provided an inaccurate prediction of the buckling load using the stability landscape methodology. In this case there is no correlation between the top of the ridge extrapolations without the contribution of the pre-load deformations and the field orthogonal to the ridge associated with $\hat{b}$. Nece, this case where correlation is not observed and an inaccurate prediction was obtained also supports the hypothesis stated at the beginning of section 6.5.

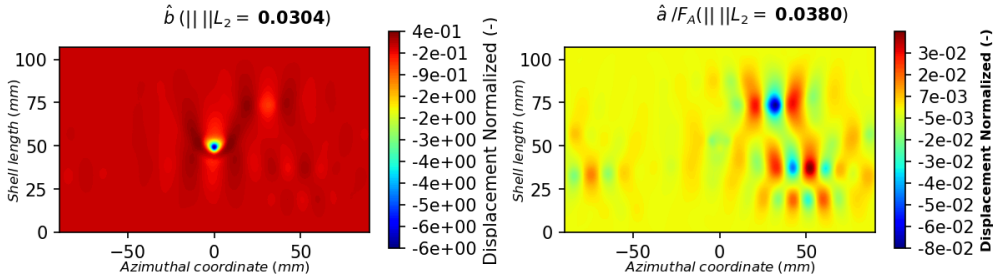

(a) $\hat{b}$ (b) $\hat{a}$

Figure 6.16 – Example of fields that are not spatially correlated supporting the hypothesis that when $\hat{a}$ and $\hat{b}$ are not correlated then predictions are not successful. Specimen B1

Lastly, figure 6.17 shows the $\hat{a}$ and $\hat{b}$ fields of specimen A6. This case provided an accurate prediction of the buckling load using the stability landscape methodology. In this case there is no correlation between the top of the ridge extrapolations without the contribution of the pre-load deformations and the field orthogonal to the ridge associated with $\hat{b}$. This case where correlation is not observed even though it provided a successful buckling load prediction is therefore against the hypothesis stated at the beginning of this section.

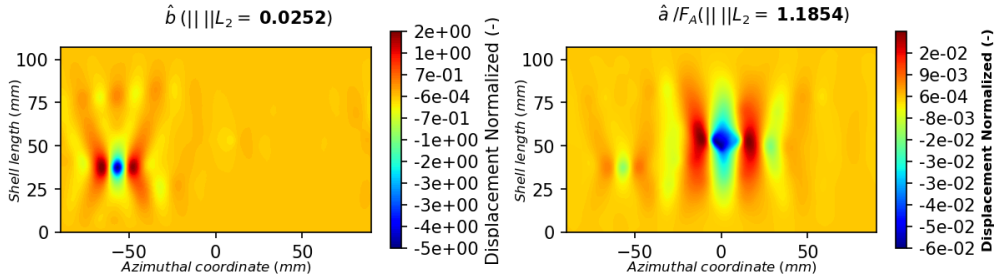

(a) $\hat{b}$ (b) $\hat{a}$

Figure 6.17 – Example of fields that are not spatially correlated refuting the hypothesis that when $\hat{a}$ and $\hat{b}$ are correlated then predictions are successful. In the case of Specimen A6 the prediction was successful

6.5.2 Conclusions

In the present section two examples that supported the hypothesis about the correlation between the top of the ridge vector without the pre-load radial deformations and the field orthogonal to the ridge associated with $\hat{b}$ were shown in figures 6.15 and 6.16. However, a Specimen A6 provided a counter-example to the hypothesis. The fields $\hat{c}$ and $\hat{c}$ associated with this case are displayed in figure 6.17. The hypothesis that if the extrapolation of the tops of the ridge without the contribution of the pre-load deformation and the field orthogonal to the ridge associated with $\hat{b}$ of a shell are correlated then a successful prediction based on stability landscapes can be provided is thus refuted.

6.6 Correlation between ridge orthogonal probing & buckling mode

The fifth hypothesis about why predictions of buckling loads are successful or not is the following one: If the fields associated with vector $\hat{b}$ and $\hat{c}$ are correlated, then the prediction of the buckling load will be successful.

6.6.1 Correlations

Figure 6.18 shows the $\hat{b}$ and $\hat{c}$ fields of specimen A7. This case provided a successful prediction of the buckling load using the stability landscape methodology. In this case there is a certain degree of correlation between the field orthogonal to the ridge associated with $\hat{b}$ and the buckling mode. This case where correlation is observed therefore supports the hypothesis stated at the beginning of section 6.6.

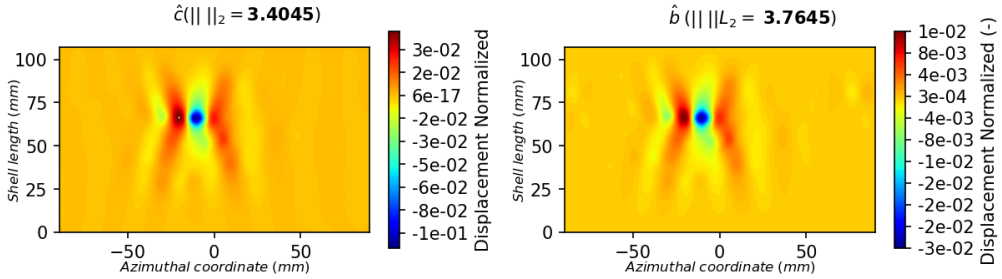

(a) $\hat{c}$ (b) $\hat{b}$

Figure 6.18 – Example of fields that are spatially correlated supporting the hypothesis that when buckling mode and $\hat{b}$ are correlated then predictions are successful. Specimen A7

Figure 6.19 shows the $\hat{b}$ and $\hat{c}$ fields of specimen B4. This case provided an inaccurate prediction of the buckling load using the stability landscape methodology. In this case there is no correlation between the field orthogonal to the ridge associated with $\hat{b}$ and the buckling mode. This case where correlation is not observed and an inaccurate buckling load prediction is obtained also supports the hypothesis stated at the beginning of the present section.

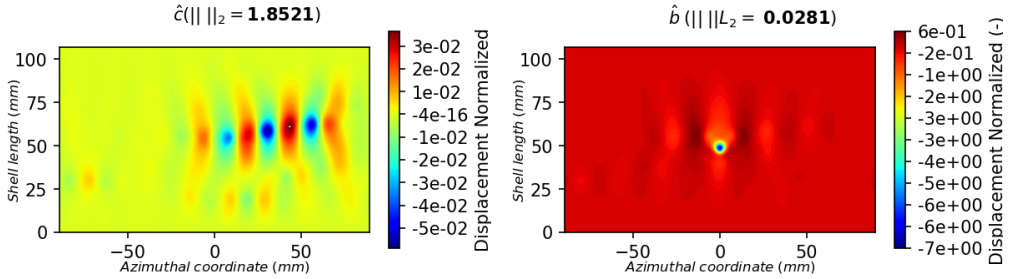

(a) $\hat{c}$ (b) $\hat{b}$

Figure 6.19 – Example of fields that are not spatially correlated supporting the hypothesis that when buckling mode and $\hat{b}$ are not correlated then predictions are not successful. Specimen B4

Finally, figure 6.20 shows the $\hat{b}$ and $\hat{c}$ fields of specimen A10. This case provided an accurate prediction of the buckling load using the stability landscape methodology. In this case there is no correlation between the field orthogonal to the ridge associated with $\hat{b}$ and the buckling mode. This case where correlation is not observed and a successful prediction is obtained is thus against the hypothesis stated at the beginning of section 6.6.

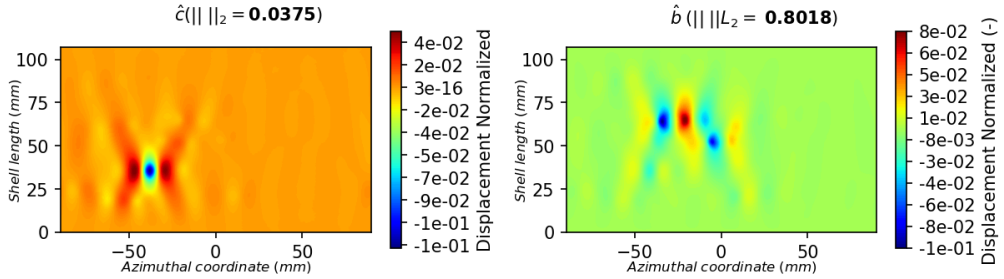

(a) $\hat{c}$ (b) $\hat{b}$

Figure 6.20 – Example of fields that are not spatially correlated refuting the hypothesis that when buckling mode and $\hat{b}$ are correlated then predictions are successful. Specimen A10 provided a successful prediction

6.6.2 Conclusions

In this section two examples that supported the hypothesis about the correlation between the top of the ridge vector without the pre-load radial deformations and buckling mode were shown in figures 6.18 and 6.19. However, a counter-example to the hypothesis was found for specimen A10. The fields $\hat{c}$ and $\hat{b}$ associated with this case are shown in figure 6.20. The hypothesis that if the extrapolation of the field orthogonal to the ridge associated with $\hat{b}$ and the buckling mode of a shell are correlated then a successful prediction based on stability landscapes can be provided is therefore refuted.

6.7 Extending local probing to complete cylindrical shells

In the previous sections the attempt to uncover the reason why the buckling load extrapolation works in some cases and it does not in others was not successful. Hence, in order to understand if the stability landscape is able to predict the buckling load of any cylindrical shell, an alternative procedure for testing was proposed. This alternative procedure consists of probing the cylindrical shell in a grid of points covering the complete domain. The aim is to construct a stability landscape in each of the locations and assess the accuracy of the predictions at those different points.

This new approach will be demonstrated with one of the synthetic specimens used in the previous sections. The case selected is one that did not provide an accurate prediction (Relative error with respect to the real buckling load greater than 5%) of the buckling load. The reasoning using one specimen that did not work is to try to find a location that would provide an accurate prediction.

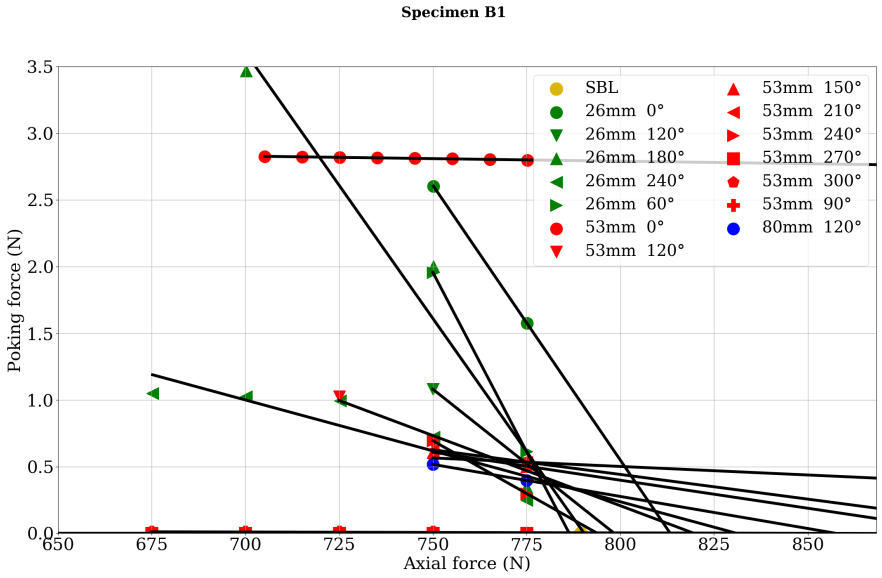

Figure 6.21 – Ridges extrapolating to different buckling loads. Specimen E used the imperfection configuration of shell NL L 1, this shell was tested with the standard testing procedure and delivered a wrong buckling load prediction.

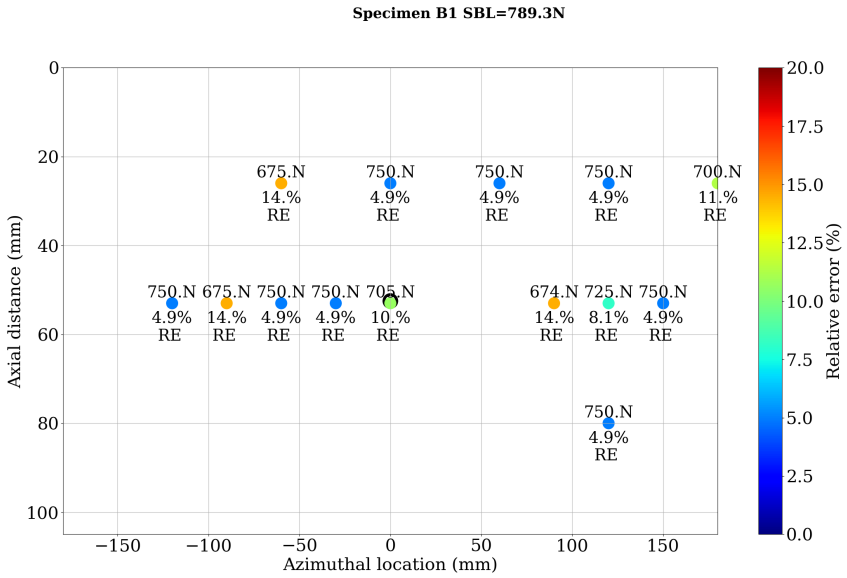

Figure 6.22 – Relative error map showing the accuracy of the predictions an the location of the locations where the predictions were constructed. The circle in the center is the location of the local imperfection. The ridge constructed 5 mm below the hole provided a buckling load prediction of 8095 N, leading to a relative error of 928 %.

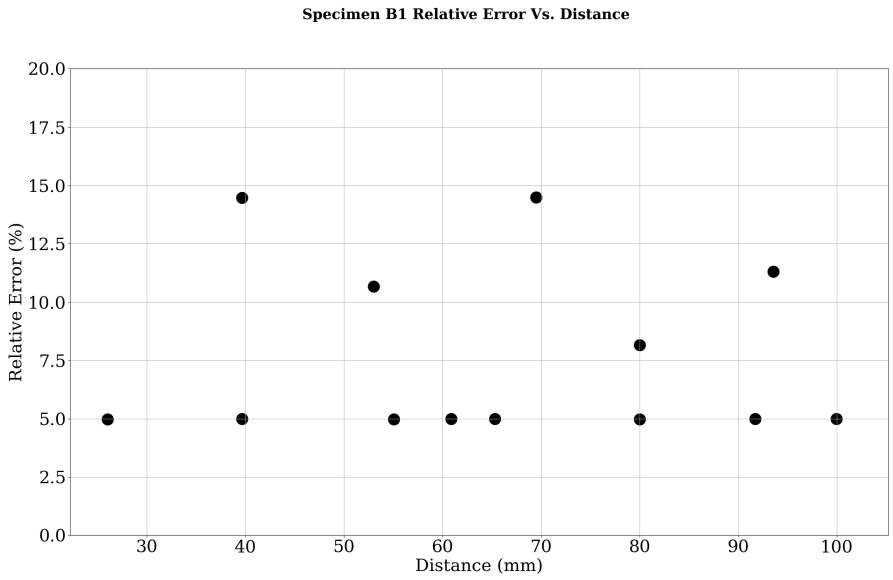

Figure 6.23 – This plot of distance versus relative error for specimen E shows that there are cases where the prediction can be successful far away from the local imperfection. The opposite is also true, there predictions that are close to the imperfection that provide wrong predictions. In the case of this imperfection, the standard prediction provided a wrong load prediction just 5 mm from the localized imperfection

The *in-silico* experiment was performed with Specimen B1. The ridges that where found at different locations are given in figure 6.21. Note that not all locations probed provided a stability landscape with a clear ridge feature. The predictions provided by each ridge are shown then in the relative error map in figure 6.22. The quality of the prediction of buckling load as a function of the distance to the localized imperfection is also presented in figure 6.23. There are 8 locations where the relative error with respect to the real buckling load of Specimen B1 is below 5%. Out of the 30 locations probed only 14 provided an stability landscape that could be used to extrapolate to a buckling load.

The locations from figure 6.22 that provided accurate prediction of the buckling load are more common in the middle section of the cylindrical shell. There are predictions that are are accurate far away from the localized imperfection represented by the black circumference of figure 6.22.

6.7.1 Conclusions

The data presented in figures 6.22, 6.23 and 6.21 shows that the alternative methodology proposed in this section is able to successfully predict the buckling load of Specimen B1. This fact suggests that in the case of Specimen B1 the probing at multiple locations is a better technique than the introduction of a localized imperfection to determine the location to

construct the stability landscape.

6.8 Conclusions

The mechanism behind the accurate predictions based on a single location remains unclear. A set of five hypotheses have been tested. During their verification process, different examples were found where the the hypotheses were satisfied. However, counter-examples were also present. Hence, no clear conclusion could be drawn about what makes predictions based on the stability landscape work only for some cases.

On the other hand, a specimen that failed to deliver an accurate prediction was tested in multiple locations with the same stability landscape methodology and in this case the prediction was successful. This fact suggests that a non-destructive methodology for cylindrical shells could be possible via performing probing experiments at different locations.

7 Conclusions

7.0.1 Dynamical systems approach applied to shell buckling

The behaviour of a cylindrical shell was modelled as a dynamical system applying the same concepts used in fluid dynamics to study turbulence and laminar-turbulent transition. The description of the cylindrical shell allowed for a fully non-linear characterization of the system. This later fact provided the possibility to study cylindrical shell buckling as a finite amplitude problem to characterize the basin of attraction associated with the different fix points of the system. Furthermore, the description of cylindrical shell buckling as a finite amplitude problem enables the definition of the critical perturbation that triggers buckling for sub-critical loads.

Dynamically unstable localized equilibrium solutions that have not been previously reported in the literature have been identified. These localized solutions lay in the boundary of the basin of attraction. The single dimple solution has a single unstable eigen-mode associated to it, making it an edge state of the system. In a variational system like the one of the cylindrical shell, this edge-state might be the minimum perturbation to exit the basin of attraction.

The concept of basin of attraction in state space can be used as a motivation to experimentally explore the point where it vanishes. The variation in size of the basin of attraction with axial compression has been shown herein. This was the foundation for the utilization of stability landscapes constructed experimentally as a prediction tool of the buckling load of cylindrical shells.

The dynamical system describing the cylindrical shell based on the DMV shell approximation shows a feature called homoclinic snaking under the continuation of the axial load parameter. This is a feature in common with other physical systems that can sustain localized solutions. The first rung state in the system was also found. Rung states are the non-symmetric states connected to the two branches present of the homoclinic snaking.

7.0.2 Localized nature of cylindrical shell buckling

In the current research, it has been verified that the initiation of buckling is a local phenomenon. The buckling process nucleates at a certain location, then it propagates through the complete shell. Once a large portion of the shell is covered with dimples, these start to coalesce and form larger ones. This later larger dimples are the deformation normally observed after the buckling test is concluded. The experimental data showing this process was collected using high-speed cameras during a set of destructive compression tests.

The large campaign of destructive compression testing of real shells with various hole sizes showed that there are dimensions of a localized imperfection that do not affect the average buckling load. i.e. the average buckling load of shells with small imperfections is very similar to the one of a shell with no local imperfection. The relevance of local imperfection with respect to the background, in the case of the specimens tested, is covered by the variability in the buckling load due to the different realization of the background imperfections.

Localized deformations play a relevant role in the buckling of cylindrical shells. However, they do not remove completely the influence of background imperfections in the buckling load of cylindrical shells for any of the local imperfection sizes studied herein. The buckling load of cylindrical shells is a function of both the localized and the background imperfections. Furthermore, the final effect of these two kinds of imperfections on the buckling load of a cylindrical shell is not a simple superposition of both imperfections, but a combined action.

In the study of realistic cylindrical shells with localized and background two regimes where identified based on their relative influences. There is a regime where the influence of the local imperfection dominates with respect to the one of the background imperfection. While the second regime features the opposite behaviour. Hence, there is a threshold at which the influence of imperfections changes prevalence. The background imperfection intensity of the specimens used in the large test campaign of chapter 4 is in the regime where the background imperfection prevails.

7.0.3 Stability landscapes

Stability landscapes are able to encode information about the stability of cylindrical shells. The ridge feature of the stability landscapes can be used to extrapolate the axial load at which the landscape vanishes. This load coincides with the buckling load of the cylindrical shell. The predictive capability of stability landscapes was established via the utilisation of a finite element model containing a single localized imperfection. In this case, the success rate was 100%. This ideal success rate is linked to the fact that there must be an axial compression force where the stability landscape vanishes. Additionally, the nearly perfect nature of the finite element model might enable sensing of the buckling event without the interference of the background imperfections present in real shells.

After the numerical verification that stability landscapes are able to predict buckling, a number

of experiments was set to study the system in the lab. The experiments consisted of the probing of the shells at a single location in the first 2 of the 3 test campaigns. In the third campaign, the shell was probed at a different location in the vicinity of the localized imperfections. The results obtained showed that only in a portion of the real experiments the buckling load of a shell could be predicted, opposed to the 100% success rate of the numerical model. The success rate varied from 86% to roughly 20%. The two different success rates can be attributed to a different implementation of the localized imperfection used to define the probing location.

The main learning outcome about the stability landscapes of real shells is that they are a features of each individual point of a cylindrical shell. There was a noticeable variability between stability landscapes constructed at nominally identical locations of nominally identical cylindrical shells. Hence, it can be said that a stability landscape is a unique signature of a particular location of a cylindrical shell.

7.0.4 Non-destructive testing procedure of cylindrical shells

The buckling load of a cylindrical shell can be predicted in a non-destructive manner via its characteristic stability landscapes. The testing procedure used in the current research consisted of probing a shell at multiple locations. The proposed non-destructive technique can be implemented numerically or experimentally. The test sequence followed is not relevant for the numerical analysis. i.e. it does not matter if the landscapes are built in one go or if individual poking curves are collected at each location before increasing to the next pre-load level. In the case of the experiment, the testing sequence is however vital and it should consist of the construction of individual poking curves at each location before increasing the pre-load. In this way, two measurements can be taken to predict if the buckling force is close. First evaluate if the maximum poking force is low and second verify that the next pre-load level is below all the current extrapolations arising from the different locations.

8 Further work

- **Numerically derived state in the edge of cylindrical shells with defects:** In the current research, the existence of complex localized solutions was shown. These complex localized solutions lay in a manifold that acts as a boundary between the un-buckled and the buckled state, the edge. This next step should focus on demonstrating that this same state space picture exists in the case of shells with defects. The validation of the picture where the state space remains the same for a real shell would open the door to demonstrating formally the existence of an optimal trajectory to transition between the un-buckled and the buckled state.

- **Minimal seed:** In the field of laminar-turbulent transition there has been a lot of interest to find the so-called minimal seed. This is the optimal perturbation in terms of energy that will trigger a fluid to transition to the turbulent regime. In the case of the cylindrical shell, because it is a variational system, the minimal seed corresponds with an edge state of the system. Hence, the calculation of of the edge state associated with imperfect cylindrical shells would be a potentially interesting approach to define worst case imperfections.

- **Advanced imaging of experiments:**

  The buckling event in cylindrical shells is very dynamic, with a characteristic time of mili-seconds. Hence, to draw valid conclusions about the initialization of buckling, high-speed imaging of the complete domain of the different experiments is required. In this case, high-speed imaging would not only allow to locate the nucleation point but also to understand more about the propagation of the event. This second point becomes important once the effect of inertia is to be taken into account.

- **Knowledge of real imperfections:**

  The documentation of the imperfections present in specimens tested via scanning of their surface would be useful data to predict the buckling load of cylinders. These imperfections could be included in finite element models to obtain the buckling load

of cylinders non destructively. The same finite element models could also be used to predict edge states of real cylindrical shells.

- **Explore larger population with the non-destructive methodology suggested numerically and experimentally:**

  In the last chapter of the thesis, a multi-location probing technique was used to successfully predict buckling of a shell with realistic imperfections. Only one case was tested. Hence, it would be very interesting to test a larger population of realistic shells with a similar procedure. The application of the proposed non-destructive methodology should also be evaluated in experiments.

A Appendix A

During the current research a Abaqus plug-in was used for the following purposes:

- Generate parametric studies
- Implementations of probing procedure
- Implementation of random self-correlated imperfections
- Combinations of localized and global imperfections

The complete plug-in can be found in the following direction:

- Git Plug-In Link (Click here!!)

B Appendix B

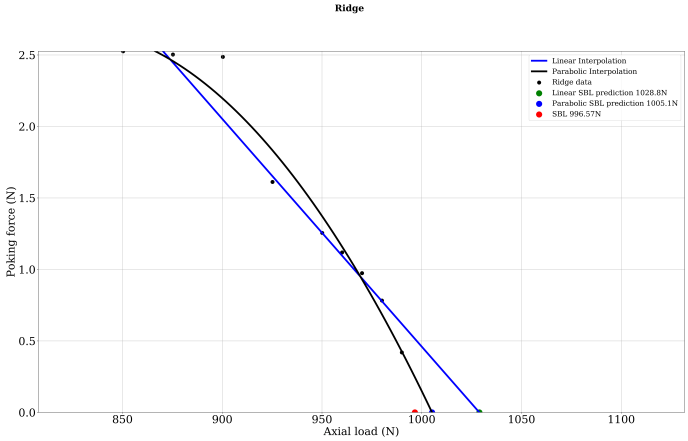

Figure B.1 – 2D projection of the ridge feature of the landscape associated with Specimen A1

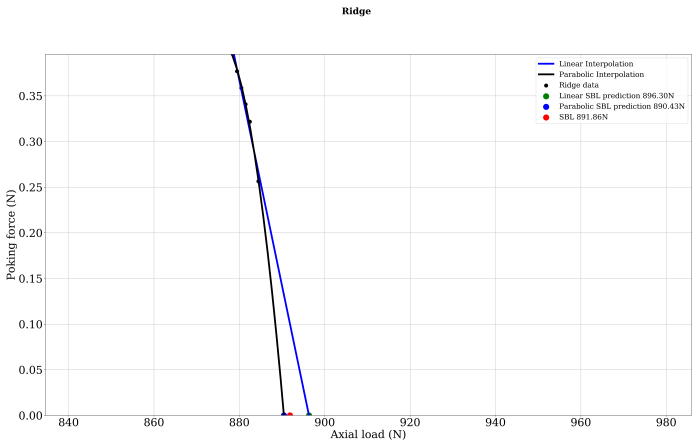

Figure B.2 – 2D projection of the ridge feature of the landscape associated with Specimen A2

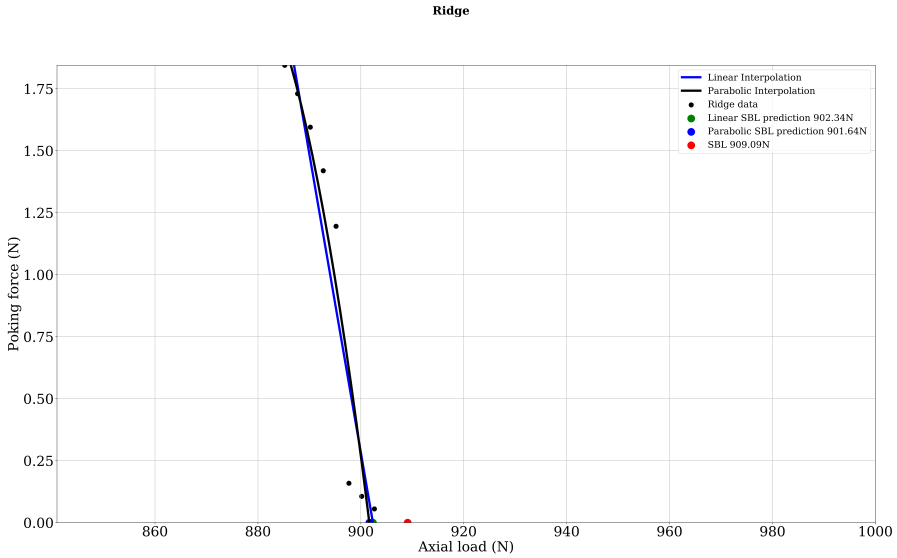

Figure B.3 – 2D projection of the ridge feature of the landscape associated with Specimen A3

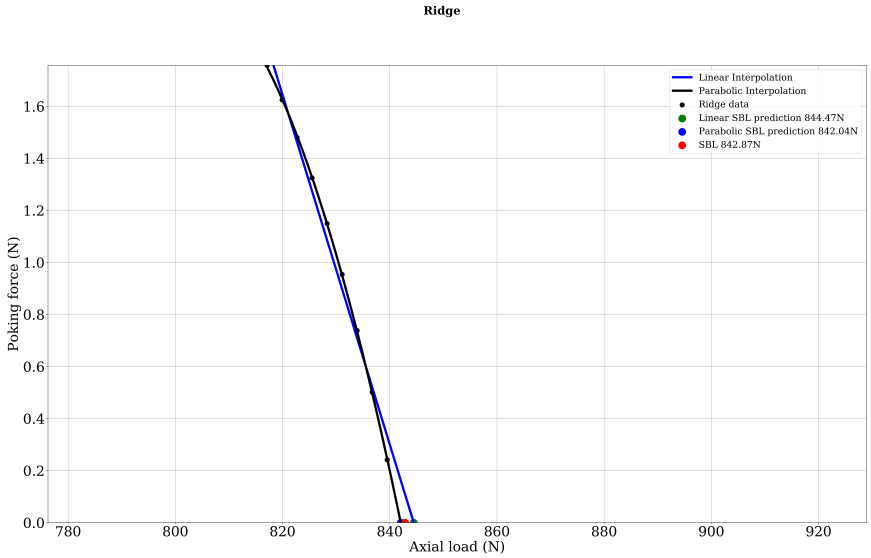

Figure B.4 – 2D projection of the ridge feature of the landscape associated with Specimen A4

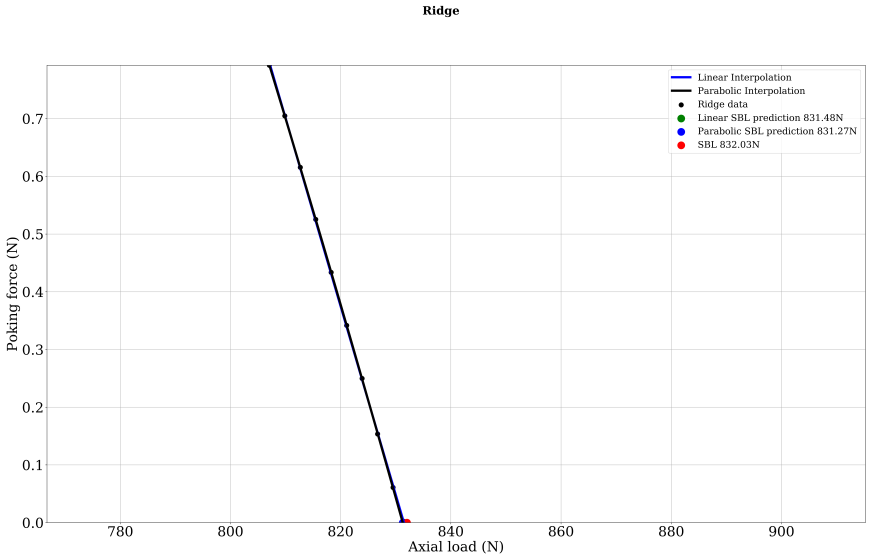

Figure B.5 – 2D projection of the ridge feature of the landscape associated with Specimen A5

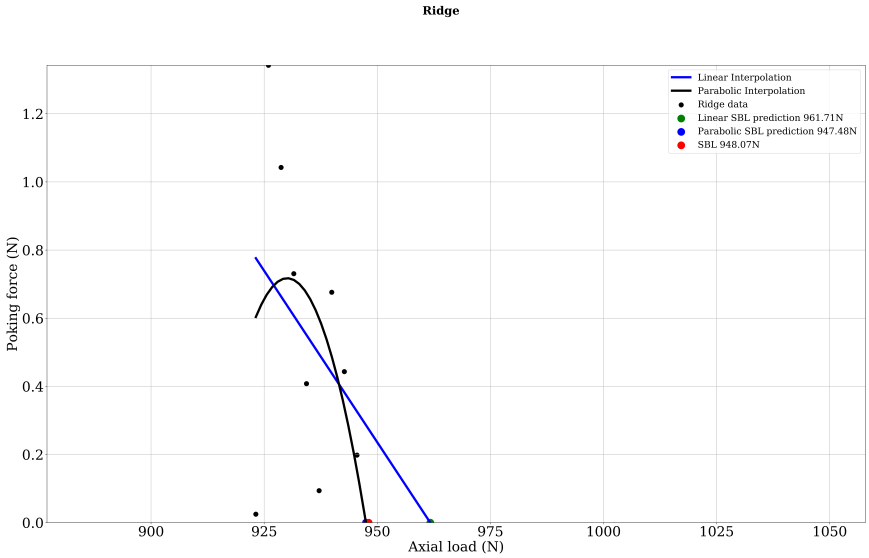

Figure B.6 – 2D projection of the ridge feature of the landscape associated with Specimen A6

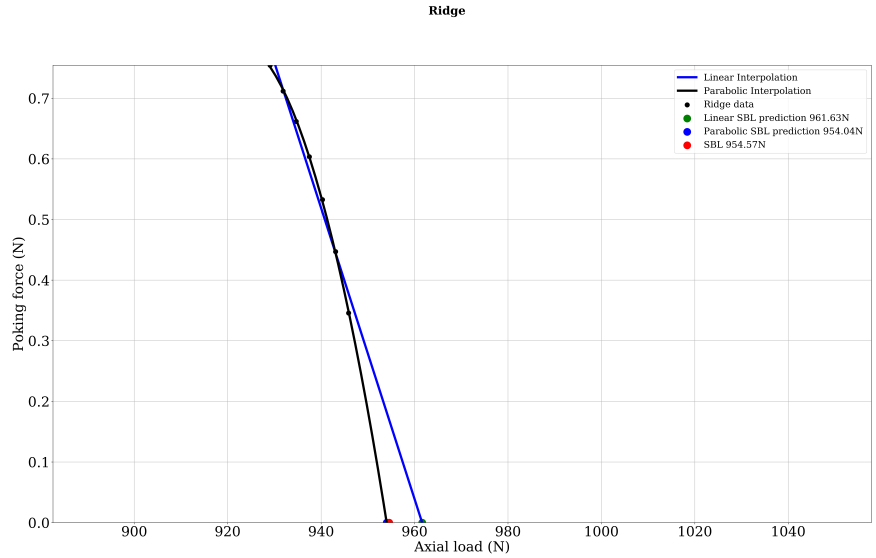

Figure B.7 – 2D projection of the ridge feature of the landscape associated with Specimen A7

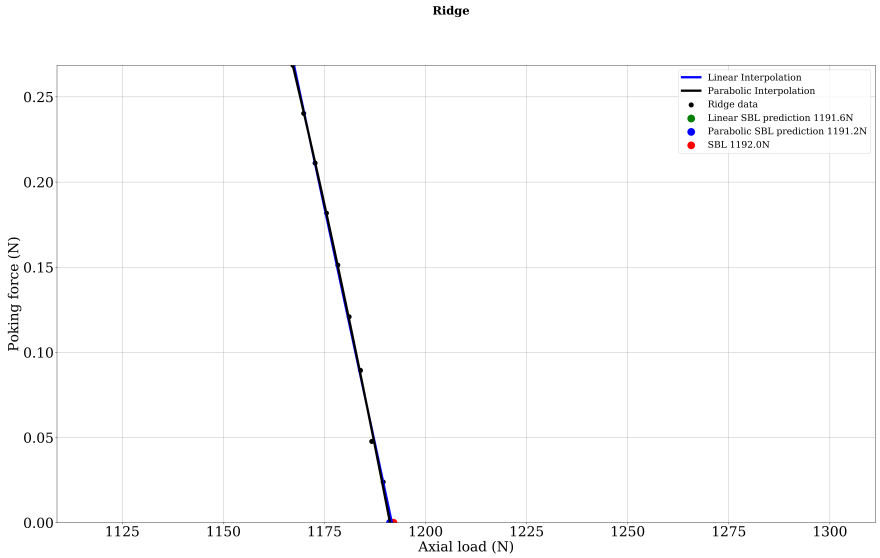

Figure B.8 – 2D projection of the ridge feature of the landscape associated with Specimen A8

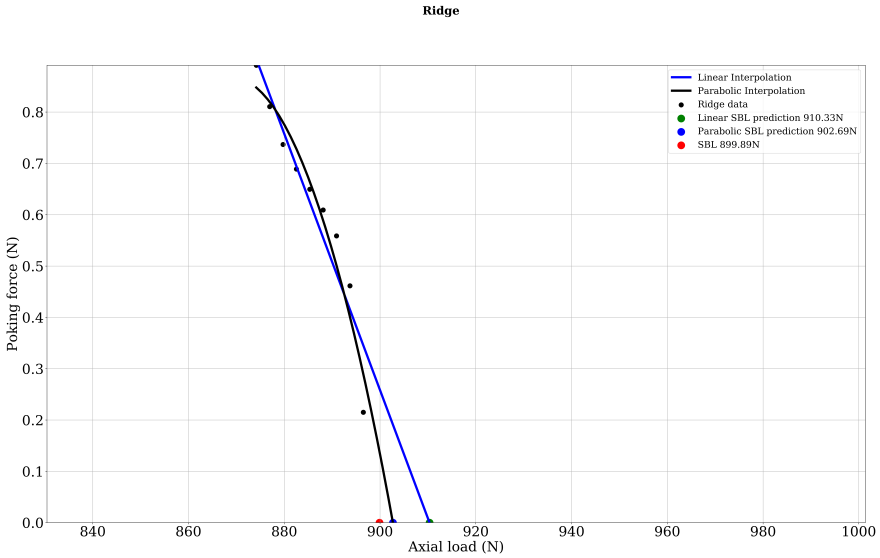

Figure B.9 – 2D projection of the ridge feature of the landscape associated with Specimen A9

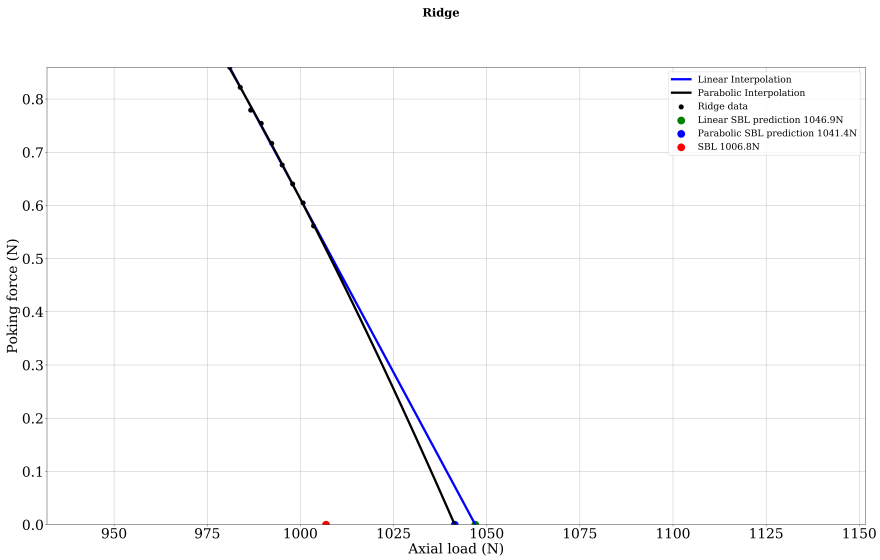

Figure B.10 – 2D projection of the ridge feature of the landscape associated with Specimen A10

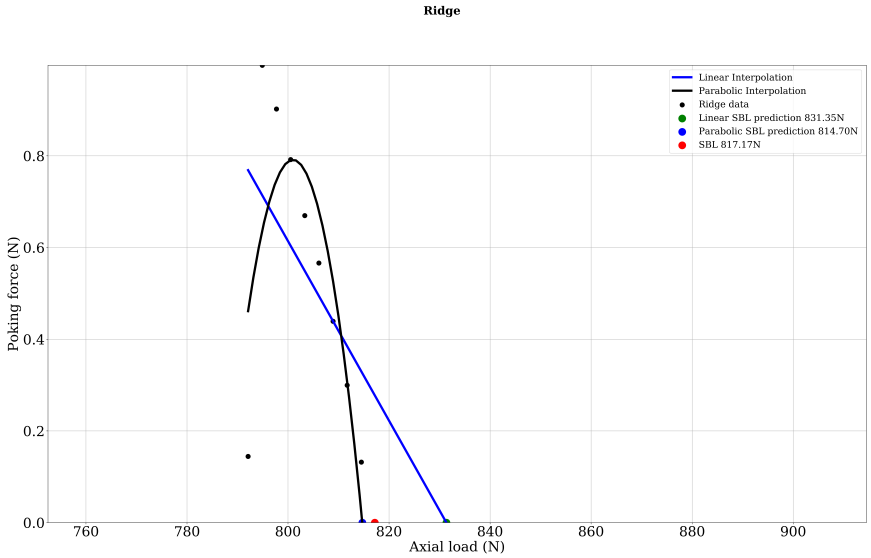

Figure B.11 – 2D projection of the ridge feature of the landscape associated with Specimen A11

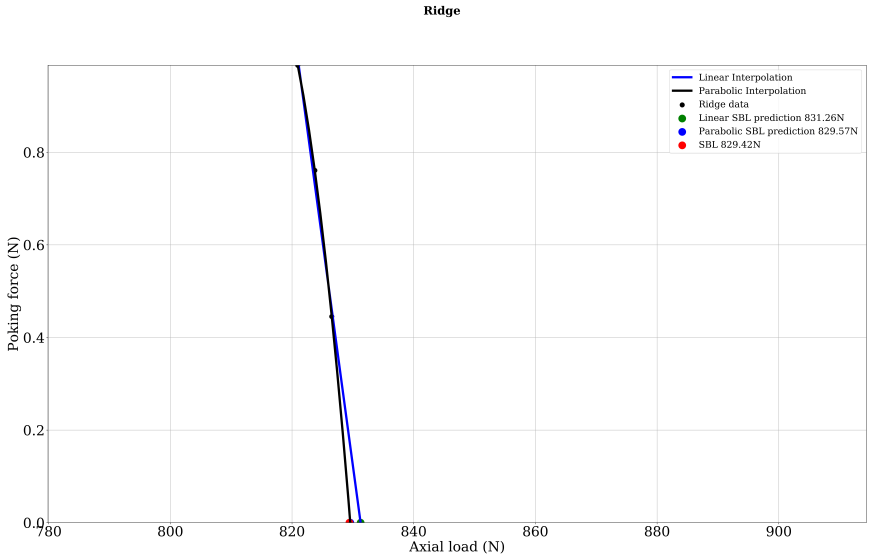

Figure B.12 – 2D projection of the ridge feature of the landscape associated with Specimen A12

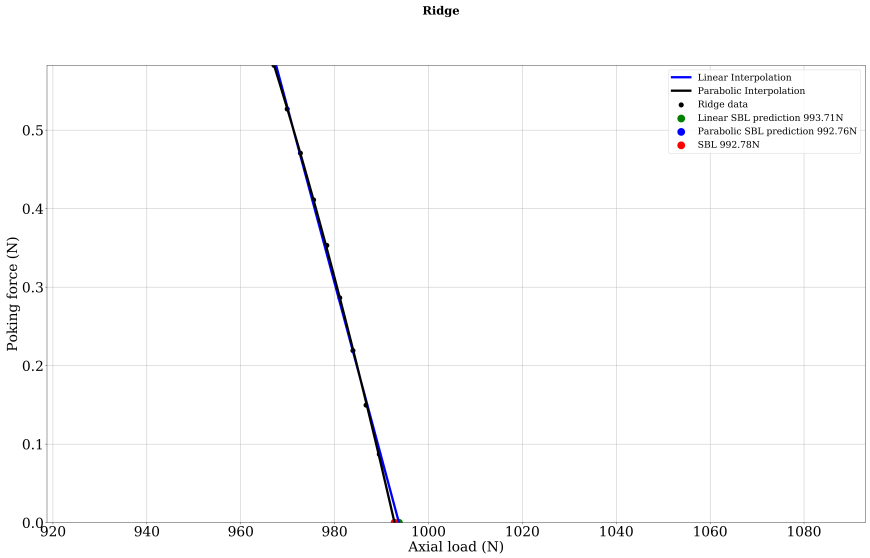

Figure B.13 – 2D projection of the ridge feature of the landscape associated with Specimen A13

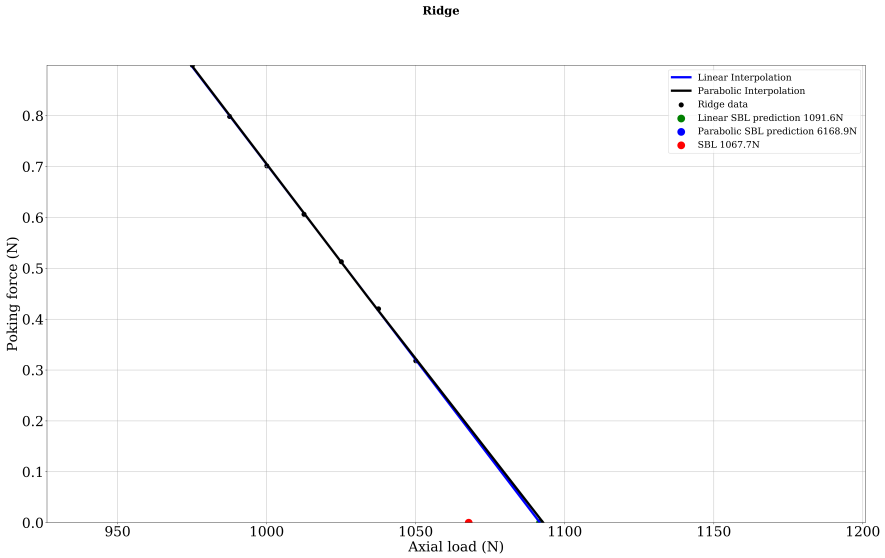

Figure B.14 – 2D projection of the ridge feature of the landscape associated with Specimen A14

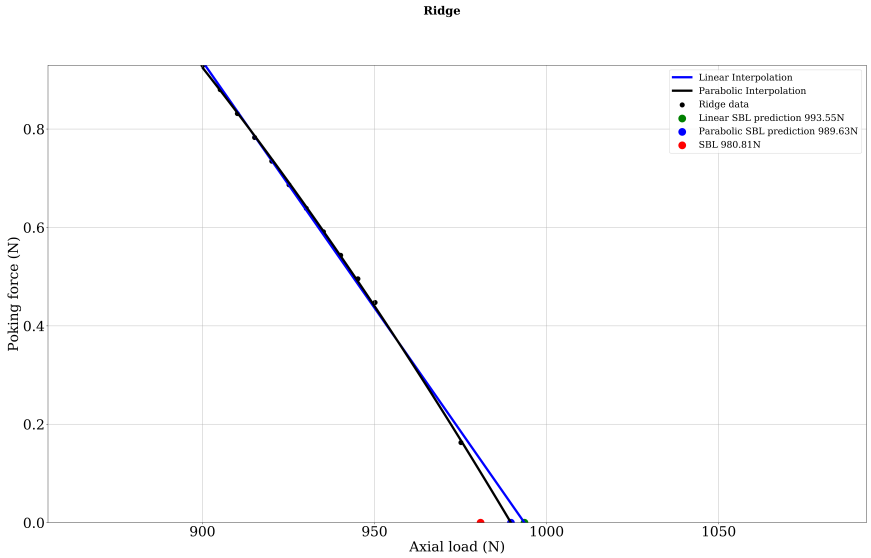

Figure B.15 – 2D projection of the ridge feature of the landscape associated with Specimen A15

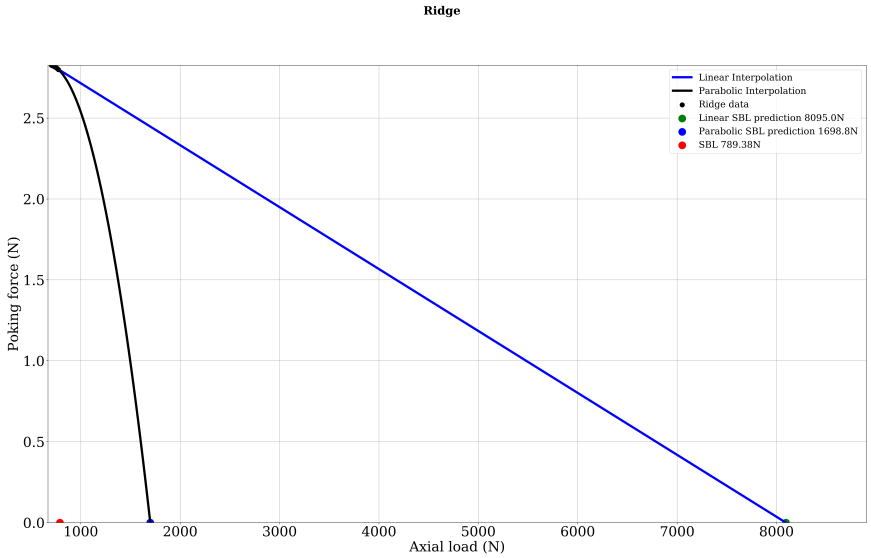

Figure B.16 – 2D projection of the ridge feature of the landscape associated with Specimen B1

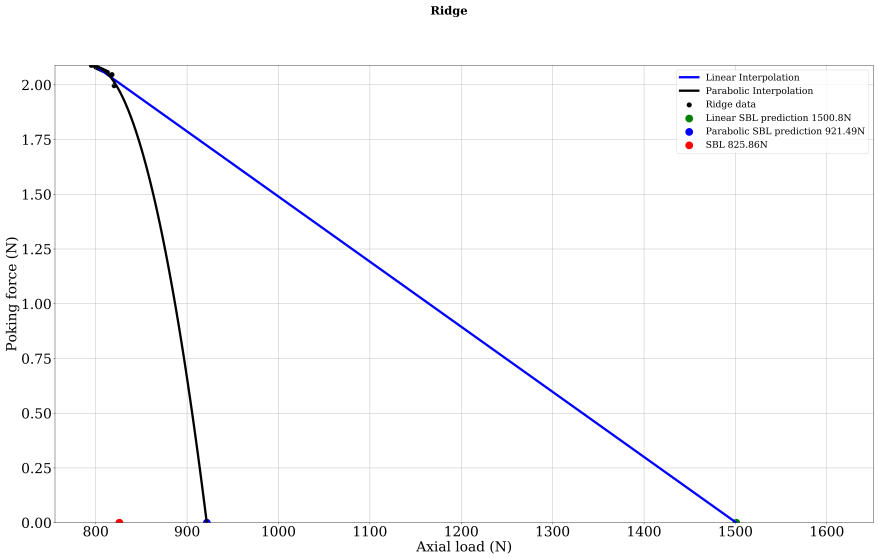

Figure B.17 – 2D projection of the ridge feature of the landscape associated with Specimen B2

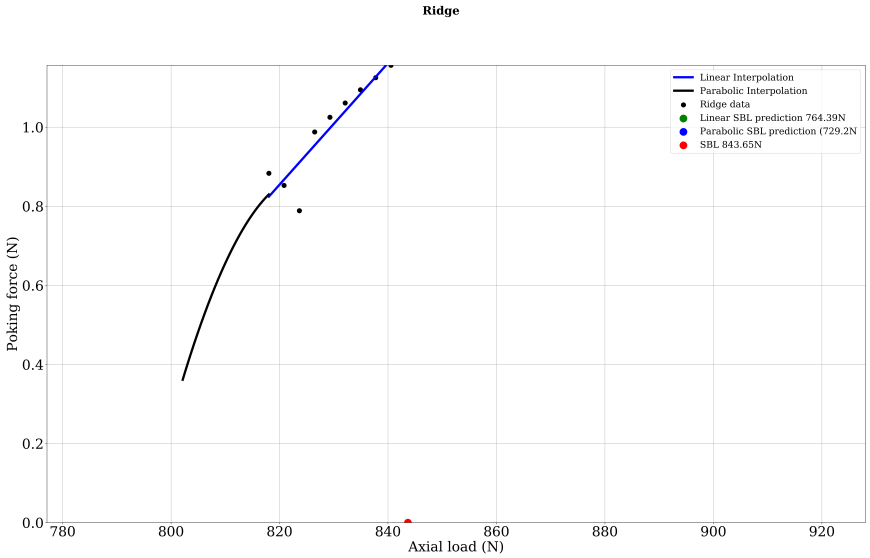

Figure B.18 – 2D projection of the ridge feature of the landscape associated with Specimen B3

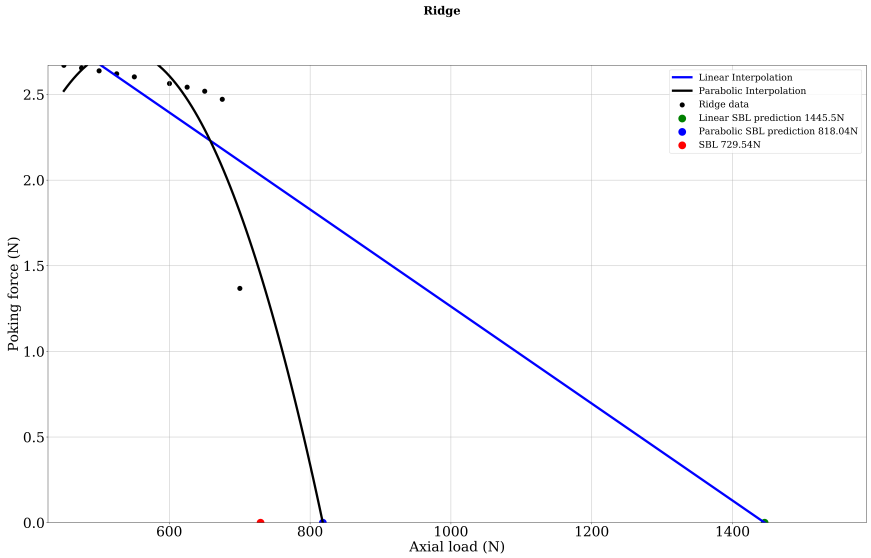

Figure B.19 – 2D projection of the ridge feature of the landscape associated with Specimen B4

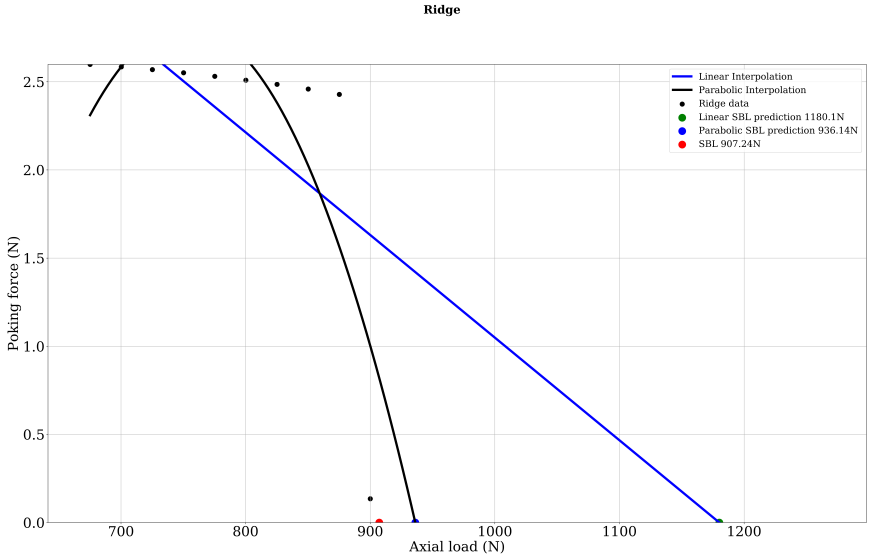

Figure B.20 – 2D projection of the ridge feature of the landscape associated with Specimen B5

Bibliography

Abbasi, A., Yan, D., and Reis, P. M. (2021). Probing the buckling of pressurized spherical shells. *Journal of the Mechanics and Physics of Solids*, 155(June):104545.

Abramian, A., Virot, E., Lozano, E., Rubinstein, S. M., and Schneider, T. M. (2020). Non-destructive Prediction of the Buckling Load of Imperfect Shells. *Physical Review Letters*, 125(22):225504.

Abramovich, H. (2021). The Vibration Correlation Technique – A reliable nondestructive method to predict buckling loads of thin walled structures. *Thin-Walled Structures*, 159:107308.

Airy, G. B. (1863). IV. On the strains in the Interior of beams. *Philosophical Transactions of the Royal Society of London*, 153:49–79.

Almroth, B., Brogan, F., and Marlowe, M. (1973). Stability Analysis of Cylinders with Circular Cutouts. *AIAA Journal*, 11(11):1582–1584.

Almroth, B. and Holmes, A. (1972). Buckling of shells with cutouts, experiment and analysis. *International Journal of Solids and Structures*, 8(8):1057–1071.

Amabili, M. (2003). A comparison of shell theories for large-amplitude vibrations of circular cylindrical shells: Lagrangian approach. *Journal of Sound and Vibration*, 264(5):1091–1125.

Amabili, M. (2008). *Non-Linear Vibrations and Stability of Shells and Plates*. Cambridge University Press, 1 edition.

Arbelo, M., Castro, S. G. P., Kalnins, K., and Khakimova, R. (2014a). Experimental characterization of buckling load on imperfect cylindrical shells using the multiple perturbation load approach. In *Proc. of European Conference on Spacecraft Structures and Materials Environmental Testing*.

Arbelo, M. A., Degenhardt, R., Castro, S. G., and Zimmermann, R. (2014b). Numerical characterization of imperfection sensitive composite structures. *Composite Structures*, 108:295–303.

Arbocz, J. and Starnes, J. H. (2002). Future directions and challenges in shell stability analysis. *Thin-Walled Structures*, 40:729–754.

Audoly, B. and Pomeau, Y. (2010). *Elasticity and Geometry: From hair curls to the nonlinear response of shells*.

Azimi, S. and Schneider, T. M. (2020). Self-similar invariant solution in the near-wall region of a turbulent boundary layer at asymptotically high Reynolds numbers. *Journal of Fluid Mechanics*, 888:A15.

Babcock, C. D. (1983). Shell Stability. *Journal of Applied Mechanics*.

Batdorf, S. B. (1947). A Simplified Method of Elastic-Stability Analysis for Thin Cylindrical Shells NACA-TR-874. Technical report, National Advisory committee for Aeronautics.

Batdorf, S. B., Schildcrout, M., and Stein, M. (1947). Critical stress of thin-walled cylinders in axial compression. NACA-TR-887. Technical report, National Advisory Commitee for Aeronautics.

Bathe, K.-J. (2014a). *Finite Element Procedures*. Prentice Hall, Pearson Education, Inc., 2 edition.

Bathe, K.-J. (2014b). *Finite Element Procedures*. Prentice Hall, Pearson Education, Inc., 2 edition.

Braides, A. (2002). *Gamma-Convergence for Beginners*. Oxford University Press.

Brogan, F. and Almroth, B. (1970). Buckling of cylinders with cutouts. *AIAA Journal*, 8(2):236–240.

Brothers, M. D., Foster, J. T., and Millwater, H. R. (2014). A comparison of different methods for calculating tangent-stiffness matrices in a massively parallel computational peridynamics code. *Computer Methods in Applied Mechanics and Engineering*, 279:247–267.

Brush, D. O., Jolly, W. L., and Almroth, B. O. (1975). *Buckling of Bars, Plates and Shells*. McGraw-Hill.

Budiansky, B. (1968). Notes on Nonlinear Shell Theory. *Journal of Applied Mechanics*, 35(2):393–401.

Burke, J. and Knobloch, E. (2006). Localized states in the generalized Swift-Hohenberg equation. *Physical Review E - Statistical, Nonlinear, and Soft Matter Physics*, 73(December 2005):056211.

Burke, J. and Knobloch, E. (2007). Homoclinic snaking: structure and stability. *Chaos*, 17(3):15,37102.

Calladine, C. (1995). Understanding imperfection-sensitivity in the buckling of thin-walled shells. *Thin-Walled Structures*, 23(1-4):215–235.

Castro, S. G. and Donadon, M. V. (2017). Assembly of semi-analytical models to address linear buckling and vibration of stiffened composite panels with debonding defect. *Composite Structures*, 160:232–247.

Castro, S. G., Mittelstedt, C., Monteiro, F. A., Arbelo, M. A., Degenhardt, R., and Ziegmann, G. (2015). A semi-analytical approach for linear and non-linear analysis of unstiffened laminated composite cylinders and cones under axial, torsion and pressure loads. *Thin-Walled Structures*, 90:61–73.

Castro, S. G., Zimmermann, R., Arbelo, M. A., and Degenhardt, R. (2013). Exploring the constancy of the global buckling load after a critical geometric imperfection level in thin-walled cylindrical shells for less conservative knock-down factors. *Thin-Walled Structures*, 72:76–87.

Champneys, A. (1998). Homoclinic orbits in reversible systems and their applications in mechanics, fluids and optics. *Physica D: Nonlinear Phenomena*, 112(1-2):158–186.

Champneys, A. R., Dodwell, T. J., Groh, R. M. J., Hunt, G. W., Neville, R. M., Pirrera, A., Sakhaei, A. H., Schenk, M., and Wadee, M. A. (2019). Happy Catastrophe: Recent Progress in Analysis and Exploitation of Elastic Instability. *Frontiers in Applied Mathematics and Statistics*, 5.

Chien, W.-Z. (1944a). The intrinsic theory of of thin shells and plates Part I -General theory-. *Quarterly of Applied Mathematics*, 1(4):297–327.

Chien, W.-Z. (1944b). The intrinsic theory of thin shells and plates. Part III -Application to thin shells-. *Quarterly of Applied Mathematics*, 2:120–135.

Ciarlet, P. (2000). *Mathematical Elasticity: Theory of Shells*, volume III. Academic Press, Elsevier.

Ciarlet, P. G. (1980). A justification of the von Karman equations. *Archive for Rational Mechanics and Analysis*, 73(4).

Ciarlet, P. G. and Paumier, J. C. (1986). A justification of the Marguerre-von Kármán equations. *Computational Mechanics*, 1(3):177–202.

Craig, J. I. and Duggan, M. F. (1973). Nondestructive shell-stability estimation by a combined-loading technique. *Experimental Mechanics*, 13(9):381–388.

Crisfield, M. (1981). A fast incremental/iterative solution procedure that handles "snap-through". *Computers & Structures*, 13(1-3):55–62.

Crisfield, M. A. (2012). *Non-Linear Finite Element Analysis of Solids and Structures: Second Edition*.

Darbyshire, A. G. and Mullin, T. (1995). Transition to turbulence in constant-mass-flux pipe flow. *Journal of Fluid Mechanics*, 289:83–114.

Dassault Systèmes Simulia Corp (2011). *Abaqus Theory Manual*.

Dassault Systems Simulia Corp. (2018). *Abaqus 6.14 Theory Guide*. Rising Sun Mills 166 Valley Street Providence, RI 02909-2499.

Davies, K. T., Huston, T. E., and Baranger, M. (1992). Calculations of periodic trajectories for the Hénon-Heiles Hamiltonian using the monodromy method. *Chaos*, 2(2):215–224.

Degenhardt, R., Kling, A., Zimmermann, R., Odermann, F., and de Araujo, F. C. (2012). Dealing with Imperfection Sensitivity of Composite Structures Prone to Buckling. In Coskun, D. S. B., editor, *Advances in Computational Stability Analysis*, pages 1–16.

Deml, M. and Wunderlich, W. (1997). Direct evaluation of the 'worst' imperfection shape in shell buckling. *Computer Methods in Applied Mechanics and Engineering*, 149(1-4):201–222.

Donnell, L. H. (1933). STABILITY OF THIN-WALLED TUBES UNDER TORSION. *National advisory committee for aeronautics*, 479.

Doyle, J. F. (2001). *Nonlinear Analysis of Thin-Walled Structures*. Springer New York, New York, NY.

Drew, H. R. and Pellegrino, S. (2002). *New Approaches to Structural Mechanics, Shells and Biological Structures*. Springer.

Elishakoff, I., Li, Y., and Starnes, J. (1996). Imperfection sensitivity due to the elastic moduli in the Roorda-Koiter frame. *Chaos, Solitons & Fractals*, 7(8):1179–1186.

Elishakoff, I., Manen, S. v., Vermeulen, P. G., and Arbocz, J. (1987). First-order second-moment analysis of the buckling of shells with random imperfections. *AIAA Journal*, 25(8):1113–1117.

Esslinger, M. (1970). Hochgeschwindigkeitsaufnahmen vom Beulvorgang duenwanndiger, axialbelasteter Zylinder. *Der Stahlbau*, 39(3):73–76.

Euler, L. (1759). On the Strength of Columns. *Academie Royale des Sciences et Belle Lettres Memoires*, Volume 13:252.

Fairbairn, W. (1859). I. On the resistance of tubes to collapse. *Proceedings of the Royal Society of London*, 9:234–238.

Fish, J. (2013). *A first course in Finite Elements*.

Flügge, W. (1932). Die Stabilität der Kreiszylinderschale. *Ingenieur-Archiv*, 3(5):463–506.

Fornberg, B. (1998). Calculation of Weights in Finite Difference Formulas. *SIAM Review*, 40(3):685–691.

Franzoni, F., Degenhardt, R., Albus, J., and Arbelo, M. A. (2019). Vibration correlation technique for predicting the buckling load of imperfection-sensitive isotropic cylindrical shells: An analytical and numerical verification. *Thin-Walled Structures*, 140:236–247.

Garcia, N. and Stoll, E. (1984). Monte Carlo Calculation for Electromagnetic-Wave Scattering from Random Rough Surfaces. *Physical Review Letters*, 52(20):1798–1801.

Gardner, N. W., Hilburger, M. W., Haynie, W. T., Lindell, M. C., and Waters, W. A. (2018). Digital Image Correlation Data Processing and Analysis Techniques to Enhance Test Data Assessment and Improve Structural Simulations. In *2018 AIAA/ASCE/AHS/ASC Structures, Structural Dynamics, and Materials Conference*, Reston, Virginia. American Institute of Aeronautics and Astronautics.

Gibson, J. E. (1965). *Linear Elastic Theory of Thin Shells*. Elsevier.

Gottlieb, D. and Orszag, S. A. (1977). *Numerical Analysis of Spectral Methods*. Society for Industrial and Applied Mathematics.

Groh, R. M. J. and Pirrera, A. (2019). On the role of localizations in buckling of axially compressed cylinders. *Proceedings of the Royal Society A: Mathematical, Physical and Engineering Sciences*, 475(2224):20190006.

Hansen, J. S. (1977). General random imperfections in the buckling of axially loaded cylindrical shells. *AIAA Journal*, 15(9):1250–1256.

Hart-Smith, L. (2015). Incontrovertible proof that the "discrepancies" in thin-shell-buckling studies are in the classical theory, not the test data. *Proceedings of the Institution of Mechanical Engineers, Part L: Journal of Materials: Design and Applications*, 229(5):398–402.

Haynie, W. and Hilburger, M. (2010). Comparison of Methods to Predict Lower Bound Buckling Loads of Cylinders Under Axial Compression. In *51st AIAA/ASME/ASCE/AHS/ASC Structures, Structural Dynamics, and Materials Conference
 18th AIAA/ASME/AHS Adaptive Structures Conference
 12th*, Reston, Virigina. American Institute of Aeronautics and Astronautics.

Hilburger, M. (2012). Developing the Next Generation Shell Buckling Design Factors and Technologies. In *53rd AIAA/ASME/ASCE/AHS/ASC Structures, Structural Dynamics and Materials Conference
20th AIAA/ASME/AHS Adaptive Structures Conference
14th AIAA*, Reston, Virigina. American Institute of Aeronautics and Astronautics.

Hilburger, M., Lovejoy, A., Thornburgh, R., and Rankin, C. (2012). Design and Analysis of Subscale and Full-Scale Buckling-Critical Cylinders for Launch Vehicle Technology Development. In *53rd AIAA/ASME/ASCE/AHS/ASC Structures, Structural Dynamics and Materials Conference
20th AIAA/ASME/AHS Adaptive Structures Conference
14th AIAA*, Reston, Virigina. American Institute of Aeronautics and Astronautics.

Hilburger, M. W. (2018). On the Development of Shell Buckling Knockdown Factors for Stiffened Metallic Launch Vehicle Cylinders. In *2018 AIAA/ASCE/AHS/ASC Structures, Structural Dynamics, and Materials Conference*, Reston, Virginia. American Institute of Aeronautics and Astronautics.

Hilburger, M. W., Lindell, M. C., Waters, W. A., and Gardner, N. W. (2018). Test and Analysis of Buckling-Critical Stiffened Metallic Launch Vehicle Cylinders. In *2018 AIAA/ASCE/AHS/ASC Structures, Structural Dynamics, and Materials Conference*, Reston, Virginia. American Institute of Aeronautics and Astronautics.

Hornung, P. and Velčić, I. (2015). Derivation of a homogenized von-Kármán shell theory from 3D elasticity. *Annales de l'Institut Henri Poincaré C, Analyse non linéaire*, 32(5):1039–1070.

Houghton, S. M. and Knobloch, E. (2011). Swift-Hohenberg equation with broken cubic-quintic nonlinearity. *Physical Review E - Statistical, Nonlinear, and Soft Matter Physics*, 84(1):016204.

Howell, P., Kozyreff, G., and Ockendon, J. (2009). *Applied Solid Mechanics*. Cambridge University Press.

Hühne, C., Rolfes, R., Breitbach, E., and Teßmer, J. (2008). Robust design of composite cylindrical shells under axial compression - Simulation and validation. *Thin-Walled Structures*, 46:947–962.

Hunt, G. W., Peletier, M. A., Champneys, A. R., Woods, P. D., Wadee, M. A., Budd, C. J., and Lord, G. J. (2000). Cellular buckling in long structures. *Nonlinear Dynamics*, 21:3–29.

Hutchinson, J. W. (2016). Buckling of spherical shells revisited. *Proceedings of the Royal Society A: Mathematical, Physical and Engineering Sciences*, 472(2195):20160577.

Hutchinson, J. W. and Thompson, J. M. T. (2017). Nonlinear Buckling Interaction for Spherical Shells Subject to Pressure and Probing Forces. *Journal of Applied Mechanics*, 84(6).

Hutchinson, J. W. and Thompson, J. M. T. (2018). Imperfections and energy barriers in shell buckling. *International Journal of Solids and Structures*, 148-149:157–168.

Hutchinson J.W. (1970). Elastic- plastic behavior of polycrystalline metals and composites. *Proc Roy Soc Ser A Math Phys Sci*, 319(1537):247–272.

Jiménez, J. (2018). Coherent structures in wall-bounded turbulence. *Journal of Fluid Mechanics*, 842:P1.

Jorabchi, K. and Suresh, K. (2011). A robust continuation method to pass limit-point instability. *Finite Elements in Analysis and Design*, 47(11):1253–1261.

Kawahara, G., Uhlmann, M., and van Veen, L. (2012). The Significance of Simple Invariant Solutions in Turbulent Flows. *Annual Review of Fluid Mechanics*, 44(1):203–225.

Khakimova, R., Warren, C. J., Zimmermann, R., Castro, S. G., Arbelo, M. A., and Degenhardt, R. (2014). The single perturbation load approach applied to imperfection sensitive conical composite structures. *Thin-Walled Structures*, 84:369–377.

Kirchhoff, G. and Hensel, K. (1883). *Vorlesungen über mathematische Physik*, volume 1. BG Teubner.

Kirchhoff, G. R. (1850). Uber das gleichgewicht und die bewegung einer elastischen Scheibe. *Journal für die reine und angewandte Mathematik*.

Knobloch, E. (1986a). On the degenerate Hopf bifurcation with O(2) symmetry. *Contemporary Mathematics*, 56.

Knobloch, E. (1986b). Oscillatory convection in binary mixtures. *Physical Review A*, 34(2):1538–1549.

Koiter, W. T. (1945). *The Stability of Elastic Equilibrium*. PhD thesis, Techische Hooge School Delft.

Koiter, W. T. (1966). On the nonlinear theory of thin elastic shells. *Proc. Kon. Ned. Akad. Wetensch.*

Koiter, W. T. (2008). *W. T. Koiter's Elastic Stability of Solids and Structures*. Cambridge University Press, Cambridge.

Kosztowny, C. J. (2021). Implementing Geometric Surface Imperfections into Sandwich Composite Cylinder Finite Element Method Models. In *AIAA Scitech 2021 Forum*, Reston, Virginia. American Institute of Aeronautics and Astronautics.

Kreilos, T. and Eckhardt, B. (2012). Periodic orbits near onset of chaos in plane Couette flow. *Chaos: An Interdisciplinary Journal of Nonlinear Science*, 22(4):047505.

Kreilos, T., Gibson, J. F., and Schneider, T. M. (2016). Localized travelling waves in the asymptotic suction boundary layer. *Journal of Fluid Mechanics*, 795:R3.

Kreilos, T. and Schneider, T. M. (2017). Fully localized post-buckling states of cylindrical shells under axial compression. *Proceedings of the Royal Society A: Mathematical, Physical and Engineering Science*, 473(2205):20170177.

Kriegesmann, B., Jansen, E. L., and Rolfes, R. (2016). Design of cylindrical shells using the Single Perturbation Load Approach – Potentials and application limits. *Thin-Walled Structures*, 108:369–380.

Landau, L. D. and Lifshitz, E. M. (1970). *Theory of Elasticity*.

Lekkerkerker, J. G. (1965). *On the stress distribution on cylindrical shells weakened by a hole*. PhD thesis, TU Delft.

Lemaitre, J. (2001). *Handbook of Materials Behavior Models*. Elsevier Inc.

Lewicka, M. P. M. m. t. P. M., Mora, M., and Pakzad, M. (2010). Shell theories arising as low energy Γ-limit of 3d nonlinear elasticity. *Annali della Scuola normale superiore di Pisa, Classe di scienze*, 9(2):253–295.

Liu, G.R. Quek, S. S. (2003). *The Finite Element Method. A Practical Course*.

Liu, Y., Zaki, T. A., and Durbin, P. A. (2008). Floquet analysis of secondary instability of boundary layers distorted by Klebanoff streaks and Tollmien–Schlichting waves. *Physics of Fluids*, 20(12):124102.

Lorenz, R. (1911). Die nicht-achsensymmetrische Knickung dünnwandiger Hohlzylinder. *Physikalische Zeitschrift Leibzig*.

Love, A. E. H. (1888). I. The small free vibrations and deformation of a thin elastic shell. *Proceedings of the Royal Society of London*, 43(258-265):352–353.

Love, A. E. H. (1927). *A Treatise on the Mathematical Theory of Elasticity*.

Lovejoy, A. E. and Hilburger, M. W. (2013). SBKF Modeling and Analysis Plan: Buckling Analysis of Compression-Loaded Orthogrid and Isogrid Cylinders. Technical report, NASA.

Lovejoy, A. E., Hilburger, M. W., and Gardner, N. W. (2018). Test and Analysis of Full-Scale 27.5-Foot-Diameter Stiffened Metallic Launch Vehicle Cylinders. In *2018 AIAA/ASCE/AHS/ASC Structures, Structural Dynamics, and Materials Conference*, Reston, Virginia. American Institute of Aeronautics and Astronautics.

Lundquist, E. E. (1934). Strength Tests of Thin-Walled Duralumin Cylinders in Compression, NACA-TR-473. Technical report, NACA.

Maso, G. (1993). *An Introduction to Γ-Convergence*, volume 8. Birk\"uauser.

Megson, T. H. G. (2007). *Aircraft Structures for engineering students*. Butterworth-Heinemann, 4 edition.

Mikulas, M., Nemeth, M., Oremont, L., and Jegley, D. (2011). Effect of Boundary Conditions on the Axial Compression Buckling of Homogeneous Orthotropic Composite Cylinders in the Long Column Range. In *52nd AIAA/ASME/ASCE/AHS/ASC Structures, Structural Dynamics and Materials Conference*, Reston, Virigina. American Institute of Aeronautics and Astronautics.

Müller, M. (2007). Passing of instability points by applying a stabilized Newton–Raphson scheme to a finite element formulation: Comparison to arc-length method. *Computational Mechanics*, 40(4):683–705.

Mullin, T. (2011). Experimental studies of transition to turbulence in a pipe. *Annual Review of Fluid Mechanics*, 43(1):1–24.

Mushtari, K. and Galimov, K. (1961). Non-linear theory of thin elastic shells. Technical report, Israel Program for Scientific Translations.

Nagata, M. (1990). Three-dimensional finite-amplitude solutions in plane Couette flow: bifurcation from infinity. *Journal of Fluid Mechanics*, 217(-1):519–527.

Niordson, F. (1985). *Shell Theory*, volume 29. North Holland.

Okubo, S., Wilson, P. E., and Whittier, J. S. (1970). Influence of Concentrated Lateral Loads on the Elastic Stability of Cylinders in Bending. *Experimental Mechanics*, pages 384–389.

Orszag, S. A. (1971). Accurate solution of the Orr–Sommerfeld stability equation. *Journal of Fluid Mechanics*, 50(04):689–703.

Page, J., Dubief, Y., and Kerswell, R. R. (2020). Exact Traveling Wave Solutions in Viscoelastic Channel Flow. *Physical Review Letters*, 125(15):154501.

Ramm, E. (1981). Strategies for Tracing the Nonlinear Response Near Limit Points. In *Nonlinear Finite Element Analysis in Structural Mechanics*, pages 63–89. Springer Berlin Heidelberg, Berlin, Heidelberg.

Rayleigh, L. (1877). *The Theory of Sound*, volume 1. The Macmillan Company, New York, 1 edition.

Reddy, J. N. (2007). *Theory and Analysis of Elastic Plates and Shells*. CRC Press, 2 edition.

Reddy, J. N. (2013). *An Introduction to Continuum Mechanics*. Cambridge University Press, 2 edition.

Reetz, F., Kreilos, T., and Schneider, T. M. (2019). Exact invariant solution reveals the origin of self-organized oblique turbulent-laminar stripes. *Nature Communications*, 10(1):2277.

Reissner, E. (1945). The Effect of Transverse Shear Deformation on the Bending of Elastic Plates. *Journal of Applied Mechanics*, 12(2):A69–A77.

Ricardo, O. G. S. (1967). An experimental investigation of the radial displacements of a thin-walled cylinder. Technical report, NASA / California Inst. of Tech. Pasadena, Pasadena.

Riks, E. (1979). An incremental approach to the solution of snapping and buckling problems. *International Journal of Solids and Structures*, 15(7):529–551.

Ritz, W. (1908). Über eine neue Methode zur Lösung gewisser Variationsprobleme der mathematischen Physik. *Journal für Reine und Angewandte Mathematik*, 135:1–61.

Roorda, J. and Hansen, J. S. (1972). Random buckling behavior in axially loaded cylindrical shells with axisymmetric imperfections. *Journal of Spacecraft and Rockets*, 9(2):88–91.

Sanders, J. L. (1959). An Improved first-approximation theory for thin shells. *NASA Technical Report R-24*.

Schenk, C. and Schuëller, G. (2007). Buckling analysis of cylindrical shells with cutouts including random boundary and geometric imperfections. *Computer Methods in Applied Mechanics and Engineering*, 196(35-36):3424–3434.

Schneider, T. M. and Eckhardt, B. (2006). Edge of chaos in pipe flow. *Chaos: An Interdisciplinary Journal of Nonlinear Science*, 16(4):041103.

Schneider, T. M., Gibson, J. F., and Burke, J. (2010). Snakes and Ladders: Localized Solutions of Plane Couette Flow. *Physical Review Letters*, 104(10):104501.

Seide, P., W. V. M. E. (1969). NASA SP-8007:Buckling of thin-walled circular cylinders. Technical report, NASA.

Southwell, R. V. (1914). V. On the general theory of elastic stability. *Philosophical Transactions of the Royal Society of London. Series A, Containing Papers of a Mathematical or Physical Character*, 213(497-508):187–244.

Southwell, V. (1932). On the analysis of experimental observations in problems of elastic stability. *Proceedings of the Royal Society of London. Series A, Containing Papers of a Mathematical and Physical Character*, 135(828):601–616.

Starnes, J. H. (1970). *The effect of a circular hole on the buckling of cylindrical shells*. PhD thesis, Caltech.

Starnes, J. H. (1972). Effect of a circular hole on the buckling of cylindrical shells loaded by axial compression. *AIAA Journal*, 10(11):1466–1472.

Strogatz, S. H. (1994). *Nonlinear dynamics and chaos: With applications to physics, biology, chemistry, and engineering*.

Thompson, J. M. T. (1969). A general theory for the equilibrium and stability of discrete conservative systems. *Zeitschrift für angewandte Mathematik und Physik ZAMP*, 20(6):797–846.

Thompson, J. M. T. and Sieber, J. (2016). Shock-Sensitivity in Shell-Like Structures: With Simulations of Spherical Shell Buckling. *International Journal of Bifurcation and Chaos*, 26(02):1630003.

Timoshenko, S. (1964). *Theory of Plates and Shells*.

Timoshenko, S. (1985). *Theory Pf Elastic Stability*.

Timoshenko, T. (1914). Buckling of a cylindrical shell under the action under the uniform axial pressure. *Bulletin of the Electrotechnical Institute*.

Toda, S. (1974). *The effects of elliptic and rectangular cutouts on the buckling of cylindrical shells loaded by axial compression*. PhD thesis, Caltech.

Toda, S. (1983). Buckling of cylinders with cutouts under axial compression. *Experimental Mechanics*, 23(4):414–417.

Uriol, I., Bisagni, C., and Hilburger, M. (2020). Scaling methodology applied to buckling of sandwich composite cylindrical shells. *AIAA Journal*.

Van Dyke, P. (1965). Stresses about a circular hole in a cylindrical shell. *AIAA Journal*, 3(9):1733–1742.

Virot, E., Kreilos, T., Schneider, T. M., and Rubinstein, S. M. (2017). Stability Landscape of Shell Buckling. *Physical Review Letters*, 119(22):224101.

Vlasov, V. Z. (1958). Basic differential equations in general theory of elastic shells. *NACA Technical Memorandum 1241*.

Von Karman, T., Dunn, L. G., and Tsien, H.-S. (1940). The Influence of Curvature on the Buckling Characteristics of Structures. *Journal of the Aeronautical Sciences*, 7(7):276–289.

Von Karman, T. and Tsien, H.-S. (1941). The buckling of thin cylindrical shells under axial compression. *Journal of Aeronautical Science*, 8.

Wagner, H., Hühne, C., and Niemann, S. (2016). Constant single-buckle imperfection principle to determine a lower bound for the buckling load of unstiffened composite cylinders under axial compression. *Composite Structures*, 139:120–129.

Wagner, H., Sosa, E., Ludwig, T., Croll, J., and Hühne, C. (2019). Robust design of imperfection sensitive thin-walled shells under axial compression, bending or external pressure. *International Journal of Mechanical Sciences*, 156:205–220.

Weller, T., Singer, J., and Arbocz, J. (2002). *Buckling Experiments: Experimental Methods in Buckling of Thin-Walled Structures*.

Wullschleger, L. (2006). *Numerical investigation of the buckling behaviour of axially compressed circular cylinders having parametric initial dimple imperfections*. PhD thesis, ETH Zürich.

Yamaki, N. (1984). *Elastic stability of circular cylindrical shells*. North-Holland, Amsterdam, 1984.

Yang, D. and Pezzulla, M. (2020). Buckling of pressurized spherical shells containing a through thickness defect. *Journal of the Mechanics and Physics of Solids*, 138.

Yılmaz, A. O. and Güdekli, E. (2021). Dynamical system analysis of FLRW models with Modified Chaplygin gas. *Scientific Reports*, 11(1):2750.

Zienkiewicz, O. C. (2013). The Finite Element Method: Its Basis and Fundamentals. *The Finite Element Method: its Basis and Fundamentals*, page iii.

Emilio Lozano
EPFL - ECPS, MED 2 2923, Station 9, 1015 Lausanne, Switzerland
(+41) 767467930
emilio.lozano@epfl.ch

EDUCATION

M.Sc. Aerospace Engineering, KTH - Royal Institute of Technology
Stockholm, Sweden. September 2011 - June 2013.

- Thesis: Minimum weight design of shell launcher structures

B.Sc. Aerospace Engineering, Universidad Politécnica de Madrid
Madrid, Spain. September 2006 - July 2011.

- Thesis: Characterization of aeroeslastic behaviour of propellers at low Reynolds number

EXPERIENCE

Teaching Assistant at EPFL November 2016 - Present
ECPS
Lausanne, VD, Switzerland.

- Course: Fluid Mechanics

PhD Candidate at EPFL November 2016 - Present
ECPS.
Lausanne, VD, Switzerland.

- Thesis work: Non-destructive prediction of the buckling load of cylindrical shells.

Development engineer January - October 2016
SAAB Aerostructures
Aerostructures analysis group
Linkoping, Sweden.

- Analysis and testing of A312neo primary structure.

Researcher June - December 2015
DLR Lightweight construction institute
Braunschweig, Germany.

- Study of the buckling behavior of cylindrical shell in the framework of Ariane 6 pre-development phase.

Development engineer January 2015 - October 2015
Airbus DS Structural analysis group
Friedrichshafen, Germany.

- Development of SAR satellite platforms R&D in the framework of the Copernicus program

Development engineer January 2013 and December 2015
Airbus DS Structural analysis group
Bremen, Germany.

- Sizing and testing of cryogenic fuel systems for the Ariane program. Vega-C upper stage tank development. R&D activities in the field of cryogenic applications of composite materials, preliminary design tools & shell buckling.